

UNDERSTANDING AND PREDICTING MICROBURSTS

by

MARILYN MITCHELL WOLFSON

S.M., Meteorology
Massachusetts Institute of Technology, 1983

B.S., Atmospheric and Oceanic Science
University of Michigan, 1979

Submitted to the Department of Earth, Atmospheric, and Planetary Science
in Partial Fulfillment of the Requirements of the Degree of
Doctor of Philosophy in Meteorology

at the

Massachusetts Institute of Technology

February, 1990

© Massachusetts Institute of Technology, 1990
All rights reserved

Signature of Author _____
Center for Meteorology and Physical Oceanography
Department of Earth, Atmospheric, and Planetary Science
February 9, 1990

Certified by _____
Kerry A. Emanuel
Professor and Director, Center for Meteorology and Physical Oceanography
Department of Earth, Atmospheric, and Planetary Science
Thesis Supervisor

Accepted by _____
Thomas H. Jordan
Department of Earth, Atmospheric, and Planetary Science
Chairman, Department Committee

MASSACHUSETTS INSTITUTE
OF TECHNOLOGY
WITHDRAWN
MAR 28 1990
FROM
MIT LIBRARIES
Lindgren

UNDERSTANDING AND PREDICTING MICROBURSTS

by

MARILYN MITCHELL WOLFSON

Submitted to the Department of Earth, Atmospheric, and Planetary Science
on February 9, 1990 in partial fulfillment of the requirements for the Degree of
Doctor of Philosophy in Meteorology

ABSTRACT

The microburst, a form of divergent low altitude wind shear, has been identified as the cause of several major aircarrier accidents in the United States. It is known that microbursts are associated with thunderstorms; most researchers accept the microburst as equivalent to the precipitation driven downdraft of the thunderstorm. A heuristic model for predicting the downdraft and outflow strength of thunderstorms given radar data and an environmental sounding, is developed based on the vertical momentum and continuity equations.

There are a number of dynamically distinct phenomena apart from the precipitation driven downdraft that can cause low altitude downdrafts and strong surface winds near thunderstorms. These phenomena are carefully differentiated and examined. My primary hypothesis is that some of the phenomena called microbursts are not part of the precipitation driven thunderstorm downdraft, as has been assumed. They are the downward branch of the violent circulating flow that develops at the leading edge of new thunderstorm outflow. When the environment into which the thunderstorm air is flowing is stratified, an undular gravity current or solitary waves can form, and I hypothesize that nonlinear gravity wave dynamics contribute to the development of low altitude downdrafts, and regions of aircraft hazard in these cases.

The primary conclusion of this work is that the fatal aircraft accidents attributed to microbursts, including the first accident for which the microburst terminology was developed, all involved the *combination* of a precipitation driven downdraft and a gust front, the turbulent region at the leading edge of old thunderstorm outflow. The stratification of the environment caused by the presence of old outflow air changes the new thunderstorm outflow pattern very little in the first 5 min when the aircraft hazard is greatest; it is only at later stages that differences arise, when the outflow eventually triggers nonlinear gravity waves ahead along the inversion duct.

In terms of the hazard to aviation, the significance of the presence of a thin layer of preexisting outflow air at the surface is not that it is capable of supporting gravity waves triggered by new outflow development. The significance is actually the extreme turbulence hazard of the gust front itself at the leading edge of the old outflow. When a thunderstorm outflow forms on top of an existing gust front, two hazardous regions become juxtaposed that would otherwise be physically separate. This combination may be what was first called a downburst, and later a microburst, by Fujita and Byers (1977).

Thesis Supervisor: Dr. Kerry A. Emanuel
Title: Professor of Meteorology
Director, Center for Meteorology and Physical Oceanography
Department of Earth, Atmospheric, and Planetary Science

DEDICATION

This thesis is dedicated to Tetsuya Theodore Fujita. His conceptual depictions of low altitude wind shear patterns, often clairvoyantly based on very few, hard-gathered data, have consistently been found to be remarkably accurate. He sparked wide research interest that has already greatly benefited the aviation community, and has rekindled meteorological interest in thunderstorm phenomenology. In the final analysis it is his word – *microburst* – and so it is to him that I dedicate mine.

ACKNOWLEDGEMENTS

Most graduate students can identify someone whose help was so important that without it, their thesis could not or would not have been completed. In my case, I can identify two – Jim Evans at MIT Lincoln Laboratory and John Anderson at the University of Wisconsin. Jim Evans recommended that Lincoln support me and continue to support me on their staff associate program, allowed me to use the facilities there to perform my research, and encouraged me constantly to finish up! And John Anderson first connected me with Lincoln long ago, and placed a high priority on performing numerical outflow simulations for my thesis at Wisconsin; discussions with him over the model results helped tremendously in focussing specific areas for research. Thank you. I *really* appreciate your help.

I thank all the members of my thesis committee – Kerry Emanuel, Fred Sanders, Earle Williams, and John Anderson – for their valuable comments and suggestions along the way and, most of all, for largely leaving me alone to pursue my own applied research interests. Kerry's and Earle's critical review of successive drafts of the thesis improved it tremendously. And Fred's timely encouragement ultimately improved it tremendously too.

Special thanks to Jerry Straka at the University of Wisconsin, who cheerfully and skillfully performed the numerical modelling experiments described in this thesis, on a whole host of computers and in a whole host of configurations. He worked late at night, on weekends, all sorts of odd times, like the magician who can keep several plates spinning aloft simultaneously without breaking a one, and managed to get the results to me on tape in record time! My correspondence with a number of other colleagues helped a great deal in focussing my research, too. I thank them all, especially Dick Doviak.

At Lincoln Laboratory, and this is the hard part, there are so many to thank. Not only for keeping my place warm so that returning to work was a seamless transition, but for their help on various parts of the thesis, with the facilities, and with "administration". Thank you to one and all, but especially Joe Cullen, Barb Forman, Rich DeLaura, Paul Biron, Lyn Neilley, Margo Liepins, Greg Rappa, Pat Pawlak, Mark Merritt, Beth Ducot, Mel Stone, Sue MacKay, and last but not least, the incredible library staff!

And finally, special thanks to my family and friends who periodically and faithfully dragged me away from the thesis. Of course, that helped the most of all.

CONTENTS

ABSTRACT	2
DEDICATION	3
ACKNOWLEDGEMENTS	4
CONTENTS	5
ACRONYMS AND ABBREVIATIONS	8
I. INTRODUCTION	9
A. Historical Perspective	9
B. The Microburst Aircraft Hazard	13
C. Hypotheses	17
D. Organization of the Thesis	19
II. THUNDERSTORM DOWNDRAFTS AND OUTFLOWS	22
A. Observations	22
1) Thunderstorms with Significant Surface Rainfall	22
2) Dry Thunderstorms	28
3) Environmental Characteristics	30
4) The Wall Jet Analogy	33
B. Effects on Low Altitude Aircraft Operations	38
C. Thunderstorms versus Microbursts	42
D. Predicting Thunderstorm Downdraft and Outflow Strength	45
1) Summary of Numerical Modelling Results	47
2) Derivation of Heuristic Prediction Model	52
3) Prediction Equations	57
(i) Vertical velocity	57
(ii) Outflow velocity	58
(iii) Comparison with Proctor's Microburst Index	59
(iv) Application of model to four storm cases	60
E. Summary	62
III. PENETRATIVE DOWNDRAFTS	65
A. Hypothesis for Microbursts	65
B. Test of Hypothesis	66
C. A Possible Example	69
1) Measurements	69
2) Synoptic Summary	70

3) Radar Data Analysis	71
4) Mesonet Data Analysis	77
5) Discussion	79
D. Summary	85
IV. LOW ALTITUDE DOWNDRAFTS IN THUNDERSTORM OUTFLOWS: NEUTRAL BOUNDARY LAYER	87
A. Pre-existing Vortex Ring Around Descending Downdraft	91
B. Frontal Circulation	98
C. Leading Vortex Ring Structure in Axisymmetric Outflow	100
1) Thunderstorm Outflow Examples	101
2) Physical Explanation of Leading Ring Formation	107
3) Laboratory Experiments	112
4) Numerical Experiment	114
D. Multiple Ring Structure in Axisymmetric Outflow	116
1) Physical Explanation of Consecutive Ring Formation	116
2) Laboratory Experiments	118
3) Numerical Experiments	121
E. Kelvin-Helmholtz Instability in the Outflow	126
1) KHI in Atmospheric Boundary Layer	127
2) Presence of KHI in Surface Gravity Currents	128
(i) Numerical simulations	128
(ii) Observations and interpretations	131
F. Horizontal Shear Instabilities	135
G. Summary	139
V. LOW ALTITUDE DOWNDRAFTS IN THUNDERSTORM OUTFLOWS: STRATIFIED BOUNDARY LAYER	142
A. Nonlinear Gravity Waves	143
B. Solitary Waves	143
C. Observations of Thunderstorm Generated Solitary Waves	147
D. Effect of Stratified Boundary Layer on Newly Formed Outflow	156
1) Laboratory Experiments	156
2) Numerical Experiments	158
(i) Model results	159
(ii) Quantitative assessment of aircraft hazard	170
(iii) Summary	175
E. Microbursts and Rotors as Solitary Waves	175

F. Variable Source Strength	178
1) Observations	179
2) Laboratory Experiments	182
3) Numerical Experiments	183
G. Summary	188
VI. ANOTHER LOOK AT THE FATAL MICROBURST AIRCRAFT ACCIDENTS .	192
A. DFW	192
B. New Orleans	201
C. JFK	204
D. Summary	204
VII. CONCLUSIONS	208
APPENDIX A. Derivation of Prediction Equations	211
1) Physical Explanations for Numerical Modelling Results	211
(i) Radius of the rain core	211
(ii) Liquid water mixing ratio	215
(iii) Environmental lapse rate	218
(iv) Height of the transition level (melting level)	219
2) Prediction Equations	222
(i) Vertical velocity	222
(ii) Outflow velocity	223
3) Comparison of Predictions with Numerical Model Results	223
4) Estimating Parameters in Prediction Equations	228
5) Predicting Other Downdraft and Outflow Parameters	230
6) Other Prediction Approaches	231
APPENDIX B. BDO Theory and the Cylindrical BDO Equation	234
1) BDO Theory	234
2) The Cylindrical BDO Equation	241
3) Solitary Waves Versus Undular Bores	247
APPENDIX C. Derivation of the Cylindrical BDO Equation	252
LIST OF FIGURES	265
LIST OF TABLES	280
REFERENCES	281
BIOGRAPHICAL NOTE	301

ACRONYMS AND ABBREVIATIONS

agl	above ground level
BDO	Benjamin–Davis–Ono equation
CB	cumulonimbus cloud
CBDO	Cylindrical Benjamin–Davis–Ono equation
COHMEX	Cooperative Huntsville Meteorological Experiment
CP-2	NCAR Doppler Weather Radar with dual–polarization capability
DB	Droegemeier and Babcock (1989)
DFW	Dallas/Ft. Worth Airport, TX (also refers to 1985 aircraft crash)
EPT	Equivalent Potential Temperature
FAA	Federal Aviation Administration
FL-2	FAA–Lincoln Laboratory Transportable Doppler Weather Radar
FLAWS	FAA–Lincoln Laboratory Operational Weather Studies
FM-CW	frequency modulated–continuous wave (radar)
isodop	contour of constant Doppler velocity
JAWS	Joint Airport Weather Studies
JFK	J.F. Kennedy Airport, New York, NY (also refers to 1975 aircraft crash)
KH	Kelvin–Helmholtz
KHI	Kelvin–Helmholtz Instability
KW	Krueger and Wakimoto (1985)
MB	microburst
NCAR	National Center for Atmospheric Research
NIMROD	Northern Illinois Meteorological Research on Downbursts
NTSB	National Transportation Safety Board
P89	Proctor (1989)
PPI	Plan Position Indicator
PROBE	Portable Remote Observations of the Environment
RHI	Range Height Indicator
TDWR	Terminal Doppler Weather Radar
UND	University of North Dakota Enterprise C–band Doppler Weather Radar
UTC	Universal Time Coordinates

I. INTRODUCTION

Wind shear is a major cause of aircarrier accidents in the United States – seven crashes since 1970 have killed 575 people – and most of these accidents have been caused by one particular form of wind shear called a microburst (Zorpette, 1986). Microbursts have been defined as small scale, low-altitude, intense downdrafts which impact the surface and cause strong divergent outflows of wind. We know they are associated with thunderstorms and are usually but not always accompanied by heavy rainfall at the ground. However, a number of meteorologically distinct phenomena associated with thunderstorms can give rise to strong downdrafts and high surface winds. Most microburst research has focussed on the main precipitation driven downdraft of thunderstorms, both with and without significant rainfall. But other downdraft types such as the evaporatively driven penetrative downdraft, and the dynamically driven downdrafts at low altitude associated with “roll clouds”, gravity currents spreading in ambient neutrally and stably stratified boundary layers, have also been associated with the microburst problem. In this thesis I differentiate between and explain the different downdraft phenomena, and assess the relative aircraft hazard of each. This research is essential to discovering exactly what atmospheric conditions are conducive to the initiation and development of microbursts, and to suggesting strategies for their prediction. The destructive nature of microbursts and the high risk they pose to the safe operation of aircraft in the vicinity of thunderstorms make their accurate prediction a very desirable goal.

A. Historical Perspective

The word “downburst” was introduced by Fujita and Byers (1977) to describe the meteorological event which caused the crash of Eastern Flight 66 at JFK airport in New York on 24 June 1975 (Fig. I-1), in which a downdraft prevented the safe landing of a jet aircraft. They determined that if a downdraft has a speed of at least 3.5 m/s at an altitude of 90 m agl, comparable to that of a jet transport following the usual 3° glideslope on final approach, and a spatial extent of 0.8 km or larger, large enough to have a noticeable effect on the aircraft (Fujita and Caracena 1977), then it qualifies as a downburst. Later the term “microburst” was created to distinguish small downbursts from larger ones, as judged by the length of ground damage they caused (Fujita, 1978, 1979); the JFK accident was reclassified as a microburst.

The analyzed data from that aircraft accident revealed a downdraft much stronger at low altitudes than the thunderstorm downdrafts previously observed (Fig. I-2). This suggested a completely different scale phenomenon; the downdraft was so much stronger that the new “burst”

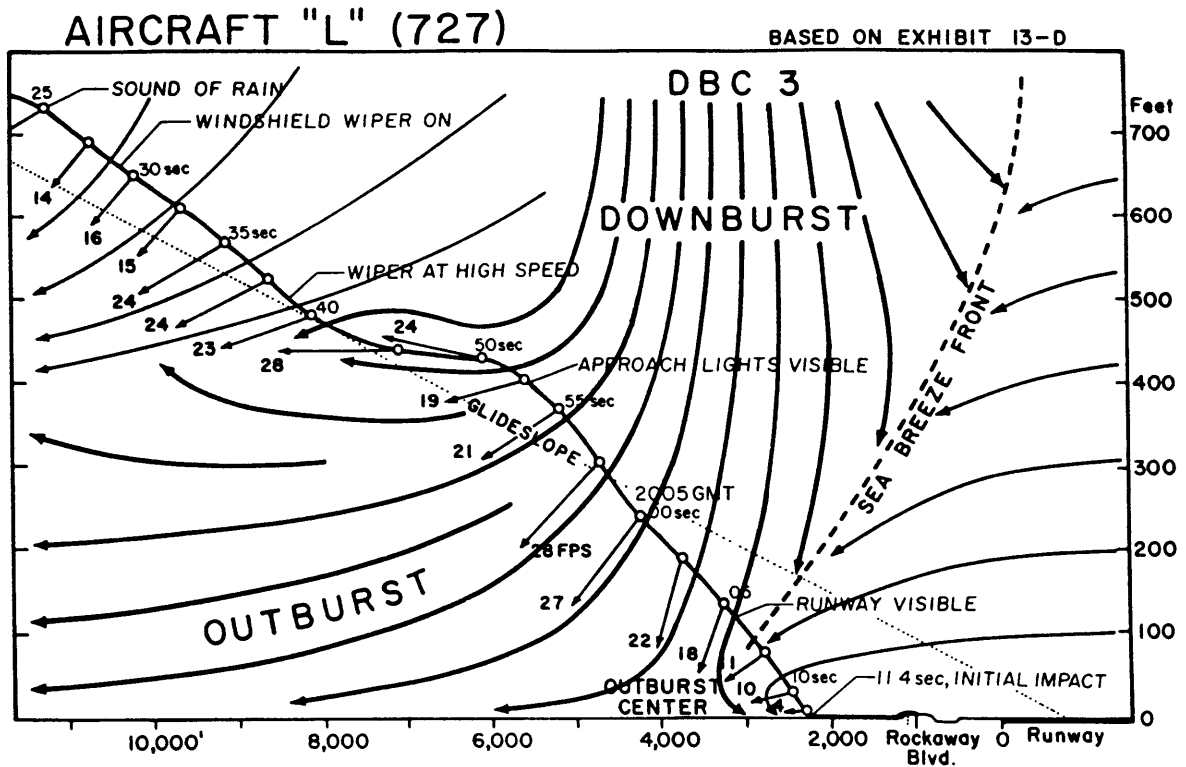


Fig. I-1. The path of Eastern Flight 66 on 24 June 1975 in the vertical plane including the glide slope of runway 22-L at JFK Airport. The downburst (later defined as microburst) speed was estimated to be 6.7 m/s (22 fps) at 60 m (200 ft) agl. Taken from Fujita (1976).

terminology was created specifically to describe it. And since Byers was one of the primary scientists working on the Thunderstorm Project (1946-47), during which highly divergent, radially spreading surface wind patterns associated with the heavy rain beneath thunderstorms were found with regularity (e.g. Fig. II-15), his agreement that this was an unusual downdraft deserving of a new name was very impressive. However, the speculative hypothesis offered to explain it involved the precipitation driven downdraft of the thunderstorm descending from stratospheric heights as the overshooting top of a cumulonimbus cloud collapsed. Research since then has shown that this hypothesis is not credible.

The confusion between the downburst, the microburst, and the well known thunderstorm downdraft has persisted. Caracena (1978) suggested that "a large scale downdraft may contain an ensemble of impulsive components of various intensities" and that "the microburst may represent a small impulsive component". Fujita (1979) essentially agreed, and suggested an analogy between the microbursts inside a downburst and the suction vortices inside a tornado. Just as a

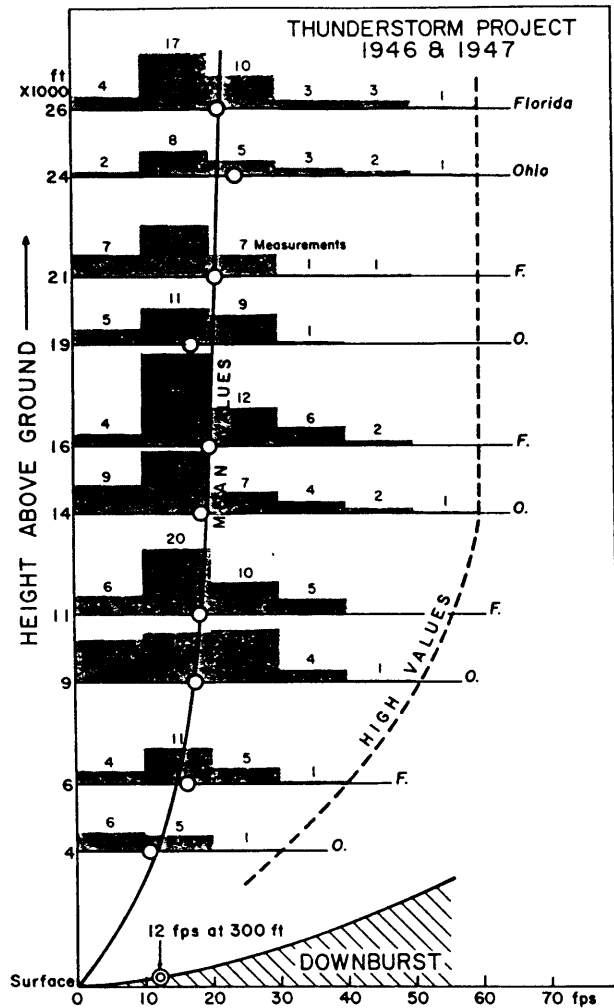


Fig. I-2. Frequencies of downdraft speeds measured by the Thunderstorm Project, 1946 and 1947 (Byers and Braham, 1949; Table 10). The observed downburst (microburst) data point from the Eastern Flight 66 crash at JFK airport in 1975 is also plotted. Taken from Fujita and Byers (1977).

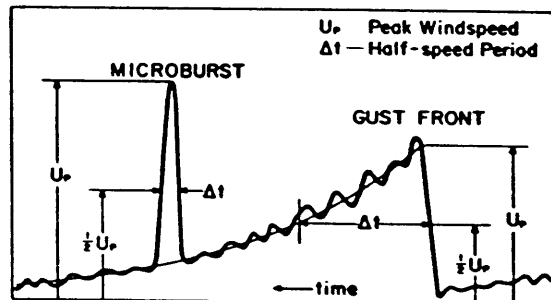


Fig. I-3. Hypothetical wind trace of a gust front and a microburst by Fujita (1980a). This type of wind trace was recorded several times during the NIMROD Project (Fujita 1979; Wakimoto 1981). As indicated, time increases from right to left.

funnel cloud aloft would not be called a tornado, so a thunderstorm downdraft aloft would not be called a downburst. Thus, Fujita realized that the downburst did not indicate a new phenomenon; it was the same as the thunderstorm downdraft, or perhaps the “downrush” defined over 20 years earlier by Fawbush and Miller (1954) to describe non-frontal thunderstorms that produced damaging surface winds. Apparently, however, the smaller, stronger microburst was something new and different, and the Eastern flight that crashed at JFK in 1975 encountered one of them.

During the first research project on downbursts and microbursts [Northern Illinois Meteorological Research on Downbursts (NIMROD) Project; Fujita 1979], the type of wind trace shown in Fig. I-3 was observed several times. It illustrates the difference between the leading edge of a thunderstorm outflow (gust front) and a microburst, in terms of the measured wind speeds and time scales. The microburst was redefined after that experiment as “an outburst of damaging winds [$\equiv >18$ m/s] on or near the ground” (Fujita and Wakimoto 1981). No real explanation for the small scale, or very high wind speeds of the microburst has ever been given.

Because of the observed proximity of the microburst to collapsing thunderstorms, the tacit assumption was made that the explanation for it involved some overlooked downdraft forcing mechanism, one that could cause an apparently average thunderstorm on an average day to produce unusually strong surface winds with small scale, strong downdrafts very near the surface. This assumption led to renewed interest in quantifying thunderstorm downdraft forcing mechanisms, but it may also have diverted attention from the investigation of thunderstorm outflow dynamics.

The assumption that the key to understanding the microburst lay in understanding the precipitation driven downdraft of thunderstorms was reinforced when The Joint Airport Weather Studies (JAWS) Project was undertaken in the Denver area (McCarthy et al. 1982). Downdrafts originating from cold-based clouds (cloud base above the freezing level) where ice processes dominate, and falling into deep, dry adiabatic boundary layers, were found to be the primary cause of small scale, divergent outflows during the summer in that part of the country. These have been called “low reflectivity” or “virga” or “dry” microbursts because often little if any rain reaches the surface (e.g., Caracena et al. 1983; Wakimoto 1985; Fujita 1985). After observing a large number of these events during the JAWS Project, the definition of the microburst itself was altered to account for any outflow with a “differential Doppler velocity across the divergence center greater than or equal to 10 m/s and the initial distance between maximum approaching and receding centers less than or equal to 4 km” (Wilson et al. 1984). This definition encompassed far weaker

winds than did the previous definition, and not necessarily a smaller and more powerful downdraft at low altitudes than the well known thunderstorm downdraft. These events, illustrated schematically at the top right of Fig. I-4, were certainly different from the type of event shown as a microburst at the bottom right of the same figure.

In this thesis, I return to the microburst originally thought to be a phenomenon so much smaller and stronger at low altitudes than the familiar thunderstorm downdraft that new terminology was deemed necessary to describe it. To begin, I make a primary distinction between: 1) the precipitation (buoyancy) driven downdraft of a convective cell, with or without significant surface rainfall, and 2) the dynamically driven downdrafts that develop behind the leading edge of, are embedded within, or are triggered by the resultant surface outflow of such a storm. This distinction is required to separate and understand the various physical phenomena being investigated as "microbursts" (Fig. I-4).

B. The Microburst Aircraft Hazard

Three major aircraft accidents account for all of the aviation fatalities attributed specifically to microbursts in the US (see Table I-1); these are the crash of Eastern 66 at J.F. Kennedy airport in New York on 24 June 1975 (112 fatalities, 12 injuries), of Pan Am 759 at New Orleans International airport on 9 July 1982 (152 fatalities, 9 injuries), and of Delta 191 at Dallas/Ft. Worth International airport on 2 August 1985 (130 fatalities, 31 injuries). No one escaped injury in any of these accidents. In all three of these cases cold thunderstorm outflow had recently spread over the area before the implicated thunderstorm took place. Is this purely coincidental or did this add a crucial ingredient to the overall hazard? The stratification of the boundary layer was not taken into consideration in any of the published reports on these accidents.

In two of the other four tabulated accidents attributed to thunderstorm low altitude wind shear in which fatalities occurred (microbursts had not yet been invented), roll clouds were noted by eyewitnesses. These were the crash of a Braniff Airways plane at Falls City, NE on 6 August 1966 and the crash of an Ozark Air Lines plane St. Louis, MO on 23 July 1973. No one escaped injury in these two accidents, either. In the Falls City crash, "ground witnesses observed the aircraft to fly into or over a roll cloud preceding a thunderstorm and shortly thereafter saw an explosion in the sky followed by a fireball falling out of the cloud. Two pieces, later identified as major portions of the right wing and empennage, were seen falling separately from the main part of the aircraft. Shortly thereafter the witnesses noted high gusty surface winds and light to moderate rain

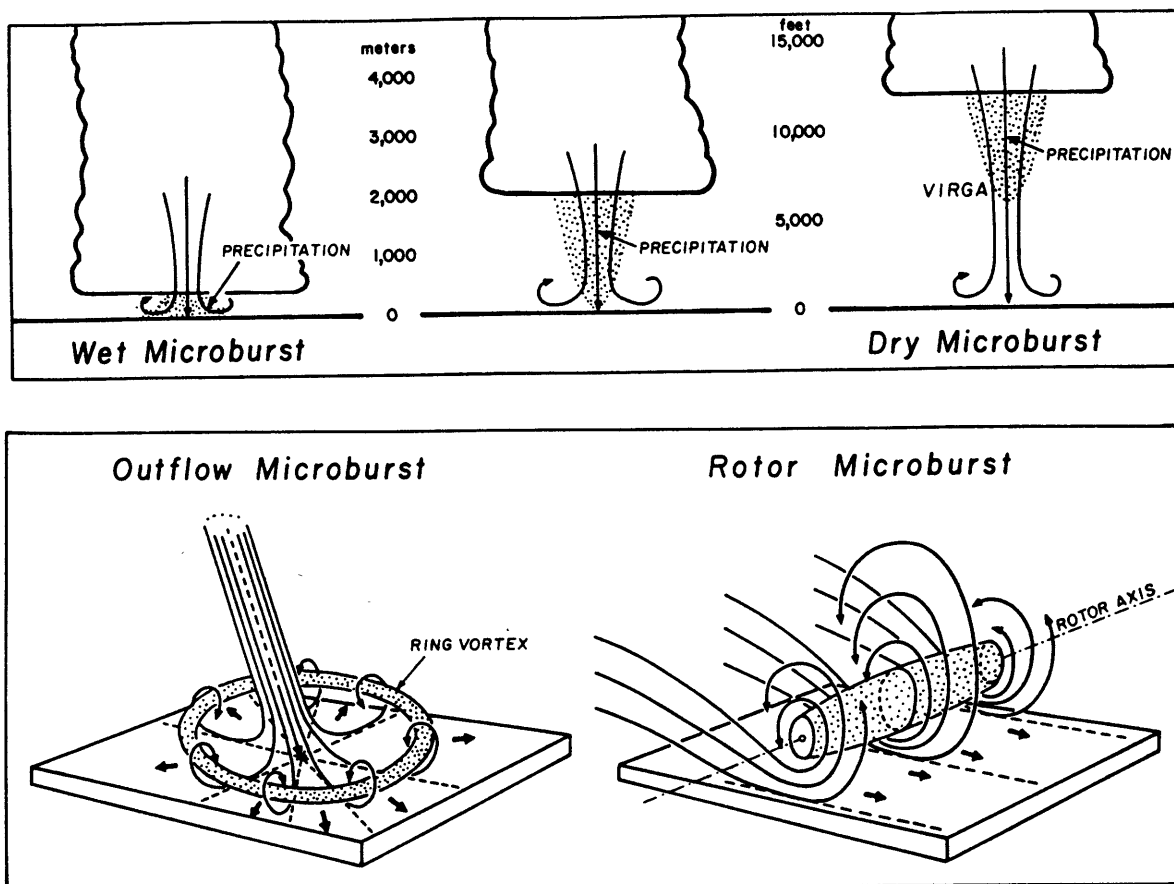


Fig. I-4. (Top) Schematic views of wet and dry microbursts. Wet microbursts are expected to occur in the wet regions of the world, while dry microbursts are commonly seen in the dry regions with high bases of convective clouds. (Bottom) Outflow microbursts are the most commonly observed type of microburst. Some rotor microbursts develop inside macrobursts behind their gust fronts. Caption and figures taken from Fujita (1985).

which accompanied the passage of a squall line through the area. The cause of the accident was determined to be inflight structural failure caused by extreme turbulence” (Rudich 1986). Roll clouds mark the ascending branch of a horizontal vortex, usually either the gust front itself, a solitary wave, or part of an undular bore (Smith 1988).

What role did the low altitude downdrafts and turbulence associated with horizontal vortices, if there were any, play in the three microburst related fatal aircraft accidents? Certainly the divergent headwind–tailwind shear of the thunderstorm outflow itself can easily become strong enough to cause an unmanageable loss of lift to an aircraft penetrating it (Fig. I-5). The performance decreasing tailwind portion of the divergent wind pattern is thought to have been the cause of the New Orleans and Dallas crashes, but the Eastern plane that crashed at JFK never encountered

Table I-1. Aircraft accidents in the United States attributable to microbursts or low altitude wind shear associated with thunderstorms. Wind speed is given in meters per second, and cell diameters are given in kilometers. F/I/U indicates number of fatalities, injured, and uninjured. Information adapted from Viemeister (1961), Fujita (1985), Rudich (1986), and Laynor (1986).

Location	Date	Winds	Diameter	Rain	Weather	F / I / U
Bowling Green	28 Jul 43	strong	10-15	yes	strong squall wind from violent downdraft fanning out at surface unusually severe turbulence	? / ? / 2
Mason City, IA	22 Aug 54	35-40	5	heavy	plane entered thunderstorm at 400-500 ft, sank in downdraft	12 / 7 / 0
Rochester NY	2 Jul 63	shifting	?	heavy	thunderstorm approaching runway from west, plane took off into heavy rain & shifting winds	7 / ? / ?
Falls City, NE	6 Aug 66	gusty	n/a	light	roll cloud preceding thunderstorm, severe turbulence	42 / 0 / 0
St. Louis	23 Jul 73	strong	?	heavy	severe thunderstorm with roll clouds, heavy rain, strong winds	38 / 6 / 0
Chattanooga	27 Nov 73	?	?	heavy	low altitude wind shear existed in heavy rain on approach	0 / 42 / 37
New York	24 Jun 75	10-17	5-10	heavy	hot smoggy day, seabreeze light, moderate, & heavy rain numerous small cells, spearhead echo 8 x 32 km	112 / 12 / 0
Denver	7 Aug 75	>12	2	light	numerous scattered showers small and weak, cell broke into 2, thunder heard, spearhead echo 8 x 16 km	0 / 15 / 119
Raleigh-Durham	12 Nov 75	?	?	heavy	unexpected heavy rain, wind-shear & downdraft at 100 ft agl	0 / 1 / 138
Philadelphia	23 Jun 76	20	4	yes	headwind increase in front of shower; scattered showers & T-storms near warm front, growing spearhead echo 13 x 27 km	0 / 86 / 20
Tuscon	3 Jun 77	14	2	none	numerous CB around airport gust front passed earlier with 25 m/s surface wind speed	0 / 0 / ALL
New Orleans	9 Jul 82	>15	2	heavy	scattered showers, 7 gust fronts nearby, recent growth of convective cloud tops	152 / 9 / 0
Detroit	13 Jun 84	10-16	?	heavy + hail	thunderstorm with heavy rain 3/4 inch hail at 100-200 ft agl turbulence, severe wind shear	0 / 0 / ALL
Dallas	2 Aug 85	22-35	4	very heavy	scattered small cells initiated on gust front out of larger cell to NW, very hot day, cloud top of MB cell 23 Kft. (questionable, NTSB reported 40-50 Kft.)	130 / 31 / 0

AIRCRAFT ENCOUNTER WITH A MICROBURST

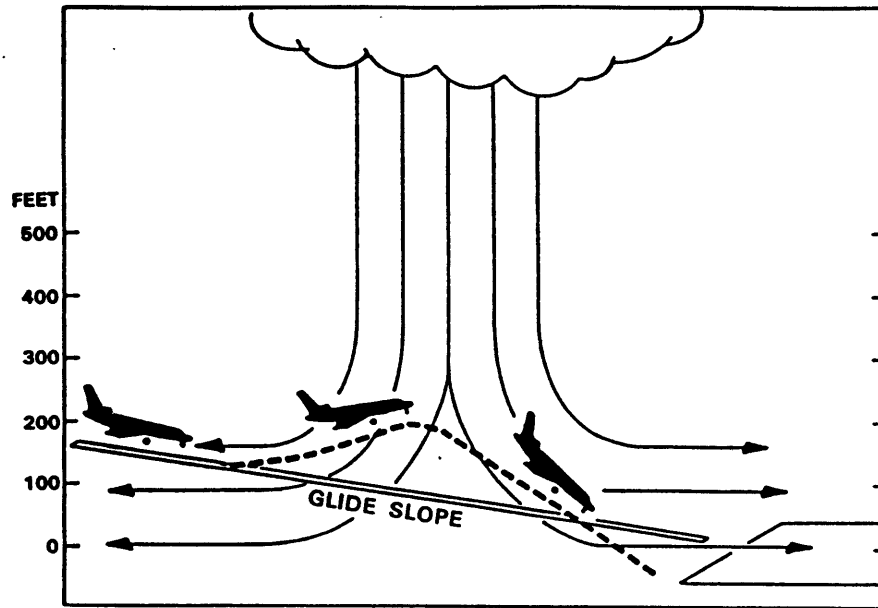


Fig. I-5. Schematic drawing of an aircraft encounter with a microburst. Notice that the increased headwind lifts the plane above its intended glideslope while the increased tailwind causes the plane to fall below its intended glideslope.

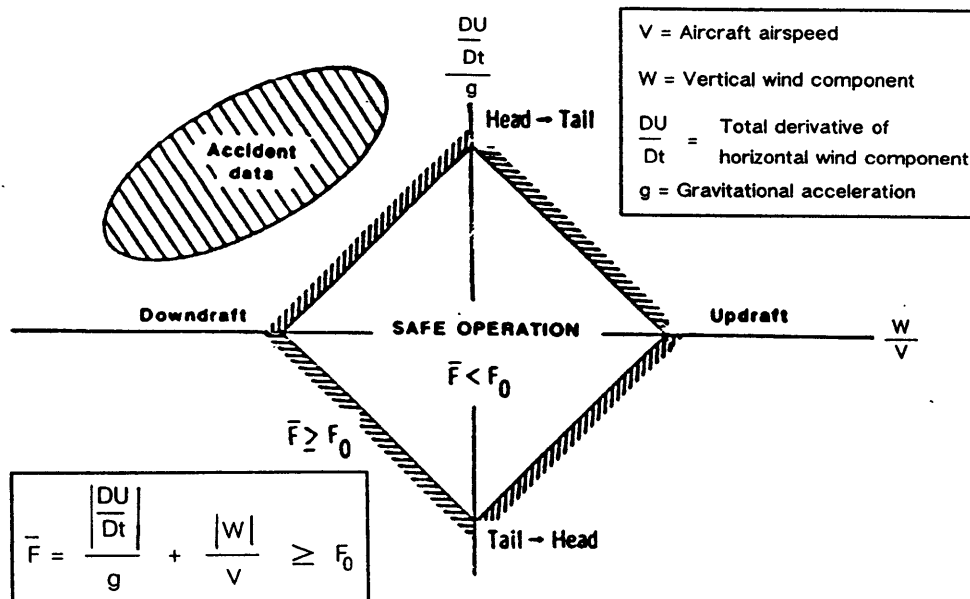


Fig. I-6. Definition of F -factor wind shear hazard index. Typical threshold values (F_0) for jet transport range from 0.10 - 0.15. Notice that all of the aircraft accidents have taken place in the quadrant associated with divergent horizontal winds and downward vertical velocities along the flight path. Adapted from Targ and Bowles (1988).

a tailwind, only a performance increasing headwind followed by an unusually strong, narrow downdraft. Figure I-6 shows that the magnitude of the downdraft velocity has at least as much effect as the horizontal wind shear on the ability of a plane to maintain its speed and glide slope profile under shear conditions (e.g., Greene 1978; Frost and Bowles 1984; Targ and Bowles 1988); it may have been underemphasized in the recent microburst work because the central downdraft of a precipitating thunderstorm typically becomes weak close to the ground. Whether or not the additional wind shear or the powerful low altitude downdrafts of horizontal vortices nearby had anything to do with the fatal microburst crashes will be examined.

C. Hypotheses

My primary hypothesis in this work is that many of the small scale, short lived, strong downdrafts at low altitudes identified as a microbursts are not equivalent to or even part of the precipitation driven downdraft of the nearby thunderstorms, as has been assumed. They are the downward branch of the circulating flow that develops at the leading edge of newly formed thunderstorm outflow. The identity and characteristics of these "waves" have not previously been carefully examined.

Clues that the flow within gravity waves may have contributed to the hazard have been available since the very earliest work on microbursts, but their significance was unrecognized until recently. In particular, the earlier passage of a gust front in nearly all of the analyzed cases indicated thunderstorm outflow was already on the ground when the microburst parent cell collapsed (e.g. Fig. I-3). A list of six known facts about microbursts summarized by Caracena and Maier (1987) included the following: "The microburst(s) occurred at about the time that a strongly forced cell had matured, *was undercut by cool outflow*, and rapidly unloaded its charge of precipitation". Results from the Thunderstorm Project in 1946 and 1947 (U.S. Weather Bureau 1948) indicated that "if new first-gust echoes appear, the first-gust line has probably passed beyond them." Most summer afternoon convection is initiated by the convergence at the leading edge of old outflow boundaries (e.g., Purdom 1982; Wilson and Schreiber 1986), and thus thunderstorm downdrafts may frequently fall into old outflow. The presence of this thin stratified layer significantly changes the subsequent outflow evolution.

If waves or vortices that had been created by, and then propagated away from, the parent storm did cause the wind spikes of the microburst, little or no rainfall would be measured for these events. The large number of "dry" microbursts detected during the NIMROD project (Fig. I-7),

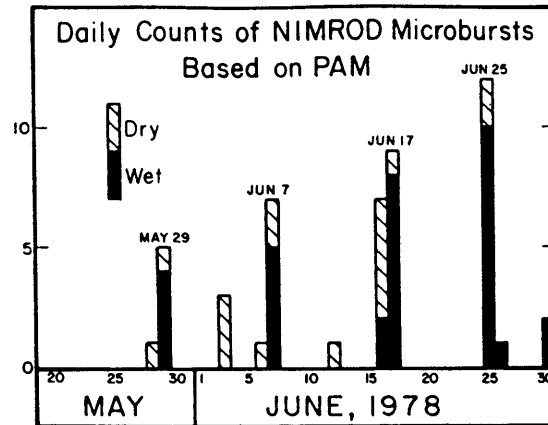


Fig. I-7. Daily count of NIMROD microbursts as determined by computer analysis of surface weather station data. The number of wet (> .25 in. rain) and dry microbursts is shown on the figure. Taken from Fujita and Wakimoto (1983a).

where the Denver type of dry or virga microbursts (Fig. I-4, top right) rarely occur, was another clue that these events were distinct from the precipitation driven downdraft. Also, the widely varying parent storm types associated with microbursts, reviewed recently by Fujita (1985) and Wolfson (1988a,b), suggested that no one particular type of storm was the cause. The effects of the ambient boundary layer stratification and overall storm geometry on the dynamical evolution of dense thunderstorm outflow may be important, previously unrecognized parts of the microburst problem.

In the simplest case, the strong outflow frontal circulation arises primarily from the axisymmetric geometry of the collapsing thunderstorm. Regardless of the ambient stratification, the leading edge of a circularly symmetric dense outflow (the gust front) will rapidly build into a deep horizontal "ring vortex" as the outflow expands. This nonlinear phenomenon is caused by radial expansion of the flow, led by a frontal discontinuity or jump. It is not caused by the angular momentum conserving spin-up of a constant volume vortex as its axis is stretched by radial expansion. No comparable build up of fluid at the gust front occurs in a planar geometry, because there is no geometrical distortion of the flow. Thus, circular gust fronts are fundamentally different from their more straight line counterparts.

A more complicated case arises when a thin layer of stably stratified air is present at the surface, such as is created by the earlier passage of cold thunderstorm outflow, a sea breeze front, or by a nocturnal inversion. This layer can act as a wave guide for gravity waves. Some of the low

altitude downdrafts and high surface winds identified as microbursts may be associated with finite amplitude gravity waves, evolving solitary waves, triggered or enhanced by the impact of the newly formed downdraft and outflow of a nearby thunderstorm. Nonlinear, one dimensional gravity wave theory can explain the amplification of these waves (vortices) under ideal circumstances to more than double their initial size. It can also explain the unusually large propagation speeds, which are greater than the corresponding linear wave speed by an amount proportional to the wave amplitude. Also, since the usually quite thin depth of the preexisting outflow pool (or other strongly stratified layer) sets the vertical scale for the nonlinear gravity waves, strong vertical velocities would be expected to persist very close to the ground. The nonlinear gravity wave dynamics provide a plausible mechanism whereby the outflow speeds in small regions can exceed predicted speed.

A related hypothesis is that the turbulence within the newly formed outflow of a thunderstorm collapsing into a such a thin stratified layer will be unusually severe. This is because the sharp increase in stratification experienced by the falling downdraft causes rapid deceleration; some of the downdraft air will begin spreading horizontally at the top of the stratified layer. More boundary layer air will be trapped under the new outflow in this situation than in the unstratified scenario. Since the new downdraft air is usually colder than the boundary layer, convective instability as well as shear instabilities will occur. An overturning takes place which gives rise to updrafts and downdrafts embedded in the outflow. These would be experienced in an aircraft as extreme turbulence and could contribute to the control problem encountered as a pilot penetrates an already hazardous divergent windshear pattern.

D. Organization of the Thesis

Many events identified in past work as microbursts were in fact the precipitation driven downdrafts of convective cells, whether or not they were accompanied by heavy rain at the surface. These events can indeed be extremely hazardous to aircraft. They have been likened to “a fluid jet striking a plate”, or the “wall jet” of fluid dynamics. The following chapter explores the environmental and geometric factors that contribute to the production of high speed, thunderstorm downdrafts and divergent outflows. A simple model is developed based on the vertical momentum and continuity equations, that can be used to predict the maximum downdraft and outflow speeds for a storm given the environmental sounding, and the peak water content and geometrical shape of the observed radar reflectivity core.

Recently the “penetrative downdraft”, a small scale evaporatively driven downdraft, has been identified as the primary cause of “wet microbursts”, microbursts accompanied by heavy rain. In the third chapter, I show that the penetrative downdraft mechanism may account for unusually strong, small scale cloud edge downdrafts at low altitudes that, in some rare cases, can reach the surface with enough intensity to qualify as a microburst. Observations of one such edge downdraft are presented. However, penetrative downdrafts are not the primary cause of “wet microbursts”, and the aircraft hazard associated with them is low.

Attention is then turned, in the fourth chapter, to various types of low altitude downdrafts that form within thunderstorm outflows, when the ambient environment is unstratified. The narrow ring of strong surface winds associated with the leading outflow vortex in axisymmetric storms has been identified as an “outflow” or “rotor” microburst. A number of past hypotheses involving these vortices and their relationship to microbursts are considered. The development of a leading vortex ring in axisymmetric outflows is explained, and the possibility of multiple ring development is explored through numerical simulations performed with the axisymmetric numerical model of Anderson et al. (1985) at the University of Wisconsin. The role of Kelvin–Helmholtz instability and horizontal shear instability in creating low altitude downdrafts within thunderstorm outflows is also examined.

The scenario in which a thin stable layer is present at the surface when the thunderstorm outflow originates is given particular attention in the fifth chapter, for this best represents the environmental conditions present at the time of the fatal microburst aircraft accidents. This is a common situation, but has only recently begun to receive attention in the scientific literature. First the theory of solitary waves applicable to the atmosphere (deep fluid) is briefly reviewed. An equation governing weakly nonlinear cylindrical gravity waves appropriate for thunderstorm outflow situations has not previously been derived; this is done and the time dependent behavior of this cylindrical Benjamin–Davis–Ono equation is examined. Some of the solitary wave events associated with thunderstorms are reviewed and the “rotor” microbursts are reexamined in this light. Numerical simulations, performed with the high resolution axisymmetric model of Anderson (1990) at the University of Wisconsin, are used for evaluation of the outflow dynamics. These give a very valuable sense of the time and space scales associated with the development of the outflow and the conditions under which strong vertical motions develop. The relative aircraft hazards

caused by an outflow spreading in a neutrally stratified boundary layer and in a stably stratified boundary layer are compared.

Once the various types of downdrafts and vortices associated with thunderstorms and thunderstorm downdrafts have been delineated, the fatal aircraft accidents attributed to microbursts can be reexamined. The Delta crash at Dallas/Ft. Worth airport in 1985, the Pan American crash at the New Orleans International airport in 1982, and the Eastern crash at JFK airport in 1976 are discussed in the sixth chapter. Broad conclusions are presented in the final chapter.

II. THUNDERSTORM DOWNDRAFTS AND OUTFLOWS

Recent work on aviation weather hazards and, in particular, on microbursts has focussed on the thunderstorm downdraft and outflow as the primary cause of low altitude wind shear. Today, the precipitation driven downdraft of a cumulonimbus cloud is commonly called a microburst when its diameter is small and its outflow is strong. To help prevent additional weather related aircraft accidents, the FAA recently awarded a contract for the production of Terminal Doppler Weather Radars (TDWRs), which will continuously monitor the airspace above major airport terminal areas (Evans and Turnbull 1989). Much effort has been put forth over the last few years in developing automated techniques for detecting microbursts, divergent thunderstorm low altitude wind shear, with these radars. The success of hazardous wind shear *prediction* will depend on accurately quantifying the factors influencing the development of the strongest thunderstorm downdrafts and outflows. Puzzling are the observations that not all storms occurring simultaneously on a given day result in strong outflows, and that storms on different days that appear quite similar in terms of their radar reflectivity signatures produce downdrafts and outflows of differing strengths.

In this chapter, I describe some of the characteristics of thunderstorms, both with and without appreciable surface rainfall, and discuss the evidence of their danger to aviation. I then focus on the identification of observable parameters that will allow quantitative prediction of the eventual maximum downdraft and outflow strengths. The simple framework that is developed helps in understanding and predicting the storms that will produce strong divergent outflows.

A. Observations

1) Thunderstorms with Significant Surface Rainfall

The observational work of Chisolm and Renick (1972), and the numerical work of Weisman and Klemp (1982; 1984) have shown that much of the complexity of convective storm evolution may be governed primarily by a limited number of environmental features. Among these are the vertical shear of the horizontal wind, the level of instability (buoyancy), the mesoscale forcing, and the influence of any nearby convection. Isolated cumulonimbus clouds, called "airmass thunderstorms", are common in areas of convective instability, high surface relative humidity, and little or no vertical wind shear. They occur in most parts of the country during the summer months.

A schematic illustration of the three basic stages in the life cycle of an ordinary thunderstorm, as determined by Byers and Braham (1949), is presented in Fig. II-1.

The time evolution of the downdraft and subsequent outflow formation in a numerically simulated axisymmetric thunderstorm is shown in Fig. II-2, min 4 – 8. A large scale horizontal circulation is generated through the pressure perturbations set up as the main precipitation driven downdraft of a thunderstorm accelerates toward the ground. When there is vertical shear of the horizontal wind present in the ambient environment, the trajectories of midlevel air into the downdraft will differ on the upshear and downshear sides of the cell (Knupp, 1987; Fig II-3). Once the downdraft forms an outflow, the large scale circulation is strengthened with the emergence of an “up-down” flow branch, labelled “a” in Fig. II-3, and shown forming in Fig II-2, min 9. (The tight closed vortex at the leading edge of the surface outflow at min 12 in Fig. II-2 is a distinctly different phenomenon, and is discussed separately in Chapter IV.)

As the environmental wind shear increases, multicellular storms (Marwitz 1972; Fig. II-4) or even isolated supercells (Lemon and Doswell 1979) are more likely to form. As isolated cells merge in a multicell storm, either because of the environmental wind shear or the synoptic or mesoscale forcing pattern, the overall geometry will become more linear. These storm formations are referred to as squall lines, instability lines, or more generally as linearly oriented mesoscale convective systems (Bluestein and Jain 1985). Especially when they contain damaging straight line surface winds, the resurrected term “derechos” (Hinrichs 1888; Johns and Hirt 1983; Przybylinski and DeCaire 1985) has been used. The characteristic radar signature of these damaging line storms has been called the “line echo wave pattern” by Nolen (1959) and the “bow echo” by Fujita (1981).

All of these storm types, from the isolated short-lived cells to the more persistent line storms and supercells, can have strong downdrafts and outflows, and have been identified as microburst parent storm types by Fujita (1985). The large persistent storms are predictable and fairly easy for aircraft to avoid. However, the airmass storms pose a critical hazard to aviation because of their relatively high frequency, rapid development, small scale, and very strong divergent surface outflows.

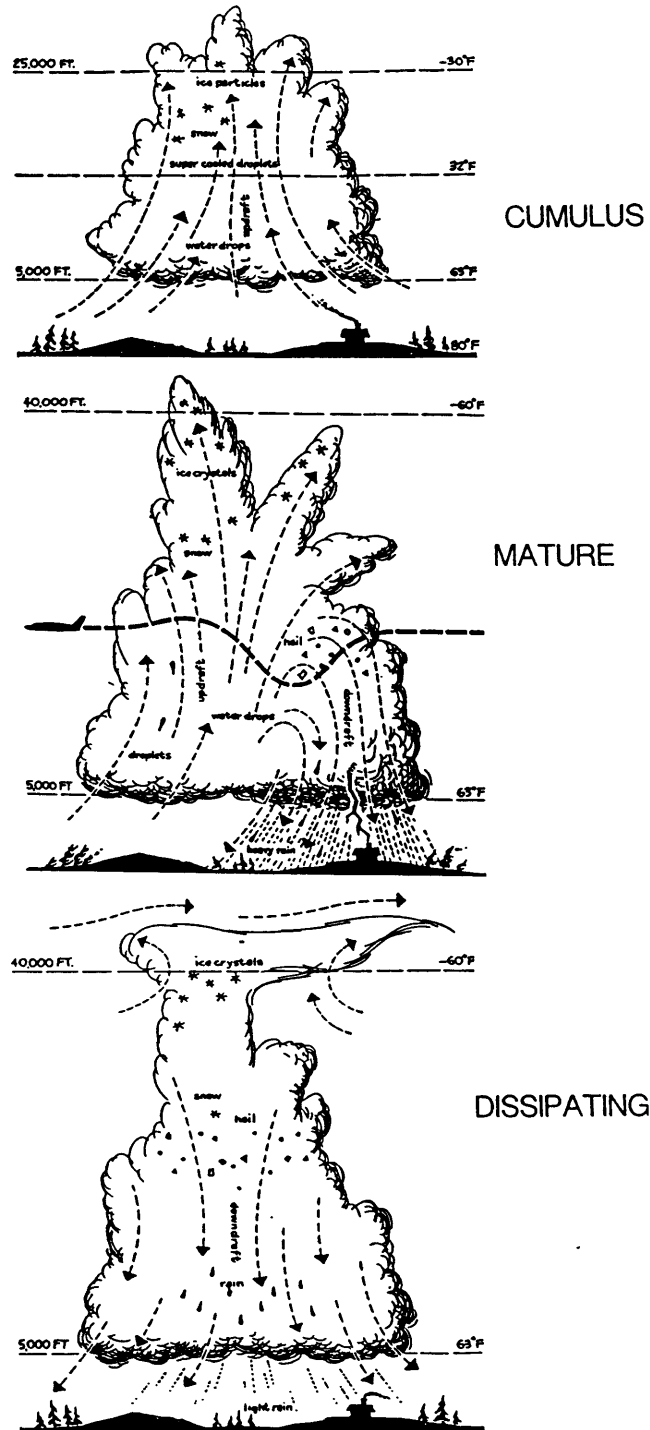


Fig. II-1. (Top) Cumulus stage of a thunderhead is characterized by updrafts throughout the cloud cell. (Middle) Mature stage of thunderhead brings rain and/or hail, lightning, thunder, and downdrafts. (Bottom) dissipating stage of the thunderhead is reached as downdrafts occur throughout the cell. Brisk upper winds may shift the cloud top, producing the familiar anvilhead. Drawn by Viemeister (1961) after Byers and Braham (1949).

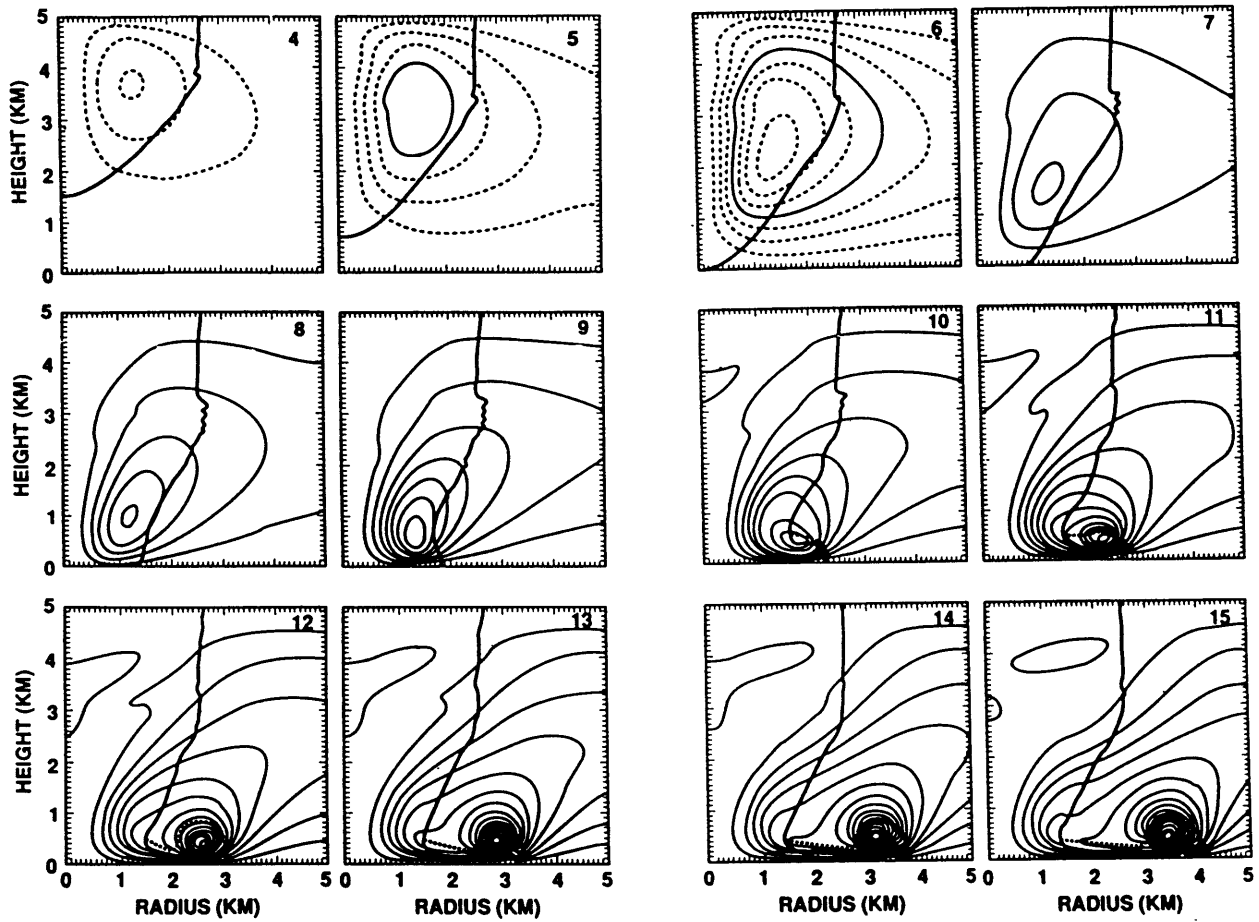


Fig. II-2. Radial-vertical cross sections from baseline axisymmetric simulation for stream function at 1 min intervals starting with 4 min and ending with 15 min. Thick solid line represents 10 dBZ radar reflectivity contour and the thick dashed line encloses area outside of precipitation shaft with temperature deviations from ambient of less than -1 K. The contour interval for stream function is 8×10^5 Kgs, with intermediate contours dashed. Taken from Proctor (1988b).

Typical features of convective cloud downdraft types.

Downdraft type	Speed (m s ⁻¹)	Width (km)	Depth (km)	Level*
Precipitation (PR)	1-15	1-10	1-5	l, m
Penetrative (P)	1-15	<1.0	1/2 to 5	m, u
Regional compensating (R)	<1	5-25	1-5	m, u
Cloud/updraft edge (L)	<1-5	<1-5	1-5	m, u
Overshooting (OS)	1-20	1-5	1-3	u

* Relative cloud level: l—low, m—middle, u—upper.

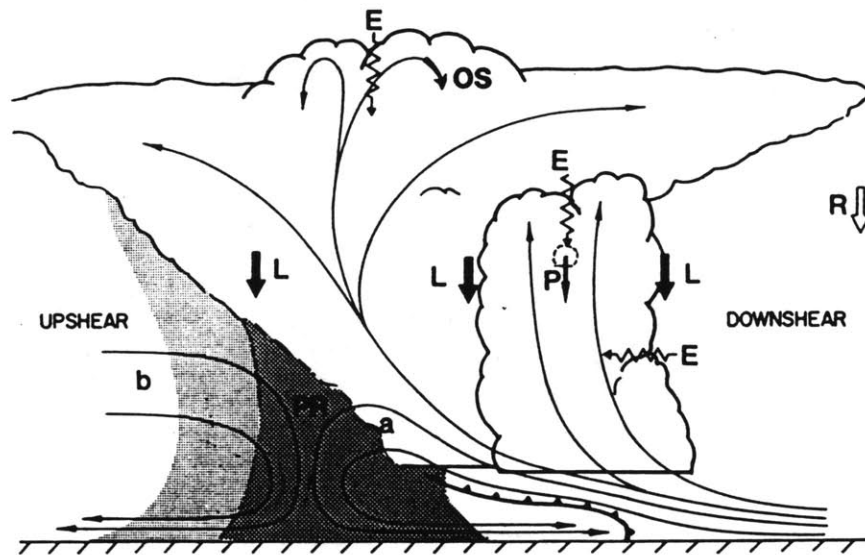


Fig. II-3. Schematic of updraft, downdraft and entrainment (inflow) flows within a typical Cb, based on a composite of observational studies and numerical model studies. All flows are storm relative; E denotes entrainment. Other symbols are defined in the accompanying table. Taken from Knupp (1987).

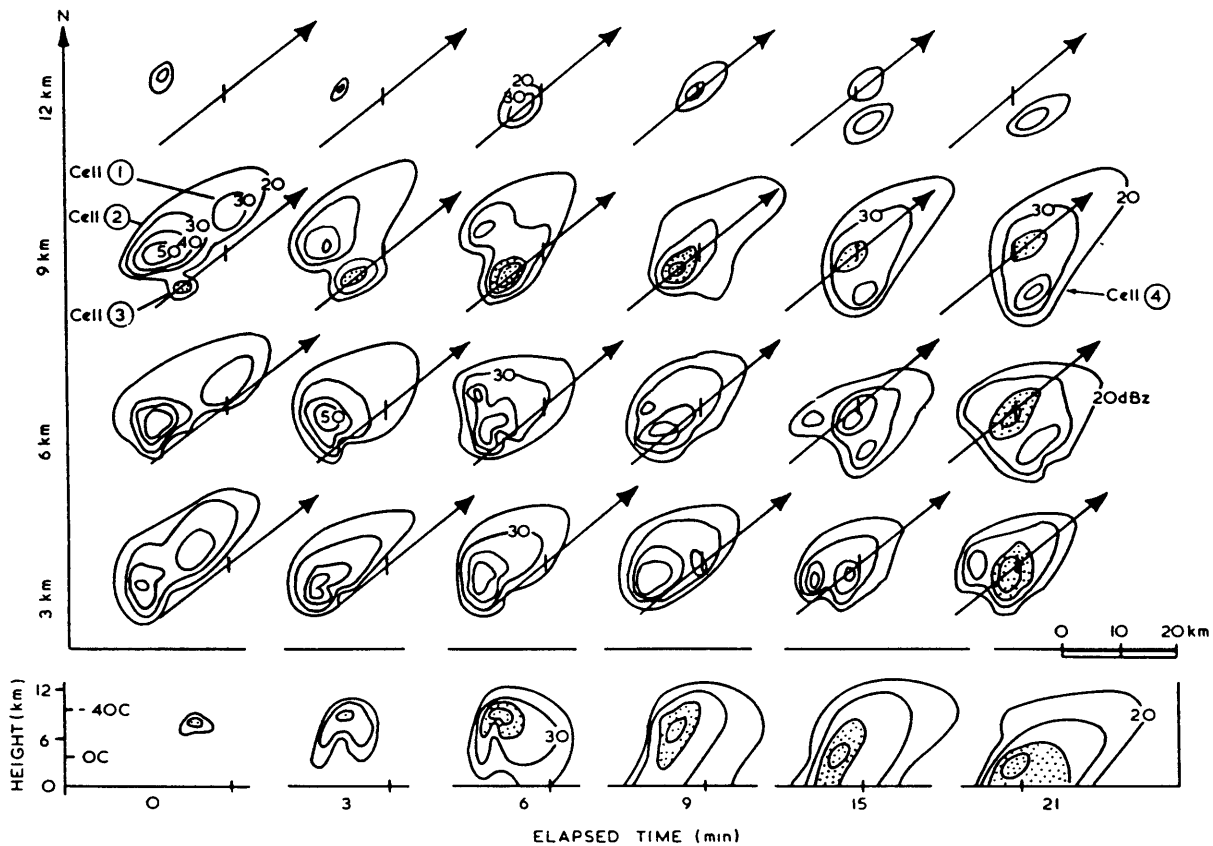


Fig. II-4. (Top) Horizontal radar sections through a multicell thunderstorm for four altitudes, at six times during the evolution of constituent cells. Reflectivity contours are at 10-dBZ intervals. Arrows depict the direction of cell motion and a geographical reference line for vertical cross sections appears at the bottom of the figure. Cell 3 is shaded to show the life history of an individual cell. (Bottom) Vertical radar sections of cell 3. From Chisolm and Renick (1972).

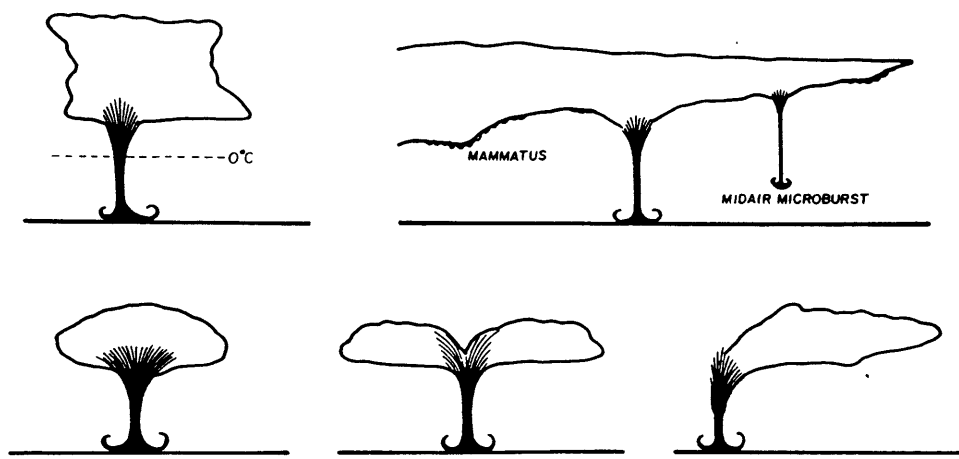


Fig. II-5. Examples of "large clouds, sometimes having the appearance of altocumulus castellanus, which produce rain or snow that may or may not reach the surface. Based on the observational evidence obtained in JAWS". Adapted from Fujita (1985).

2) Dry Thunderstorms

Another microburst parent storm type identified by Fujita (1985) is the isolated altocumulus cloud in the semi-arid regions of the country (Fig. II-5). Since the JAWS project took place near Denver in 1982, a great deal of attention has been given to downdrafts that originate from these benign looking, high based (~ 4 km agl), shallow (2 km deep) stratocumulus or cumulus congestus clouds. The clouds often have glaciated tops and lack the rapidly rising convective towers of typical lower based cumulonimbus clouds (Wakimoto 1985), although some small convective turrets can occasionally be seen (Hjelmfelt et al. 1986). Virga is commonly visible below cloud base (giving rise to the term "virga microburst") but often little or no rain reaches the ground (thus "dry microburst"). Even when rain does reach the ground, it might not be coincident with the strongest downdrafts at low altitudes (Sinclair et al. 1988; Parsons and Kropfli 1990).

Braham (1952) briefly mentioned this virga downdraft phenomenon, and Krümm (1954) characterized the "dry thunderstorm over the plateau area of the United States" quite accurately. Brown et al. (1982) also documented this type of storm, and noted that its damaging outflow could qualify as a "downburst". They predicted what the JAWS investigators later found, that this type of storm is much more common than was generally recognized at the time. In 1987 and 1988, 70% of the summer storms that produced significant outflow winds in the Denver area were this type (Cullen and Wolfson, 1990). Possibly because of the orographic forcing, quasi-linear storm formations made up of these high based stratocumulus clouds commonly occur; these have been called "microburst lines" by Hjelmfelt and Roberts (1985) and Hjelmfelt et al. (1989).

As the virga downdraft accelerates below the broad source region of the cloud, compensating convergence develops which causes the shaft to narrow. The frontal area of the accelerating downdraft eventually broadens into a "mushroom-like" cap and its fluid resistance increases. This creates a very distinctive shape seen in both Doppler radar observations (Fig. II-6) and numerical simulations (Fig. II-7). The horizontal divergence of the vorticity broadened frontal area has been identified as a "mid-air microburst" by Fujita (1985; Fig. II-5). Proctor (1989) found that an initial precipitation distribution made up entirely of snow particles was most effective in generating this type of low reflectivity downdraft. This agrees well with Knupp's (1989) conclusion that the dual contribution of melting and evaporation below cloud base gives these events their "burst-like" character.

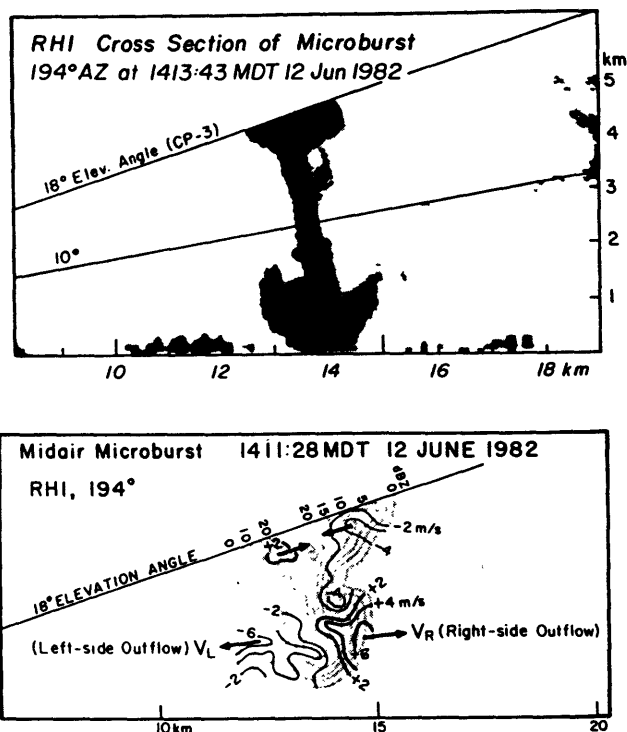


Fig. II-6. (Top) RHI cross section of a virga shaft. (Bottom) Contours of reflectivity and Doppler velocity for the same virga shaft shown in top panel, except 2:15 min earlier. Taken from Fujita and Wakimoto (1983b).

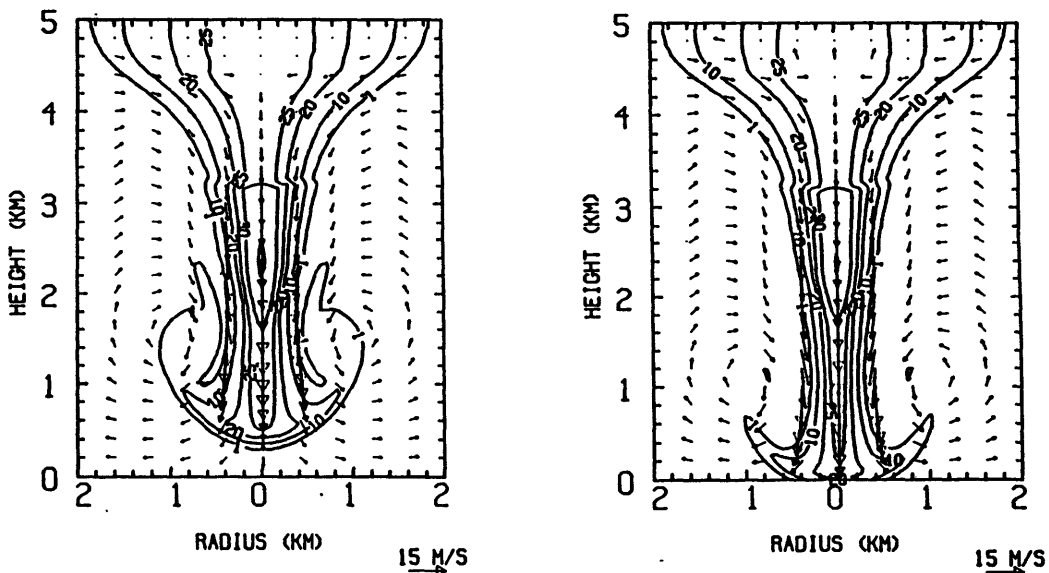


Fig. II-7. Axisymmetric model simulated radar reflectivity and superimposed vector field for a snow driven microburst at a) 22 min and b) 23 min after initiation. The contour values are 1, 10, 20, 25, 30, and 35 dBZ. Taken from Proctor (1989).

Both the isolated single cell and linear multicell dry thunderstorm types can have very strong downdrafts and outflows, even in the absence of much precipitation. Suitable conditions for their development have mainly been observed over the high plains east of the Rocky Mountains. The larger scale line storms are more persistent and easy to predict, but they may move slowly and can force long suspensions of airport operations if they enter the terminal area. The unpredictable isolated cells are perhaps even more hazardous than their heavy rain counterparts: their downdraft and outflow strengths are comparable, but they can occur much more frequently in environments that are conducive to their development, and they can be difficult to detect because their radar reflectivity is sometimes quite weak.

3) Environmental Characteristics

Attempts to generalize the thermodynamic characteristics of the environments in which ordinary thunderstorms with strong downdraft potential as well as the high based cumulonimbus clouds of the high plains form have been quite successful. Caracena et al. (1989) describe these environments as the "wet" and "dry" extremes, respectively. Typical soundings for each regime are presented in Figure II-8. The "wet" sounding is marked by a deep, nearly saturated layer with a moist adiabatic lapse rate, topped by an elevated dry layer (Caracena and Maier 1987). There is also a surface layer of neutral stability, and any capping inversion layer is not deep (Sohl et al. 1987). In the "dry" regime, a deep, dry adiabatic subcloud layer with a dew point depression $>30^{\circ}\text{C}$ is common, and a moist layer around 500 mb nearly always occurs (Caracena et al. 1983; Wakimoto 1985; Caracena and Flueck 1988). This moist layer supports the parent clouds of the downdrafts. Although these extreme storm types are quite different, the physics governing their downdraft and subsequent outflow formation are identical. The only differences are the relative contributions of various factors to the vertical forcing of the downdraft air.

Mesoscale dynamical forcing is also important in determining the strength of the resulting cumulonimbus convection. Caracena and Maier (1987) list strong boundary layer forcing, probably from convergence at the leading edge of cool outflow from a dissipating storm nearby, as an important factor contributing to the growth of a storm that ultimately produced a strong divergent outflow. The elongated and rapidly propagating radar echo that characterized the storm, likened to the "spearhead" shaped echoes associated with three downburst related aircraft accidents by Fujita and Caracena (1977), was indicative of this discrete propagation or secondary cell develop-

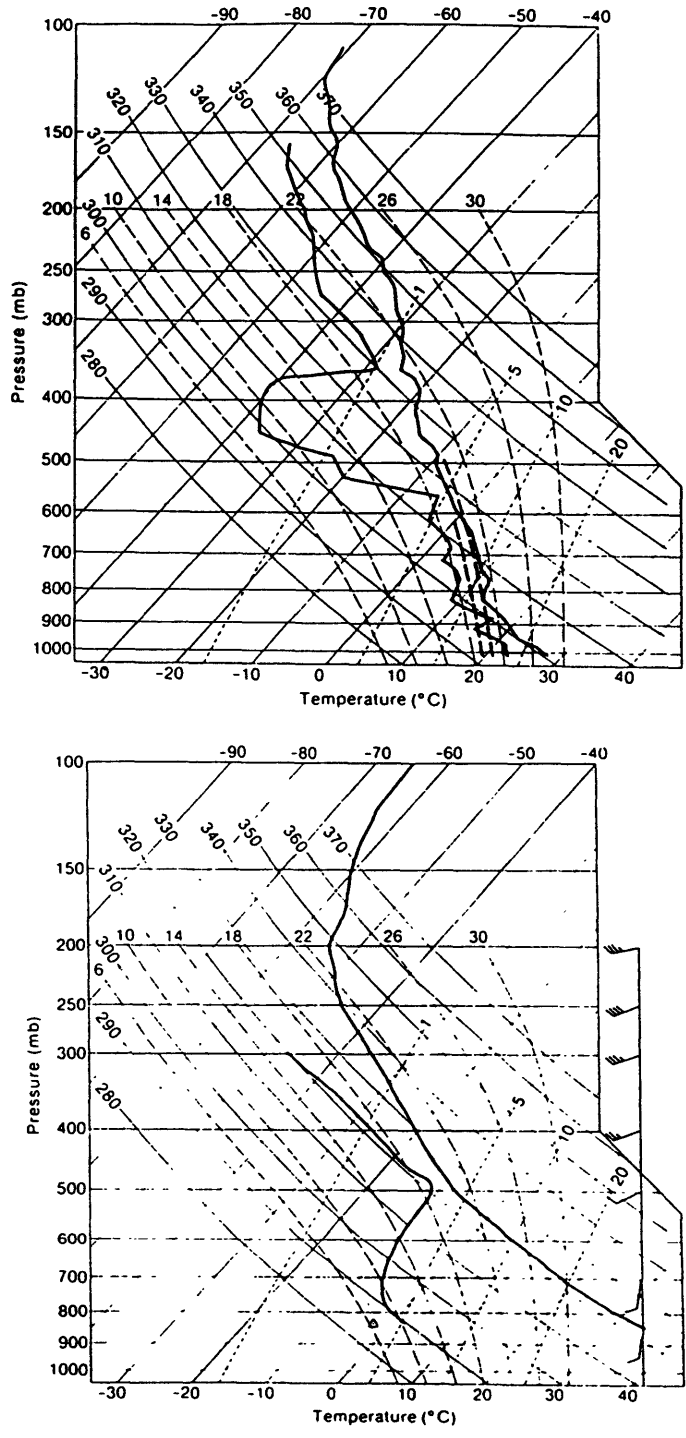


Fig. II-8. In both panels, the temperature is plotted on the right and the dew point temperature is plotted on the left. (Top) Environmental sounding from Florida on a day when thunderstorms with strong downdrafts formed. The heavy dashed line at right represents a hypothetical downdraft that produces a maximum wind speed of 22 m/s; at left represents a downdraft colder by 1°C that produces a maximum wind gust of 31 m/s. From Caracena and Maier (1987). (Bottom) A composite of five afternoon soundings by Brown et al. (1982) for convective events that produced damaging surface winds associated with high-based cumulonimbi in the Front Range area of Colorado. Taken from Caracena et al. (1989).

ment. The following was presented in a report from the Thunderstorm Project (U.S. Weather Bureau 1948).

As the cold, fast-moving air associated with the downdraft underruns the warmer air ahead, it appears to 'trigger' the development of new radar echoes. They are labelled 'first-gust echoes' in Fig. II-9. The appearance of such echoes usually indicates both the presence and direction of movement of the first gust. After several minutes the first-gust echo frequently coalesces with the 'parent' echo to form an amoeboid projection such as 'A' in Fig. II-9.

Typically only 3-5 km in diameter, these cells with their "amoeboid projections" were essentially identical to those described as spearhead echoes, based on photographs from NWS radars 130-205 km away, by Fujita and Caracena. The overshooting cloud tops observed on satellite for

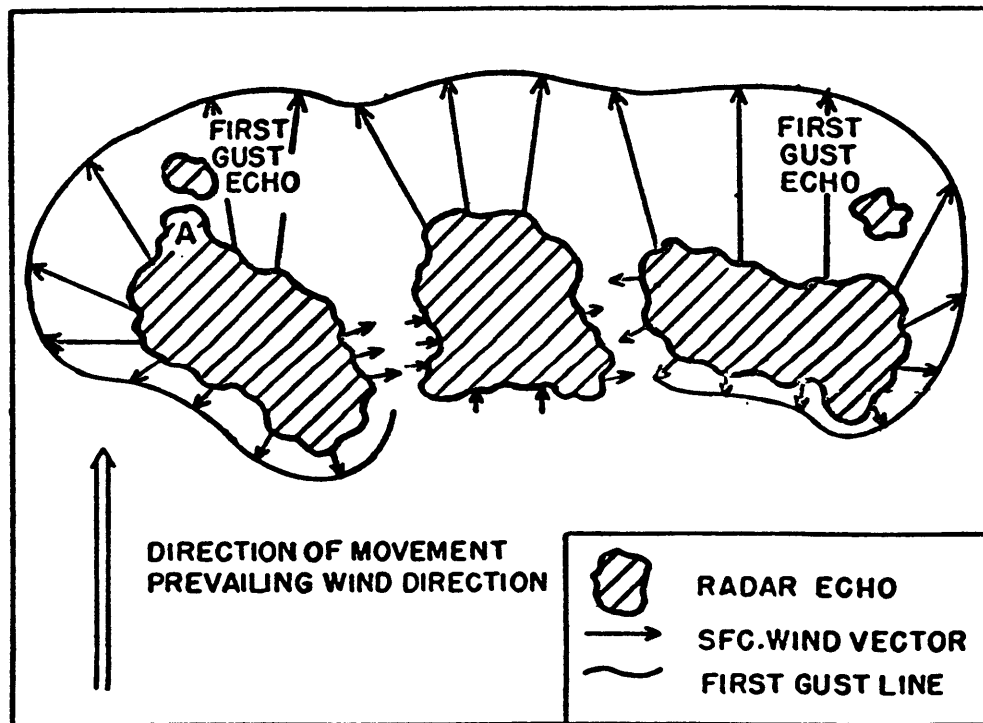


Fig. II-9. Outflow pattern of the surface wind under a line of radar echoes. Taken from U.S. Weather Bureau (1948).

at least one of those spearhead echo accident cases may have been additional evidence of the strong boundary layer forcing, rather than any indication of the source height of the downdraft air. Schlesinger (1984) has shown that in particularly intense convection, updraft air can overshoot its equilibrium level, cool, and then descend, but it remains near the cloud top.

4) The Wall Jet Analogy

Recently meteorologists have discussed the similarities between the wall jet and the diverging flow of a thunderstorm downdraft as it reaches the ground (Hjelmfelt 1988; Proctor 1988b). Byers and Braham (1949) were also aware of this physical analogy: "When the cold downdraft of a cell reaches the surface layers of the atmosphere, it spreads out in a fashion similar to that of a fluid jet striking a flat plate." A schematic illustration of impinging and radial wall jets is shown in Fig. II-10. The impinging wall jet is the flow, first described mathematically by Glauert (1956), that results "when a jet of air strikes a surface at right angles and spreads out radially over it". In their review article on the subject, Launder and Rodi (1983) note that "formally, we can regard a wall jet as a boundary layer in which, by virtue of the initially supplied momentum, the velocity over some region in the shear layer exceeds that in the free stream".

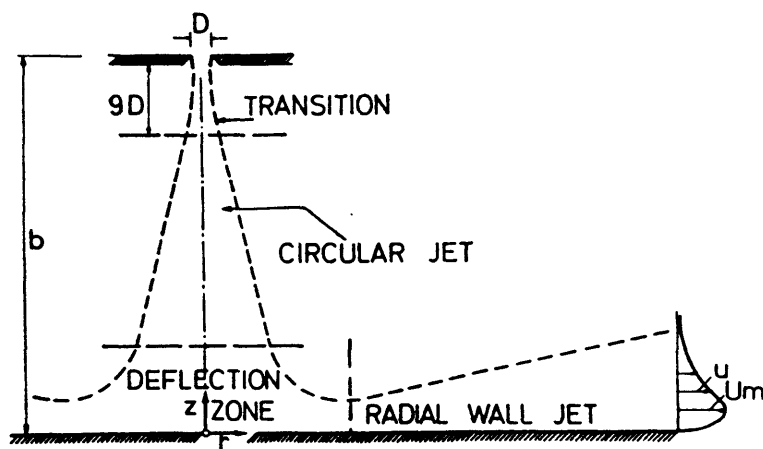


Fig. II-10. Schematic description of impinging and radial wall jets. D is the orifice diameter, u is the local mean velocity in the radial (r) direction, and U_m is the maximum radial velocity. Taken from Poreh et al. (1967).

The radial profile of radial velocity can be separated into two zones (Fig. II-10): the “deflection zone” or “developing region” under the impacting jet, where simple potential flow would predict a linear velocity increase with radius (r), and the “wall jet zone” or “developed region” beyond the radial velocity maximum, where the similarity solution predicts a $1/r$ decay of the radial velocity. Experimental evidence has shown that the velocity in the wall jet region actually varies as $1/r^{1.1}$ because of the effect of shear at the wall (Poreh et al. 1967).

Hjelmfelt (1988) has carefully compared the radial velocity profiles for several thunderstorm outflows with the profile expected for a laboratory wall jet, and found that they are basically similar, but that the outflow data decay much more rapidly with range past the velocity maximum (Fig. II-11). This is because some of the outflows are colder than the surrounding air and because the downdrafts are not continuous in time. Measurements of surface wind speed near the point of maximum radial velocity would indeed reveal a “burst-like” rapid increase and then decrease with time as the transient outflow evolved. This is illustrated in Fig. II-12, where time series of radial wind speed “measured” at four ranges from the center of a numerically modelled axisymmetric storm (Fig. V-14) are shown. The peak surface wind speed was measured at 1.5 km range. Both the rate of wind speed increase and the peak speed measured depend strongly on location relative to the storm. Thus, simple proximity to the storm is part of the explanation for sharp peaks in measured time series of surface wind speed. Such measurements cannot be interpreted correctly without information about the source location.

Fujita (1981) showed the vertical distribution of horizontal flow in a thunderstorm outflow had a strong jet-like maximum very near the surface. Proctor (1988b) specifically compared Fujita’s observed profile, his own numerically simulated outflow profile, and the average profile measured in laboratory wall jets (Bakke 1957), and found them all to be quite similar (Fig. II-13). The deflection of flow at the plate represents a vortex generation process relevant to the understanding of high surface wind speeds in thunderstorm outflows. The streamwise vorticity generation near the wall will be opposite in this developing flow region from in the developed flow region (Fig. II-14). There is a strong production of positive horizontal vorticity in the developing region, where the vertical velocity is being reduced to zero and the radial velocity is just beginning to increase with range from the center of the downdraft. The vortex stretching mechanism is responsible for this vorticity production. If a strong horizontal vortex or shear zone is already present at

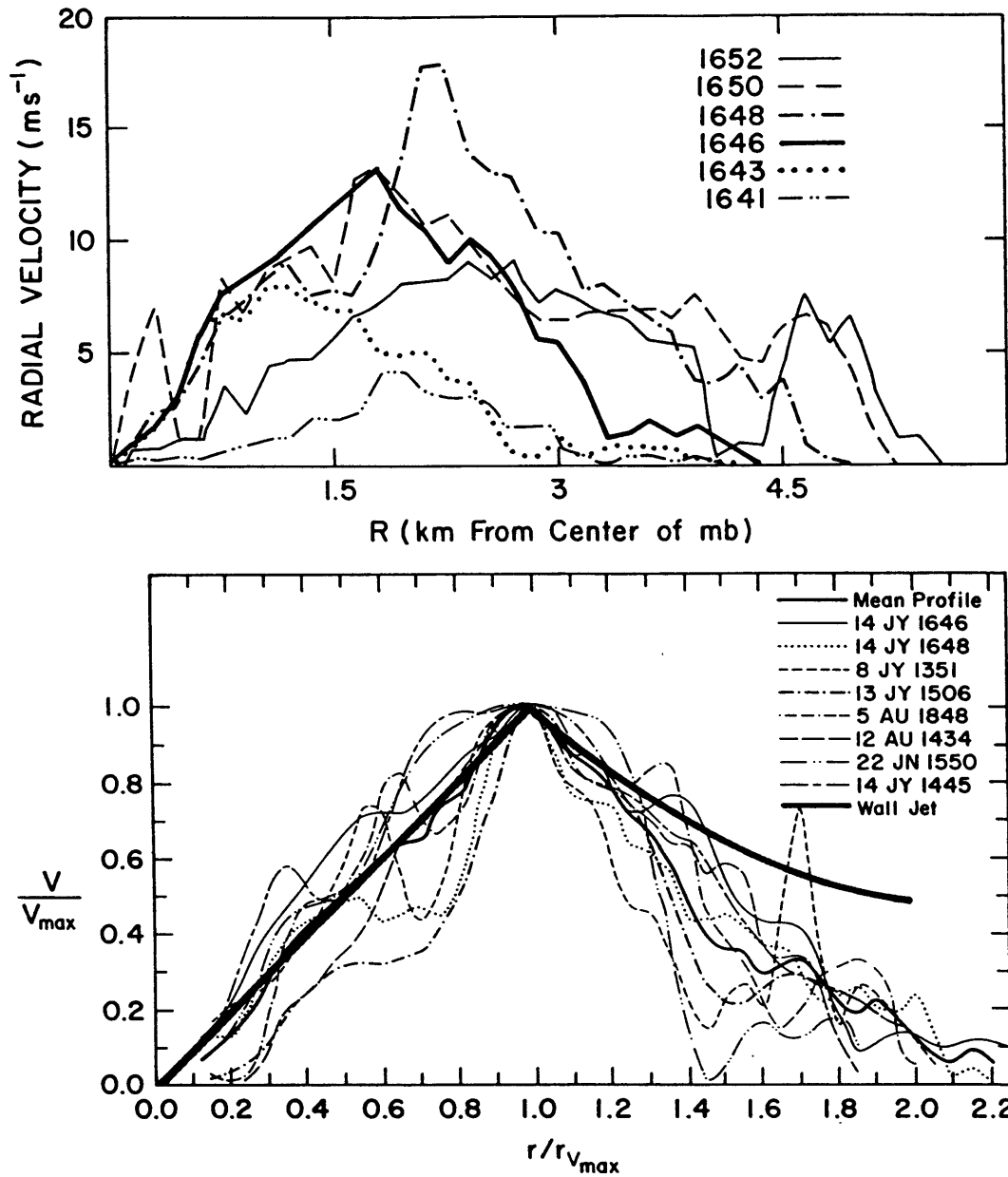


Fig. II-11. Radial velocity along azimuth of V_{\max} vs radius from downdraft center. (a) Velocity vs radius for six times for an outflow observed on 14 July 1982 by the CP-3 radar. (b) Normalized velocity vs scaled radius for several cases from the Denver area at the time of maximum observed outflow differential velocity. Velocity is normalized to the maximum for each outflow and radius is scaled to the radius of the maximum velocity. Heavy dark line is mean profile; very heavy dark line is profile predicted from laboratory wall jet studies. Taken from Hjelmfelt (1988).

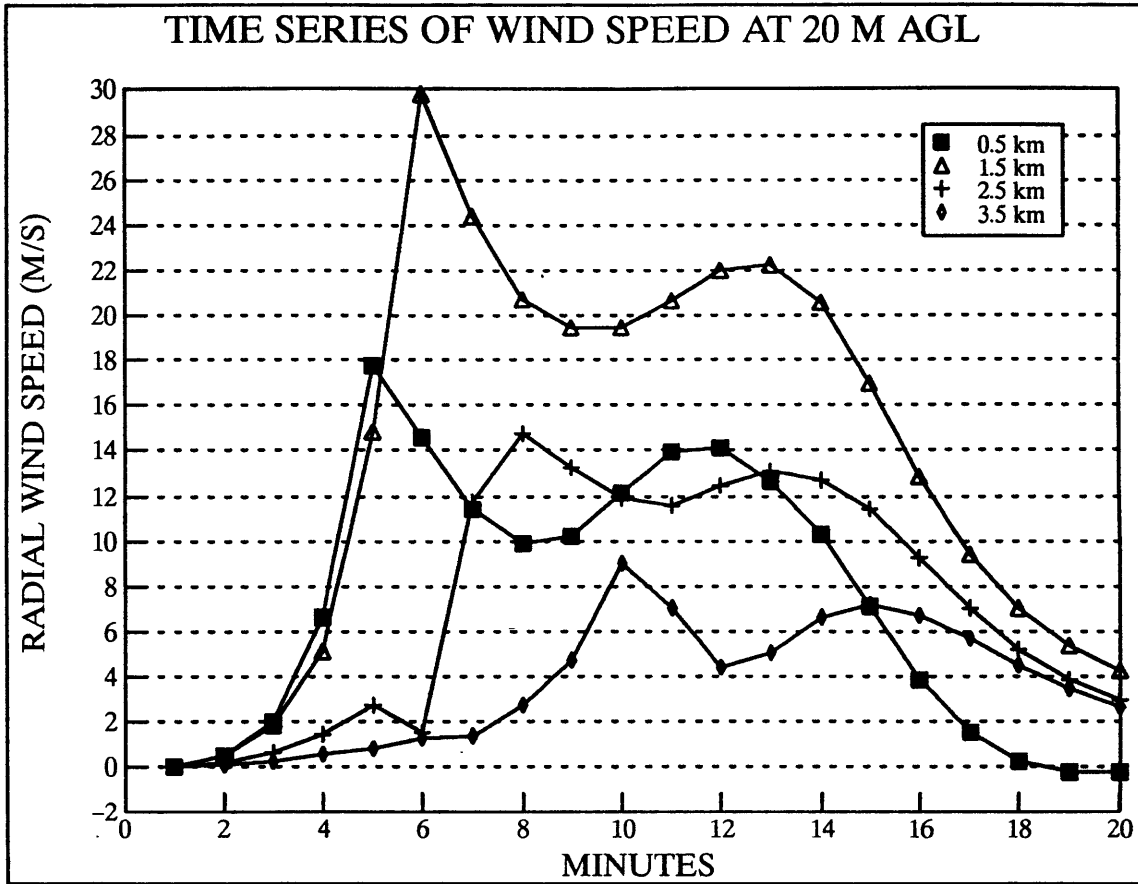


Fig. II-12. Time series of radial wind speed at 20 m agl and at the four indicated ranges from the center of the axisymmetric numerically simulated storm shown in Fig. V-14 (neutral boundary layer).

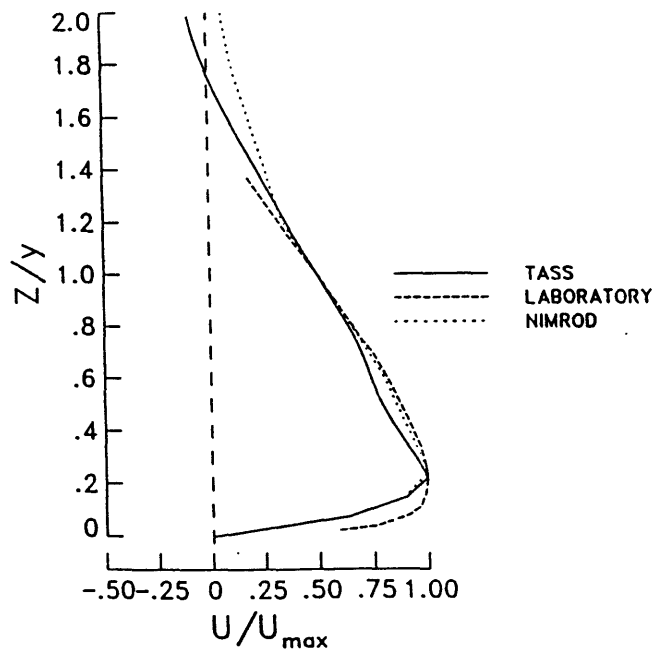


Fig. 11-13. Nondimensional vertical profiles of thunderstorm outflow. The solid curve represents the profile from Proctor's (1988b) simulated DFW case; the long-dashed line represents profiles measured in laboratory wall jets by Bakke (1957); and the short-dashed line represents a profile measured with Doppler radar by Fujita (1981; his Fig. 30), after the translation speed of the storm is subtracted out. Taken from Proctor (1988b).

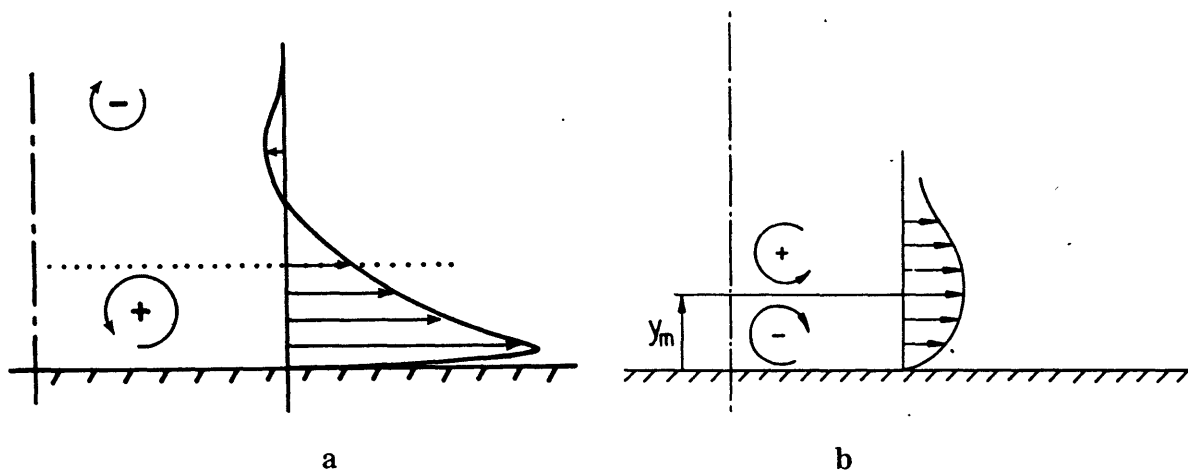


Fig. 11-14. Streamwise vorticity generation in the three-dimensional wall jet. (a) Developing flow region; (b) developed flow region. Adapted from Launder and Rodi (1983).

the edge of the downdraft, as it is in many of the neutral density downdrafts observed in Denver, its vorticity will greatly intensify upon impact.

Shapiro and Benton (1988) developed a similarity model of axisymmetric, steady, non-swirling convection which they “closed” by specifying the solenoidal forcing to the vorticity equation. They showed that axial jets form in updrafts and wall jets form in downdrafts because of the vorticity balance necessitated in nonlinear thermodynamically coupled convective flow over a rigid plate. Their result was sensitive only to the magnitude and not the precise form of the forcing. This suggests that the outflow from thunderstorm downdrafts striking the ground should regularly display the wall jet structure.

B. Effects on Low Altitude Aircraft Operations

The Thunderstorm Project (Byers and Braham 1949) was undertaken after World War II specifically to investigate the “weather hazard that had caused many serious accidents to commercial and military aircraft, namely, the thunderstorm.” The goal was to provide a detailed description of the thunderstorm in all its phases, but in particular, to understand how the thunderstorm affects aircraft operations, both in flight and on or near the ground. The hazard to an aircraft taking off or landing, due to unexpected wind changes during thunderstorm conditions, was well recognized even at that time. Ten out of 56 accidents involving commercial or private aircraft attributed to thunderstorms during the years 1938 to 1945, appear to have been caused by such wind changes (U.S. Weather Bureau, 1948).

Byers and Braham used five minute averaged data from a network of 55 (Florida, 1946) to 62 (Ohio, 1947) recording weather stations, with an average spacing of roughly 3 km, to analyze in detail the surface meteorological conditions during the life cycle of thunderstorms. An example of their work is presented in Fig. II-15. Byers and Braham (1949) summarized their results on the thunderstorm, as it affects low altitude and surface aircraft operations, as follows:

1. The marked change in the surface wind accompanying thunderstorms occurs along the edge of the outward-flowing cold air which has come down as the downdraft in the rain area.
2. The downdraft, and consequently the gusty surface winds, first appears shortly after the start of heavy rain from a particular cell.
3. A ring of high gusty winds spreads outward from the cell, the speed of advance being greatest in the direction of the prevailing wind flow.

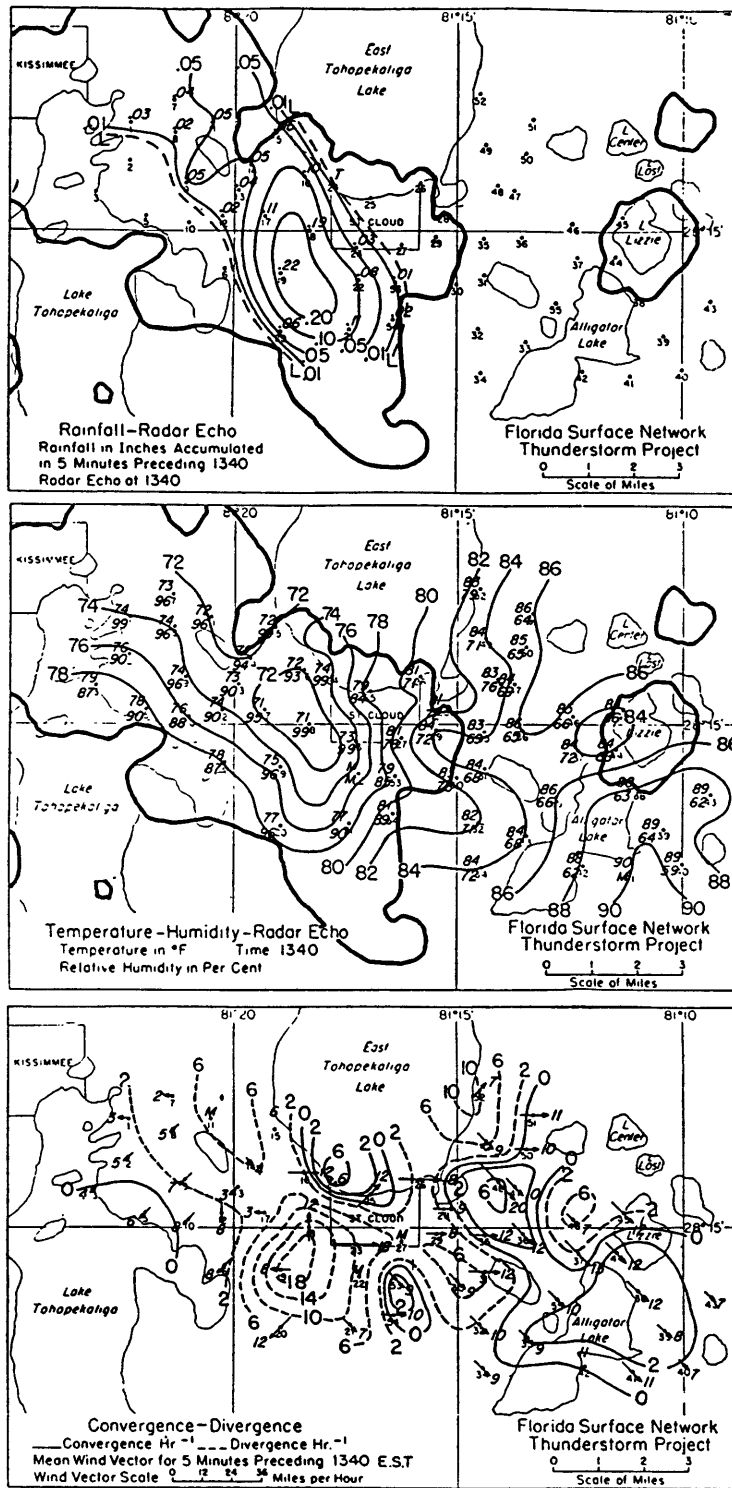


Fig. II-15. Surface analysis of a thunderstorm complex that occurred on 9 July 1946 near Orlando. Data presented are identified in the lower left corner of each panel. Notice the strong divergence coincident with the surface rainfall maximum. Taken from Byers and Braham (1949).

4. The maximum gust speeds associated with a given cell occur very close to the rain area from it and at the time when the downdraft first reaches the ground. Therefore the more distant the storm, the less violent the surface gusts. A station near the center of a cell at the time when the downdraft reaches the surface may experience gusts of a magnitude comparable with the most severe found within the storm itself.
5. The wind will invariably blow outward from the rain area after the passage of the discontinuity surface.
6. The strength of the gustiness at any particular location decreases after the passage of the discontinuity surface. An airplane whose take-off is delayed approximately 5 min after the passage of the first gust will not encounter exceedingly heavy turbulence in the surface air layers. It must be remembered, however, that this take-off, if made into the wind, will take the airplane toward the region of the thunderstorm downdraft.
7. The maximum turbulence in the surface winds occurs in the lowest few hundred feet.

One of the first explicit illustrations of the hazard posed by thunderstorm downdrafts to aircraft flying at low altitudes depicted the unusual conditions which led to the crash of an aircraft taking off from Kano, Nigeria in 1956 (Fig. II-16). A similar illustration by Viemeister (1961), produced a few years later, included more details of the meteorological conditions encountered during that same crash (Fig. II-17). Stewart (1958) provides the observations, made by the airplane's captain, of the weather encountered at Kano both before and during takeoff. Apparently the captain knew there were thunderstorms in the vicinity and "had taken steps to assure himself that the nearest squall line was much too far away to present any risk". He also was assured that "a thunderstorm to the north-east of the aerodrome was a local storm and would move little". As he took off, it was overcast, heavy rain began to fall, and visibility progressively decreased. The captain did not recall feeling "any signs of turbulence or sink", but was "horrified suddenly" when he noticed how fast the air speed was dropping, especially since he expected it to be building fairly rapidly. The official accident report concluded that "the accident was the result of loss of height and air speed caused by the aircraft encountering, at approximately 75 m (150 ft) after take off, an unpredictable thunderstorm cell which gave rise to a sudden reversal of wind direction, heavy rain and possible downdraft conditions."

There are not enough data available to determine whether any outflow boundaries crossed the airport or helped initiate the encountered storm. However, it seems fairly clear that a cumulonimbus cell grew explosively directly over the departure end of the Kano runway, and reached the

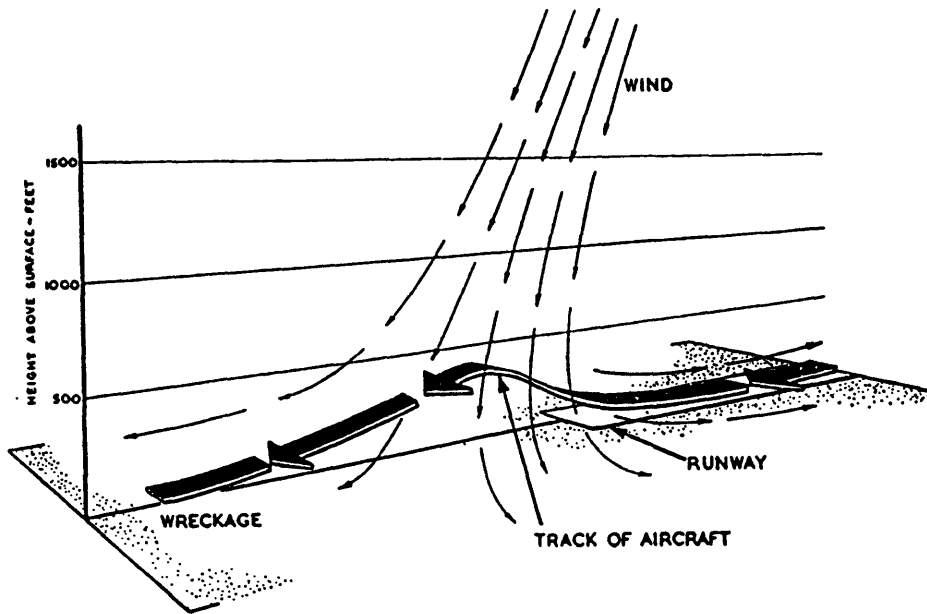


Fig. II-16. The unusual conditions which led to the Kano accident in 1956. The height indications are those of the accident investigation committee. Taken from Stewart (1958).

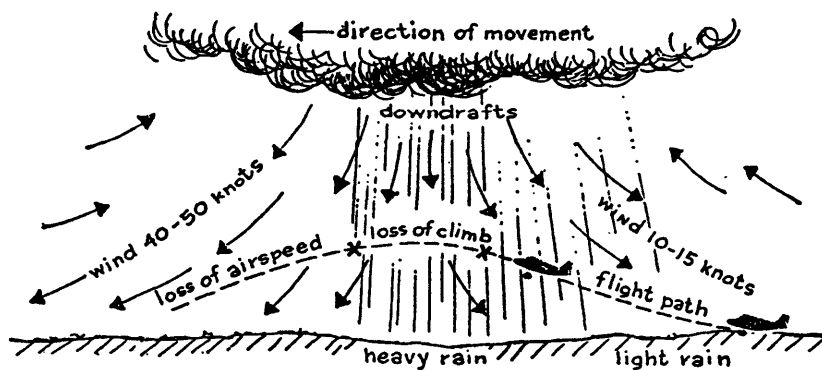


Fig. II-17. Downdrafts from a thunderstorm can be hazardous to an airplane during a take-off. Drawn by Viemeister (1961) to illustrate in general the meteorological conditions encountered by the plane that crashed taking off at Kano in 1956.

mature stage just as the plane which eventually crashed was taking off. Stewart concludes his description of the accident with the following note.

Violent turbulence is a generally known danger to aircraft and cumulo-nimbus clouds are avoided because of it; the line squall, with its roll-cloud formation, is also known and avoided. But the thunderstorm cell was not perhaps sufficiently widely recognized as a possible cause of powerful downdrafts until the results of the investigation into this accident ... were made known.

C. Thunderstorms versus Microbursts

Today the precipitation driven downdraft of a cumulonimbus cloud is commonly called a microburst, when the storm cell diameter and outflow (as seen with Doppler weather radar) are such that the velocity differential at the surface is greater than 10 m/s, over a distance less than 4 km (defined by Wilson et al. 1984). The dimension of 4 km apparently originated from the arbitrary planetary scale system defined by Fujita (1981), in which the earth's circumference of 40,000 km is the upper limit, and scale divisions are made in steps of two orders of magnitude each, at 400 km, 4 km, and 0.04 km. The speed differential of 10 m/s, when combined with this spatial scale, was meant to represent the threshold of wind shear hazardous to jet aircraft, reflecting the original intent of the new burst terminology.

However, the accompanying downdraft that this divergent shear implies is far weaker than the first definition of "downburst" (downward velocity of at least 3.5 m/s at 90 m agl; Fujita and Byers 1977). Recent studies analyzing the aerodynamic effects of wind shear on aircraft (Frost and Bowles 1984; Elmore and Sand 1989) have shown that most of the storms being called microbursts would not cause aircraft accidents (Fig. II-18; see also Fig. I-6). Jet transport performance is marginal in a divergent horizontal wind shear of ~ 12 m/s per km, roughly five times greater than the threshold microburst. During the first operational demonstration of the TDWR system (Turnbull et al. 1989), the decision was made to increase the microburst threshold from 10 to 15 m/s differential outflow, based on feedback from the aviation community. Apparently warnings on events that remained weaker than this new threshold were considered a nuisance.

The most narrow, rapidly evolving thunderstorms, with their powerful downdrafts and severe surface outflows do indeed represent a very real, critical hazard to aviation. It can certainly be argued that the microburst concept has served as a valuable reminder to pilots of just how dangerous low altitude operations near strong localized thunderstorms can be, especially when the down-

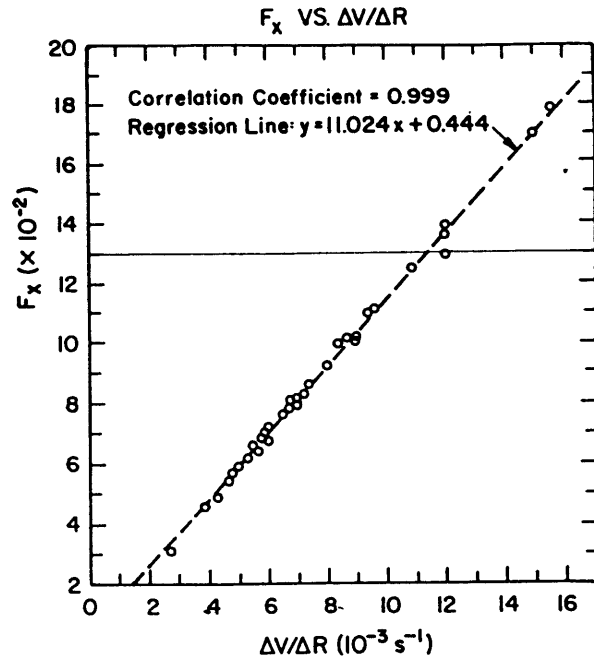


Fig. II-18. Plot of F_x , a measure of the rate of change of the longitudinal (along-flight) component of winds normalized by the acceleration of gravity, vs $\Delta V/\Delta R$, the Doppler differential velocity divided by the distance over which it occurs, detected by radar at the surface in 39 microbursts in the Denver area. F_x more precisely measures the performance loss of an aircraft in a wind shear encounter. The horizontal line at $F_x = 0.13$ indicates the approximate value at which jet transport performance becomes marginal. Taken from Elmore and Sand (1989). Note that no account has been taken of the vertical velocity in this measure of F -factor (Fig. I-6).

drafts first reach the ground. It hopefully has eliminated the false sense of security pilots seem to have had at finding only small storms, 3–6 km in diameter, on their airborne radar displays (Fujita and Caracena 1977). The microburst terminology has helped dramatize the thunderstorm aviation hazard, and to change it now would surely be detrimental. However, I suggest it is undesirable to call the downdrafts and outflows from thunderstorms “microbursts” in the scientific literature for the following reasons.

- There is no consensus on a precise defining threshold. There does not appear to be any meteorologically significant scale separating thunderstorm downdrafts that qualify as microbursts, under Wilson’s post-JAWS definition, from those that do not (Fig. II-19), nor is the intended aircraft hazard interpretation precise (Fig. II-18).

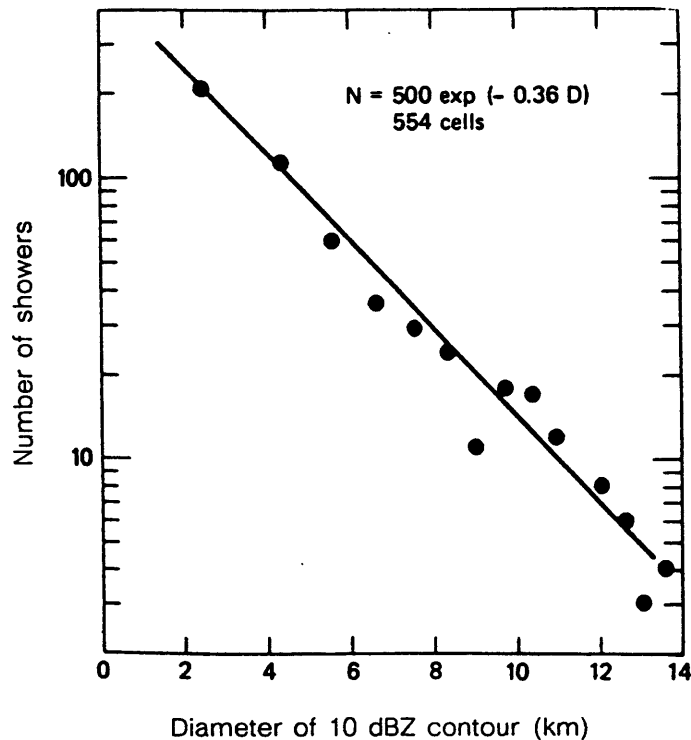


Fig. II-19. Distribution of the number of radar echoes from summer rainshowers according to the diameter of the 10 dBZ contour. The data were collected near Wallops Island, VA during the 4 months from May through August, 1973. The radar was operated in a fixed raster scan mode, once each 30 min, from 3:00 – 11:30 pm EST every day. Taken from Konrad (1978).

- The “downrush” had already been introduced by Fawbush and Miller in 1954 to describe the extreme case of damaging winds from non-frontal thunderstorms. The “downburst” was also meant to signify the downdrafts from such storms (Fujita 1979).
- “Microburst” was originally specifically introduced to describe something different, a downdraft smaller and stronger at low altitudes than the previously observed thunderstorm downdrafts or the “downrushes”. As proven by the evidence presented from the Thunderstorm Project, plenty of small, strong thunderstorms with divergent outflows *had* previously been observed. Researchers had also fully appreciated that surface conditions are most hazardous just when the downdraft reaches the ground.
- “Microburst” must now be joined with qualifiers such as wet, dry, outflow, and rotor (Fig. I-4) to convey any precise meaning. Other qualifiers such as stationary, travelling, radial, twisting, midair, and surface (Fujita 1985) have also been used.

In a recent edition textbook on meteorology (Moran and Morgan 1989), the following entry appears under the heading "Downbursts".

Severe, and sometimes not so severe, thunderstorms can produce a **downburst**, a strong downdraft that, upon reaching the surface, diverges horizontally as an outburst of destructive winds. We can simulate this flow by aiming a garden hose nozzle downward so that the stream of water strikes the ground and bursts outward. Downbursts blow down trees, flatten crops, and wreck buildings in a starburst pattern of destruction. On the basis of size, a downburst is classified as either a macroburst or a microburst.

Paragraphs follow specifically describing the macroburst (> 4 km) and the microburst (< 4 km). It is truly unfortunate that this terminology has trickled down into elementary textbooks. It sounds as if the downburst is something other than the expected thunderstorm downdraft, graphically described first by Byers and Braham (1949) using the garden hose analogy.

For the reasons cited previously, I will continue the traditional use of the thunderstorm terminology to describe the precipitation driven downdraft from a convective cell. The virga downdrafts of the Western Plateau that originate from thunderstorms with cloud bases above the freezing level do have a characteristically smaller scale, and they do produce short lived strong "burst-like" downdrafts and outflows, with little or no rain at the surface. Knupp (1989) has shown this is caused by the rapid, combined cooling from simultaneous melting and evaporation that takes place in the subsaturated air below cloud base. Perhaps "dry microbursts" is not a bad name for these downdrafts. But they are different from the phenomenon first described as a microburst, so I will continue to reserve that terminology.

D. Predicting Thunderstorm Downdraft and Outflow Strength

Much effort has been put forth over the last few years in quantifying the factors influencing the development of the strongest thunderstorm downdrafts and outflows. One of the apparent mysteries is that thunderstorms with quite different downdraft and outflow strengths can occur simultaneously, in the same environment. These observed differences are probably due to variations in reflectivity, storm geometry, boundary layer forcing, or the proximity and strength of neighboring convection. Some researchers feel there is no hope of predicting these differences without high speed four dimensional numerical simulations that are periodically updated with observations of the current convective state of the atmosphere (e.g., Talagrand and Courtier 1987; Courtier and Talagrand 1987). However, I suggest that if one is interested in a 5 min predic-

tion of the maximum downdraft and outflow speeds from a particular thunderstorm cell, and the environmental stability characteristics are known, then the observations of the mature cell contain all the necessary information.

Another apparent mystery is that storms with similar reflectivity levels on different days produce very different strength outflows. Because of the proportionality between reflectivity and liquid water content, and between water content and vertical acceleration, some researchers argue there should be a monotonic relationship between downdraft/outflow strength and reflectivity. Yet evidence is to the contrary (Fig. II-20). This is because environmental factors that promote the thermodynamic generation of negative buoyancy are of crucial importance, and because account is rarely taken of the overall storm geometry which governs the relationship between the maximum downdraft and outflow strengths.

Occasionally storms occurring at the same time with apparently identical reflectivity structures, produce outflows of different strengths. Because reflectivity is exponentially related to water content, a small difference in reflectivity between high reflectivity cells translates into significantly different downdraft forcing. Instead of studying storms by examining their reflectivity fields on a

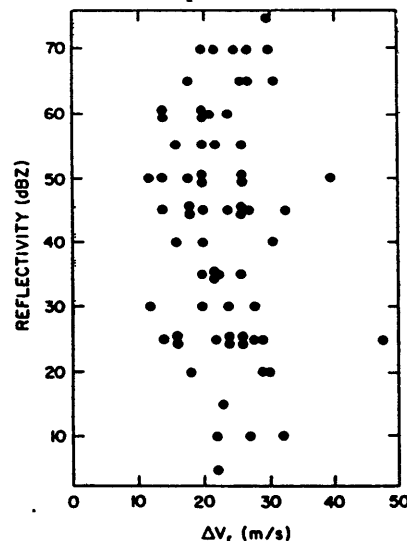


Fig. II-20. Doppler-observed maximum low-altitude velocity differentials (ΔV_r) associated with microbursts, versus the radar reflectivity at a height of 500 m. Observations from the JAWS project near Denver. Taken from Wilson *et al.* (1984).

linear dBZ scale with the usual 3–5 dBZ increments, researchers should use a scale linear in water content, which is directly proportional to the forcing due to precipitation drag. Maxima in the water content field provide a good indication of where downdrafts will begin to form.

Wakimoto and Bringi (1988) discuss three storms with weak, moderate, and strong differential outflow strengths that occurred on three different days for which the soundings appeared to be quite similar. In addition to the suspected differences in the initial storm forcing, subtle differences in the vertical temperature structure, such as the height of any stable layers or inversions, also appear to play an important role in the ultimate downdraft strength.

Numerical models developed in recent years can provide a tremendous amount of insight into the resolution of these apparent mysteries. In the remainder of this chapter, I focus on interpreting the results of recent numerical modelling studies according to simple physical arguments and on quantifying the information in a way that is useful for predicting thunderstorm downdraft and outflow strength.

1) Summary of Numerical Modelling Results

Numerical models have been used to study isolated thunderstorms in a number of different ways. One approach has been to initialize a three dimensional environment with an observed sounding of temperature, humidity, and winds (or an axisymmetric environment with temperature and humidity only), provide a surface thermal or convergence zone to kick off the convection, and integrate the system forward in time. This produces a simulation of the entire life cycle of the thunderstorm, often with results that are quite similar to those observed in nature. Probably the best examples of the utilization of this kind of model to understand the structure of the low level precipitation driven downdraft, and its relationship to upper level downdrafts, are given in the papers by Knupp [1987, 1988, 1989; see also the review article by Knupp and Cotton (1985)]. Other examples are given by Anderson (1990), Proctor (1988a), Orville et al. (1986), Hjelmfelt et al. (1986), and Tripoli and Cotton (1986). These models have been used in the past to study supercells, tornadoes, and thunderstorm updraft structure with great success (e.g., Klemp and Wilhelmson 1978; Weisman and Klemp 1982, 1984; Weisman et al. 1983; Klemp and Rotunno 1983; Miller and Moncrieff 1983; Schlesinger 1984).

Another approach has exploited the numerical modelling result that the greatest increase in vertical acceleration of the main storm downdraft occurs somewhat below the freezing level; well

above this level, models indicate that precipitation loading initiates descending motion, but cooling due to sublimation and evaporation contributes little to the downward acceleration. The three-dimensional or axisymmetric models are initiated with a sounding and either a specified cooling rate or a mass of water, graupel, snow, or hail above the freezing level. These "subcloud" models allow higher resolution and more control over the parameter space to be examined, but do not predict the amount of condensate that will form. Examples utilizing this approach are given in the papers by Proctor (1985, 1988b, 1989), Droegemeier and Babcock (1989), Droegemeier (1988), Droegemeier and Davies-Jones (1987), Krueger (1988), Krueger et al. (1986), Krueger and Wakimoto (1985), Anderson et al. (1985), Thorpe et al. (1980), Mitchell and Hovermale (1977); and Teske and Lewellen (1977).

A third approach has used one-dimensional models with detailed cloud physics, in which the environmental profiles of temperature and humidity are specified. While pressure effects cannot be included [but see Holton (1973)], these models effectively isolate factors influencing downdraft strength such as the environmental lapse rate, and precipitation size distribution, phase, and amount. Examples include the work by Srivastava (1985, 1987), Mahoney and Rodi (1987), Betts and Silva Dias (1979), and Kamburova and Ludlam (1966).

Relying primarily on the modeling results of Knupp (1987, 1988), Proctor (1988b, 1989), and Srivastava (1985, 1987) the following conclusions can be drawn.

- 1) The precipitation driven downdraft is confined to the lowest, least stable layers of the atmosphere. The maximum downdraft *speed* occurs around 1.0 km agl. This is much lower than the distribution in Fig. I-2 suggests; a downdraft speed of 20 m/s at 500 m agl could account for the depicted downburst speeds of 3.7 m/s at 90 m agl. The evolution of the vertical velocity in the lowest 2 km of the axisymmetric numerical storm simulation shown in Fig. V-14, is illustrated in Fig. II-21. Notice how the peak descends from about 1.4 to 1.0 km from $t = 3$ min to 4 min (time of maximum), and how rapidly the vertical velocity decreases thereafter. It would be very difficult for almost any observational system to capture the actual maximum in vertical velocity.
- 2) The upper limit for air reaching the surface within a downdraft is that level at which the equivalent potential temperature in the atmosphere equals the saturation equivalent potential in the boundary layer; there is no mechanism whereby air potentially warmer than this can be brought down all the way to the surface. Based on observations and numerical model

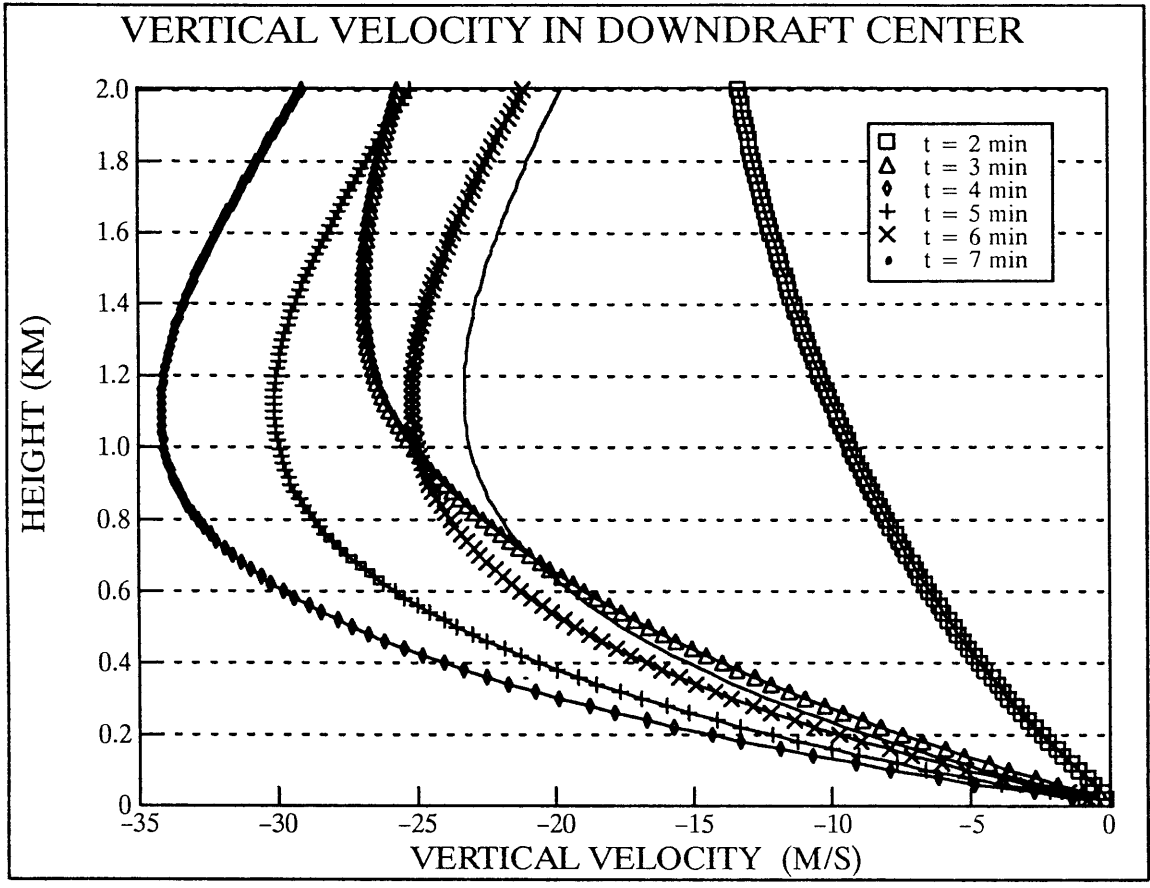


Fig. II-21. Vertical velocity on the central axis in the lowest 2 km of the axisymmetric numerical simulation shown in Fig. V-14 (neutral boundary layer). Six different times are shown around the time of maximum vertical velocity ($t = 4$ min).

results, Knupp (1987) has defined a “transition level” as the level at which the lapse rate changes from neutral or conditionally unstable to absolutely stable or moist adiabatic. Because greater stability of air feeding downdraft circulations produces slower descent rates (e.g., Kamburova and Ludlam 1966), the upper limit to air entering the downdraft is found to be the “transition level” in the sounding, but this is only true if it is below the level at which the equivalent potential temperature matches the saturation value in the boundary layer.

- 3) Downdraft descent rates increase with increasing low level environmental temperature lapse rate. Also, the higher the sounding transition level, the deeper the neutral or conditionally unstable layer, and thus the stronger the downdrafts that will develop. A similar relationship holds for the melting level. The maximum downward *acceleration* found below the level of the minimum in equivalent potential temperature will generally occur roughly 1 km below the melting level, where the effects of loading, melting, and evaporation are all strong. An environmental humidity distribution with low relative humidity at the source region of the downdraft, but high relative humidity at the surface (virtually warmer surface air), favors stronger downdrafts and outflows. Thus, it is actually the environmental lapse rate of virtual temperature that is important.
- 4) The greater the mixing ratio of water in the downdraft, the stronger the downdrafts that will develop. This is both because of an increase in precipitation loading, and because there is more water available to undergo phase changes. However, the optimal *radius* of the water mass region for producing strong downdrafts is ~ 1 km. Water cores that are more spatially extended cannot fall as rapidly because they must oppose proportionately stronger perturbation pressure forces that arise in response to the vertical motion. The wider cores also produce weaker divergent shear at the surface, but they do produce stronger and deeper outflows because of the increased mass flux. Cores narrower than this optimal radius are susceptible to mixing, and they tend to become dilute and finally disappear before they reach the surface.
- 5) The cooling rate depends most strongly on the particle size distribution, with smaller particles providing more efficient cooling (Fig. II-22). Under some circumstances larger drops, with their greater terminal fall speeds, are able to produce deeper stronger downdrafts by spreading the cooling over a greater depth.

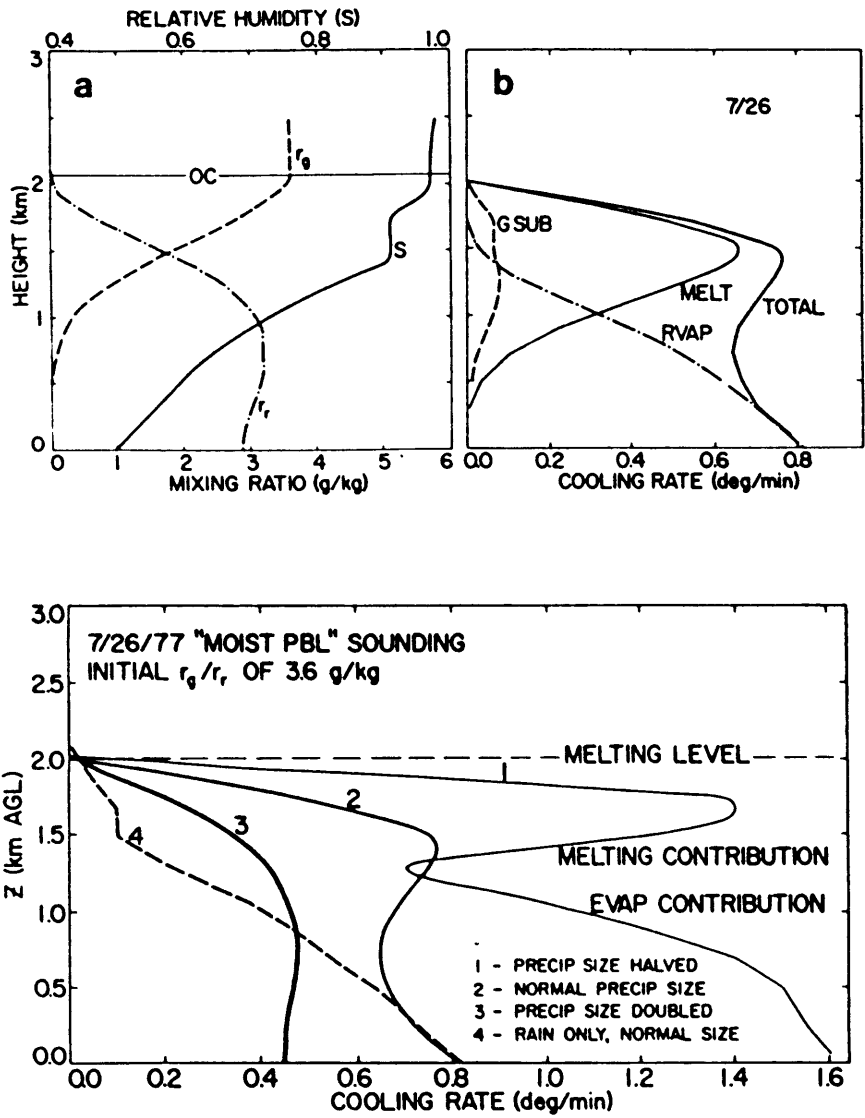


Fig. II-22. (Top) (a) Profile of relative humidity (S) used in the calculations presented in (b). Resultant mixing ratios of graupel and rain (r_g and r_r) are shown. (b) Profiles of cooling rates from sublimation of graupel (GSUB), evaporation of rain (RVAP), melting of graupel (MELT) and the sum of all three (TOTAL). These quantities were obtained by simulating the release of graupel from above the melting level [labelled OC in (a)], and then computing subsequent melting, sublimation, and evaporation as the precipitation descended into a motionless environment (i.e., $w=0$). Assumed precipitation size distributions are given by Eqs. (8) and (9) in Knupp (1988). (Bottom) Total precipitation-induced diabatic cooling rates (sum of raindrop evaporation, graupel sublimation, and graupel melting) as a function of precipitation size. Curve 2 is the same as the curve labelled TOTAL in the Top panel. Both figures were taken from Knupp (1988).

6) The cooling rate also depends on the phase of the water present. Assuming all of the water is in the form of graupel at the freezing level, the cooling rate just below this level will be dominated by melting with a small contribution from sublimation. The cooling rate will begin to be dominated by evaporation only after most of the graupel has melted (Fig. II-22). Proctor (1989) showed that snow and graupel are most effective in producing strong downdrafts in environments typified by a dry neutral layer extended from the ground to above the melting level, with moisture present at the top of the neutral layer, such as occurs commonly in Denver in the summertime. He also showed that hail is most effective at producing strong downdrafts in environments more typical of summertime convection in other parts of the country. However, Krueger et al. (1986) and Srivastava (1987) show that variations in precipitation rate or mixing ratio are much more important than the variations in the phase of precipitation present, in determining the eventual strength of the downdraft (Table II-1).

Table II-1. Maximum downdraft speed (m/s) versus maximum precipitation rate at cloud base (mm/hr) for precipitation made up of rain only, snow, and graupel. Taken from Krueger et al. (1986).

Case	10 mm/hr	30 mm/hr	70 mm/hr
Rain only	7.9	11.5	14.8
Snow	8.6	10.3	13.2
Graupel	7.3	10.4	13.1

2) Derivation of Heuristic Prediction Model

Proctor (1989) concludes his work by noting that since the ratio of the maximum thunderstorm outflow speeds to downdraft speeds “was found to be quite sensitive to environmental conditions, radius of the downdraft, and precipitation type”, it may be difficult to estimate one given the other. This conclusion is far too pessimistic, because there are some simple, physical relationships that have not yet been exploited. I use the published axisymmetric numerical model output of Proctor (1989), Krueger and Wakimoto (1985), and Droegemeier and Babcock (1989) to show

that expected physical relationships are indeed consistently observed, even though the models are quite different. Based on these findings, prediction equations for the maximum downdraft and outflow velocities are derived that depend on the environmental conditions, the precipitation mixing ratio, and shape of the thunderstorm precipitation core. An overview of the derivation is presented here and the details are given in Appendix A. The equations developed are valid over most of the modelled parameter ranges, and they predict well the observed downdraft and outflow speeds in a number of published case studies.

The vertical momentum equation is used to indicate the expected dependence of the vertical velocity on the various forcing mechanisms at work in the thunderstorm downdraft. Neglecting entrainment, the Boussinesq form of the vertical momentum equation can be written as (e.g., Knupp and Cotton 1985):

$$\frac{dw}{dt} = g \frac{\theta'}{\theta_0} - g (l + i) - \frac{P'_z}{\rho_0} \quad (\text{II.1})$$

where w is the vertical velocity, t is time, g is the gravitational acceleration, θ_0 is the potential temperature of the environment which varies only in height and θ' is the difference in potential temperature between a parcel and the environment, $(l + i)$ is the mass mixing ratio of liquid water plus ice, P' is the perturbation pressure, ρ_0 is the density which varies only in height, and the subscript z denotes partial differentiation in height. Perturbation pressure buoyancy itself (as opposed to its vertical gradient) and frictional effects are ignored. Buoyancy effects of humidity in the environment have not been included but they can be easily by substituting virtual temperature for temperature in Eq. (II.1).

The rationale behind the model development is to relate each term in the vertical momentum equation to the observable environmental or storm characteristics that are physically responsible for its ultimate magnitude. A number of simplifying assumptions have to be made. The total vertical acceleration is approximated as:

$$\frac{dw}{dt} \sim \left(\frac{w^2}{2} \right)_z \quad (\text{II.2})$$

This represents the left hand side of Eq. (II.1). Making this substitution, and integrating Eq. (II.1) in height, the following dependence of the vertical velocity on the height of the downdraft column results.

$$w^2 \sim \text{forcing} \cdot \Delta z$$

Knupp (1987) showed that this downdraft height can be related to the "transition level" in the sounding. The downdraft velocity data from the cases he investigated do show this square root dependence on the height of the transition level (Appendix A). Addis (1984) showed a similar dependence of the vertical velocity on the height of the downdraft column in his convective storm outflow modelling work.

The first term on the right hand side of Eq. (II.1) is the temperature buoyancy. For a given condensate mixing ratio, the downdraft velocity will increase as the lapse rate in the subcloud environment increases from stable values toward neutral largely because of the resultant temperature buoyancy contribution to the vertical acceleration. Studies have shown that for strong downdrafts and outflows to occur at lapse rates below about 7 K/km, high reflectivity must be present. However, when the lapse rate approaches the dry adiabatic value, almost any concentration of precipitation can produce strong downdrafts (Fig. II-23), especially if the subcloud layer is deep. Srivastava (1985) calculated the temperature excess of descending air parcels over their ambient environment for various subcloud lapse rates and liquid water mixing ratios, using a model based on evolution equations for raindrop mass and size distribution, thermodynamic energy, water substance, and vertical velocity. His tabulated data show a quadratic dependence of this temperature difference on lapse rate for a given liquid water mixing ratio:

$$\theta' \sim \Gamma^2 \tag{II.3}$$

or, substituting in Eq. (II.1) and using the simplified Eq. (II.2),

$$w^2 \sim \Gamma^2 \Delta z$$

By comparison with the axisymmetric numerical model data (shown in Appendix A), it was discovered that this relationship did indeed hold true for a given precipitation mixing ratio. As the mixing ratio increases, greater downdraft velocities are achieved, but the linear dependence of vertical velocity on lapse rate does not vary. The mixing ratio dependence of the temperature

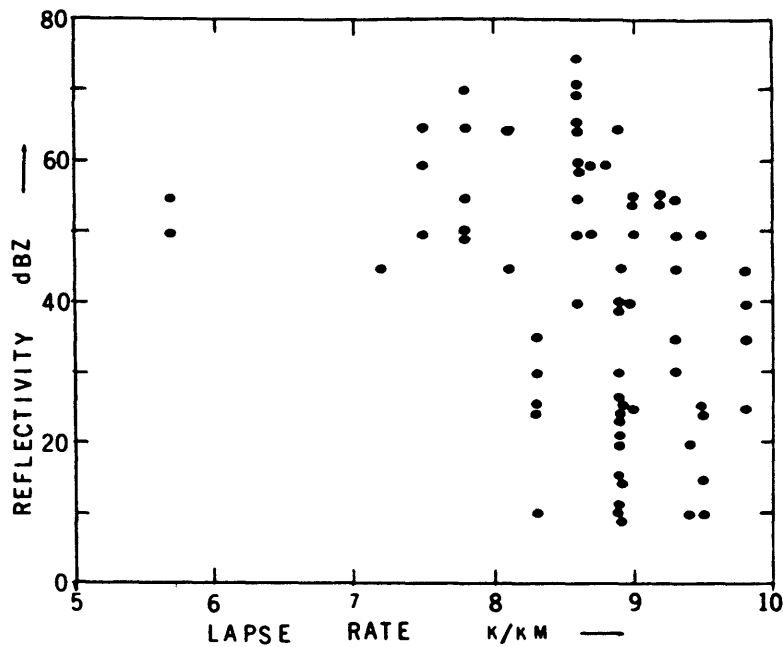


Fig. II-23. Each point represents a microburst identified during the JAWS project by radar observations. The ordinate is the reflectivity factor for the microburst at a height of about 500 m agl. The lapse rate of temperature in the environment was obtained from special radiosonde observations. Taken from Srivastava (1985).

buoyancy represents one part of the vertical acceleration due to total water concentration, and can be represented by an undetermined function of the mixing ratio:

$$w^2 \sim [\Gamma^2 + f(L)] \Delta z$$

Note that L is used to represent the total mixing ratio instead of $(l + i)$ as in Eq. (II.1) because no account is taken of the phase of the water mass present. The temperature buoyancy effects from the total water content can be quantitatively incorporated in the precipitation loading term.

The second term on the right hand side of Eq. (II.1) is the contribution of precipitation loading to the vertical acceleration. The form of that term, combined with the simplifying approximation of Eq. (II.2), gives the following dependence of the vertical velocity on the precipitation content:

$$w^2 \sim L \Delta z$$

Comparison with numerical model results (Appendix A) showed that if L was interpreted as the peak value of a Gaussian distributed precipitation region, then the vertical velocity also depended equally strongly on the vertical depth (Gaussian half amplitude width in the vertical) of that precipitation region. Representing this depth as D , the velocity dependence can be expressed as:

$$w^2 \sim L D \Delta z$$

The parameters L and D will ultimately be estimated from radar reflectivity which depends strongly on the precipitation drop size distribution present in the storm. Many equations relating reflectivity to water content that account for these different distributions have been derived. The choice of equation will depend on the type of convection present (perhaps the peak reflectivity observed), the climatic region, the season of the year, etc. This choice is critical because while the acceleration depends only on the total water content, the cooling rate depends most strongly on the particle size distribution. All of the known dependence of the vertical velocity on precipitation size distribution and phase will be contained in this choice.

The third and final term on the right hand side of Eq. (II.1) is proportional to the vertical gradient of the perturbation pressure. For this thunderstorm downdraft application, the pressure perturbation of interest is created largely by the descending downdraft itself, and it generally opposes the downward motion. If all other forcing remains equal, the vertical velocity will vary inversely with the downdraft radius, at large radii, because of the induced pressure perturbation (Appendix A). But the same induced pressure perturbation sets up the horizontal pressure gradient that ultimately drives the divergent outflow as the downdraft reaches the ground; the pressure is thus the connection between the downdraft and outflow. Based on the continuity of mass and on dimensional grounds, it can be seen that:

$$\frac{u}{w} \sim \frac{\text{width}}{\text{height}} \sim \frac{1}{A}$$

where u is the outflow velocity from a cylindrical downdraft reaching the ground, and A is the aspect ratio of the downdraft defined as the ratio of its height to width. The third term on the right

hand side of Eq. (II.1) will be neglected, and the pressure effects will be incorporated in a prediction equation for the ratio u/w .

The predicted outflow speed will depend not only on the vertical velocity and the aspect ratio of the downdraft, but on the temperature of the downdraft air as well. Fawbush and Miller (1954) modelled this dependence of horizontal wind speed with a cubic equation in temperature based on observations, but Proctor (1989) recently found that a linear relationship was roughly as accurate. However, there are no theoretically obvious reasons for either the cubic or linear relationships. One theoretical guideline that could be used is the well known equation for the speed of the leading edge of a density current that is thin relative to the depth of the fluid in which it is propagating (e.g., Simpson 1987):

$$V = \sqrt{2 g h \frac{\Delta\rho}{\rho}}$$

where V is the gravity current speed, $\Delta\rho$ is the density difference across the front, ρ is the density of the less dense fluid, and h is the depth of the density current. The horizontal flow behind the leading edge is often faster than, but directly proportional to the speed of the front, so the dependence on density difference should be the same. Since the fractional potential temperature difference across the front is proportional to the fractional density difference, Eq. (II.3) would imply the outflow speed was related linearly to the lapse rate:

$$\frac{u}{w} \sim \Gamma$$

Comparison with numerical modelling results (Appendix A) showed there was indeed a dependence of the outflow speed on the lapse rate that could be modelled as linear, but not enough data were really available to determine if the dependence was of higher order or not. Thus a linear dependence between the outflow speed and the lapse rate was assumed, and the best fit coefficients were derived.

3) Prediction Equations

(i) Vertical velocity

In the preceding section, the dependence of vertical velocity on the radius and depth of the precipitation core, the precipitation mixing ratio, the environmental temperature lapse rate, and

the height of the transition level was inferred by simple physical arguments. These results were confirmed through comparison with results from three published axisymmetric numerical modeling studies in Appendix A. These quantitative results were combined into one predictive equation for the maximum vertical velocity:

$$W^2 = [7.3 \Gamma^2 + 9.75 L D - 480] \frac{T_r}{3.3} \quad (\text{II.4})$$

where W is the maximum downdraft velocity in m/s, Γ is the mean temperature lapse rate from the surface to the freezing level in K/km, L is the precipitation mixing ratio in g/Kg, D is the depth of the precipitation core in km, and T_r is the transition level of the sounding in km. If evaluating the terms on the right hand side of Eq. (II.4) produces a negative number, W should be interpreted as negligibly small.

(ii) *Outflow velocity*

The dependence of the ratio of the maximum outflow speeds (U) to the maximum downdraft speeds (W) was found to depend strongly only on the aspect ratio (A) of the precipitation core (i.e. ratio of vertical to horizontal extent), with a weak dependence on the environmental lapse rate. These results were combined into a predictive equation for the ratio U/W which, when combined with Eq. (II.4), provides a predictive equation for U alone:

$$\frac{U}{W} = \left(\frac{.75}{A} + .65 \right) \frac{\Gamma}{9} \quad (\text{II.5})$$

where all of the variables have been defined above. If the predicted value of U/W is less than 1.0, the value should be set equal to 1.0. For example, when the lapse rate is dry adiabatic, $U/W = 1$ for aspect ratios ≥ 2.75 .

In applying Eqs. (II.4) and (II.5), a three dimensional radar reflectivity field would be searched for storm "cells", significant maxima in the field, to locate the sites of potential strong downdrafts. A bi-Gaussian distribution would then be fit to these regions, after they had been converted from reflectivity to water mixing ratio. The peak value of the Gaussian mixing ratio distribution would be used for L , the depth at half maximum for D , and the ratio of D to the width at half maximum would be used for A . Because information on the downdraft width is available through application of this model, the surface divergence as well as the downdraft and outflow

speeds can be predicted. Indicators of aircraft performance loss that depend not only on the differential velocity, but on the horizontal divergence and the vertical velocity as well, can readily be calculated (e.g., Frost and Bowles 1984; see Fig. I-6).

(iii) *Comparison with Proctor's Microburst Index*

It is interesting to compare these predictive equations with the predictive equation for surface outflow speeds derived by Proctor (1989):

$$I = \frac{\left[H_m^2 (\gamma - \gamma_o) + H_m \frac{\{ Q_v (1 \text{ km AGL}) - 1.5 Q_v (H_m) \}}{3} \right]^{0.5}}{5} \quad (\text{II.6})$$

where I is the index equal to twice the outflow velocity, H_m is the height of the melting level (m agl), Q_v is the ambient vapor mixing ratio (g/Kg), γ is the ambient mean lapse rate between the ground and the melting level (K/m), and γ_o is a constant equal to .0055 K/m. Thus the lapse rate has to exceed 5.5 K/km to make a positive contribution to the index. When downdrafts with the same precipitation content and radial distribution were initiated from the same altitude into environments with different ambient characteristics, Eq. (II.6) predicted outflow speeds that matched well those derived by running the model.

This index can be rewritten in a form more similar to the vertical momentum equation:

$$U^2 = \left[\Delta T + \frac{\Delta Q_v}{3} \right] \frac{\Delta Z}{100}$$

where U is the surface outflow velocity, ΔT is the temperature difference implied by the difference between the ambient lapse rate and .0055 K/m, ΔQ_v is the difference between the vapor mixing ratio at 1 km agl and the melting level, and ΔZ is the height of the melting level. Now it can be seen that ΔQ_v in Proctor's equation plays the role of a virtual contribution to the buoyancy and of the water loading forcing of the downdraft. The latter relies on the observation that the ultimate water content of the thunderstorms that develop is usually high when the low level water vapor mixing ratio is high. No direct account is taken in Proctor's index of the resultant precipitation mixing ratio or the depth/aspect ratio of the precipitation core, so it cannot predict differences in the outflow strength of cells occurring on the same day. However, since only one cell per day (per "environment") was studied, and all the numerical simulations were initiated with identical water

masses, these factors did not enter his equation. It can be anticipated that the predictive equations (II.4) and (II.5) will be valid over a much larger parameter range than the index in Eq. (II.6).

(iv) Application of model to four storm cases

Recent papers by Wakimoto and Bringi (1988) and Kingsmill et al. (1989) gave enough data on a "strong" airmass thunderstorm that occurred near Huntsville, AL on July 20, 1986 to estimate the parameters needed for predicting the downdraft and outflow velocities via Eqs. (II.4) and (II.5), and to compare the predictions with what was actually observed. Enough data were also presented for predictions on two other storms, July 13 and July 16, 1986. Wakimoto and Bringi (1988) noted that the soundings on these two days were similar to the July 20 sounding, but that these storms resulted in only "weak" and "moderate" outflows, respectively.

To estimate the parameters needed for the prediction equations, the reflectivity values were first converted to liquid water content using an equation derived by Burrows and Osborne (1986) for the volume concentration of water, and normalized by the ambient density at that height. A Gaussian shape was subjectively fitted to the resulting distribution to give the liquid water content at the peak (L), the core depth (D ; the Gaussian width at half amplitude), and the core aspect ratio (A). By fitting a bi-Gaussian distribution to the liquid water content field, the data characteristics match as closely as possible the water content fields used to initiate the numerical models from which the equations were derived. The other required parameters were derived from the published soundings.

The model estimates for these three high reflectivity cases are compared with the actual data in Table II-2. The simple model given by Eqs. (II.4) and (II.5) has correctly ranked these seemingly similar but identifiably quite different storms according to their outflow strength. This suggests that thunderstorm downdraft and outflow strength might be predicted quite adequately with standard radar reflectivity data and a proximity sounding. Because radar reflectivity increases when frozen condensate melts, part of the increased acceleration from the thermodynamic effects of ice is incorporated even in this simple model.

Wakimoto et al. (1989) studied a low reflectivity storm that occurred in the Denver area on July 9, 1987 with multiple Doppler radars and photogrammetric analyses. The model estimates for this case are also given in Table II-2. In contrast to the previous high reflectivity cases, this case had only 25 dBZ or 0.2 g/Kg peak water content in the core. Thus the second term on the right

Table II-2. Application of predictive model to 4 storm cases. The variables given are identified in Eqs. (II.4) and (II.5). The asterisks indicate outflow values estimated from single Doppler radar data; the vertical velocities for those cases were not estimated. The other data were derived from multiple Doppler analyses.

	A	D	dBZ	L	Tr	Γ	W	U
July 20, 1986								
(Strong)	1.8	2	63	27	2.2	7.2	16.8	16.8
						actual:	13	17
July 13, 1986								
(Weak)	1.25	1.5	57	10	2	7.0	4	4
						actual:	?	7 *
July 16, 1986								
(Moderate)	1.0	2	60	34	1.2	7.0	14	14
						actual:	?	9 *
July 9, 1987								
(Low dBZ)	1.0	2	25	0.2	4	9.4	14.3	21.5
						actual:	13.4	> 15

hand side of Eq. (II.4) is essentially negligible in this case. Again in contrast to the first three cases, the first term on the right hand side of Eq. (II.4) is very large in this case because of the nearly dry adiabatic lapse rate between the surface and the freezing level. The result is a downdraft and outflow strength comparable to the “strong” high reflectivity storm of July 20, 1986.

The ability of the model given by Eqs. (II.4) and (II.5) to correctly rank, and fairly closely estimate, the eventual downdraft and outflow velocities in these four quite different cases adds confidence to the assertion that it approximately captures the essential physics of accelerating downdrafts and outflows. The timing of the downdraft may be anticipated by descent of the storm center of mass (e.g., Goodman et al. 1989). By developing a physically based predictive system rather than one based on correlations of precursory Doppler radar features aloft with subsequent outflow development, there is hope that the system can remain reliable as the storms it has to detect change from the very dry virga shafts in Denver to the very wet thunderstorms in the humid southeastern part of the country.

E. Summary

The precipitation driven downdraft of the thunderstorm and the divergent surface wind pattern that results when it first reaches the ground has been recognized as a severe hazard to low altitude and surface aircraft operations since at least 1949. Today this phenomenon is commonly called a microburst by the aviation community and general public and by some meteorologists. This suggestive terminology serves a useful purpose for increasing awareness of aviation weather hazards, but in scientific disciplines its imprecise use has confused identification of various distinct severe weather phenomena. The introduction of new terminology suggests that something new has been discovered, yet the thunderstorm downdraft is not new to meteorology even in its most narrow, powerful form.

The impetus to understand the “microburst” has renewed the scientific efforts to understand and quantify the factors that determine the strength of the main thunderstorm downdraft. The downdraft analogy with the wall jet, drawn first by Byers and Braham over 40 years ago, has been quantitatively applied and shown to be quite accurate. The radial dependence of outflow winds in a wall jet illustrates how the surface winds measured near a storm will depend strongly on the distance from the center of the downdraft. Numerical models developed in recent years have provided an excellent tool for investigating thunderstorm downdraft forcing mechanisms. The

following conclusions can be drawn from the numerical modelling results of Knupp (1987, 1988), Proctor (1988b, 1989), and Srivastava (1985, 1987).

- The precipitation driven downdraft is confined to the lowest, most unstable layers of the atmosphere.
- The observed upper limit for air entering the downdraft is the “transition level” in the sounding, defined as the level at which the lapse rate changes from neutral or conditionally unstable to absolutely stable or moist adiabatic (Knupp, 1987), as long as this level is below the upper limit for air reaching the surface defined in terms of the equivalent potential temperature.
- The higher the sounding transition level, the stronger the downdrafts that will develop.
- Downdraft descent rates increase with increasing environmental temperature lapse rate.
- An environmental humidity distribution with low relative humidity at the source region of the downdraft, but high relative humidity at the surface, favors stronger downdrafts and outflows. Thus, it is actually the environmental lapse rate of *virtual* temperature that is important.
- The maximum downward acceleration will occur roughly 1 km below the melting level, where the effects of loading, melting, and evaporation are all strong.
- The maximum downdraft speed typically occurs around 1.0 km agl. This is much closer to the surface than was previously thought.
- The optimal radius of the water mass region (with the depth and peak water content held constant) for producing strong downdrafts is ~ 1 km; larger storms produce progressively weaker downdrafts because of the larger induced pressure perturbation near the ground, and smaller storms weaken by proportionately greater volume mixing with the environment. The outflow speed equals the downdraft speed at roughly this optimal 1 km scale. The ratio of the outflow speed to the downflow speed increases linearly with the radius of the storm.
- The greater the precipitation mixing ratio in the downdraft, the stronger the downdrafts that will develop.
- The cooling rate depends most strongly on the particle size distribution, with smaller particles providing more efficient cooling. Under some circumstances larger drops are able to

produce deeper stronger downdrafts by spreading the cooling over a greater depth. The cooling rate also depends on the phase of the water present.

- Variations in total precipitation mixing ratio have a much greater influence on the maximum downdraft speeds than variations in the precipitation phase or size distribution.

By interpreting these recent results according to simple physical arguments, it was possible to derive prediction equations for the maximum downdraft and outflow speeds of an observed thunderstorm that show quantitatively which observable environmental and storm parameters are important, and how they should be combined to obtain realistic forecasts. The equations satisfactorily reproduce the published numerical results from three different models, and predict the downdraft and outflow strengths observed in four different published storm case studies. They also begin to resolve a number of apparent mysteries concerning which storms produce the strongest downdrafts and outflows and why. However, they were derived from sparse numerical model data, and have not been rigorously compared with observations. Also, they do not incorporate the effects of environmental wind shear or storm geometries other than axisymmetric.

The remaining work in this area should 1) continue the systematic numerical experimentation, including tests on sensitivity to storm geometry, core aspect ratio, height of the transition level (and its use versus melting level or level of the minimum in equivalent potential temperature), virtual temperature lapse rate, ice content, and (with a three dimensional model) environmental wind shear, and 2) confirm these predictions with numerous observational case studies and statistics. Case studies that examine a number of different storms occurring on the same day, within a confined time period, are particularly valuable. Even if the actual downdraft speeds cannot be verified, Eqs. (II.4) and (II.5) combined show the expected dependencies of the outflow speeds, which are measured well with Doppler radars and surface anemometers. The observational studies must involve some specific research on how and when to best estimate the needed parameters from Doppler radar data.

III. PENETRATIVE DOWNDRAFTS

Penetrative downdrafts, small scale turbulent downdrafts driven by evaporative cooling, have been identified recently as the primary cause of wet microbursts (Caracena et al. 1989). They have previously been identified quite convincingly as the dominant mechanism for mixing within "fair weather" cumulus clouds (Squires 1958; Telford 1975; Paluch 1979). Emanuel (1981) pointed out that penetrative downdrafts can account for many of the observed properties of cumulus clouds that cannot be explained by simple entraining plume models. Among these are the lateral distribution of cloud properties (observations show there is little variation across the cloud whereas laboratory plumes and thermals have roughly Gaussian distributions), the magnitude of the actual compared to the adiabatic liquid water content (actual is much smaller than adiabatic), the frequent appearance of dry holes in the bases of clouds, and the weak dependence of maximum liquid water content on cloud diameter in all but the smallest clouds. Penetrative downdrafts are unlike classical convection in that they require turbulent mixing to provide both the liquid water and unsaturated air needed to fuel the evaporative cooling that drives them. In this chapter, I review the evidence for a connection between penetrative downdrafts and wet microbursts.

A. Hypothesis for Microbursts

Emanuel (1981) used similarity theory to develop a quantitative model for predicting the properties of penetrative downdrafts. He showed that they have a characteristically small scale, and can penetrate deep into clouds with downward velocities comparable to those of buoyant updrafts. He went on to suggest that perhaps the penetrative downdraft mechanism could be responsible for the downburst (later renamed microburst) of Fujita and Byers (1977). He argued that because the scale of the main thunderstorm downdraft is determined by the region of falling precipitation, "the comparatively small scale of downbursts suggests that these are a consequence of a dynamically distinct mechanism". Perhaps the penetrative downdraft mechanism could account for the high intensity and small scale of the microburst. The entrainment of dry air into the penetrative downdrafts would occur not through the cloud top but at midlevels ($\sim 4-6$ km agl), near the minimum in equivalent potential temperature. In mature thunderstorms, air is systematically entrained at these levels to compensate for the displaced air of the accelerating downdraft. The strong negative vertical gradient of equivalent potential temperature below this level, plus the

high liquid water content of the updraft core nearby, sets up an environment with the potential for supporting intense penetrative downdrafts.

Caracena (1988) and Caracena et al. (1989) have identified these penetrative downdrafts as “wet microbursts” (Figs. III-1 and III-2) based on Emanuel’s conjecture, but no additional theoretical or observational evidence was cited. Perhaps the penetrative downdraft provided a suitable mechanism for creation of the “small impulsive components” in Caracena’s (1978) hypothesized “ensemble of impulsive components” within a downdraft.

Also, it is clear from Figs. III-1 and III-2 that this version of the “wet microburst” is not the same phenomenon as Fujita’s version of the “wet microburst” (see Fig. I-4, top left), the well known precipitation driven downdraft of a thunderstorm. The penetrative downdraft is a smaller downdraft within the larger precipitation driven downdraft. Acknowledgement of this discrepancy would help prevent unnecessary confusion.

B. Test of Hypothesis

The only study I am aware of that actually investigated the plausibility of Emanuel’s tentative hypothesis was performed by DiStefano (1983). Using a sounding collected by the National Severe Storms Laboratory near a damaging downburst wind storm that occurred in Oklahoma on 13 April 1981, DiStefano tested the hypothesis that the downburst could be a penetrative downdraft. He used the similarity model for a penetrative thermal developed by Emanuel (1981), and initiated it with a dry thermal starting at the level of minimum equivalent potential temperature in the environment (Fig. III-3; 430 mb or ~ 6.6 km agl), with a sufficient initial radius so as to remain unsaturated throughout its descent. The thermal was allowed to fall through “clouds” with various values of cloud water content. The thermal failed to reach the surface even when falling through a cloud with the maximum possible, pseudo-adiabatic water content (10.8 g/Kg for this sounding).

The environment in DiStefano’s model was then adjusted to reflect the minimum equivalent potential temperature of 315 K recorded by the surface weather stations during the downburst, representing better the source of the downburst in the cooler midlevel air some distance to the west. The resultant vertical velocities of the thermal as a function of depth for various ambient cloud water contents are shown in Fig. III-4. They were qualitatively similar to the experiments performed with the actual unadjusted sounding, but the downdraft velocities achieved were larger.

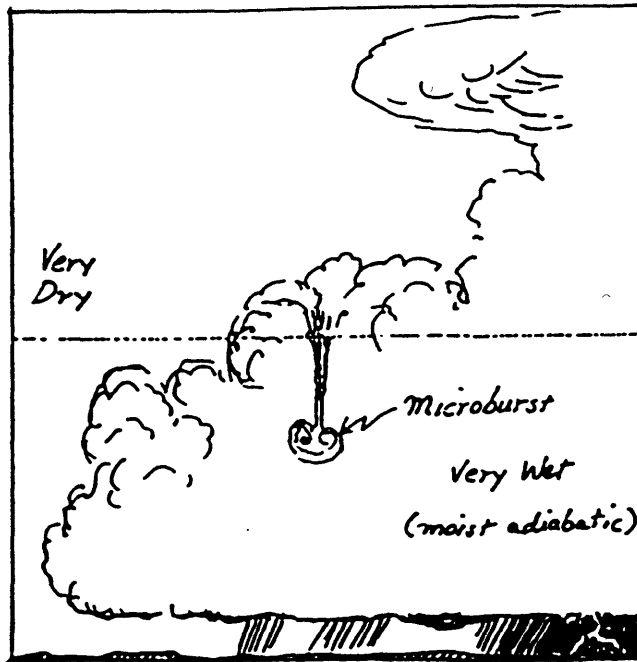


Fig. III-1. A model of a typical wet microburst environment characterized by a very dry midtropospheric layer overlaying a deep, wet, lower troposphere. Taken from Caracena (1988).

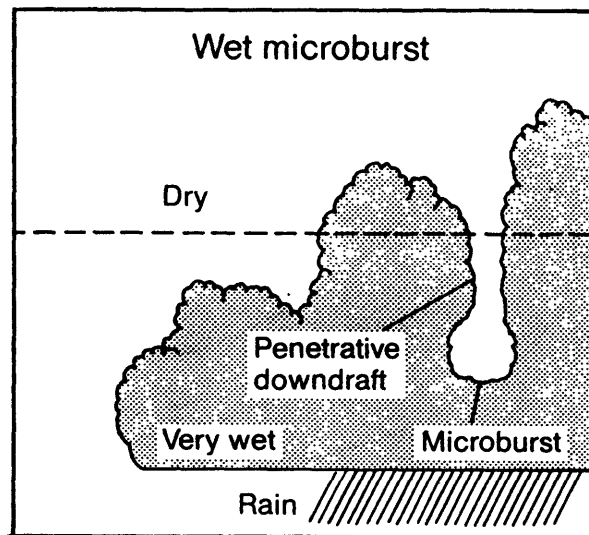


Fig. III-2. Conceptual model of environmental extreme associated with wet microbursts. The wet extreme is characterized by a dry source layer that ejects pockets of dry air into underlying rain-filled and saturated air, producing the evaporation that can result in a microburst. The cloud tops are not drawn to scale; they can extend as high as 15 km agl in wet microburst storms. Taken from Caracena et al. (1989).

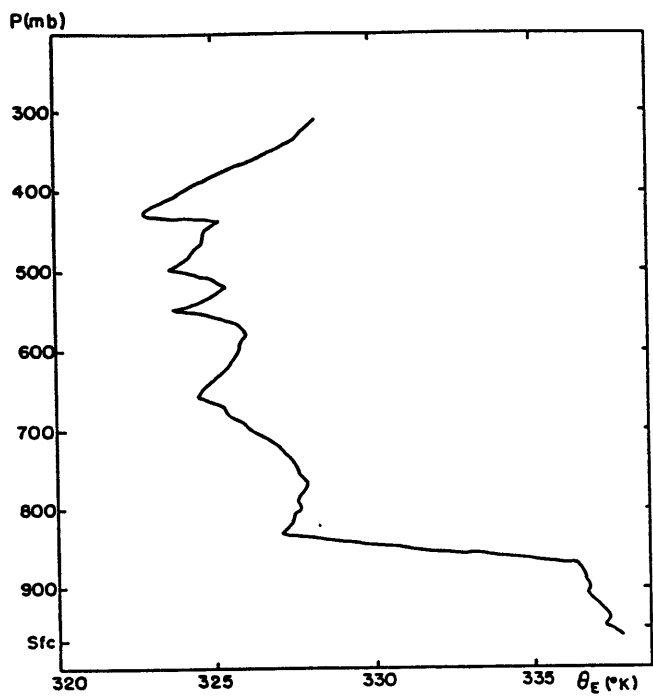


Fig. III-3. Vertical profile of equivalent potential temperature from the Tuttle sounding of 0205 GMT, 14 April 1981. Taken from DiStefano (1983).

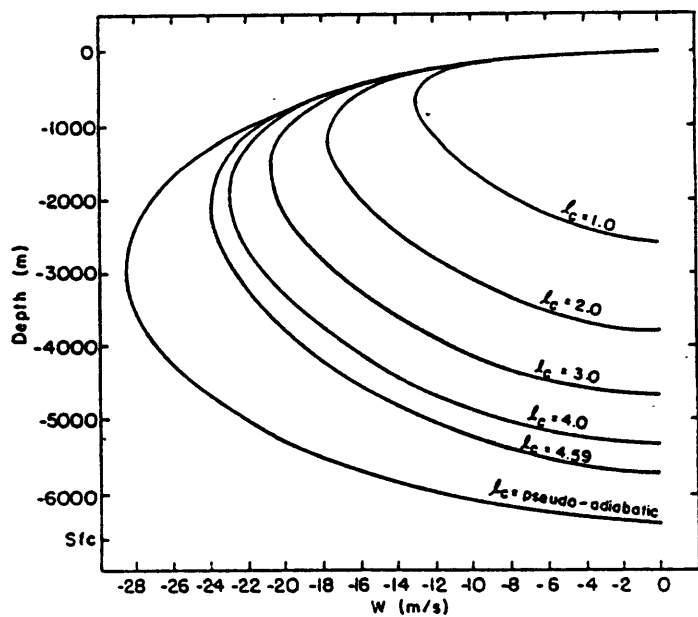


Fig. III-4. Vertical velocity versus depth of penetrative thermals for various distributions of cloud liquid water content (g/Kg). The pseudo-adiabatic value of cloud water content was 10.8 g/Kg. The initial equivalent potential temperature of the penetrative thermal was 315 K. Taken from DiStefano (1983).

However, even for the largest cloud water content possible, the penetrative downdraft did not reach the surface.

DiStefano concludes that “the penetrative downdraft mechanism has difficulty accounting for some of the properties of the observed downburst in this case. It seems more likely that evaporation of falling precipitation into a relatively undiluted, unsaturated downdraft is responsible for the large velocities and low temperatures observed at the surface. There remains the problem of explaining the relatively small space and time scales of the downburst.” The crucial distinction DiStefano makes here between the penetrative downdraft and the precipitation driven downdraft is exactly the difference between the “wet microburst” of Caracena (1988) and Caracena et al. (1989), and that of Fujita (1985).

C. A Possible Example

Although the penetrative downdraft mechanism could not account for the downburst in DiStefano’s case, it may possibly account for a type of cloud edge downdraft. Knupp’s (1987) schematic drawing of the airflow within a typical cumulonimbus cloud (Fig. II-3) shows the penetrative downdraft (P) at the top of and inside a growing cumulus cloud. The figure also shows a series of downdrafts at the edges of the cloud or updraft (L). Knupp suggests that these edge downdrafts “may be forced by cloud edge evaporational cooling and localized updraft mass flux compensation.” The cloud edge downdraft observed on 25 June 1985 near Memphis TN, and discussed in the following sections, was perhaps responsible for a short lived, small scale wind gust of close to 20 m/s at the surface. Associated with this gust was air of extremely low equivalent potential temperature, suggesting that it descended with a minimum of dilution from upper levels.

1) Measurements

As part of the 1985 FLOWS (FAA-Lincoln Laboratory Operational Weather Studies) Project (Evans and Turnbull, 1985), Doppler radar data and mesonet data were collected on thunderstorms in the Memphis, TN area (Fig. III-5). The primary radar used was FL-2, a transportable pencil beam S-band Doppler weather radar built by Lincoln Laboratory for the FAA (Evans and Johnson, 1984); the University of North Dakota operated an Enterprise C-band Doppler radar. The mesonet stations operated by Lincoln Laboratory for the FAA are modified PROBE stations obtained from the Bureau of Reclamation in 1983 (Wolfson et al. 1984). New data collection platforms permit the collection and transmission to the GOES satellite of 1-min averages of wind

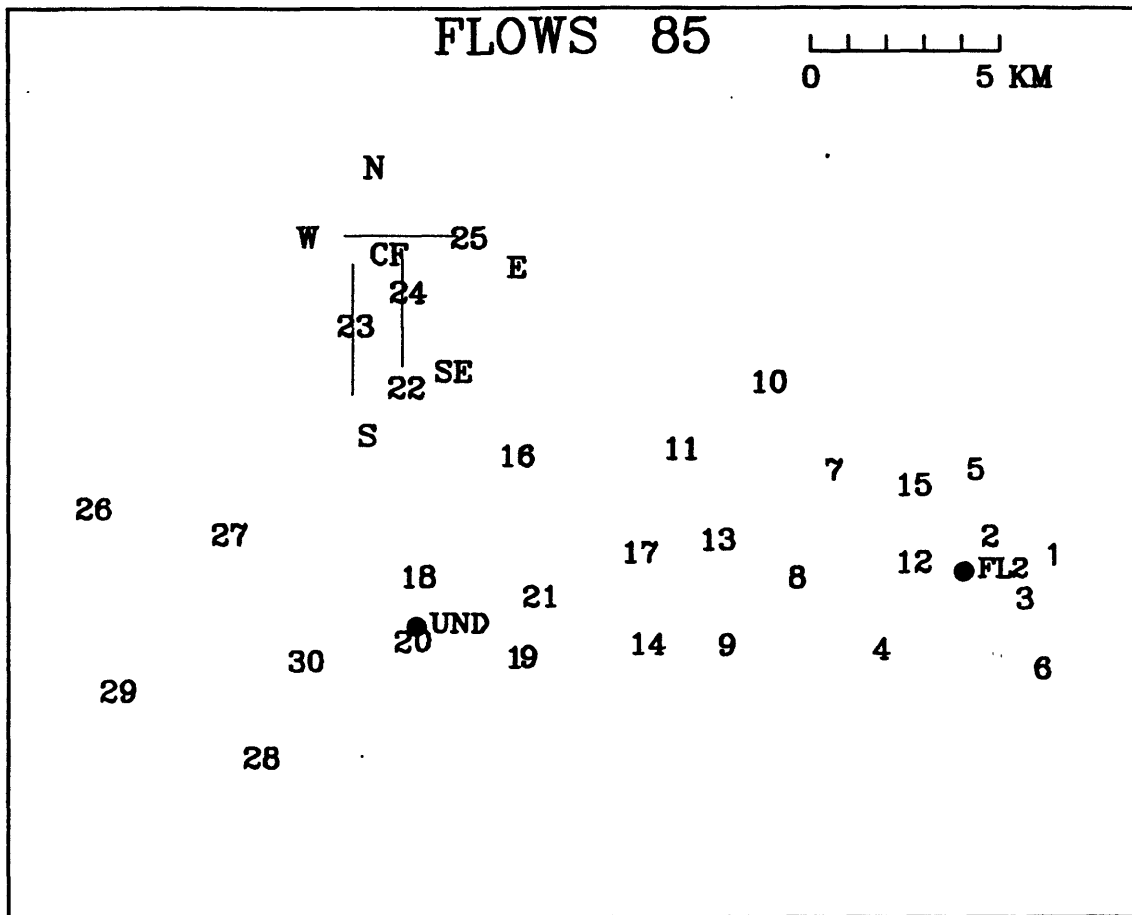


Fig. III-5. Map of the FLOWS 1985 mesonet and radar configuration near Memphis, TN. Mesonet station numbers indicate the station location, letters like "CF" and "E" indicate the FAA LLWAS stations (center field, east, etc.), and the black spots indicate the radar locations. The three lines near the LLWAS stations schematically depict the runways at the Memphis International Airport.

speed and direction, temperature, relative humidity, pressure, and precipitation amounts and the peak wind speed each minute. Extensive sensor refurbishment and calibration have greatly increased the accuracy of the data (Wolfson et al. 1986; Wolfson 1989).

2) Synoptic Summary

On 25 June 1985, high pressure dominated the weather pattern over the entire southeast part of the country, and was continuing to build especially in eastern Tennessee and near the coast in southern Mississippi and Louisiana. Winds were light (below 3 m/s) at the surface, with a primarily southerly component until 1400 UTC, when the direction became variable. The temperature rose from an overnight low of 22°C to a maximum of 34°C at about 1730 UTC. The storm of

interest occurred between 1730 and 1900 UTC; during this time the temperature fell but it rose again to its previous maximum after 1900. The winds began to pick up during the storm period, and the direction became more easterly and finally northerly at the surface. Surface pressure was slowly falling during this time. The surface dew point temperature was approximately 18°C until the storm period, during which it fluctuated sharply.

Upper level winds were light (< 5 m/s) from the south-southeast below 3 km, had a westerly component between 3 and 6 km agl, and were from the north-northeast above that level. The strongest northerly winds of 18 m/s were recorded at the 200 mb level. A broad weak axis of maximum cyclonic vorticity was analyzed at 500 mb from southern Illinois through central Tennessee, and it was along this zone that convection first developed. The lifted index was about -3. At 1200 UTC, the dew point depression was less than 10°C up to 700 mb, but above that level the atmosphere was very dry. The 25 June 1985, 1200 UTC profile of equivalent potential temperature appropriate for the Memphis area, made from a composite of the soundings from Little Rock and Centreville, is shown in Fig. III-6.

3) Radar Data Analysis

Both FLOWS radars began collecting data around 1700 UTC on 25 June 1985 and continued into the next day. Convection had already begun, as isolated cells were spotted near the Memphis airport. The storm of interest was actually made up of a number of smaller, closely spaced cells. Figure III-7 shows range-height (RHI) cross sections through the core of the storm, along the 299° azimuth from FL-2, at 1807 UTC and 1825 UTC. Notice how the older cells are closer to the radar, and the new cells, appearing aloft, are farther away. The initial precipitation accumulation level is between 7 and 8 km agl. The freezing level is shown as the dashed line at 4 km agl. At the later time, the storm tops are higher (11 km up from 9.5 km) and the reflectivity levels within the new cells have increased. The lower parts of the cells tilt toward the radar, under the influence of the westerly winds, and the parts above 6 km tilt away, from the easterly component of the upper level winds.

The edge downdraft and wind gust of interest occurred between 1823 UTC and 1825 UTC, almost directly over mesonet station No. 23 (see Fig. III-5). Since the two Doppler radars have nearly orthogonal viewing angles to this region, it was possible to derive the three dimensional windfield using the dual Doppler algorithm described by Doviak et al. (1976). The vertical velocity

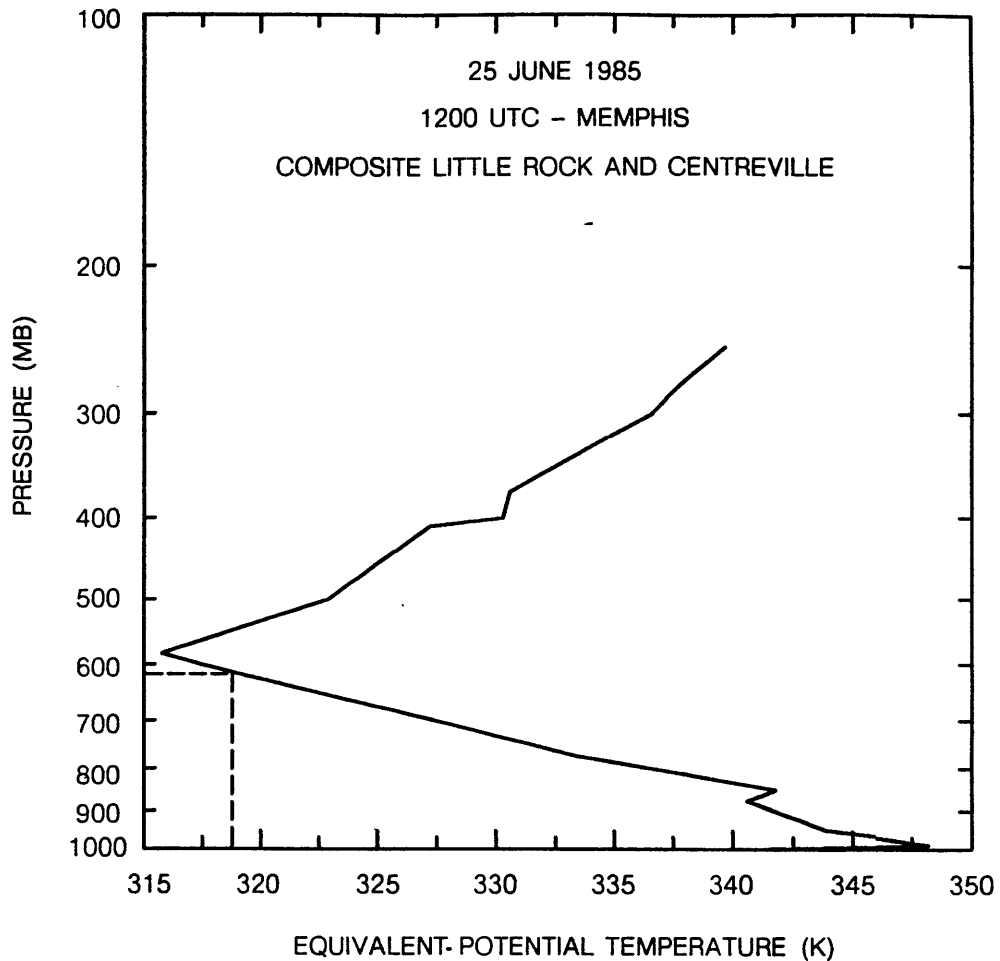


Fig. III-6. Profile of equivalent potential temperature plotted versus pressure (log scale) for 25 June 1985 in the Memphis area. Sounding is composite of soundings from Little Rock and Centreville. Dashed lines indicate the minimum value of equivalent potential temperature recorded at the surface, and its possible source altitude.

was derived using the equation of continuity with a constant logarithmic rate of change of density with height.

Figure III-8 shows the surface dual Doppler windfield at the time the high surface winds were recorded at mesonet station No. 23 (plotted for reference as shaded circle). The downdraft contours from the 1.5 km level, labelled in m/s, are overlaid for comparison. The downward motion along the edge of the cell, coincident with the "weak echo notch" in the reflectivity field, is three times as strong as the downdraft in the core of the storm (> 15 m/s vs. > 5 m/s). The reflectivity field was smoothed as a result of the Cartesian layering process used before derivation of the dual Doppler winds; the "notch" is actually even sharper than it appears in Fig. III-8. The

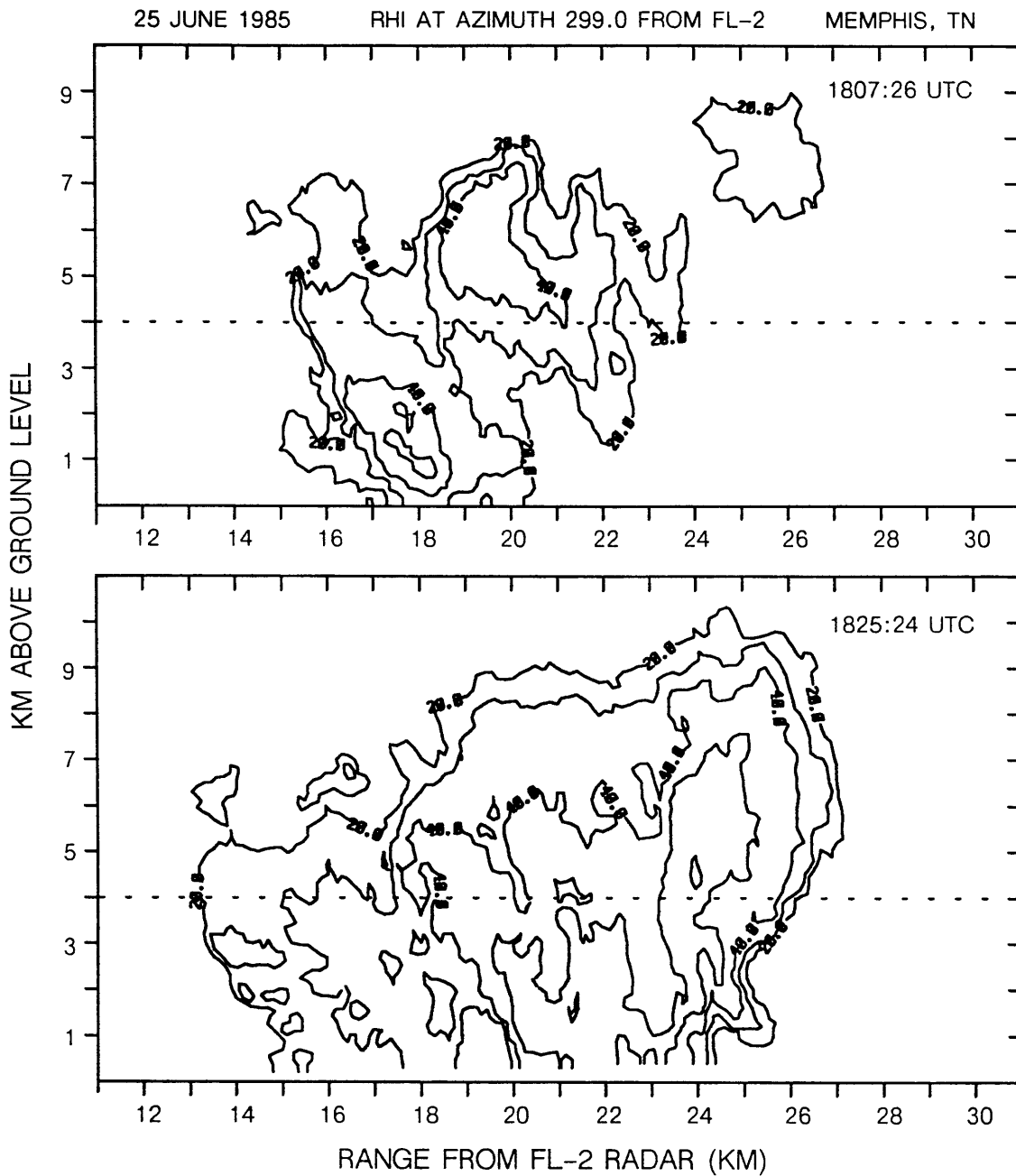


Fig. III-7. RHI cross sections at 299° from FL-2 radar through the multicell complex at two times 18 min apart. (Top) 1807:26 UTC, (Bottom) 1825:24 UTC. Reflectivity is contoured in 10 dBZ increments from 20 to 50 dBZ. The dashed line in each cross section shows approximate height of the freezing level.

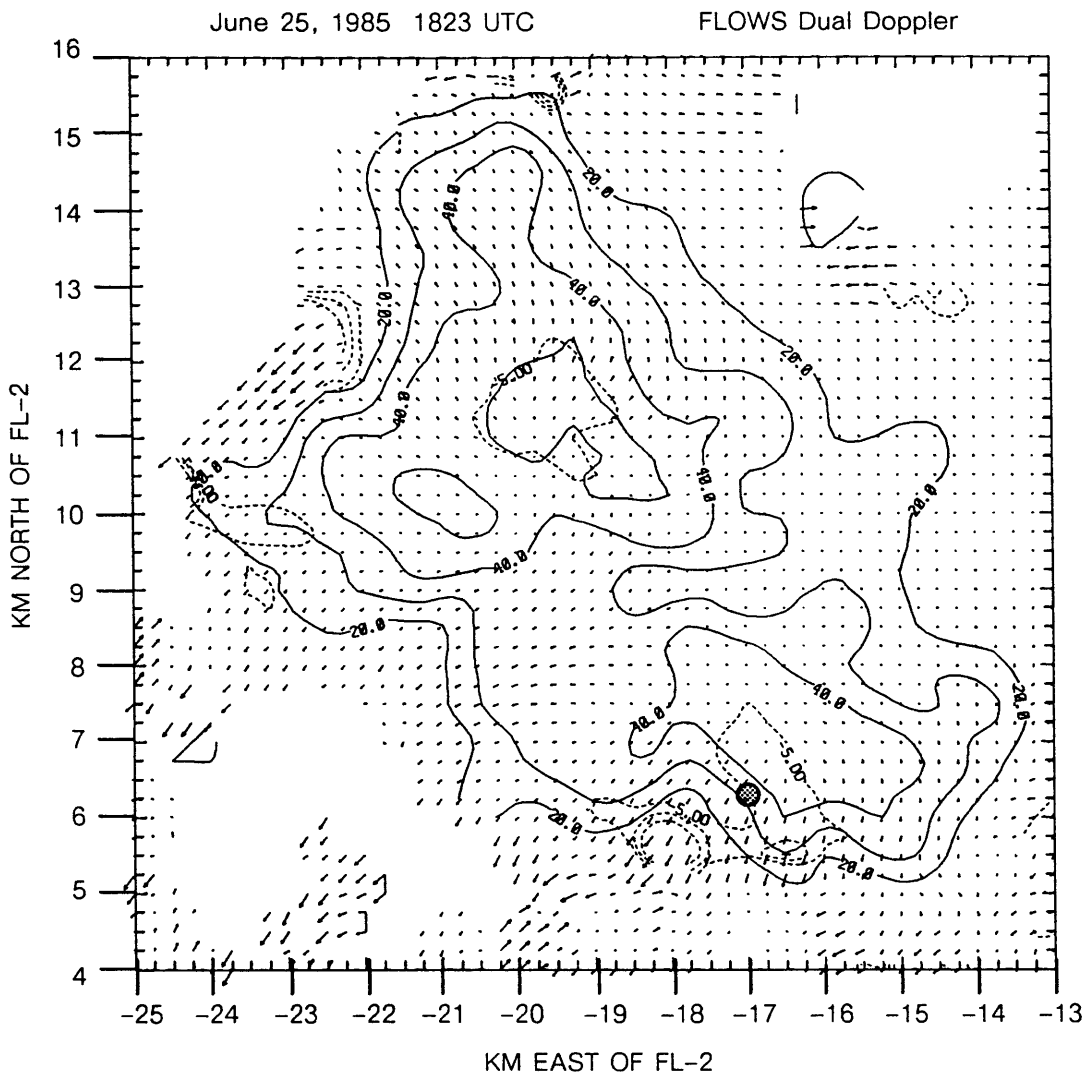


Fig. III-8. Dual Doppler surface winds on 25 June 1985 at 1823 UTC. Maximum wind vector, equal to one grid space, is 18 m/s. Solid contours are surface reflectivity in 10 dBZ increments from 20 to 50 dBZ. Dashed contours are downward vertical velocity at 1.5 km agl in 5 m/s increments. Small shaded circle near (-17.0, 6.3) is mesonet station No. 23.

edge downdraft near station No. 23 is extremely small, on the order of 1 km in diameter. Another area of strong outflow is located at the northwest edge of the storm, coincident with another, larger edge downdraft. However, this is the upshear side of the storm, possibly making the forcing for this downdraft somewhat different.

The reflectivity notch is much sharper at upper levels (Fig. III-9, 1.3 km agl near station No. 23), and is definitely associated with weak cyclonic rotation (not shown). Although the radar scan sequence did not permit derivation of the vertical velocity above 1.5 km in this region, it appears from the radar RHI scans that the downdraft is originating between 2 and 3 km agl. Figure III-10 shows an RHI cross section at azimuth 291°, directly over station No. 23. Notice how the echo weakens rapidly below the 3 km level, and how the “notch” is no longer present above that level.

Other authors have described radar reflectivity “weak echo notches”, but they have been either associated with larger scale upshear inflow into the storm core, downshear wake inflow, or they have remained unexplained (Weisman et al. 1983; Knupp and Cotton 1985; Elmore 1986; Roberts and Wilson 1986). In the case presented here, a strong narrow downdraft was found coincident with one of the seemingly random variations in reflectivity at the edge of the high reflectivity storm cells. These “random” variations may indicate indirectly the thermodynamic structure of the environment and the potential for evaporative cooling.

In addition to Knupp (1987), other authors have also discussed “cloud edge” downdrafts. Fritsch (1975) and Bretherton (1987) discuss the compensating downdraft around a rising isolated cumulus tower; Bretherton (1987) showed analytically that this downdraft occurs partly within the cloudy region but his was a linear study and did not include turbulent mixing mechanisms. Sinclair (1973) presented aircraft measurements at the 10 km level through an intense convective storm that occurred in Colorado that showed edge downdrafts of ~ 5 m/s flanking the main storm updraft of ~ 20 m/s. However, these downdrafts soon became positively buoyant because the cooling rates from sublimation are slower than adiabatic warming rates of air forced downward by the vertical pressure gradient forces associated with localized mass compensation. The edge downdraft shown here originated at much lower levels in the atmosphere where significant cooling from evaporation could take place.

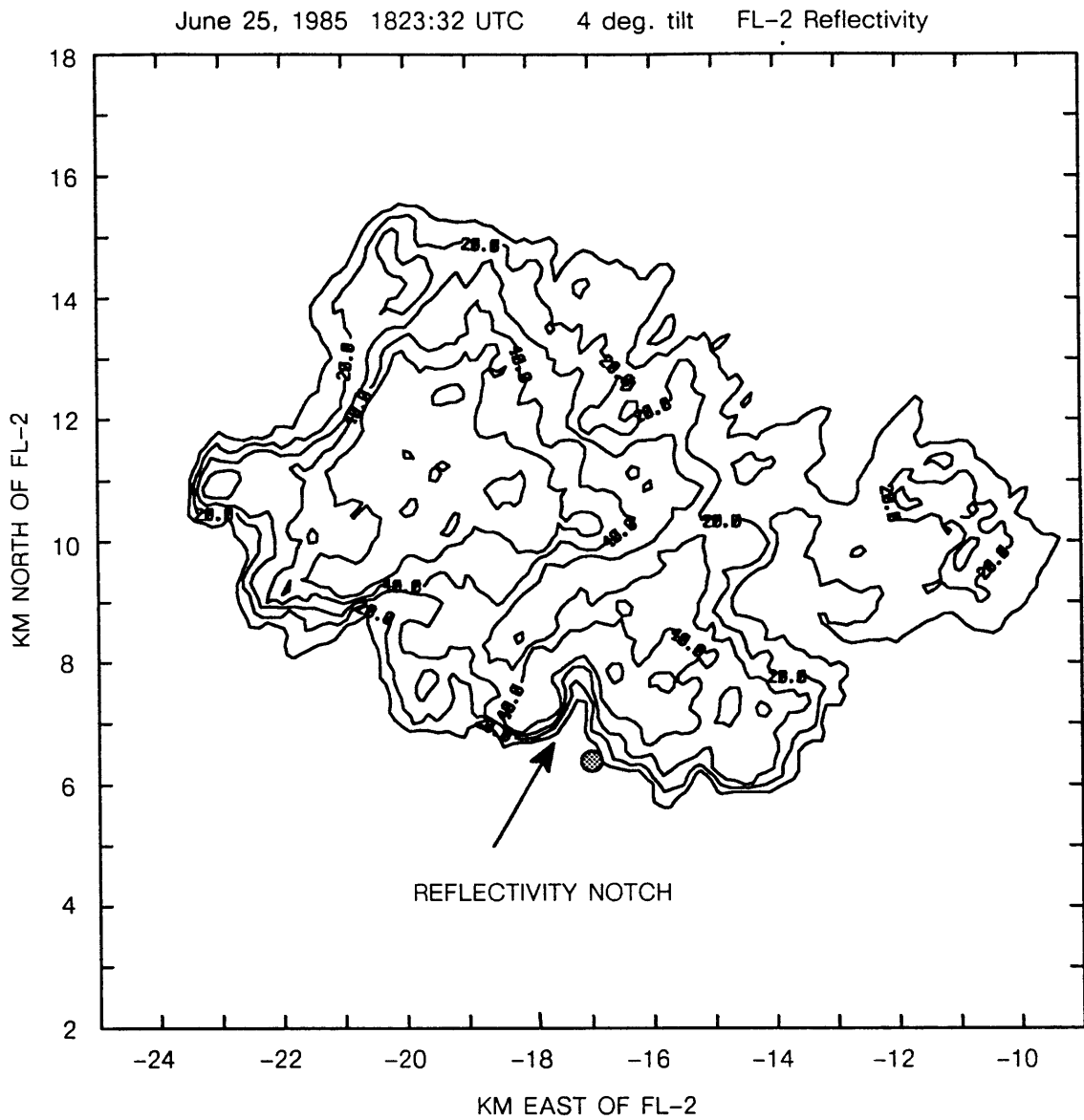


Fig. III-9. FL-2 4.0° elevation angle PPI display of multicell storm near Memphis, TN on 25 June 1985. Notice the hook area of reflectivity next to a spiral weak echo region (notch) near the southern edge of the storm. The height of this area, at this range, is about 1.3 km agl. There are a number of these edge reflectivity spirals around the multicell complex. Small shaded circle near (-17.0, 6.3) shows position of mesonet station No. 23 at the surface.

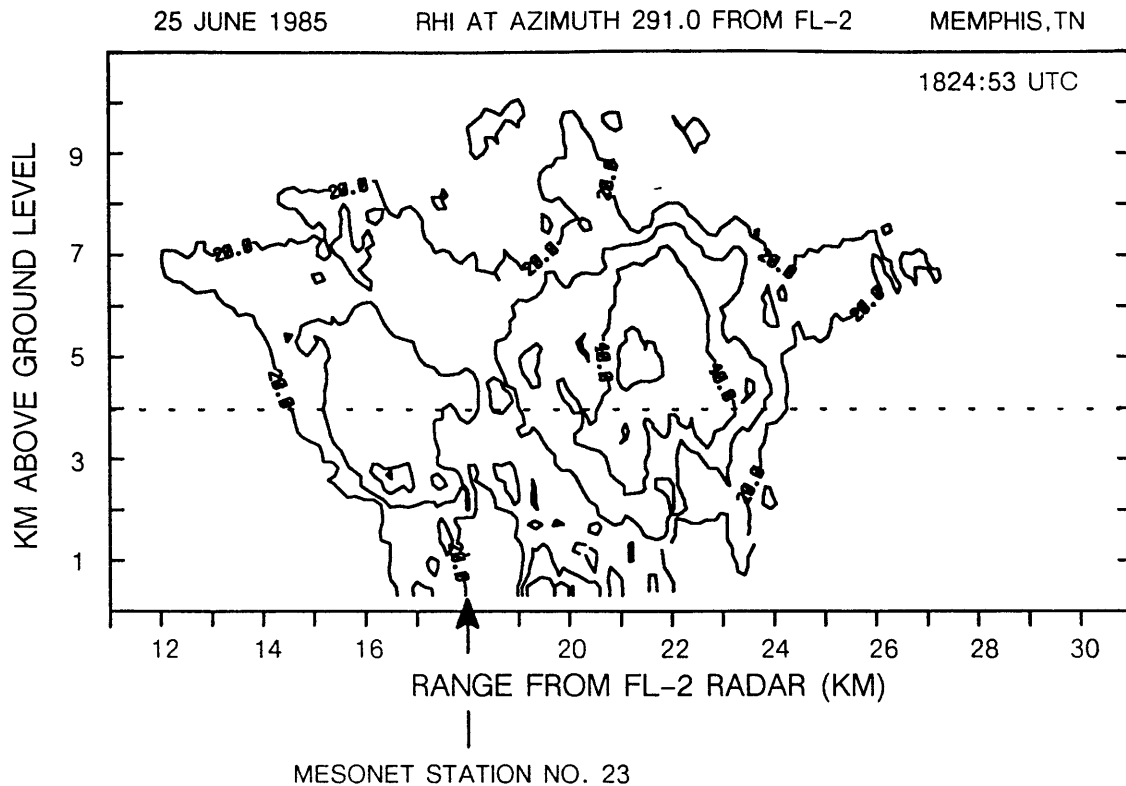


Fig. III-10. RHI cross sections at 291° from FL-2 radar through the multicell complex at 1824:53 UTC. The arrow below the RHI shows the location of FLOWS mesonet station No. 23.

4) Mesonet Data Analysis

Time series of variables measured at station No. 23, centered on the time of the wind gust, are presented in Fig. III-11. The wind first increased gradually from below 5 to around 8 m/s as the temperature began to fall and the dew point began to rise slightly. As the wind speed reached its peak of 19.2 m/s, the temperature and dew point both fell 2–3°C. During this time, the air was nearly saturated and the pressure reached a maximum. The winds quickly dropped back down around 7 m/s, the pressure began to fall, the temperature rose sharply, but the dew point fell another 4.5°. It was at this time (1825) that the equivalent potential temperature (EPT) reached its minimum of 318.8 K. Referring back to Fig. III-6, air with this EPT was present in the atmosphere at about 610 mb, close to the freezing level (4 km agl). This supports the earlier observation that the downdraft associated with the weak echo notch in the radar reflectivity field was

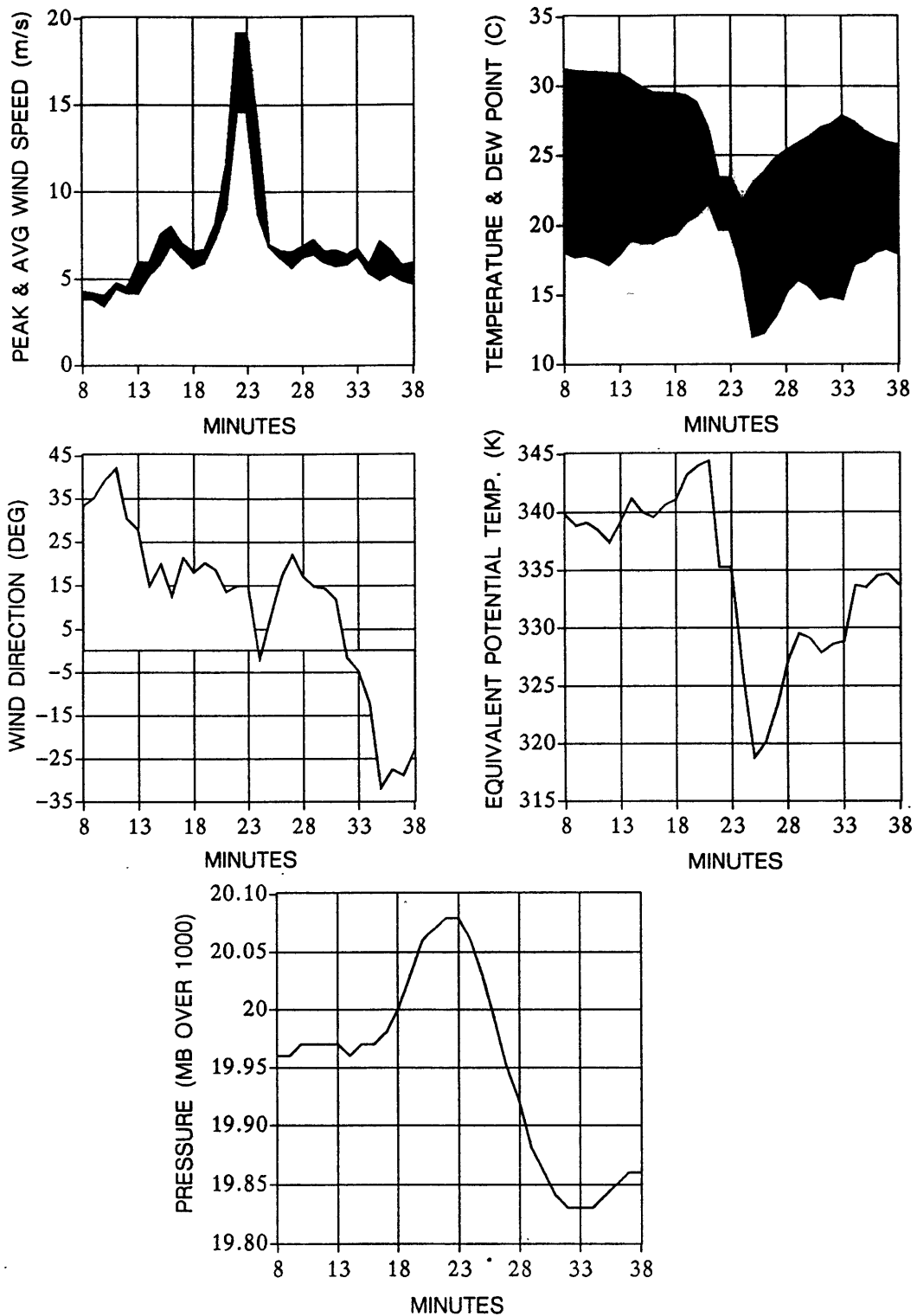


Fig. III-11. Data from FLOWS mesonet station No. 23 on 25 June 1985. Minute "8" on the horizontal axes corresponds to 1808 UTC, minute "38" to 1838 UTC. No rainfall was recorded. Average wind speed is the average over 1 min of 5 s samples; peak wind speed is the largest 5 s sample within the minute. Negative wind directions are from the northwest, positive - northeast.

originating at or below this level. No rainfall was recorded at the station. The winds remained primarily northeasterly throughout the event.

To determine just how localized this event actually was, a series of synoptic maps showing the winds and equivalent potential temperature recorded by the surface weather stations in the vicinity of station No. 23 was plotted. This series is shown in Fig. III-12. All of the surrounding stations were eventually impacted by thunderstorm outflow air, but only station No. 23 measured wind speeds > 10 m/s and air with an EPT near the atmospheric minimum. The surface winds and EPT contours suggest that the edge downdraft was much smaller in scale and shorter lived than the main cell downdraft. The EPT near No. 23 initially (1821) increases slightly, perhaps as the outer, well-mixed layer of the edge downdraft reaches the surface. It then rapidly decreases, over an area roughly 1-2 km wide, to a value close to the atmospheric minimum (318.8 K vs. 315.5 K) by 1825. A tongue of low EPT air proceeds southwest from station No. 23, reflecting the northeasterly winds there. The edge downdraft air quickly mixes with the intensifying storm scale outflow, characterized by a higher EPT of 330-335 K and a more northwesterly direction.

5) Discussion

Based on the thermodynamic properties of the edge downdraft air, it is estimated that precipitation amounting to approximately 7.5 g/Kg was evaporated into it during its descent to the surface. In estimating the source height of the downdraft, both thermodynamic and radar evidence pointed to approximately 4 km, around the freezing level. The radar data also indicated that dry air was brought very close to air with enough precipitation to reflect 45-50 dBZ in a sort of spiral at the edge of the cloud, giving rise to the observed pronounced weak echo notch seen on the 4.0° PPI scan.

The dual Doppler windfield analysis at 1823 UTC revealed downward vertical velocities in the edge downdraft of over 15 m/s at 1.5 km agl, roughly three times those of the main storm downdrafts coincident with the reflectivity cores. Analyses at lower levels showed that the edge downdraft had slowed to about 12 m/s near the surface. A rough estimate of the vertical velocities that could be achieved for a penetrative downdraft can be made from the results of DiStefano's work in Fig. III-4. He used a minimum environmental EPT close to that observed here, but the altitude of his minimum was 6.6 km agl, whereas the observed minimum for this case was just over 4 km agl. Using this lower altitude, Fig. III-4 suggests that a downdraft speed of 12 m/s at the surface could be achieved for a cloud liquid water content > 3 g/Kg. It is probable that this amount

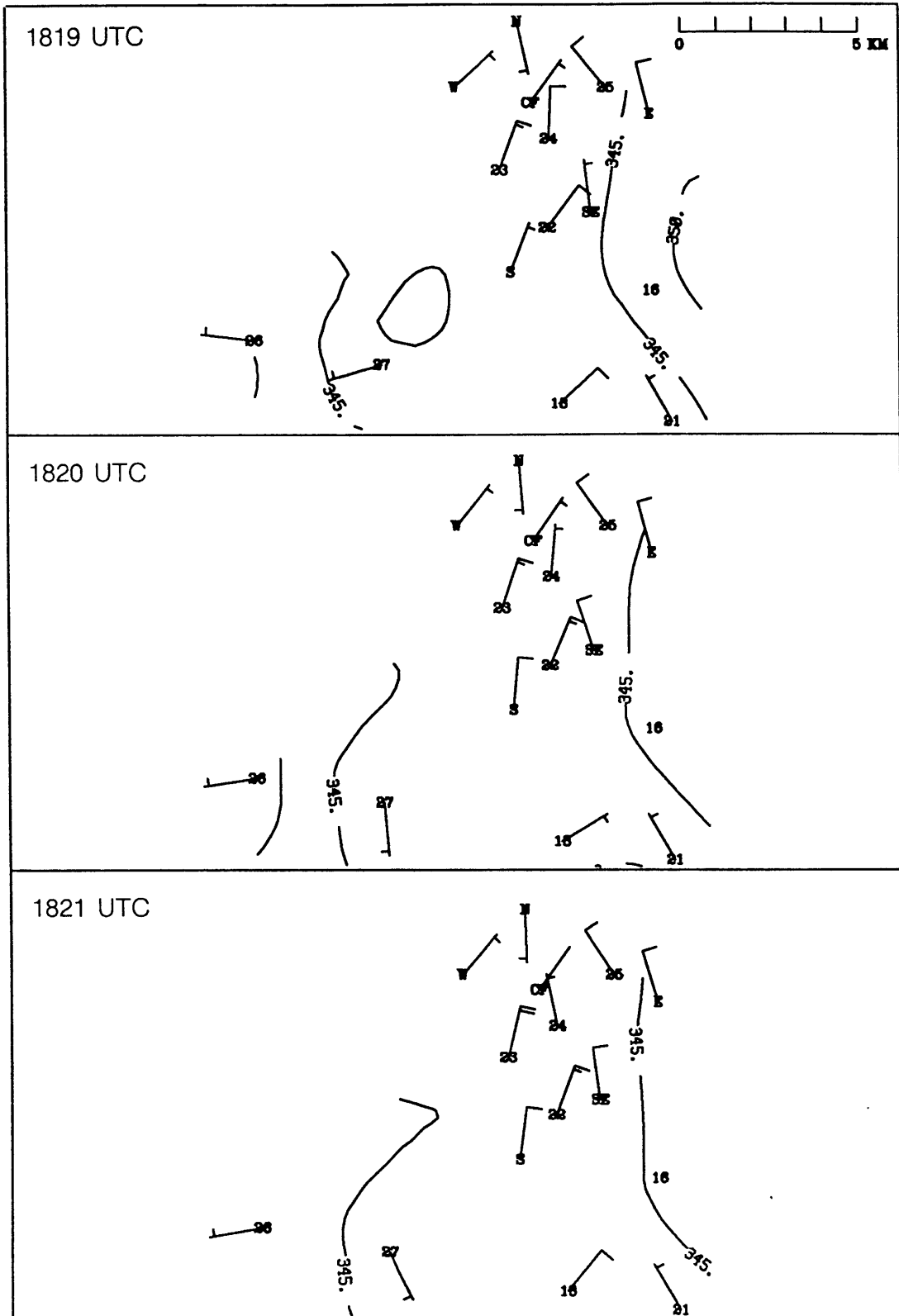


Fig. III-12. FLOWS 1985 mesonet and LLWAS winds (one full barb = 5 m/s) and contours of equivalent potential temperature in 5 K increments. Minutes 1819, 1820 and 1821.

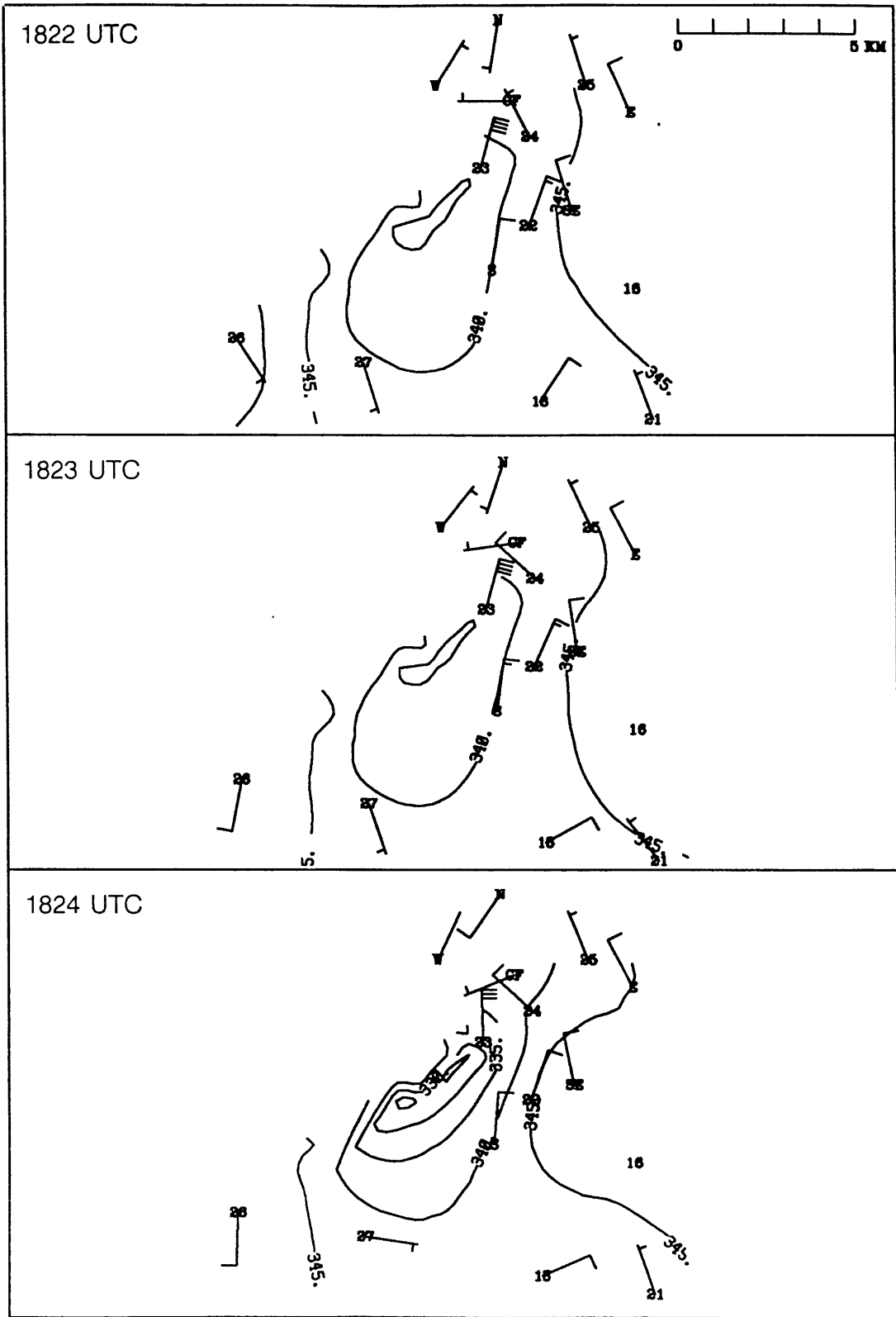


Fig. III-12 (cont.) Minutes 1822, 1823, and 1824 UTC.

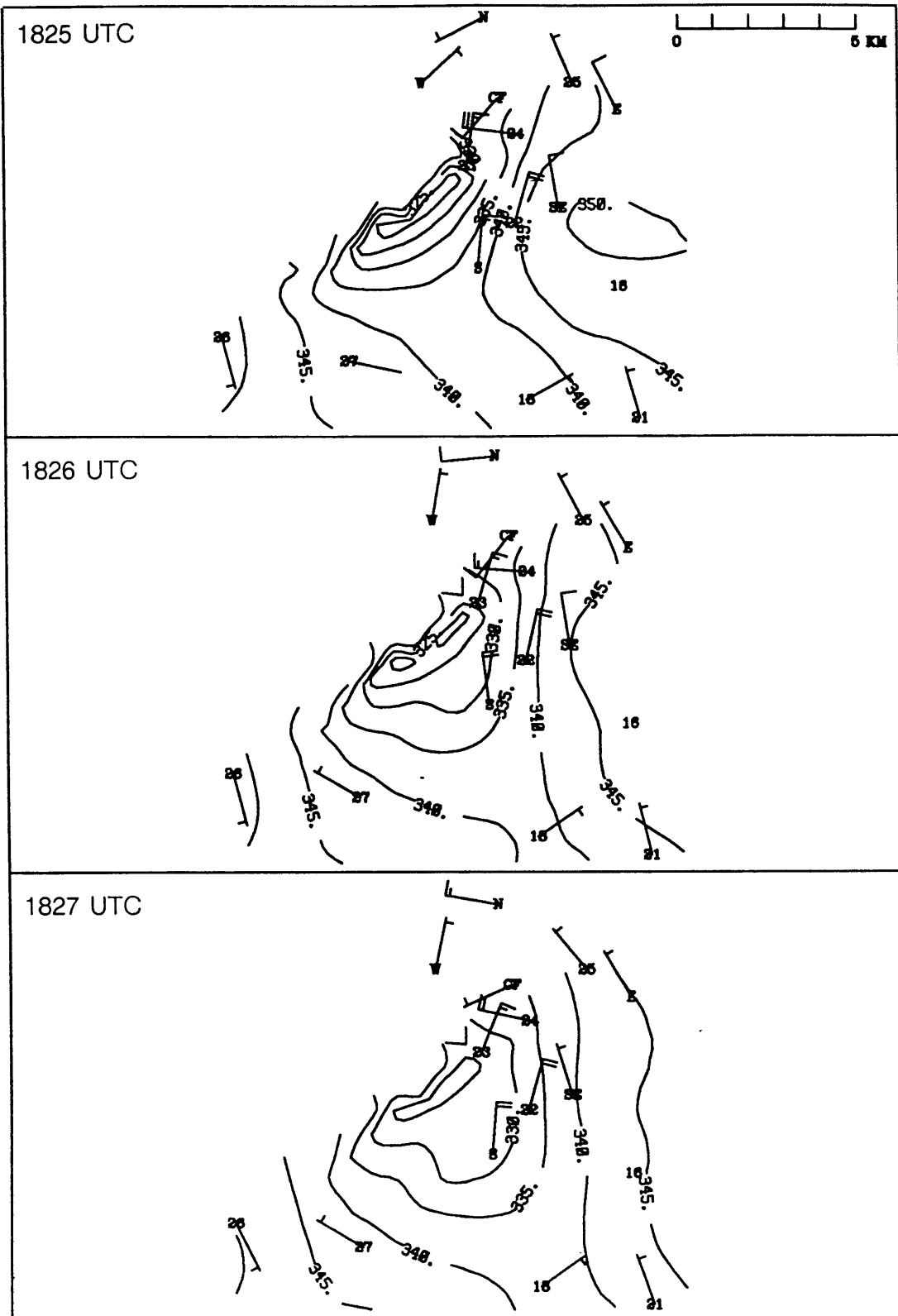


Fig. III-12 (cont.) Minutes 1825, 1826, and 1827 UTC.

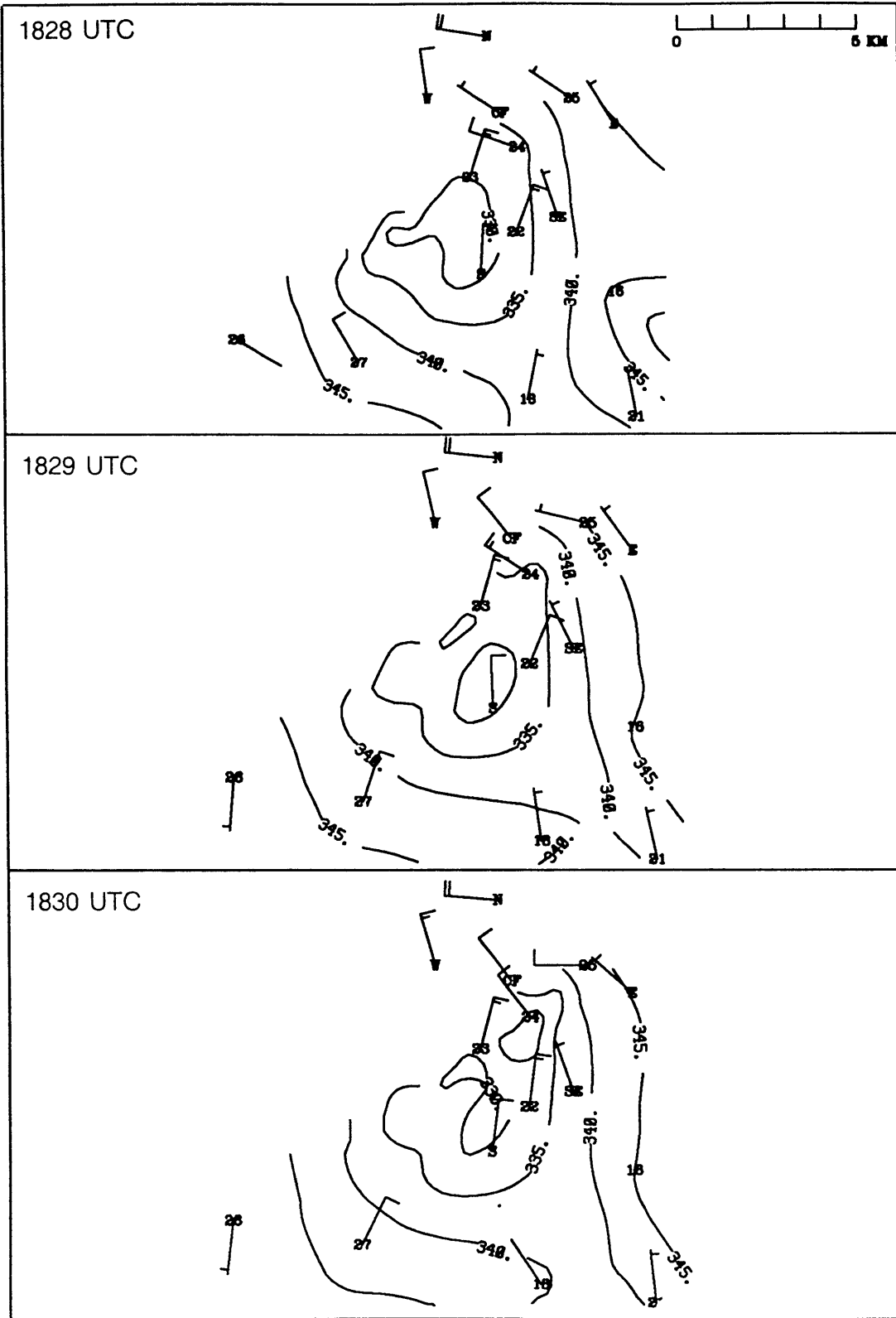


Fig. III-12 (cont.) Minutes 1828, 1829, and 1830 UTC.

of cloud water was available for evaporation, making plausible the hypothesis that this small rotating downdraft consisted of dry air entrained at the very edge of the storm at or just below the freezing level, and was forced downward solely by the negative buoyancy generated as water evaporated into and cooled the dry airmass.

The horizontal scale of this "edge" downdraft was $\sim 1-2$ km, about as small as it could be without being destroyed by mixing (Srivastava 1985). It also appears as though the selection of this scale was "free" rather than "forced" as it might be when a zone of falling precipitation of a given size is introduced into dry air from above. In this case, the dry air was brought into contact with the precipitation droplets (likely of small size relative to those contained in the high reflectivity core) at the edge of the storm near the freezing level, probably as a result of a weak horizontal pressure gradient set up as the downward vertical acceleration increased within the storm at that level. There was a ready source of precipitation through the mixing generated by the cyclonic circulation set up at the edge of the cell as the small downdraft began to accelerate downward. The downdraft became saturated only at the outer layers, but precipitation must have evaporated into and reduced the temperature of the core. The unusually high Doppler spectrum width values associated with this feature (not shown) indicate a high rate of kinetic energy dissipation (Labitt 1981; Bohne 1981; Knupp and Cotton 1982), and thus small scale turbulence and rapid mixing within the downdraft.

Until now, the evidence that penetrative downdrafts could reach the surface and cause small scale, strong wind gusts has remained unconvincing. However, in this case, the evidence seems to point to a similar if not identical phenomenon. One of the assumptions of the self-similar model for penetrative downdrafts developed by Emanuel (1981) was that the entrainment velocity be proportional to a representative downdraft speed; if one imagines the entrainment occurring as the vertical vorticity of the column increases, and the vorticity increasing as the downward vertical acceleration increases, then this assumption is actually quite realistic. The equivalent potential temperature of a "true" penetrative downdraft would be highly diluted at the bottom of its trajectory as a result of the mixing in of surrounding saturated air. Although the edge downdraft here still contained a core of nearly undiluted air surrounded by a layer of well-mixed air, it never strictly reached the end of its potential downward trajectory and was presumably still accelerating when it reached the surface.

Thus it appears that this type of downdraft could be an example of a "cloud-edge" entrainment instability analogous to the cloud-top entrainment instability leading to penetrative downdrafts. In this case the entrainment is not attributable to the upward growth and expansion of convective elements, but rather (probably) to the dynamic entrainment initiated by the horizontal pressure gradient set up around the region of enhanced vertical acceleration in a mature cumulonimbus cloud. It is likely that the equivalent potential temperature must rapidly decrease with height, especially below the freezing level, for this instability to exist. Also, if the horizontal perturbation pressure gradient were stronger (the vertical acceleration stronger), and/or the cell were smaller in diameter, the inflow of dry air may have reached the main core of the storm, and quite likely strengthened the downward vertical acceleration in that region. But in that case, the only distinguishable downdraft would have been coincident with the storm precipitation core.

D. Summary

Observations of a possibly new type of narrow downdraft, one that occurred at the edge of a cumulonimbus cloud at low levels, have been presented. The radar data showed slow, multicell storm growth away from the radar, and a weak divergent surface outflow of generally 6 m/s at most. The edge downdraft produced a short lived, small scale wind gust of nearly 20 m/s associated with air of very low equivalent potential temperature at the surface. The reflectivity field showed a number of weak echo notches at the edges of the cells, where it was determined that dry air was probably mixing with precipitation.

I have observed a few cases in which these edge downdrafts were present, but no others in which a significant flow at the surface could reasonably be attributed to them. In most cases, the outflow from the main storm downdraft overwhelms any flow from the edge downdrafts as it would the flow from any embedded penetrative downdrafts; what is sometimes seen on radar is a reduction in the reflectivity at the outflow edge in a small region, perhaps as dryer air arrives from aloft. The downdraft case presented here is quite unusual.

The surface wind trace observed for this event would qualify it as a microburst according to Wakimoto (1985) and Fujita (1985; see also Fig. I-3). However, this cloud edge downdraft is different from other precipitation driven downdrafts that have been called "wet microbursts", does not appear as one of Fujita's many possible types of "dry microbursts", and is definitely not a "rotor microburst" (see Figs. I-4 and II-5). These reasons, together with my own observations and the evidence presented by DiStefano (1983) that penetrative and cloud edge downdrafts

rarely reach the surface with much intensity, lead me to suggest strongly that this type of event not be called a microburst of any kind. The name "penetrative downdraft" is quite adequate, and much more illuminating.

IV. LOW ALTITUDE DOWNDRAFTS IN THUNDERSTORM OUTFLOWS: NEUTRAL BOUNDARY LAYER

Proof of the hypothesis that the unusually strong, small scale, short lived downdraft called a microburst could be a phenomenon distinct from the precipitation driven downdraft, that it could be the downward branch of the circulation around a large horizontal vortex, requires first the examination in general of low altitude downdrafts within thunderstorm outflows. There are a number of different fluid dynamical mechanisms through which they can arise, but these have not previously been differentiated in the thunderstorm, gust front, or microburst literature.

Horizontal vortices have been called vortex rolls, roll clouds, head waves, rotors, solenoidal circulations, secondary surges, pressure jumps, Kelvin-Helmholtz billows, and microbursts; they can be seen in some form in nearly every study that describes the detailed structure of a thunderstorm outflow. In Fujita's book *The Downburst* (1985), only one of eight microbursts in which aircraft accidents occurred, and one of thirteen other microburst cases presented, could *not* be identified with some kind of horizontal vortex from the depicted analyses. Roll clouds have long been known to pose an extreme hazard to aircraft (e.g., Chapter I.B). However, since the introduction of the microburst, they have been largely relegated to the category of the "ordinary" gust front which, because of its convergent wind shear pattern, it is considered to be a less hazardous form of low altitude wind shear (Fig. I-6). This conclusion is incorrect in some cases.

The crash of Delta Flight 191 at Dallas Ft. Worth International Airport (DFW) on 2 August 1985 heightened the interest in horizontal vortices embedded in, and at the leading edge of thunderstorm outflows. It was the first "microburst" accident to occur with a digital flight data recorder on board, allowing the unique determination of the winds through which the aircraft flew. Both Fujita (1986) and Caracena et al. (1986) independently determined that the aircraft encountered three vortices as it emerged from the center of the main thunderstorm downdraft into increasing tailwinds (Figs. IV-1 and IV-2).

To explain these observations, Fujita (1986) hypothesized that three separate downdrafts occurred in place, each narrower than and contained entirely within the former, giving rise to three concentric outflow vortices. The only problem with conjecture of the sort Fujita offered is that it is apparently perceived as authoritative by the meteorological and pilot communities. The information in the Southwest Airlines manual shown in Fig. IV-3, derived from the FAA Wind-shear Training Aid, was based on Fujita's DFW analysis.

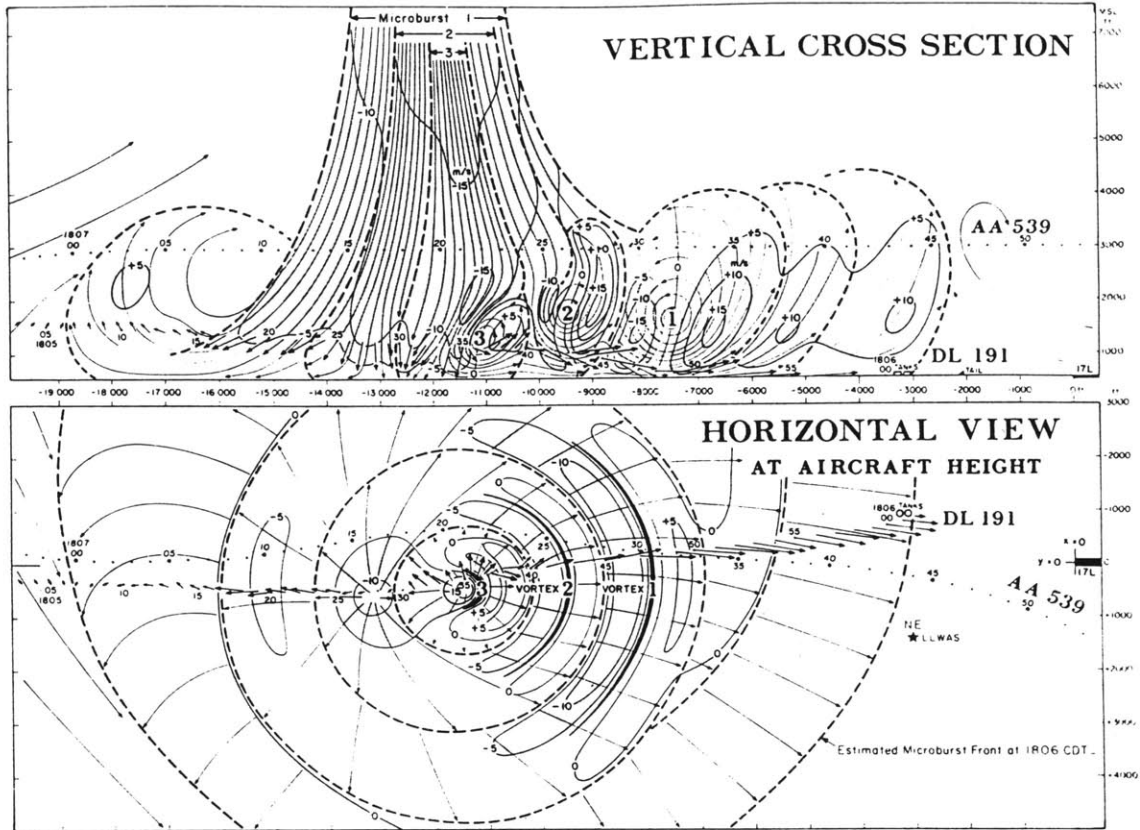


Fig. IV-1. Vertical cross section and horizontal plan view of the microburst at Dallas/Ft. Worth International Airport in which Delta Flight 191 crashed on 2 August 1985, as reconstructed by Fujita (1986).

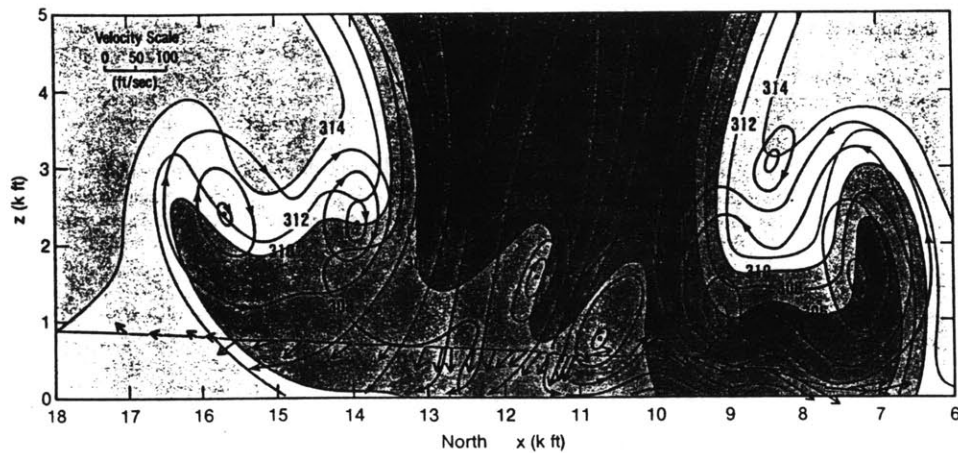


Fig. IV-2. A conceptual model of the vertical airflow structure in the DFW microburst, based on analysis of flight recorder data by Bach and Wingrove (1985). Labelled contours are potential temperature (K); lines with arrows are streamlines. Arrows along dashed line (flight track) are vector winds encountered by the aircraft. Taken from Caracena et al. (1986).

Adverse Weather Operation

More than one microburst can occur in the same weather system. Pilots are therefore cautioned to be alert for additional microbursts if one has already been encountered or observed. If several microbursts are present, a series of horizontal vortices can form near the ground due to several microbursts being embedded in one another (figure below). Conditions associated with these vortices may produce very powerful updrafts and roll forces in addition to downdrafts.

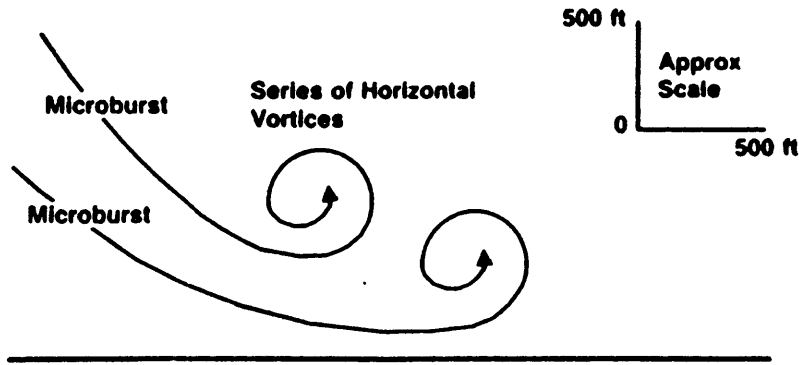


Fig. 9. Horizontal Vortices. A series of horizontal vortices can form near the ground due to microbursts embedded in one another.

Windshear Effects on Airplanes - Vertical Windshear Response

Vertical winds exist in every microburst and increase in intensity with altitude. Such winds usually reach peak intensity at heights greater than 500 feet above ground. Downdrafts with speeds greater than 3000 feet per minute can exist in the center of a strong microburst. The severity of the downdraft the airplane encounters depends on both the altitude and lateral proximity to the center of the microburst.

Perhaps more critical than sustained downdrafts, short duration reversals in vertical winds can exist due to the horizontal vortices associated with microbursts. This is shown in the figure below.

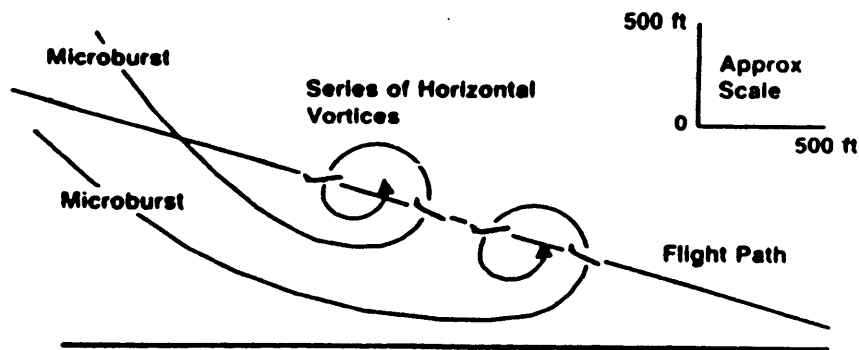


Fig. 22. Encounter with microburst horizontal vortices. Rapid updraft downdraft variations due to horizontal vortices can cause uncommanded pitch changes and may result in momentary stick shaker activation well above normal stick shaker speeds.

Fig. IV-3. The concept of a series of horizontal vortices being caused by several microbursts embedded within one another appears in two places in the Southwest Airlines Operations Manual, Pilot Windshear Guide, revised 27 November 1987. Text from the manual was retyped.

Other hypotheses for the DFW vortices have also been offered. Caracena (1987, 1988) suggested the embedded vortices resulted from multiple vortex rings that formed around the descending downdraft and were “injected” into the outflow. Linden and Simpson (1985) and Droegemeier and Babcock (1989) both hypothesized that the vortices were finite amplitude Kelvin-Helmholtz billows. Linden and Simpson were the first to suggest that “it is the wind-shear and downdraft at the rear of this vortex, occurring relatively close to the leading edge of the outflow, that are probably responsible for the danger of flying through a microburst.” Perhaps it is more than coincidental that scrutiny of the first microburst case for which unambiguous wind data were available led to this conclusion. However, I will show in this and the following chapter that none of the proposed hypotheses for the identity of the observed vortices are plausible.

Various observational and numerical studies of microbursts (thunderstorm outflows) and gust fronts with horizontal vortices have provided only limited physical insight. With the complete wind and pressure fields known, it has been possible to deduce, for example, that the circulation around the horizontal vortices in the outflows is usually in cyclostrophic balance (e.g., Droegemeier and Wilhelmson 1987). However, diagnosis of the relationship between the consistent pressure and wind fields, or the quantification of the terms involved in the production of horizontal vorticity still does not really explain the vortex generation mechanisms. Very little interpretation of the observational and numerical model results has been attempted. The lack of a simple physical model for horizontal vortices within thunderstorm outflows has led aeronautical engineers, who need to generate windfields like the DFW microburst for flight simulators, to analytically combine downdrafts with a number of vortex ring filaments (e.g., Bray 1986; Ivan 1986; Schultz 1988) or with some sort of parameterized turbulence (Roberts and Wan 1985).

In this chapter, the various mechanisms that can generate low altitude downdrafts associated with horizontal vortices in thunderstorm outflows spreading in a neutral environment are described. The following chapter is devoted to understanding the additional vortex generation mechanisms that arise when the thunderstorm outflow spreads in a stably stratified boundary layer. With each vortex type, examples from the literature are given in which the events were referred to as microbursts or component features of microbursts. Understanding these vortices is important in understanding not only microbursts but in understanding many of the past gust front studies as well.

A. Pre-existing Vortex Ring Around Descending Downdraft

A model of the evolution of the microburst wind field based on results from the Joint Airport Weather Studies (JAWS) project near Denver, CO developed by Wilson et al. (1984) shows horizontal vortices forming before the outflow reaches the surface, and persisting at the leading edge as the fairly deep outflow spreads (Fig. IV-4). Fujita (1985; Fig. II-5) has dubbed this the "mid-air microburst". Well before the DFW accident, Caracena (1982) suggested that the microburst actually *was* a vortex ring embedded in a thunderstorm downdraft, based on data from the JAWS project.

In the virga downdrafts commonly observed in Denver, depicted schematically in Fig. IV-4, the downward acceleration begins below the broad, high altitude cloud base as partially or completely frozen precipitation is introduced into the dryer air below. The visible virga shaft narrows as air converges into the downdraft. Eventually, perhaps when the downward acceleration diminishes, the frontal area of the accelerating downdraft broadens into a "mushroom-like" cap. The distinctive shape this creates was illustrated previously in Figs. II-6 and II-7. This type of flow appears to have the characteristics of the spherical vortex of a sinking "thermal" at the leading edge, followed by a negatively buoyant "plume". These have been called "starting plumes" by Turner (1973), and are created when a steady source of negative buoyancy is suddenly turned on. They dilute much less rapidly than isolated thermals because about half the fluid entering the leading spherical vortex continues to come from the downdraft above. It can be expected that in

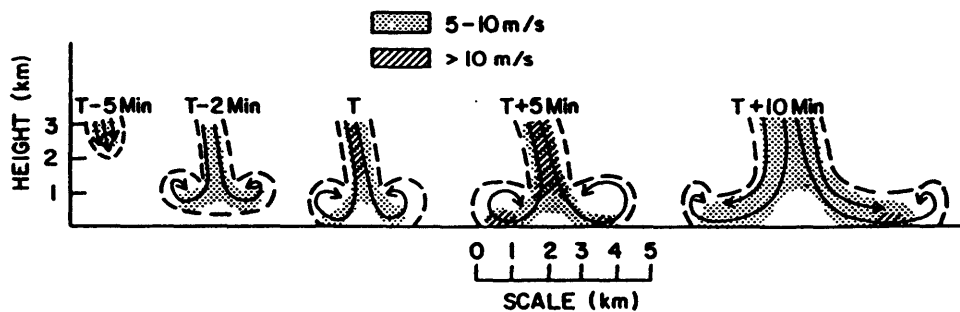


Fig. IV-4. Vertical cross section of the evolution of the microburst wind field based on a summary of data collected in the JAWS project. T is the time of initial divergence at the surface. The shading denotes the vector wind speeds. The outer dashed boundary represents wind speeds less than 5 m/s. Taken from Wilson et al. (1984).

some cases only the thermal-like spherical vortex will remain; this model has already been suggested for one virga shaft observed during the JAWS project, based on aircraft observations (Mahoney 1983).

Bedard and Caplan (1987) documented this type of vortex circulation once it reached the ground with high resolution measurements from the 300 m tower located at the Boulder Atmospheric Observatory (Fig. IV-5). Notice in particular that the associated temperature changes are less than 1°C. Both Fujita (1985) and Bedard and LeFebvre (1986) indeed found that the temperature was just as likely to rise as it was to fall by 1-2°C when the air from these virga downdrafts reached the surface. Waranauskas (1985) further developed the concept of the "rotor" microburst and provided photographic evidence of the horizontal vortex at the leading edge of an outflow in Colorado (Fig. IV-6).

But these "rotors" must be carefully distinguished from vortices embedded within or at the leading edge of cold outflows, or vortices (waves) propagating in thin stable boundary layers. These "neutral density" vortices form either at the leading edges of virga downdrafts descending from high altitude clouds or at the leading edge of the newly forming outflow, and spread in a boundary layer with a dry adiabatic or superadiabatic lapse rate. Haase and Smith (1989a) have clearly shown the differences between the outflow leading structure in the purely inertial (same temperature as environment) and the cold outflow cases, with their two dimensional numerical model. In the purely inertial case, the vertical motions are large even at small times, and this leads to a deep vertical penetration of the outflow air. However, when the outflow is cold, vertical motions are suppressed everywhere except at the leading edge. If the virga outflows observed in Colorado are slightly colder than the ambient surface air, they adjust within a couple of minutes because of the intense surface heating, and the entire outflow usually dissipates rapidly.

The formation of a spherical vortex and associated divergence at the leading edge of the descending downdraft is apparently characteristic only of the virga type downdrafts from the high based dry thunderstorms of the western plateau. Biron and Isaminger (1989) compiled statistics on the frequency of this "mid-air" divergence from Huntsville and Denver (each dataset contained over 200 storm cells). In 75% of the Denver cases, this divergence was observed an average of 1 min before the surface outflow reached the threshold divergence of 10 m/s differential velocity. However, in Huntsville, where essentially all of the storms were accompanied by significant surface rainfall, only 2% of the cells showed this feature. In those rare cases, the divergence

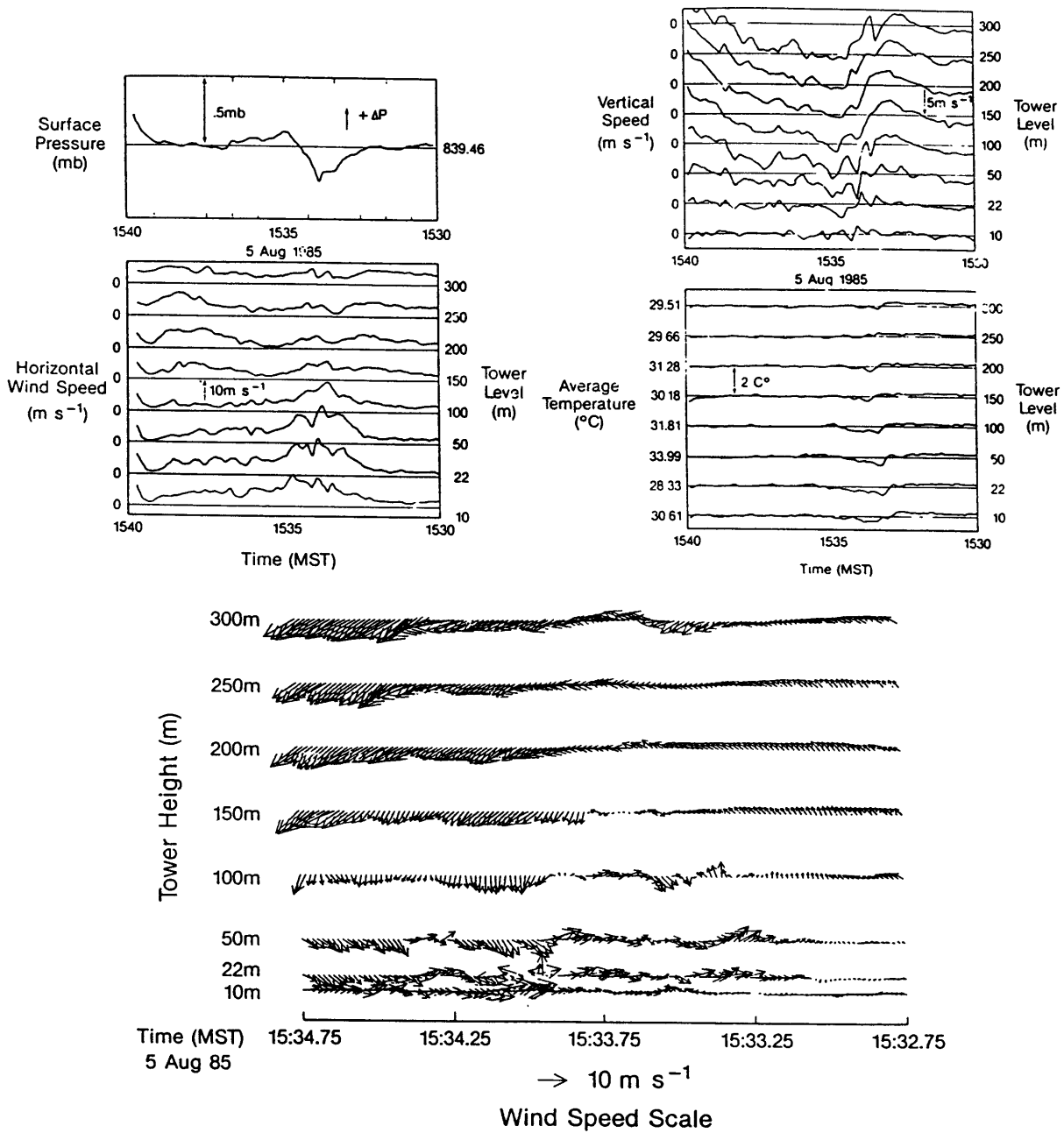


Fig. IV-5. (Top) Pressure, temperature, horizontal wind speed, and vertical wind speed measured at the Boulder Atmospheric Observatory tower (described by Kaimal and Gaynor 1983). (Bottom) Vector field associated with the outflow vortex passing through the tower. The values shown are 1 s averages of 10 Hz samples. Taken from Bedard and Caplan (1987).

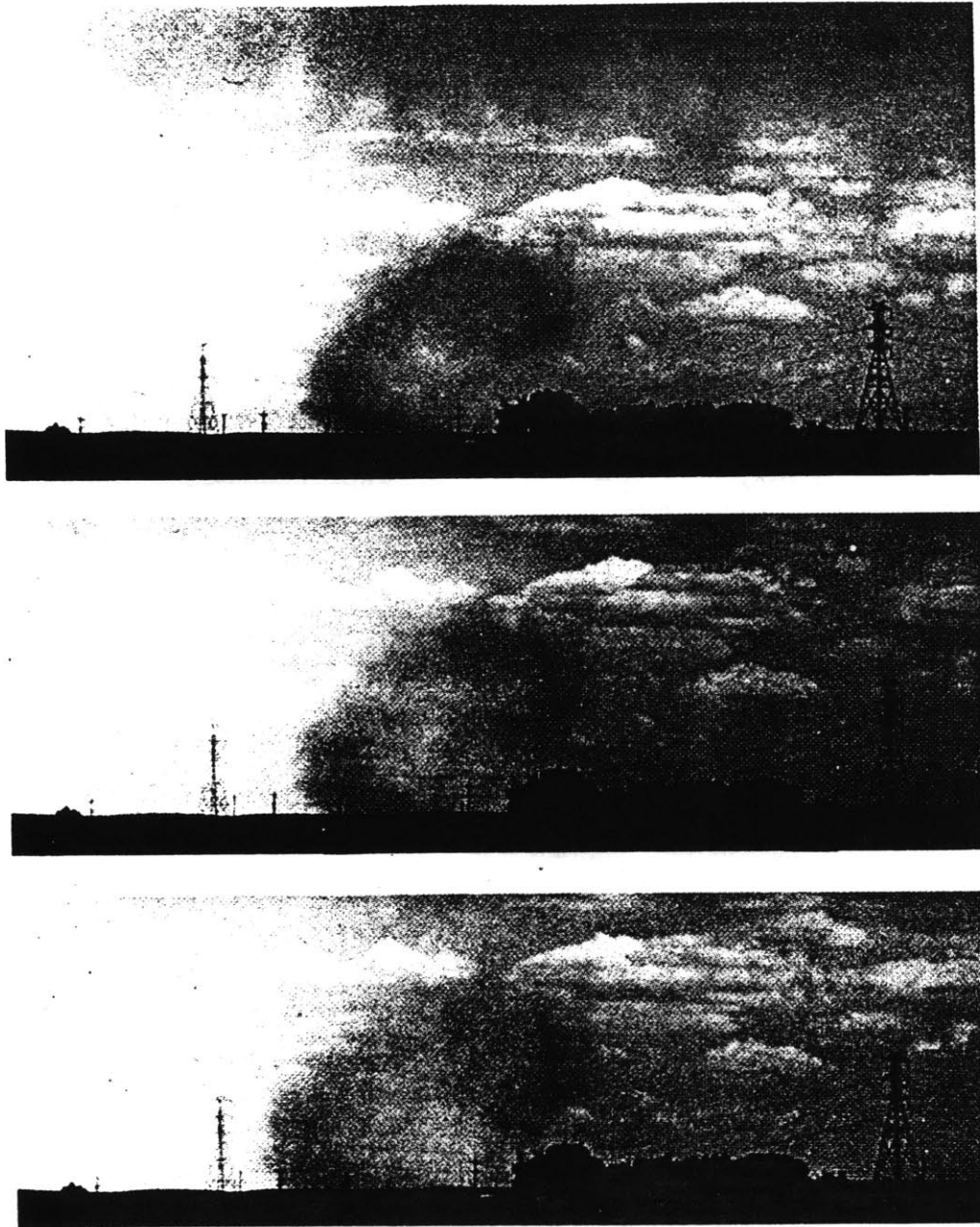


Fig. IV-6. A sequence of telephoto pictures showing the curling features of the dust cloud behind the leading edge of the outflow from a "virga microburst". The pictures were taken by Brian Waranauskas looking south from the CP-3 site on 15 July 1982 during the JAWS project. Taken from Fujita (1985).

occurred an average of 2 min *after* the surface outflow reached its threshold, apparently revealing nothing more than the deepening surface outflow.

The formation of a vortex at the leading edge of a downdraft was investigated by Daly (1967) in a numerical study of nonlinear two fluid Rayleigh–Taylor instability. He found that “when the ratio of the fluid densities is small and the Reynolds number is sufficiently large, Kelvin–Helmholtz instabilities develop along the fluid interface during the later stages of the calculations. The growth of these protuberances enlarges the frontal area of the downward falling Rayleigh–Taylor spike and increases its fluid resistance. A balance is achieved between fluid resistance and body force so that, for sufficiently small density ratio, the steady–state spike velocity is constant.” The results of his numerical calculations are shown in Fig. IV–7. Notice that the smaller the density difference between the two fluids, the larger the growth rate of the vortex; the density difference is a measure of the “stiffness” of the interface and its ability to resist the shearing motion. Yet the density ratio between the downdraft and the ambient air, whether it is 1.005 for a virga case or 1.05 for a heavy rain case, cannot account for the observed differences in the shape of the leading downdraft edge. It may be that the formation of the vortex takes time that is only available for a downdraft falling a great distance as in the virga case, or it may be that deformation at the leading edge of a strongly accelerating downdraft destroys any vortices that begin to form.

It is now possible to see why Caracena’s (1987, 1988) recent hypothesis for the multiple vortices found in DFW outflow is flawed. His hypothesis apparently involves multiple vortex rings originating in the shear zone at the edge of the downdraft, stretching and intensifying upon reaching the surface, and being injected into the outflow. All analyses of the downdraft associated with the crash of Delta 191, including that by Caracena et al. (1986), show that the downdraft air was $\sim 8^{\circ}\text{C}$ colder than the ambient surface air. Ground observers reported seeing Delta 191 disappear into a “wall of water”, so it is apparent that the downdraft was also filled with heavy rain. The crew on board Delta 963 (four flights ahead of Delta 191) reported seeing a bowl shaped protrusion below the overcast, which they found contained heavy rain as they tried unsuccessfully to completely avoid it. Observers on the ground reported seeing an hourglass shaped rain shaft at the time of the crash. These descriptions are reminiscent of the shape of the 10 dBZ contour in Fig. II–2 (bowl shape, min 5; hourglass shape, min 9), and of the photographs of heavy rain shafts published by Smith (1986). The DFW downdraft was probably still accelerating when it descended below cloud base; it is unlikely that it formed even one persistent vortex ring during its descent.

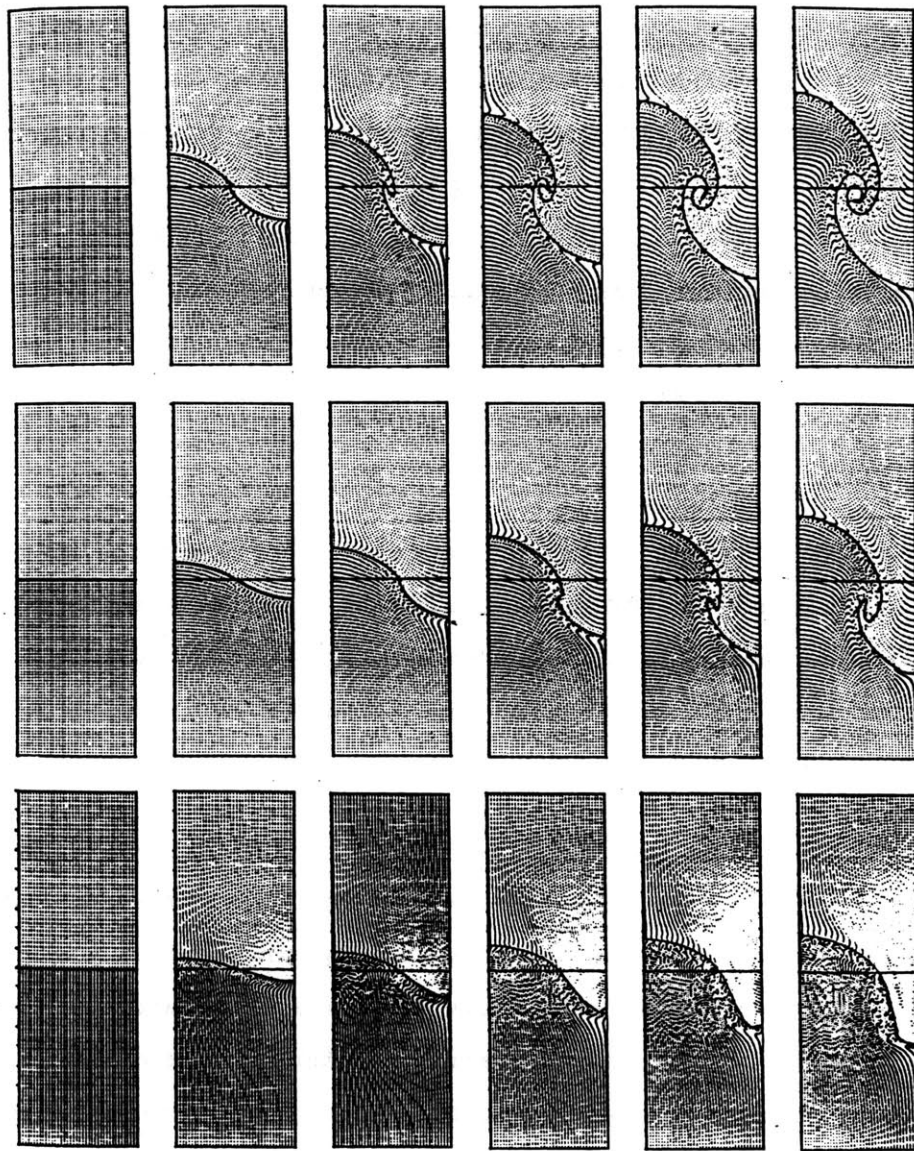


Fig. IV-7. Three particle plots showing interface instabilities at different density ratios. Top series: 1.1 : 1 density ratio at times 0, 0.089, 0.179, 0.269, 0.358, 0.425. Middle series: 2 : 1 density ratio at times 0, 0.045, 0.089, 0.179, 0.224. Bottom series: 10 : 1 density ratio at times 0, 0.025, 0.049, 0.073, 0.097, 0.121. Taken from Daly (1967).

The experiment conducted by Didden and Ho (1985), which inspired Caracena's hypothesis, did show enhanced vortices at the edge of a 3.81 cm wide jet with an exit velocity of 7.5 m/s striking a plate 15.24 cm away (Fig. IV-8). However, the mean jet flow in that experiment was continuously modulated, i.e. pulsed artificially, to enhance and "close off" the small instabilities that would naturally form (e.g., List 1982). The experimental flow had a Reynolds number 5 orders of magnitude smaller than that appropriate for atmospheric downdrafts, and so was more resistant to turbulent diffusion (e.g., Chen and Chang 1972). This experiment did not provide a reasonable analogue to atmospheric downdrafts (nor was that the intent).

Even if the DFW downdraft had been similar to the "dry" type that achieves a steady state terminal fall velocity, the formation and maintenance of multiple, well developed vortices has never been documented. For multiple vortices to be created, additional "downdraft fronts" would have to form in the virga shaft at about 1-4 min intervals. Although it could happen, the precipitation condensation processes that lead to the development of these downdrafts do not generally display periodicity on this time scale.

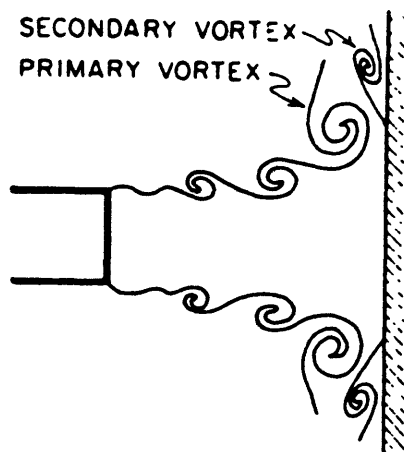


Fig. IV-8. Schematic diagram of modulated air jet exiting nozzle and striking plate. Taken from Didden and Ho (1985).

However, since some unsteadiness is always present, it is fair to suppose that a similar strength downward pulse could form, and another region of vorticity could develop along the virga shaft. Maxworthy (1972) has shown that in this case, when two broadened vortex "rings" of similar strength were created some distance apart along a common path, "the rearward one became distorted by the velocity field (including the wake) at the forward one and squeezed into it through the rear stagnation point. It then wrapped itself around the inner ring to form a *single* large vortex." Although his modelled flow also had a Reynolds number much lower than atmospheric values, it does raise an interesting possibility. The figure he presents as evidence [his Fig. 10 (d)] suggests that the observed wing-like irregularities along the reflectivity shaft of the downdraft shown in Fig. II-6 just might be the remains of such a process. In any case, however, multiple vortex rings do not remain.

B. Frontal Circulation

Density currents have been generally described as "the stable parallel gravity flow of one fluid relative to another that results from *small* differences in their densities" (Daly and Pracht 1968). Simpson (1987) has described a wide variety of geophysical flows that qualify as density currents, and has examined the factors that influence their behavior through numerous laboratory experiments. One type of environmental gravity currents is the cold outflow from a thunderstorm (Fig. IV-9) spreading in a neutrally stratified boundary layer. Since Byers and Braham (1949) originally studied the surface signatures of passing thunderstorm gust fronts, there have been a number of studies devoted to quantifying the structure and life cycle of both observed thunderstorm outflows (e.g., Goldman and Sloss 1969; Charba 1974; Goff 1976; Hall et al. 1976; Greene et al. 1977; Frank and Moninger 1977; Wakimoto 1982; Klinge et al. 1987; Mueller and Carbone 1987; Mahoney 1988) and numerically simulated outflows (e.g., Mitchell and Hovermale 1977; Teske and Lewellen 1977; Thorpe et al. 1980; Zeman 1982; Addis 1984; Anderson et al. 1985; Crook and Miller 1985; Seitter 1986; Droegemeier and Wilhelmson 1987; Haase and Smith 1989a).

The primary horizontal vortex in a dense outflow spreading in an unstratified environment is the leading circulation in the head of the current (Fig. IV-9). Benjamin (1968) has shown that "there must inevitably be breaking at the front of a deeply submerged gravity current". This breaking occurs on the rearward side of the head wave, leaving an elevated head wave and a trailing wake and body of the current. Simpson and Britter (1979) showed that the head depth of a

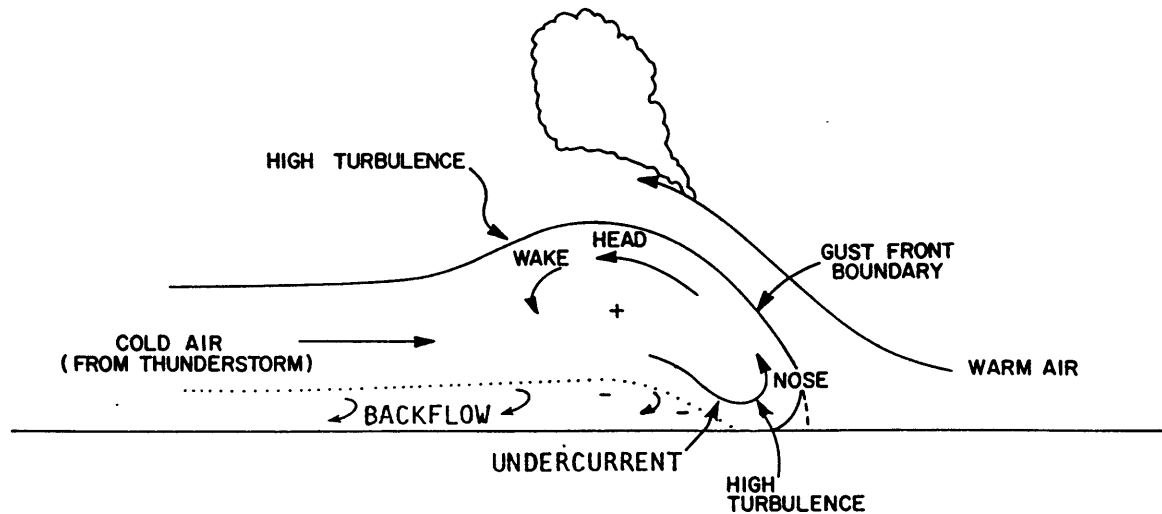


Fig. IV-9. Schematic representation of an atmospheric density current. Taken from Goff (1976).

density current is roughly twice the depth of the following flow, although in laboratory experiments the relative head height increases sharply as the depth of the dense current relative to the ambient fluid decreases below 0.2 (as in the atmosphere).

This vorticity in the head wave is forced by the horizontal buoyancy gradient across the outflow front; for a cold outflow the positive radial buoyancy gradient forces a positive (counter-clockwise) circulation looking into the r - z plane, especially when the pressure gradient is primarily vertically oriented and pointing downward. Mitchell and Hovermale (1977) first quantified this acceleration by applying the circulation theorem to the numerically modelled potential temperature and pressure fields of a gust front (Fig. IV-10). A solenoidal field exists when the potential temperature surfaces are inclined with respect to pressure surfaces, and thus this frontal circulation is commonly called a "solenoidal" circulation.

A steady state can be achieved when the density current is forced by continuous inflow; this is approximately true for the large scale outflow from a squall line consisting of periodically collapsing cells. These flows can also become quasi-two dimensional. On the other hand, the cold outflow from a single cell can rarely be considered continuous, and its axisymmetric geometry strongly influences the characteristics of the initial flow. Compared with two dimensional flow, the axisym-

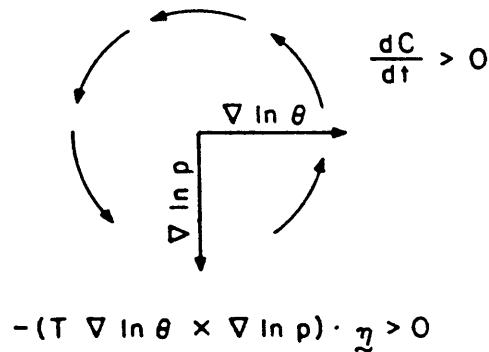
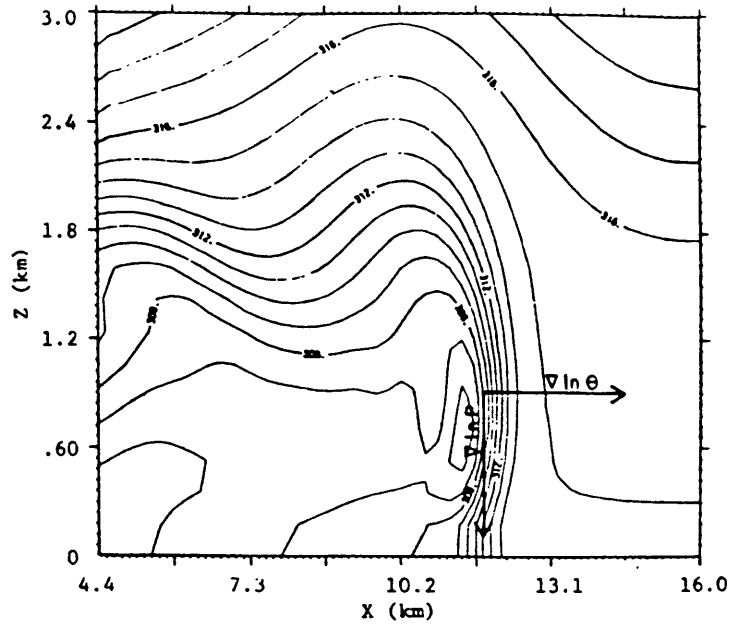


Fig. IV-10. Illustration of the positive circulation acceleration at a numerically modelled gust front. η is the unit normal vector out of the plane. The potential temperature, θ , is contoured in 1 K intervals from 306 to 319 K. C is the circulation, t is time, T is temperature, and p is pressure. Taken from Mitchell and Hovermale (1977).

metric outflow will have a more intense, and larger (relative to the following flow) leading vortex because of the rapid geometrical expansion and, as a result, will have stronger downdraft velocities closer to the surface. This process is explained in the following section.

C. Leading Vortex Ring Structure in Axisymmetric Outflow

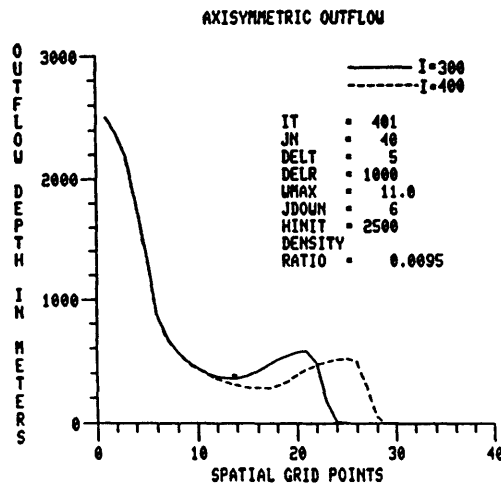
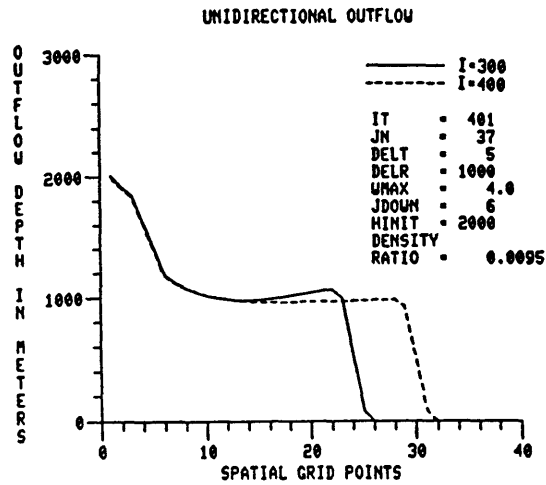
A characteristic of axisymmetric outflows of dense fluid is the formation of a "raised rim" or ring at the leading edge of the outflow. This vortex ring has been called an "outflow microburst" by

Fujita (1985; Fig.I-4). The simple one-dimensional, nonlinear, hydrostatic, incompressible model of Addis (1984) shows this "head" is much more pronounced in an axisymmetric flow than in a unidirectional flow (Fig. IV-11). A photograph from a field experiment testing the release of dense gas into a calm atmosphere (Johnson 1985), shows this feature very clearly (Fig. IV-12). An idea of the time and space scales involved in the release can be gotten from the plan view of the dense cloud (Fig. IV-13) drawn from a similar experiment by Picknett (1981).

1) Thunderstorm Outflow Examples

Smith (1986) provided visual observations of thunderstorms associated with heavy precipitation in Kansas that showed horizontal vortices at the leading edges of the outflows. Fujita (1985) published an excellent time sequence of photographs by Smith showing the vortex forming as the cold air from a thunderstorm rain shaft spread at the surface. Doppler radar observations of axisymmetric thunderstorm outflows consistently show the rapid formation of a leading outflow vortex ring. Fig. IV-14 is a composite representation of the average conditions at the time of maximum outflow for 13 mature thunderstorms observed in Memphis, TN. A well developed deep outflow ring, with which the maximum surface winds were associated, was apparent in every case. Wakimoto (1982) includes a leading "precipitation roll" as part of the canonical life cycle of thunderstorm gust fronts based on data from the NIMROD project (Fig IV-15). He did not differentiate between circular and more linear gust fronts, or between neutral and stably stratified boundary layers. In fact, all of the outflows he studied formed in environments with strong surface nocturnal inversions, so the persistent roll in the late mature and dissipating stages may have an alternative interpretation in terms of solitary waves. This is explored further in the next chapter.

One isolated axisymmetric thunderstorm collapsing into a neutral boundary layer was thoroughly measured during the COHMEX project in Huntsville, AL (Dodge et al. 1986), and has been studied extensively by a number of researchers (e.g., Kingsmill et al. 1989; Tuttle et al. 1989; Wakimoto and Bringi 1988; Goodman et al. 1988 and 1989; Fujita and Black 1988; Wakimoto 1988). A vertical cross-section taken with the NCAR CP-2 Doppler radar through the center of the storm at the time of maximum outflow is shown in Fig. IV-16. The structure of the outflow velocity toward the radar (dashed contours) clearly shows not only the deep leading edge, but the apparent separation of the leading ring from the outflow, and the formation of a second deep vortex behind.



Definitions of Model Terms

IT	maximum extent of the time grid
JN	maximum extent of the space grid
DELT	time step (s)
DELR	space step (m)
WMAX	downward flow rate at center of downdraft ($m s^{-1}$)
JDOWN	horizontal extent of the downdraft on the grid
Rdown	radius or width of downdraft $R_{down} = (JDOWN - 1) \times DELR$
HINIT	initial central (incompressible) column height (m)
DENSITY RATIO	$\Delta\rho/\rho \doteq -\Delta T_v/T_{v_{env}}$

Fig. IV-11. (Top) Unidirectional model simulation. Outflow depth as a function of horizontal distance at the 300th and 400th time steps is shown. Initial column height 2000 m. (Bottom) Comparable axisymmetric simulation. Initial column height 2500 m. The accompanying table gives the definitions of model terms shown in the figures. Taken from Addis (1984).

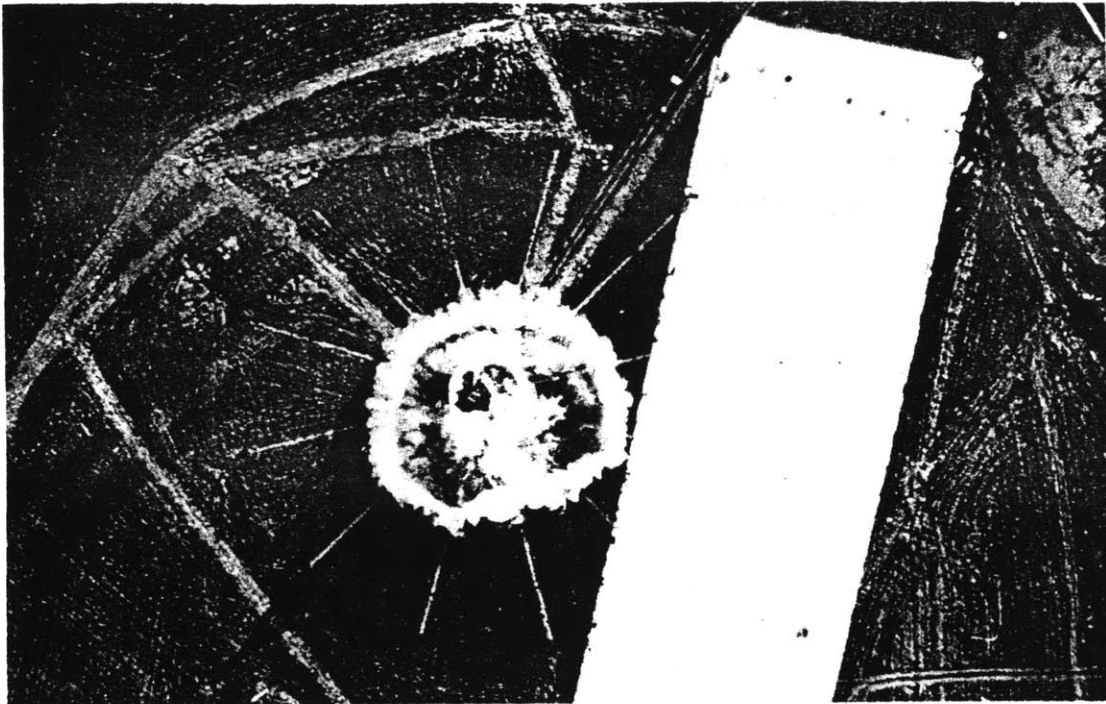


Fig. IV-12. Instantaneous release of dense gas into calm air seen from above in the Thorney Island experiments. Taken from Johnson (1985).

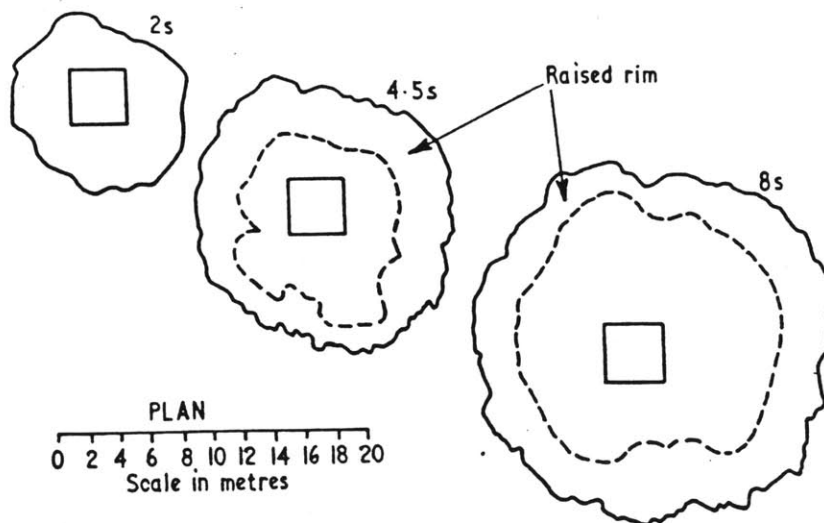


Fig. IV-13. Plan view of a dense cloud, similar to that shown in Fig. IV-12, at various times after release in calm conditions. Taken from Picknett (1981).

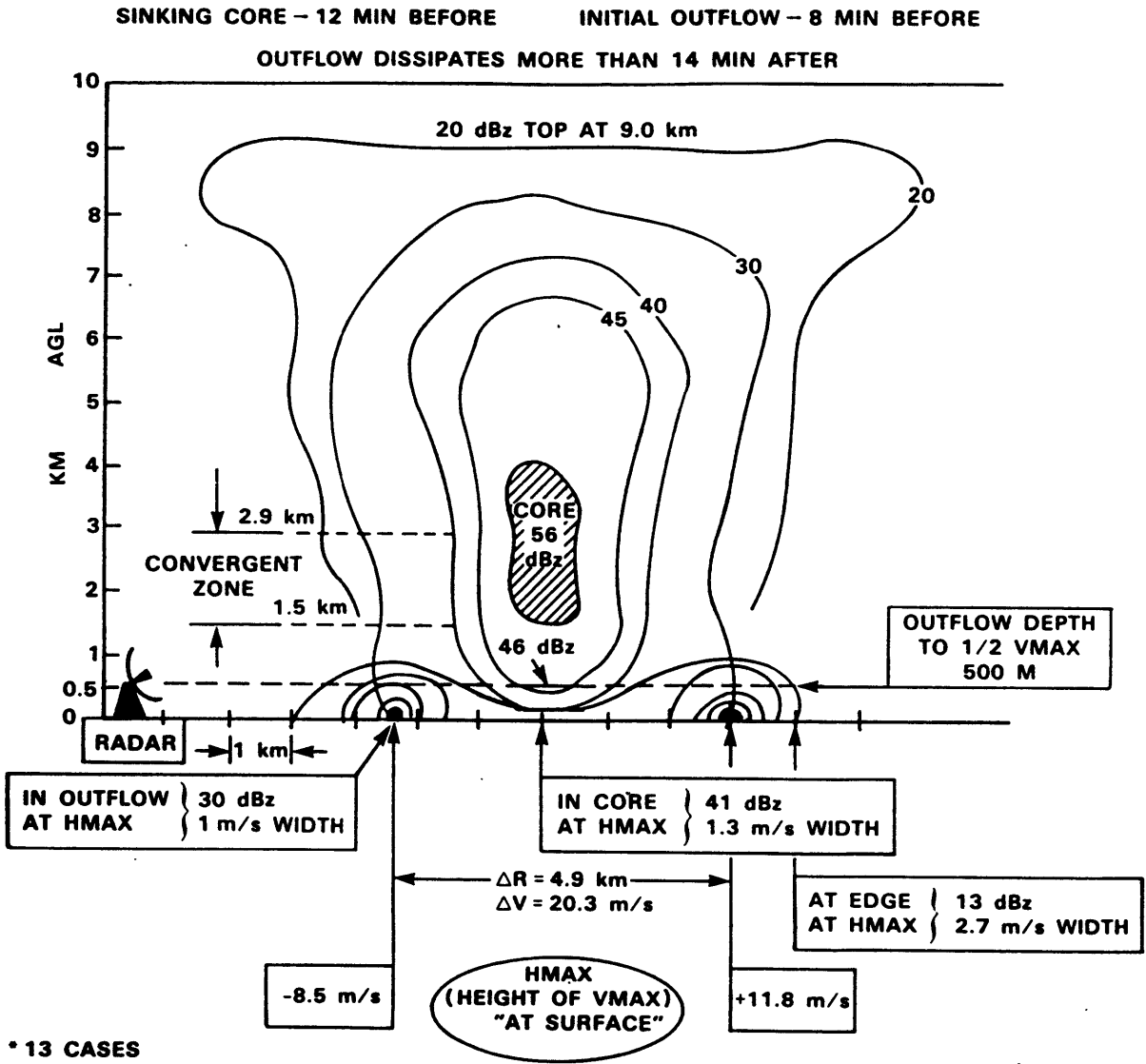


Fig. IV-14. Schematic representation of the average conditions at the time of maximum outflow measured for 13 Memphis cases of collapsing thunderstorms. The strongest winds were measured in the lowest radar beam (essentially "at surface"). The average maximum outflow wind speed differential was 20.3 m/s over a distance of 4.9 km. In the upper part of the figure, reflectivity is contoured, and labelled in dBz. Below 1 km, the Doppler velocity is schematically contoured to show typical isodop pattern at time of maximum outflow speeds.

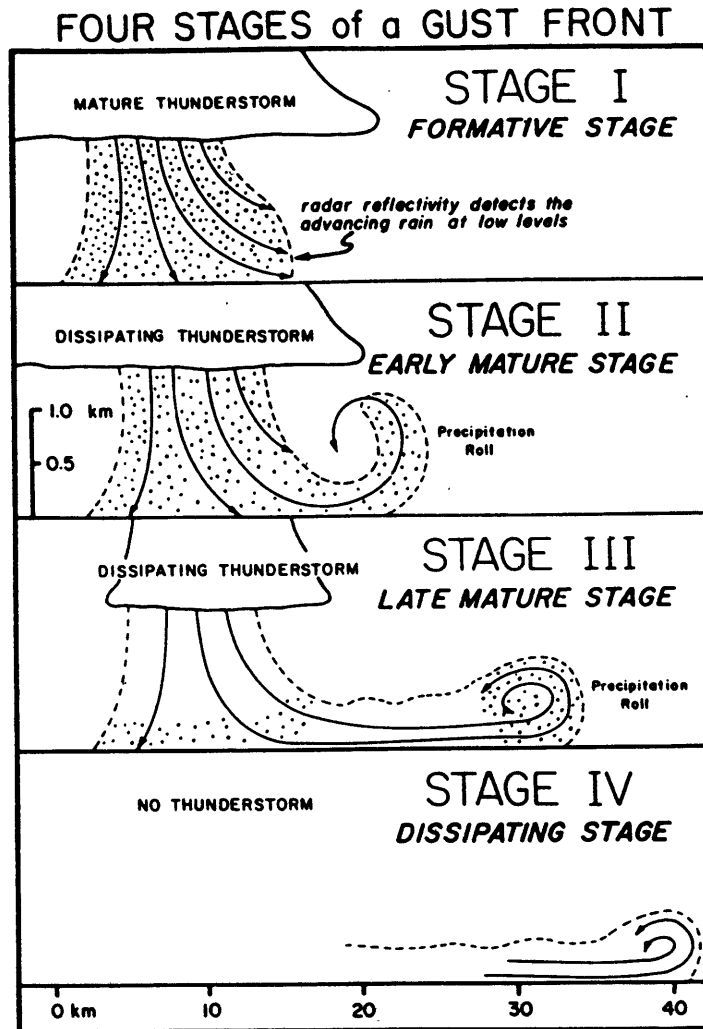


Fig. IV-15. The four stages of a thunderstorm gust front. The advancing precipitation roll at low levels is detected by the radar. The "precipitation roll" is a horizontal roll formed by airflow that is deflected upwards by the ground. Taken from Wakimoto (1982).

Fujita (1984) proposed a vortex ring stretching model for the leading edge of an axisymmetric outflow based on analysis of a fairly average thunderstorm that produced small scale, short lived winds over 50 m/s at Andrews Air Force Base near Washington, D.C. in August, 1983. In his model, the vortex initially develops aloft around the descending downdraft (as observed in the JAWS virga cases) and, as it reaches the surface, it stretches and "runaway vortex rolls" give rise to the strong microburst winds (Fig IV-17). Linden and Simpson (1985) suggested the vortices in the DFW outflow were finite amplitude Kelvin-Helmholtz (KH) billows. They identified the large leading vortex, created in their axisymmetric laboratory experiment with salt water spreading radially into fresh water (Fig IV-18), as a KH billow.

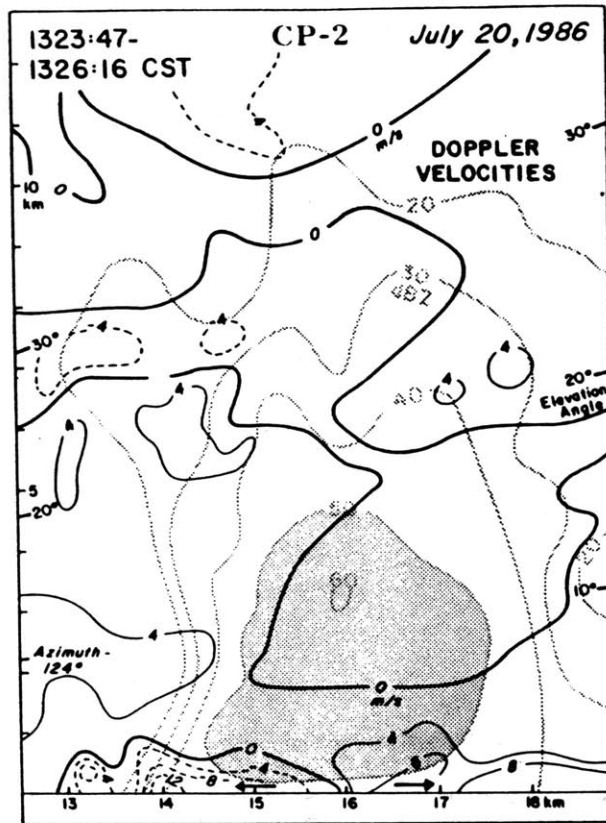


Fig. IV-16. RHI cross-section taken with the CP-2 Doppler radar on July 20, 1986 during the COHMEX project in Huntsville, AL. Contours of reflectivity are stippled, as is the entire region greater than 50 dBZ. Doppler velocities are contoured in solid (positive, away from radar) and dashed (negative, toward radar) lines. Taken from Wakimoto and Bringi (1988).

This process of formation of an intense leading vortex “ring” in an axisymmetric gravitational flow has been qualitatively explained as a result of radial expansion of the circumference, and thus the head wave vortex axis, of the dense outflow (Fujita 1984; see Fig. IV-17). The argument offered is that, “because the fluid volume in a vortex is (approximately) conserved, its cross-sectional area must decrease. Conservation of angular momentum about the center line of the vortex then implies that the vorticity increases.” (Linden and Simpson 1985). This qualitative model for the leading vortex in dense axisymmetric outflows has been inconsistently formulated without the benefit of complete observations. It is essentially incorrect; the volume of the leading vortex is not conserved but steadily increases with time. Strong surface winds and strong downdrafts at low altitudes in an axisymmetric thunderstorm outflow will be associated with this leading vortex region. It is thus a very important part of the microburst problem, and needs to be understood.

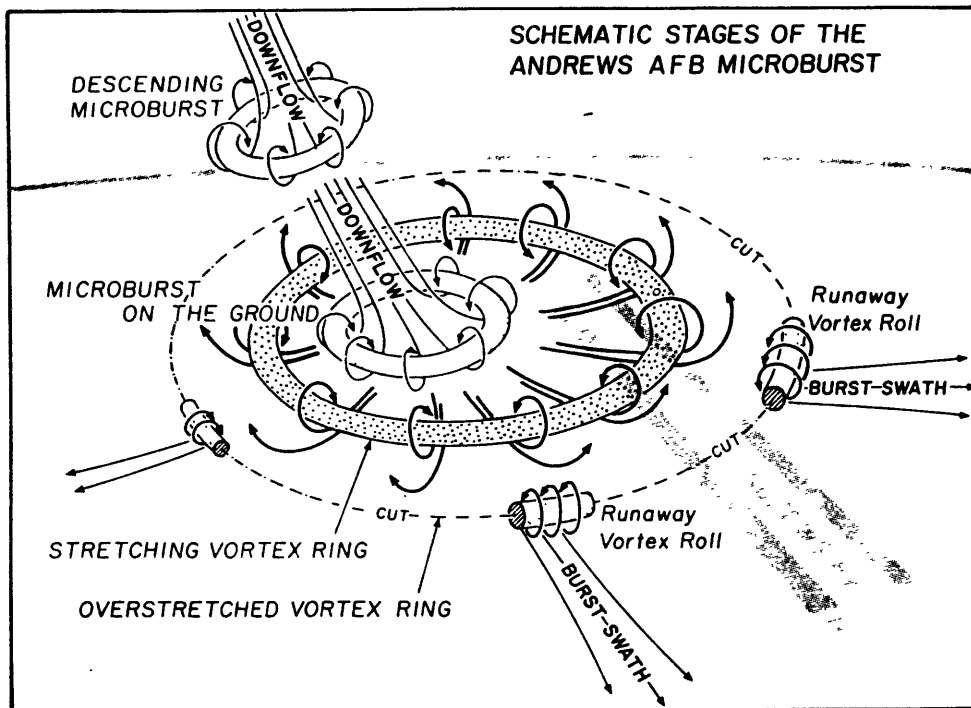


Fig. IV-17. Depiction of the four stages on the Andrews Air Force Base microburst. They are: 1st stage (descending stage): midair microburst descends, 2nd stage (contact stage): microburst hits the ground, 3rd stage (mature stage): stretching of the ring vortex intensifies storm, 4th stage (breakup stage) runaway vortex rolls induce burst swaths. Taken from Fujita (1984).

2) Physical Explanation of Leading Ring Formation

The correct model for understanding the formation of a leading vortex ring in dense, axisymmetric outflows has been described in two key research papers. Rottman and Simpson (1984) developed a nonlinear "dam-break" model of a finite volume release of heavy fluid, and compared axisymmetric and parallel flows with their laboratory model results. Garvine (1984) has similarly modelled the axisymmetric continuous inflow case, and has additionally allowed for frontal entrainment and friction. His research, which perhaps best explains the processes involved in development of the leading ring structure in axisymmetric flows, is summarized below. (Liberal use has been made of his published work without repeated references in what follows.)

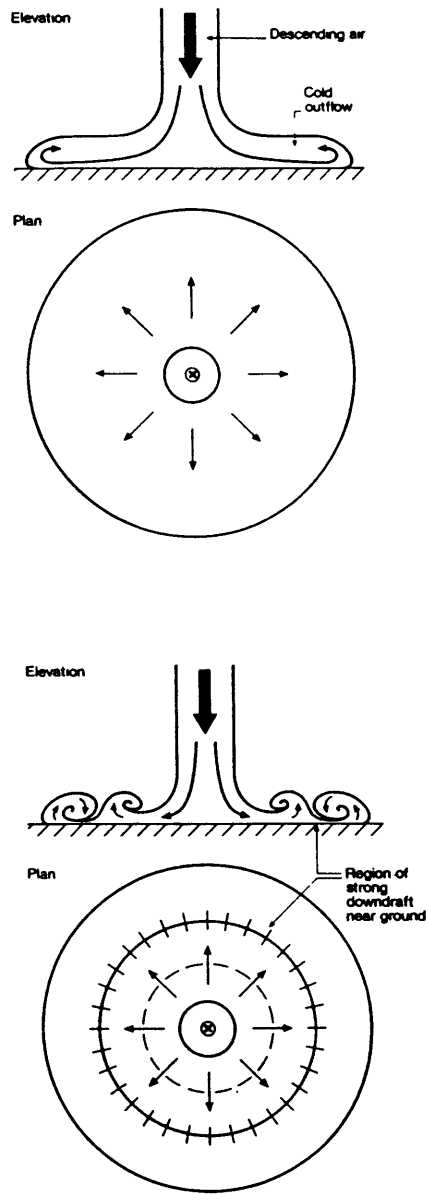


Fig. IV-18. (Top) A simple idealized picture of the descent of cold air from a thunderstorm. The hazard to aircraft is thought to be due to the variations of horizontal wind. The width of the descending air is <4 km, and the depth of the outflow along the ground is a few hundred meters. (Bottom) The early stages in the development of a microburst. Most of the spreading mass of cold air is concentrated into an intense leading-edge vortex. This is sometimes followed by a second vortex. The horizontal scale is similar to that in the top picture. Taken from Linden and Simpson (1985).

Garvine modelled the case of a radially spreading surface buoyant flow with a continuous source to help explain the observed characteristics of river plumes, created where fresh water empties into coastal seawater. A thin layer of buoyant water spreads radially under the force of gravity, with a sharp frontal boundary at the leading edge. In cases with strong radial spreading, weaker interior consecutive fronts have been observed. (These are discussed further in the subsequent section IV.D.)

The main body of the plume is modelled using the inviscid nonlinear shallow water equations, and the frontal boundary is represented by a jump condition. The Boussinesq approximation is made, and wind stress, mixing, and the Coriolis acceleration are all neglected. The difference in density between the buoyant fluid and the surrounding fluid is constant, so the radial pressure gradient and the fluid velocity are vertically uniform. With these approximations, the governing equations of mass continuity and radial momentum for the main plume body are:

$$(c^2)_t + \frac{(rc^2u)_r}{r} = 0$$

$$u_t + \left(\frac{u^2}{2} + c^2\right)_r = 0$$

where $c \equiv \sqrt{g'd}$ is the long internal wave speed (g' is the reduced gravity, and d is the depth of the gravity current), t is the time from initial fluid release, r is the radial distance from the source center, u is the radial velocity, and the subscripts denote partial differentiation with respect to that variable. These two equations together form a hyperbolic system with a pair of characteristic lines given locally by:

$$\frac{dr}{dt} = u \pm c \quad (\text{II.1})$$

along which the corresponding characteristic equations are:

$$du \pm 2dc = \mp \frac{cu}{r} dt \quad (\text{II.2})$$

The “+” (upper) and “-” (lower) families of characteristics represent the nonlinear, internal gravity waves that propagate upstream and downstream, respectively, at phase speed c relative to the outflow, and at absolute wave speed $u \pm c$ relative to fixed coordinates. Garvine was able to

solve the characteristic equations (II.2), which are ordinary differential equations, using standard finite difference methods. The equations corresponding to Eqs. (II.1) and (II.2) for parallel flow are identical except for the term on the right hand side of (II.2), which represents the effects of radial expansion on the flow.

The frontal discontinuity at the leading edge of the outflow was handled numerically in a manner analogous to shock fitting in compressible gas flow. At each time step, the fluid speed and wave phase speed behind the front, and the speed of the front itself relative to the ambient fluid, were determined. The required jump conditions were formulated to allow the inclusion of the effects of friction (specified as the fractional extent of the frontal zone over which friction is important), and upward or downward entrainment.

The results of a sample calculation with no entrainment are shown in Fig. IV-19. The scaled interface depth of the modelled river plume is shown, but this can also be interpreted as the interface height of a cold thunderstorm outflow. The most prominent feature of the flow is the clear emergence of a ridge, at first indistinct, but later quite distinct with a sharp dip (dubbed the "trailing front", in contrast to the "leading front"). This trailing front became so steep that Garvine treated it numerically as a second front with its own jump conditions. The width of the ridge or ring feature increases with time, and the interface height within the ring is about 20% greater at the leading front than at the trailing front.

The characteristics plane for this sample calculation is shown in Fig. IV-20. The leading front, the trailing front, and representative characteristics, including their reflections off the leading front, are shown in scaled R (radial dimension), T (time) space. Two distinct flow regimes, the ring itself and the spreading regime from the source to the ring, can be seen. The downstream propagating "plus family" of characteristics have nearly invariant slopes, i.e., $(u + c)$ changes little. However, the opposite is true of the slope of the "minus family" characteristics. In Fig. IV-20, the labelled "First Reflected Characteristic" has the same shape as all of the other characteristics in the "minus family". Notice how its slope sharply increases with R . This positive curvature is the essential feature of these upstream propagating characteristics, and is a direct result of the radial spreading.

As the fluid expands radially, the fluid at the leading edge of the current begins to accelerate outward. However, the acceleration of the fluid just behind the front is limited by the front itself, and these disturbances will propagate back away from the front. The first waves to be reflected off

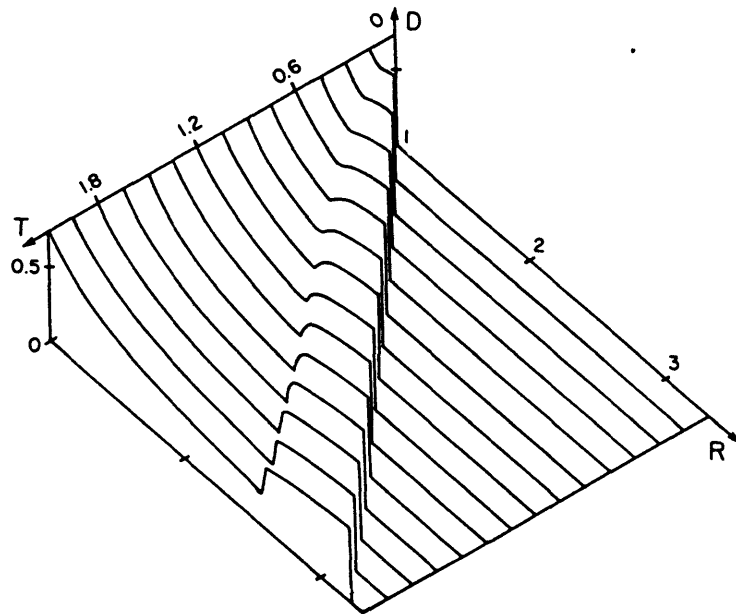


Fig. IV-19. Isometric projection of scaled interface depth (D) as a function of scaled range (R) and time (T). Taken from Garvine (1984).

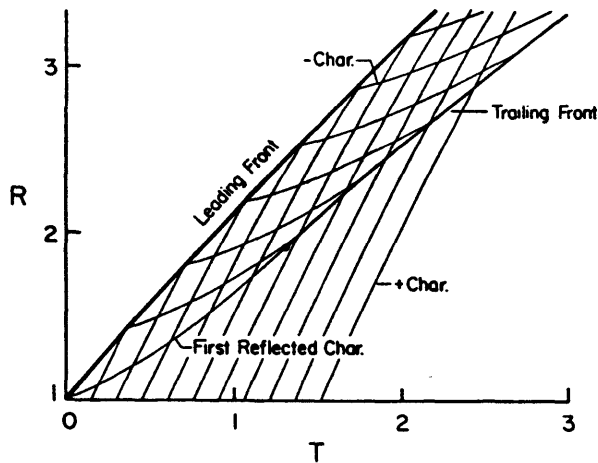


Fig. IV-20. The characteristic (R, T) plane for the sample calculation showing the leading front, trailing front, and representatives of both families of characteristics for $0 < T < 3$. The solid dot indicates where fitting of the trailing front began. Taken from Garvine (1984).

the leading front (minus family) have low initial wave speed ($u - c$), since c is relatively high in the deeper flow near the front. They are later overtaken by reflected waves from further upstream in the ring, nearer the steady spreading regime. As shown in Fig. IV-20, this overtaking is in the form of wave coalescence, a necessary condition for the formation of an interior front. The reflected waves continue to accumulate within the ring at the trailing front, causing the trailing edge of the ring to deepen.

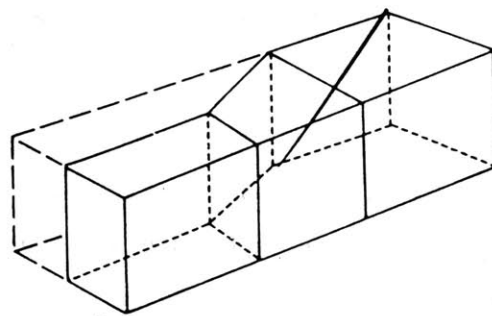
The volume of the ring feature, proportional to the product of the mean radius and the ring width and depth, continually increases with time as a result of inflow into the ring through the trailing front. In the case of no entrainment, it had increased by a factor of 6 by the time the leading front had reached a distance of about 10 times the source radius. With entrainment, the results are qualitatively the same, but the increase in volume is not as marked because fluid is lost at both fronts. This basically refutes the argument that the frontal ring in axisymmetric outflows is a vortex tube that undergoes stretching as the flow expands.

In a parallel, two dimensional flow released from a line source, both plus and minus families of characteristics would be straight lines, corresponding to internal waves of *zero* amplitude. All properties of the flow except for the position of the front would be uniform in time and space. No changes in the flow state would occur, and to an observer moving with the flow at the frontal speed, the flow would appear steady. Neither the trailing front nor the radial ring would form.

“The nonlinear, internal wave dynamics inherent in formation and continuance of this [leading radial ring] structure requires reflection of downstream propagating internal waves off the leading front to form upstream propagating waves whose absolute wave speeds ($u - c$) increase with radial distance, because of continued plume spreading. This radial gradient in wave speed results in wave coalescence with subsequent ring and interior bore formation. The two crucial flow properties to ring formation, then, are the leading front and radial, gravitational spreading. In the absence of either no ring could form” (Garvine 1984).

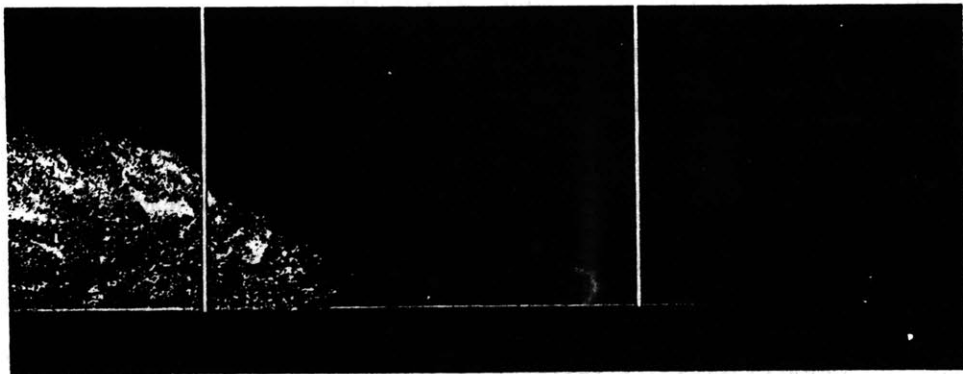
3) Laboratory Experiments

A simple laboratory experiment was performed to illustrate the pronounced difference between the leading edge of an advancing gravity current in parallel versus axisymmetric flow (Linden and Simpson 1985). A widening tank (Fig. IV-21) was built to allow an initially parallel flow to rapidly double in width, simulating the effects of radial expansion. The effect of widening the

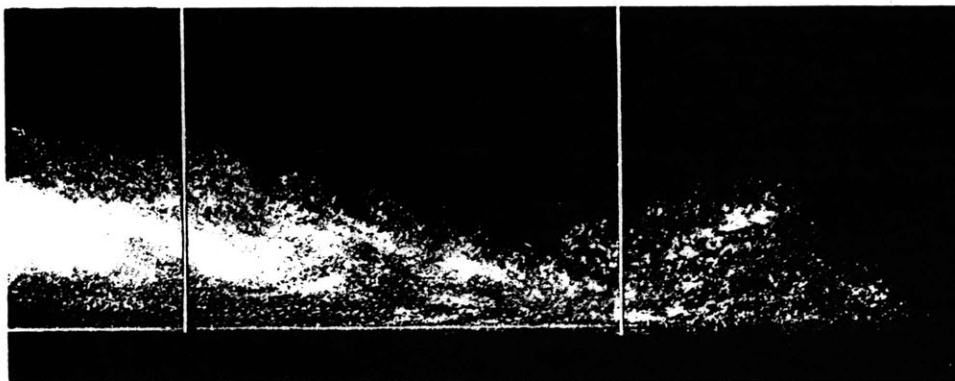


Widening tank

Fig. IV-21. Tank to test the effect of widening on the form of the head of a gravity current, originally in a channel with parallel sides. Taken from Simpson (1987).



(a)



(b)

Fig. IV-22. The effect of widening the channel of the form of a gravity current head. The width increases from 10 cm to 20 cm between the two white lines which are 30 cm apart. The time interval is 5.7 s, and g' , the reduced gravity, is 14 cm/s^2 . Taken from Simpson (1987).

channel on the form of the gravity current head is shown in Fig. IV-22. This is described by Simpson (1987) as an experiment that demonstrates “that the vorticity already being produced at the leading edge of an advancing current is sufficient to produce this intense roll-up of the leading edge when it is stretched”.

A close look at Fig. IV-22 shows that the vortex cross-sectional area has not been reduced during the expansion (taking the back edge of the leading vortex in the parallel flow at the interface “dip” halfway between the left edge of the photograph and the first white line); in fact, it may well have increased. The formation of the pronounced leading vortex ring is not the result of a constant volume vortex tube spinning up as it is stretched, and its cross-sectional area reduced, under the constraint of conservation of angular momentum. This development would perhaps better be described as a “build-up” rather than a “roll-up” of the leading edge.

The radial expansion *is* the cause of “the descent at the rear of the leading-edge vortex to extend to within a short distance from the ground”, as claimed by Linden and Simpson; this is simply the actual fluid motion corresponding to the formation of the interior front simulated by Garvine. And the radial expansion, combined with the presence of a leading front, does cause an increase in vorticity at the leading edge of the current. The radially accelerated flow decelerates sharply as the front is approached, producing a strong convergence at the leading front. This increases the vorticity through the “stretching” term in the horizontal vorticity equation, but it is wrong to think of the entire axisymmetric gravity current front or “rotor” as a single vortex tube. (The solenoidal generation of vorticity, proportional to the horizontal buoyancy gradient, continues just as in the case of parallel flow.)

4) Numerical Experiment

Proctor (1988b) has used an axisymmetric model to simulate the wind conditions through which Delta 191 flew when it crashed on landing at DFW airport on August 2, 1985. He initiated the model with a sounding characterized in particular by a 2.5 km deep dry adiabatic surface layer. Cross-sections at various times through the simulated flow clearly show the continuous build up of cold outflow air into a deep leading vortex ring (Fig. IV-23). The data in the top panel (11 min into the simulation) match best the data from the on-board flight data recorder. Although this model very accurately simulated most of the characteristics of the DFW microburst, it was unable to “capture the strong vertical velocity oscillations, which were especially prevalent along the southern end of the Delta profile”. In Chapter V, the possible role that the thin stable layer at the

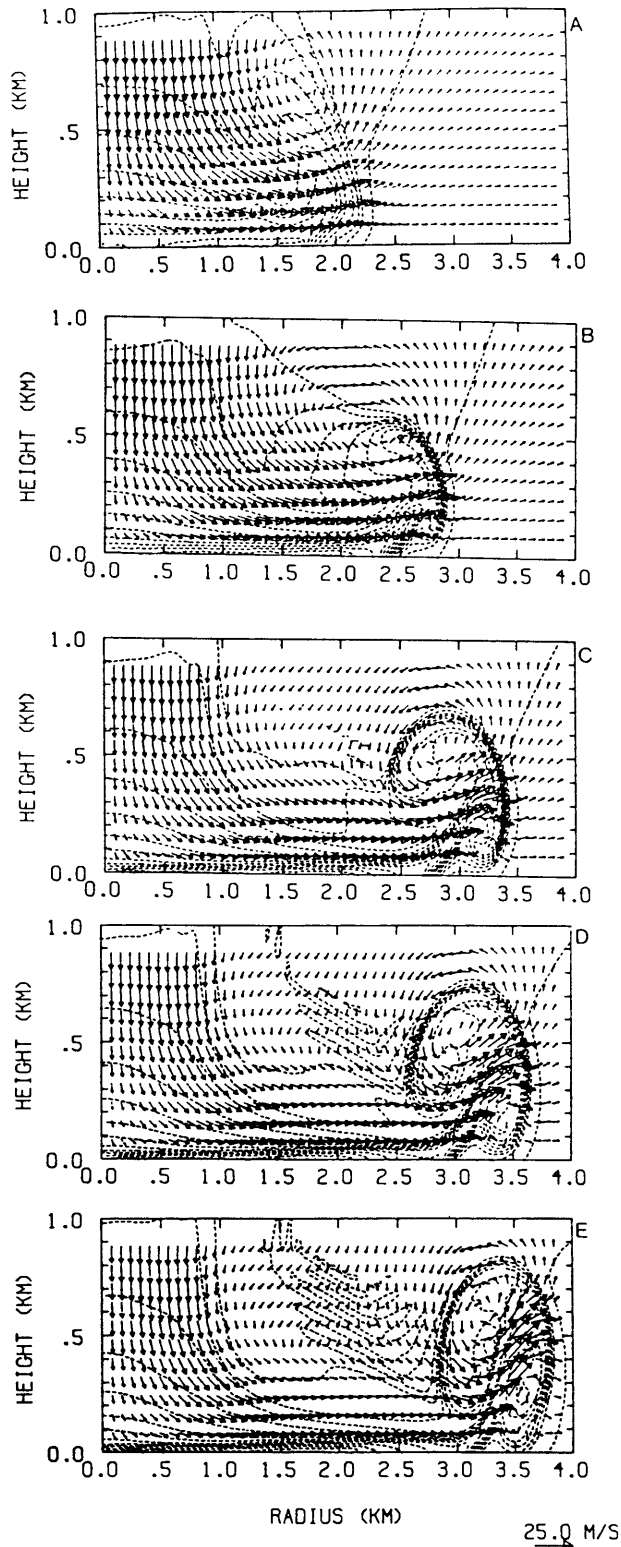


Fig. IV-23. Radial-vertical cross-sections of temperature deviation from ambient and superimposed wind vectors from Proctor's axisymmetric DFW simulation (neutral boundary layer). The fields are at (a) 11 min, (b) 12 min, (c) 13 min, (d) 13.5 min, (e) 14 min. The contour interval for temperature deviation from ambient is 1 K. The vertical coordinate is magnified relative to the horizontal. Contours with negative values are indicated by dashed lines. Taken from Proctor (1988b).

surface (created as old, relatively cool outflow from a distant thunderstorm swept over the airport area 15 min before the accident) may have played in the outflow evolution is investigated.

D. Multiple Ring Structure in Axisymmetric Outflow

In addition to the leading vortex ring created in an axisymmetric density current flow, in some cases weaker consecutive interior fronts of smaller radius are seen. An example of these can be seen in the spreading at a neutral density level in a stably stratified atmosphere of discharge from three closely located power plant cooling towers is given in Fig. IV-24. An analogous example is given in Fig. IV-25, where the concentric fronts formed as heated water used in cooling power plant condensers emptied into Lake Michigan. Similar consecutive fronts have been observed, for example, in Norwegian fjords by McClimans (1978) and in river plumes discharging into the ocean by Gross (1972). However, atmospheric and oceanic examples in which the ambient fluid is clearly unstratified are difficult to find. This makes it impossible to rule out the identification of these consecutive interior fronts with internal undular bores generated by the spreading density currents (e.g., Simpson 1987, Ch. 7.5).

Since cold thunderstorm outflows frequently spread into neutral boundary layers, confirmation of the possibility of interior front formation in the case of an axisymmetric density current flowing into an unstratified environment is important in understanding the microburst problem, and in particular in understanding the nature of the observed embedded vortices in the DFW microburst which caused Delta 191 to crash on landing. The hypothesis of Linden and Simpson (1985; Fig. IV-18) involved the formation of a interior vortices in dense outflows, which they identified as Kelvin-Helmholtz billows. The observations of the July 20, 1986 thunderstorm during COHMEX appear to show the leading vortex separating from the flow and a second raised vortex forming (Fig. IV-16). Garvine's (1984) model, described in the preceding section, can only predict formation of the leading ring. He puts forth the following plausible argument, consistent with his model results, to explain the secondary front formation mechanism. (Again, liberal use has been made of his published work in the following two paragraphs.)

1) Physical Explanation of Consecutive Ring Formation

The inflow Froude number ($Fi = u/c$) is usually greater than 1, i.e., the flow is usually supercritical, in axisymmetric plume field observations (Garvine 1977). This is because the strong radial spreading produces a rapid drop in the outflow depth with a corresponding drop in the phase

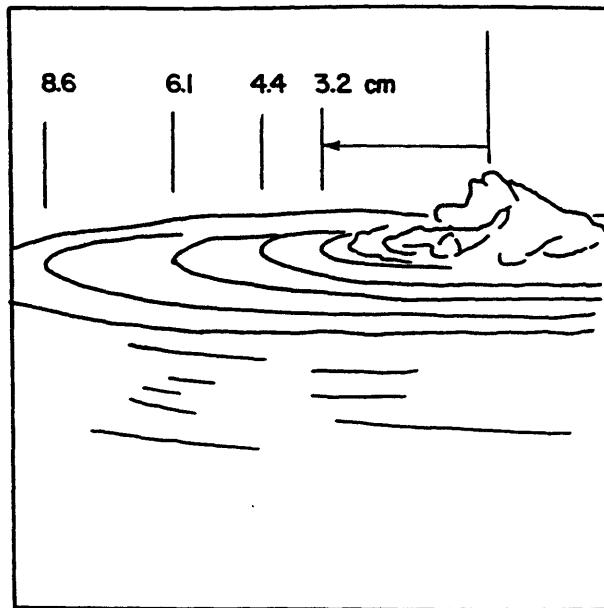


Fig. IV-24. Line sketch for a series of radial ring discontinuities in a horizontal spreading cooling tower plume from John E. Amos Power Plant, drawn by Chen (1980) from a photograph by Kramer and Seymour (1976).

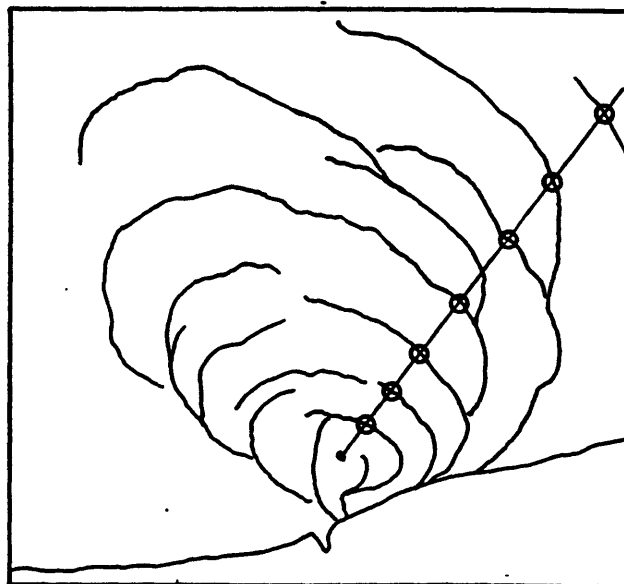


Fig. IV-25. Line sketch for a series of radial ring discontinuities in horizontally spreading cooling water discharge plume from Sheboygan Power Station, drawn by Chen (1980) from airborne thermal imagery by Scarpace and Green (1973).

speed c . But the drop in outflow depth also sets up a radial pressure gradient that accelerates the flow outward. These two effects combined produce an inflow Froude number that increases monotonically as the flow expands (in the idealized steady flow solution). For some value of Fi greater than 2, the interface will become unstable and mixing will occur in the form of Kelvin-Helmholtz (KH) billows. [Stern (1975, p. 152) showed that the interface is stable for $Fi < 2$.]

This Froude number threshold will be crossed at a particular radius, estimated to be about 1.4 times the source radius, where turbulent mixing will begin. At this point the outflow will be disrupted as mixed turbulent fluid penetrates into the outflow layer. But at the upstream edge of this turbulent gap a new "leading" front will form separating the fluids of different density. Now, as this flow expands, the process of ring formation will begin again, behind this ring the spreading flow will become unstable, generate another gap and new front, and so on. Some of the field observations of river plumes with consecutive fronts show the gaps to be thin in comparison with the ring width, indicating that the radial extent of the turbulent mixing is quite narrow.

2) Laboratory Experiments

This explanation implies that the source of outflow must be continuous (or persist at least until the outflow edge reaches roughly 2 source radii from the origin) for secondary or multiple front development to occur. The laboratory experiments of Rottman and Simpson (1984), involving finite volume fluid releases in an axisymmetric geometry, appear to support this. Figure IV-26 shows the sector tank they used to form the axisymmetric outflow. The shadowgraphs showing the results of two experiments are shown in Fig. IV-27. In (i), the dense fluid height was 25% of the total fluid depth, and in (ii), it was equal to the fluid depth. Rottman and Simpson conclude, for finite volume fluid release, that only the leading vortex ring will develop for small fractional depths, and that multiple fronts will develop for fractional depths near unity. The latter case is more analogous to the continuous inflow case because the finite volume of fluid is larger.

Close inspection of Fig. IV-27 (i) shows that a gap and a weak secondary front did temporarily form, but they quickly disappeared as the depth continued to decrease in response to the radial spreading. Perhaps the inflow Froude number, and not the initial fractional depth is the more precise parameter governing the flow development. The turbulent eddies result from KH instability of the density current interface behind the leading ring. Garvine's estimate of gap for-

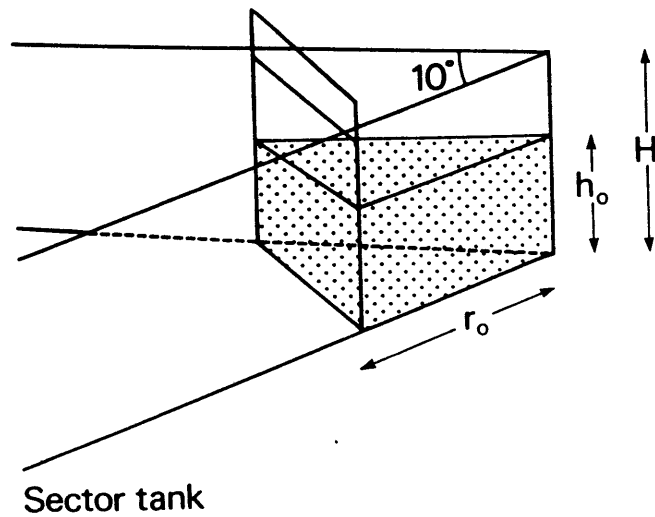


Fig. IV-26. Tank in the form of a sector for the release of a fixed volume of dense fluid to form an axisymmetrical gravity current. Taken from Simpson (1987).

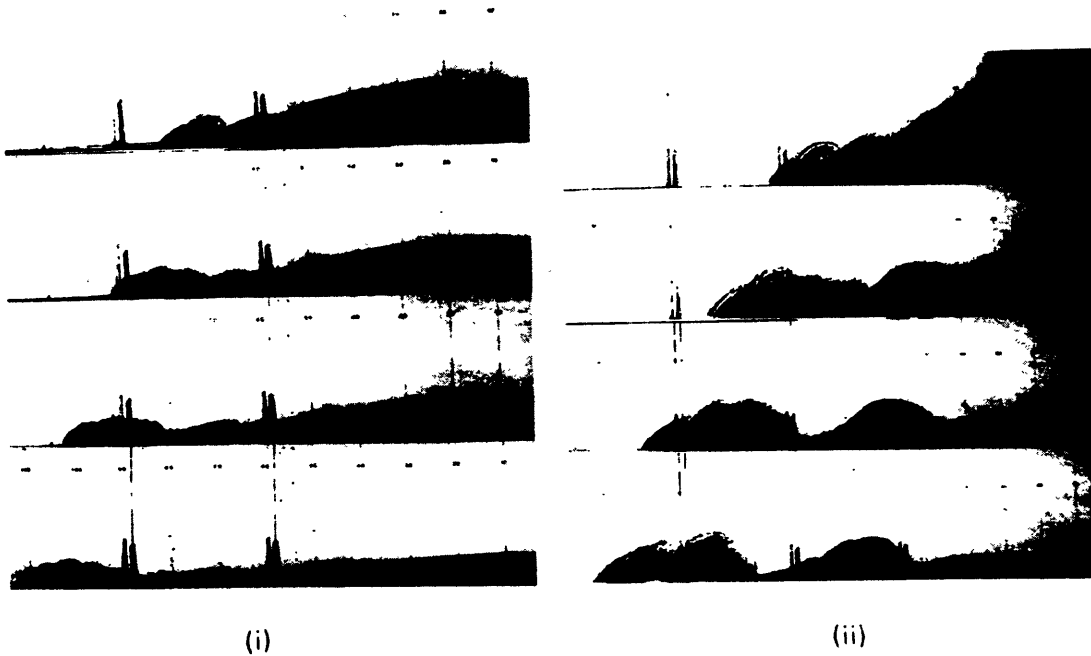


Fig. IV-27. Shadowgraphs of a volume of salt water collapsing into fresh, in the sector shaped tank shown in Fig. IV-26. Total depth is 40 cm, and reduced gravity, g' , is 47 cm/s^2 . (i) $h_0/H = 0.25$; (ii) $h_0/H = 1$. In both experiments, r_0 was 60 cm; this distance is indicated in the figures by the first double vertical lines (from the right). The thin vertical lines are spaced 10 cm apart. H , h_0 and r_0 are identified in Fig. IV-26. Taken from Simpson (1987).

mation at a radius of ~ 1.4 "lock-lengths" (source radii) is approximately realized in these finite release experiments.

Also, a close look at Fig. IV-27 (ii) shows that after formation of the second front, the leading ring continued to widen. The last shadowgraph shows a gap forming within the leading ring under the action of turbulent mixing, suggesting that the leading front itself could split into two rings. It appears that this same behavior was observed in dense gas release experiments performed by Havens and Spicer (1984). This may represent an additional mechanism for consecutive front development in axisymmetric density flows; the interface of the deep leading ring itself becomes unstable to KHI as opposed to the thin layer of fluid remaining in the spreading regime behind the ring. Another explanation involving secondary vortices created in the frictional boundary layer is suggested by the numerical experiments described in the following section.

Simpson (1987, Ch. 12.5) notes that "a gravity current which is spreading out after passing through a narrow slot often shows periodic oscillations in the form of the head". The accompanying picture shows a radially expanding flow with multiple fronts; the continuous flow through the narrow slot in the wall behaved as if it were originating from a point source. The author does not link these "periodic oscillations" with the multiple front formation shown in IV-27 (ii), but it appears that the two phenomena are at least related.

It is interesting that Grundy and Rottman (1986), who studied the existence of similarity solutions of the shallow water equations for gravity currents with comparable inertia and buoyancy forces, found that no solution existed for axisymmetric flow that could satisfy the boundary condition on the axis of symmetry. It was possible to find solutions for plane flow. They suggest that these results indicate "the source conditions remain important no matter how large the spreading pool of heavy fluid becomes", and that "this excludes the possibility of a similarity solution" for axisymmetric flows. It has been postulated that the lack of a similarity solution is related to the formation of consecutive fronts in the physical flow (Chen 1980). Similarity solutions are possible, and compare well with laboratory experiment results, for axisymmetric flows for which the driving buoyancy force is balanced by viscous drag (Huppert 1982; Didden and Maxworthy 1982; Maxworthy 1983).

3) Numerical Experiments

The preceding discussion gave a plausible but unproven explanation for multiple front formation in axisymmetric density currents, and limited laboratory evidence that they do actually form from a continuous point source inflow or a deep finite volume fluid release. However, no convincing evidence for repeated front formation in dense axisymmetric thunderstorm outflows spreading in a neutral environment has ever been presented.

Numerical simulations of slab symmetric (two dimensional) atmospheric gravity currents by Haase and Smith (1989a) were performed to determine the dependence of the density current on the inflow Froude number (Fi). They held the temperature and depth of the inflow constant, and increased the inflow speed to increase Fi . Figure IV-28 shows vertical cross-sections of potential temperature for three values of Fi . As Fi increases, "the depth and strength of the feeder flow increases and at the larger values of Fi , the momentum imparted to the fluid has an increasing effect on the structure of the gravity current head". For the case with $Fi=1.13$ (the largest value illustrated), the "head has more of the character of a starting vortex than that of a simple gravity current. Cold air bulges up to form a second hump behind the head and associated with this is a second local maximum of [the horizontal gradient of potential temperature]." These results do suggest that the inflow Froude number is an important parameter in governing the structure of the leading gravity current front and in determining if and when multiple fronts will form.

A series of axisymmetric numerical simulations were performed at the University of Wisconsin with Anderson's (1990) model*, to see if multiple front development could be expected to occur in the dense outflow from an isolated thunderstorm collapsing into a neutral boundary layer. The complete axisymmetric numerical study corresponding to Haase and Smith's (1989a) two dimensional study was not undertaken. Instead, a cooling source designed to produce an outflow similar in size, temperature, and strength to that observed in the DFW accident was used to initiate the model, and the outflow structure produced with various downdraft durations was examined. Initiation of the outflow through the use of a cooling source aloft is more realistic than specifying the outflow depth, temperature distribution, and speed at the edge of the domain.

* In performing these experiments, all I did was specify a cooling pattern as a function of time; Drs. Jerry Straka and John Anderson used their expertise to determine appropriate grid spacing, diffusion coefficients, cooling function magnitudes, and to actually run the models as well. Digital model output data were shipped to me for analysis and display.

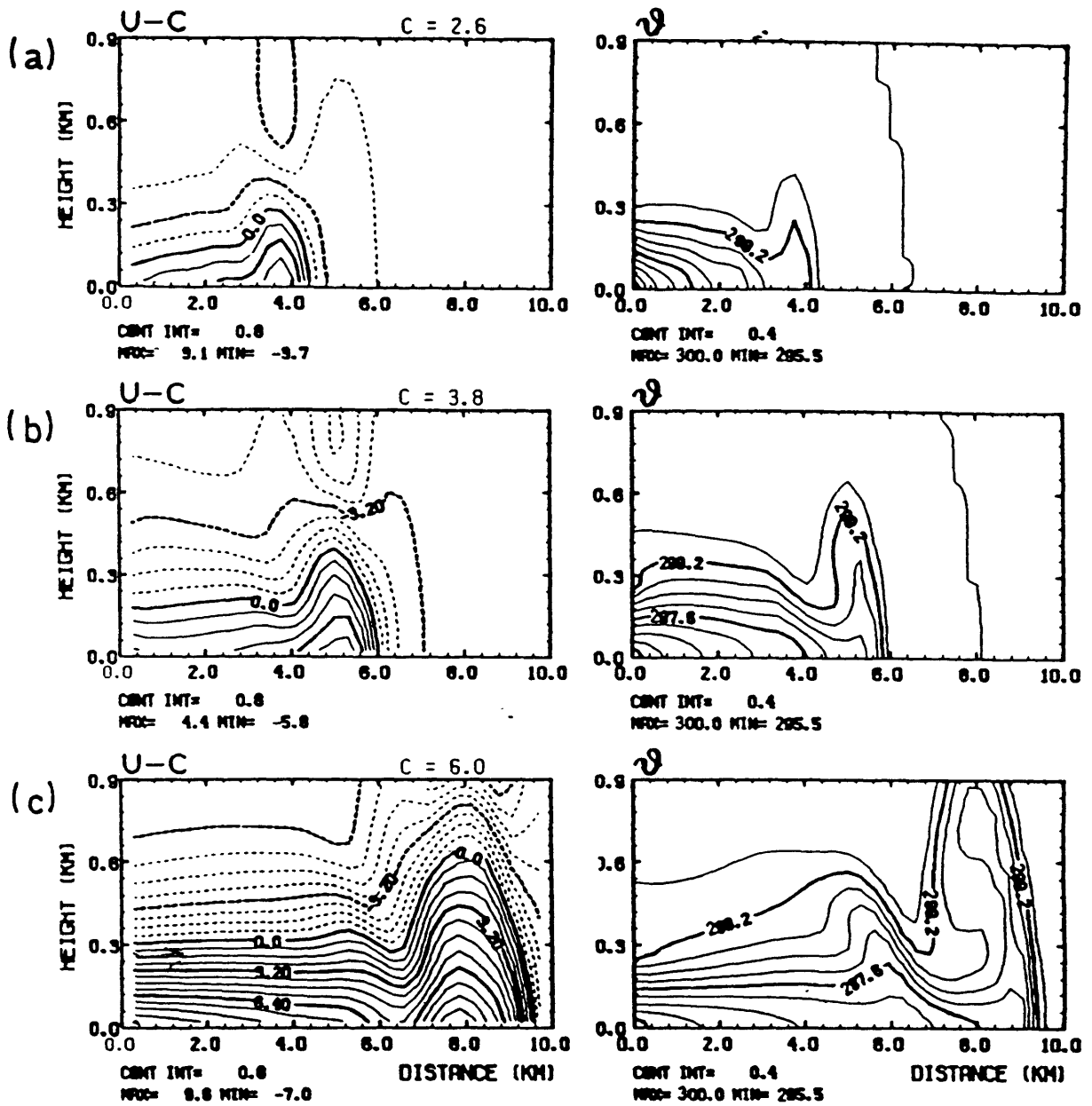


Fig. IV-28. Isotachs of $(u-c)$ in m/s (left) and isentropes in K (right) for different mean inflow speeds, and thus different inflow Froude numbers. In each case the depth and temperature of the inflow air were held constant. (a) $Fi = 0.28$, (b) $Fi = 0.56$, (c) $Fi = 1.13$. Taken from Haase and Smith (1989a).

In each experiment, the horizontal and vertical grid resolution was 75 m, the time step 0.5 s, the domain 300 grid points wide by 100 high, and the eddy diffusion coefficient 40 m²/s. The choice for this latter parameter was based on the results of Howells et al. (1988). The environmental lapse rate was dry adiabatic (300 K) up to 5 km agl, and stable above (4 K/km). The cooling source was Gaussian in shape, with a radius of 1.5 km, and a depth of 4 km, centered 3.75 km above the surface. In each experiment, the cooling was gradually increased within one minute to the constant value of -0.075 °C/s, and was held constant for a length of time (4, 10, 16, and 36 minutes in each of the four experiments, respectively). It was then turned off, again within 1 min and kept off for the duration of the simulation. The nominal dependence of the cooling function on time is shown in Fig. IV-29.

In each of the experiments, shown in Figs. IV-30 and IV-31, the leading vortex ring, characteristic of axisymmetric dense flows, does form. The downflow behind the leading vortex brings relatively warm air near the surface in a narrow region, creating a second region of large surface temperature gradient behind the outflow head. This could be considered a second front, but it is not the phenomenon of consecutive interior front development. Not until minutes 16-17 does anything that could be interpreted as the development of a second front occur, and it takes the form of a splitting of the leading vortex. This is caused by vorticity of the opposite sense, created in

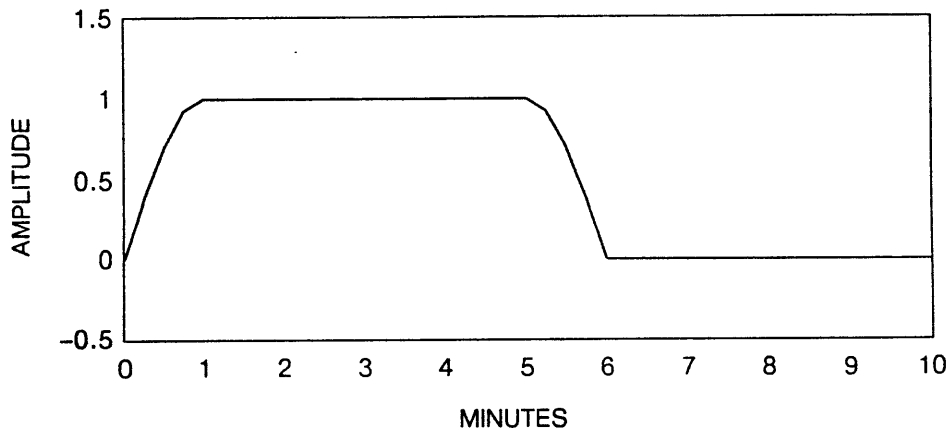


Fig. IV-29. The nominal dependence of the cooling functions on time for constant cooling rate experiments. The base cooling rate in each was -0.075 °C/s. The function shown has 4 min of constant cooling, from minute 1 to 5. This interval of constant cooling was lengthened to 10 min, 16 min, and 36 min in the other three experiments. The experiments each continued for at least 14 min after the cooling was turned off.

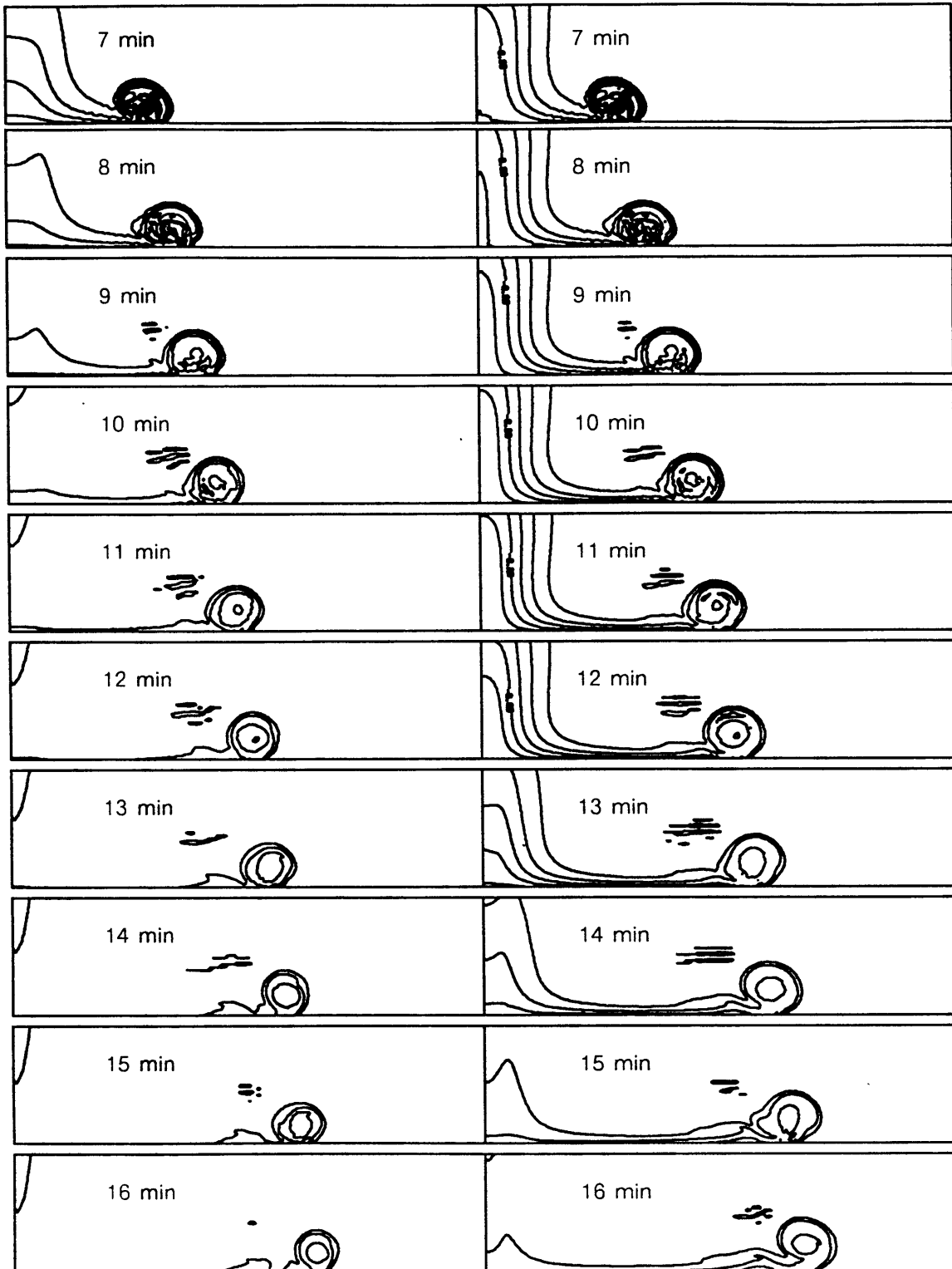


Fig. IV-30. Constant cooling experiment. The flow is shown every minute from 7 min to 16 min into the simulations. The cooling in the simulation at left ended at 6 min; at right, cooling ended at 12 min. Potential temperature is contoured every 2°C ; uppermost continuous contour shown is -2°C . Domain shown is 12 km wide and 3 km high.

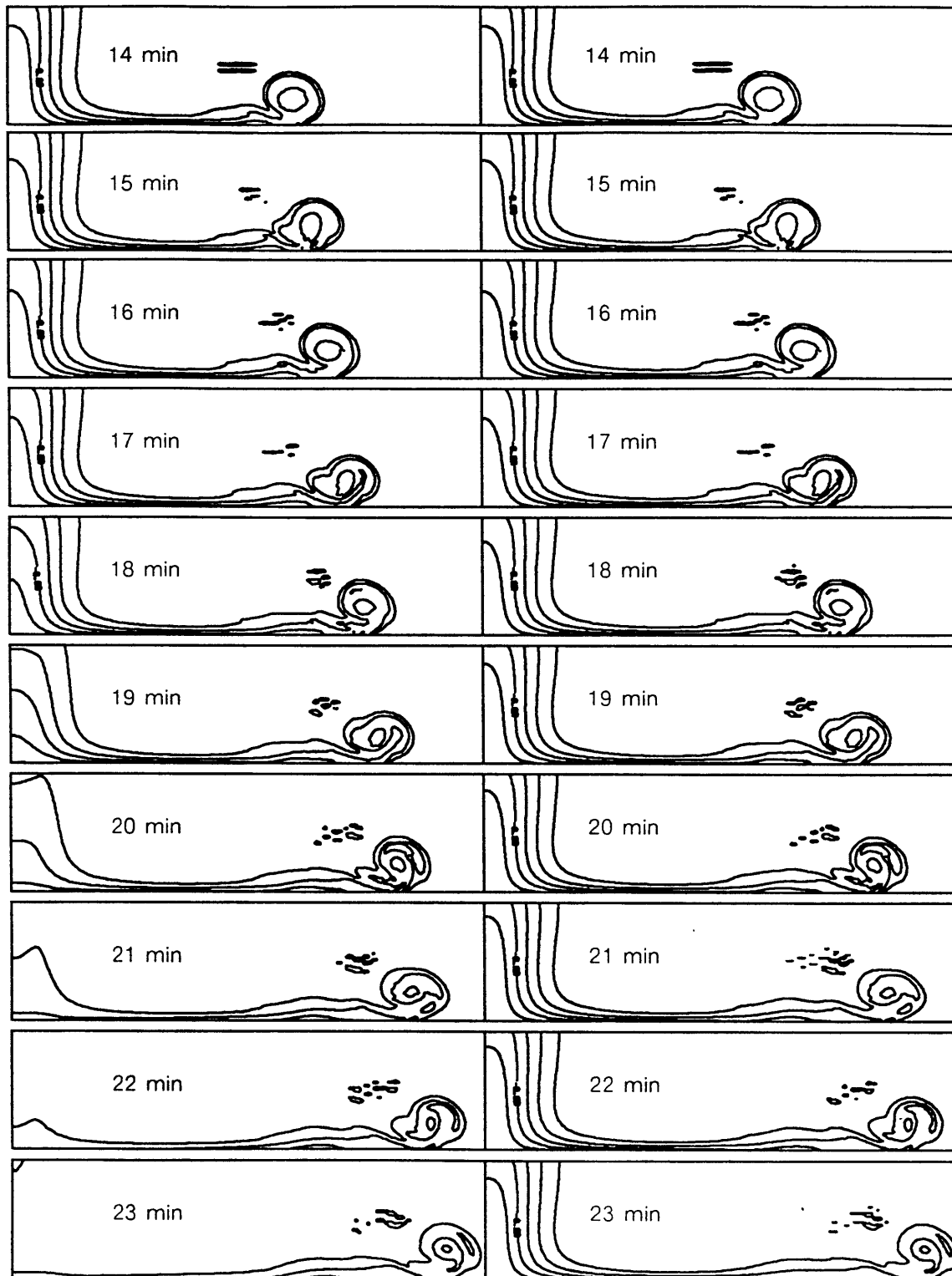


Fig. IV-31. Constant cooling experiment. The flow is shown every minute from 14 min to 23 min into the simulations. The cooling in the simulation at left ended at 18 min; at right, cooling remained constant during depicted times. Potential temperature is contoured every 2°C ; uppermost continuous contour shown is -2°C . Domain shown is 12 km wide and 3 km high.

the frictional boundary layer, traveling up and around the primary leading vortex (e.g., Proctor 1988b, Fig. 10). If closed streamlines develop, this is called a secondary vortex (Fig. IV-8). The frictional generation of this counter vorticity is related to maintenance of the overhanging nose of the gravity current. This break up of the leading front occurs in the 10 min, 16 min, and constant forcing (36 min) experiments, proving that it is independent of the closing off of the cooling. These results strongly suggest that Linden and Simpson's (1985) hypothesis for the three embedded vortices in the DFW outflow is incorrect. However, the axisymmetric model does not allow the incorporation of wind or wind shear in the environment, and these may be important factors in multiple front development. Also, although these numerical simulations are appropriate for simulating the DFW thunderstorm outflow (with a neutral boundary layer), a full set of numerical experiments in which a wide range of inflow Froude numbers is tested should be performed. The possibility that pulsation of the source (downdraft) strength creates these consecutive interior fronts is investigated in Chapter V.

E. Kelvin-Helmholtz Instability in the Outflow

Kelvin-Helmholtz billows have been suggested as the identity of the vortices embedded in the DFW outflow by Linden and Simpson (1985), based on a laboratory model and by Droegemeier and Babcock (1989), based on a slab symmetric numerical experiment with anisotropic subgrid scale damping. In the preceding section, numerical simulations appropriate for the atmosphere analogous to the laboratory models were used to show that Linden and Simpson's hypothesis is implausible. Here, the conclusions of Droegemeier and Babcock are investigated more fully.

Kelvin-Helmholtz instability (KHI) arises from small perturbations in a stably stratified fluid with a vertical wind shear maximum strong enough for the Richardson number (Ri), defined as:

$$Ri(\Delta Z) = \frac{g}{\bar{\Theta}} \left(\frac{\Delta \Theta}{\Delta Z} \right) / \left(\frac{\Delta V}{\Delta Z} \right)^2$$

where ΔV is the magnitude of the vector wind shear over a layer depth ΔZ and $\bar{\Theta}$ is the mean potential temperature, to fall below the critical value of 0.25 in a layer. Figure IV-32 illustrates the growth of billows in an unstable flow.

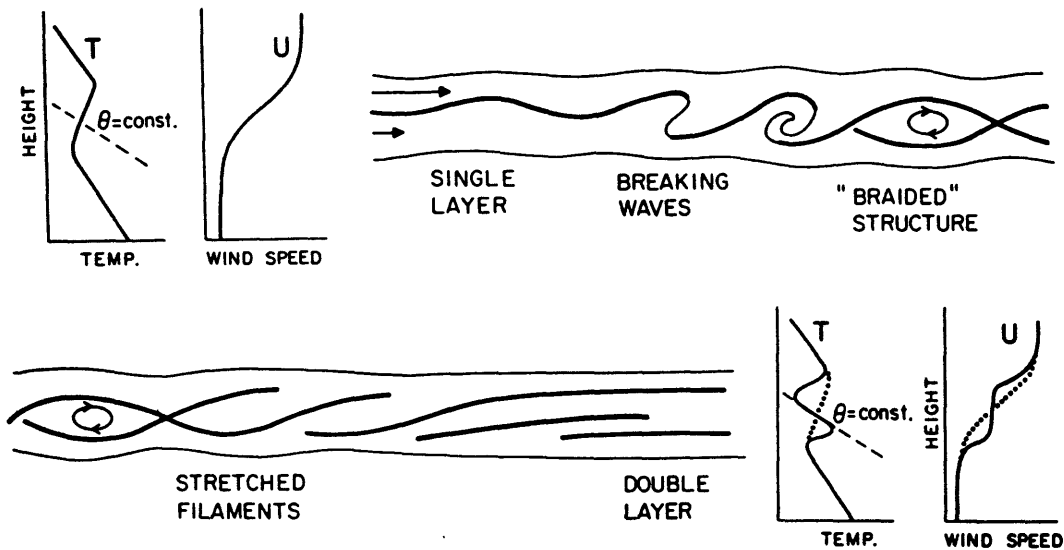


Fig. IV-32. Illustration of the stages in the development of an individual Kelvin-Helmholtz billow, a wave pattern sometimes leading to cloud formation at the wave crests. Thick lines correspond to the detectable clear air radar echo, which starts as a single layer (upper half of figure) and finishes as a double layer (lower half of figure). Schematic vertical profiles of temperature and wind speed are indicated before and after occurrence of Kelvin-Helmholtz instability. Taken from Hardy (1972).

1) KHI in Atmospheric Boundary Layer

KHI has been shown, in past observational research studies, to be responsible for waves and turbulence in the atmospheric boundary layer. Gossard et al. (1970) first used a high resolution FM-CW radar to produce remarkably detailed pictures of KH billow structure at 200 – 400 m agl. Proximity balloon soundings showed that the Ri criterion for instability was met in the layer in which wave breaking was occurring. Emmanuel (1973) used an acoustic sounder to reveal KHI in the lowest 150 m of the boundary layer, and compared these data with those from a nearby meteorological tower. Ri within the wave-like layers was between 0.02 and 0.25, and there was evidence for KHI occurring on many scales and contributing to a diffuse and broad shape to the base of the large billows. The observed horizontal wavelengths were also in agreement with those predicted by theory. Blumen (1984) showed the development, and breakdown into turbulence, of KHI atop two different nighttime drainage wind events in the Boulder Valley of Colorado, using the same acoustic sounder and tower data sources used by Emmanuel. Simpson et al. (1977) show

evidence of “bubbly” wave-like flow, presumably corresponding to KHI, in aircraft data collected through and behind the head of a sea breeze front in England. Young and Johnson (1984) have documented “micro- α -scale” vertical eddy structure, probably a manifestation of KHI, in the frontal zone of a cold front in Colorado using tower data.

The influence of a lower boundary on the classical theory of KHI was investigated by Lalas et al. (1976) and by Lindzen and Rosenthal (1976), and the complete stability problem of a stratified parallel shear flow in a boundary layer setting was analyzed by Davis and Peltier (1976). They showed, through linear stability analysis, that the presence of a lower boundary destabilized the flow, and that disturbances with the character of internal gravity waves were possible, but that the KH disturbances grew faster. The recent work by Smyth and Peltier (1989) suggests that the relationship between shear flow instability and linear wave overreflection is not completely clear, and that more research is needed. In thunderstorm outflow and other thin boundary layer applications, however, the inclusion of nonlinearity in the stability analysis is essential to describing the observed dynamical phenomena.

2) Presence of KHI in Surface Gravity Currents

The presence of closed “rotor” circulations within strong, cold thunderstorm outflows, and the presence of the stably stratified shear zone at the top of the outflow layer has led a number of investigators to hypothesize that these closed rotors are unstable KH billows. The dynamic similarity between thunderstorm outflows and gravity currents, presumably established by Charba (1974), and the clear identification of KH billows in laboratory flows (e.g., Simpson 1969), have also fueled this hypothesis. Certainly the conditions for KHI can be met, and KHI can be occurring on some scales, while simultaneously nonlinear gravity waves with large closed circulations are also present. However, the interpretation of the closed vortices or rotors as finite amplitude gravity waves appears to have received little attention in the literature.

(i) *Numerical simulations*

Droegemeier and Wilhelmson (1987) chose to numerically simulate thunderstorm “outflows with very high spatial resolution in an attempt to explicitly depict the details of outflow morphology”. They state that their model resolution was chosen to be high enough to resolve, rather than parameterize, the physically important mixing processes such as KHI. Their control simulation designed to illustrate the basic features of outflow turbulence began with a 2 km high column of

cold air with a temperature deficit of 6 K, at the edge of a slab-symmetric grid with 100 m spacing. This control simulation, shown in Fig. IV-33, remarkably resembles the laboratory flows with KH billows shown by Simpson. Several billows in different stages of development can be seen.

However, in order to get this billow development, the vertical subgrid scale mixing coefficient had to be made 10 times smaller than the horizontal coefficient. This is extremely unrealistic, and a somewhat unusual choice for a "control" case. This type of scheme has also recently been criticized by Haase and Smith (1989a). Droegemeier and Wilhelmson themselves freely admit that the scheme is dynamically inconsistent. The relevance of the control simulation illustrating the well-developed KH billows is further called into question by the more realistic "variable mixing" simulations, with *equal* horizontal and vertical mixing coefficients, shown in the two lower panels of Fig. IV-33. Neither of these simulations show the large well-defined closed rotors of the control simulation. These more realistic cases each have a broadened shear layer along the top of the outflow which is the result of subgrid scale mixing, and a turbulent region at the back of the gust front head, clearly the vestige of the KH billows that develop when vertical mixing is suppressed. But it is probably incorrect to call this diffuse, turbulent region a single "billow".

At the time this numerical modelling study was performed, Droegemeier and Wilhelmson (1986) stated that "to date, no outflow modelling studies (e.g., Mitchell and Hovermale 1977; Seitter 1983) have produced turbulent eddies similar to those found in the laboratory experiments." Given the discussion in the previous paragraph and the evidence in Fig. IV-33, it may be fair to claim that, still, no outflow modelling studies have realistically simulated these eddies. The Reynolds numbers of laboratory flows are five to eight orders of magnitude smaller than those relevant for thunderstorm outflows in the atmosphere, so that it is not immediately clear that similar billow formations should even be expected. Thomas and Simpson (1985) showed that by artificially increasing the turbulence or "dynamic roughness" in their laboratory flows with an oscillating grid, they could attain more realistic bulk Reynolds numbers for comparison with atmospheric flows. In an experiment they performed appropriate for simulating a turbulent shear flow, KH waves could be identified only at the very nose of the current, and a disorganized region of turbulent eddies was all that could be identified behind. Linden and Simpson (1986) point out that in the absence of turbulence, the internal gravity current circulation maintains a large horizontal buoyancy gradient at the leading edge, which keeps the buoyancy forces and thus the vertical wind shear large, and enhances the KHI. Any turbulence that tends to weaken the vertical

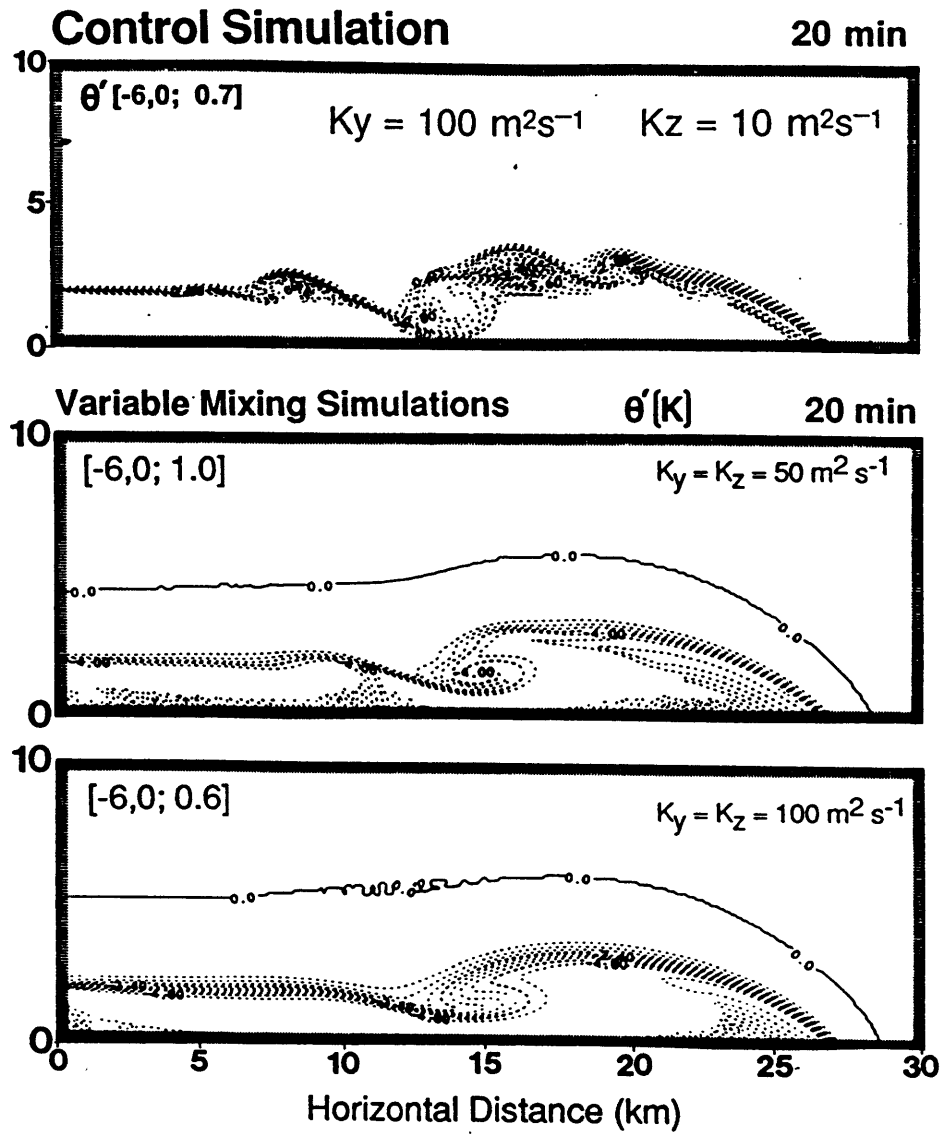


Fig. IV-33. Contour plots of perturbation potential temperature from the control simulation (top) and two variable mixing simulations (bottom two panels) at 20 min into each simulation. The vertical depth of the domain is 10 km, the width, 30 km. The contoured values range from -6 to 0 K in each plot, but the contour interval in the top plot is 0.7 K, middle 1.0 K, and bottom 0.6 K. The numerical damping coefficients specified in the horizontal (K_y) and vertical (K_z) are labelled in each plot. Adapted from Droegemeier and Wilhelmson (1987).

stratification behind the head weakens the gravity current flow, because the density of the current arriving at the front is continuously reduced.

(ii) *Observations and interpretations*

Hall et al. (1976) suggested that the wind shear associated with the turbulent billows within a density current originating from a line of storms more than 20 km away, posed a hazard for aircraft at low altitude. Their vertically pointing acoustic sounder data provided a very detailed picture of the multi-layer wave structure within the gravity current as it passed overhead. The wave characteristics were consistent with KHI, but did not appear to involve deep closed circulations within the cold outflow. Davis and Peltier (1976) suggest that the resonant internal gravity wave modes they found in their investigation of the stability of parallel shear flow may provide an explanation for these multiple thin scattering layers, observed also by Gossard et al. (1970) and Metcalf (1975). Einaudi and Finnigan (1981) studied a shear-generated internal gravity wave in the planetary boundary layer, the acoustic sounding of which showed strong reflections from an inversion between 500 and 700 m agl. They suggest the overall wave structure was typical of a KH wave with a critical level at 1.1 km agl.

At the time the Droegemeier and Wilhelmson (1986; 1987) modelling study was performed, the evolution of KH billows had not yet been observed in actual thunderstorm outflows. Their numerical study is now referenced as primary evidence that KHI does occur as closed, sustained vortices in outflows. Perhaps the first observational analysis to effectively document KH billows atop a thunderstorm outflow was performed by Mueller and Carbone (1987). They showed that KHI developed along the top of the cold outflow near the surface front, propagated rearward, and dissipated in the wake of the head region. Some of their vertical cross-sections through the quasi-two dimensional gust front do indeed show closed vortices with wavelengths and amplitudes matching well those predicted by KHI theory.

However, there is an alternative interpretation for the time sequence of their “KH billow b” shown in Fig. IV-34. The environment ahead of the advancing gravity current was characterized by a neutrally stable layer 1.2 km deep, topped by a second such layer approximately 4 degrees warmer (potential temperature), from 1.2 to 3.3 km agl, and a third layer, 2 degrees warmer still, from 3.3 to 5.0 km agl. Based on radar data, the authors found that the depth of the cold outflow was 1.2 km, just equal to the height of the first inversion. They mention that this inversion “appeared to act as a duct for the cold outflow”, but they did not suggest how this might impact the

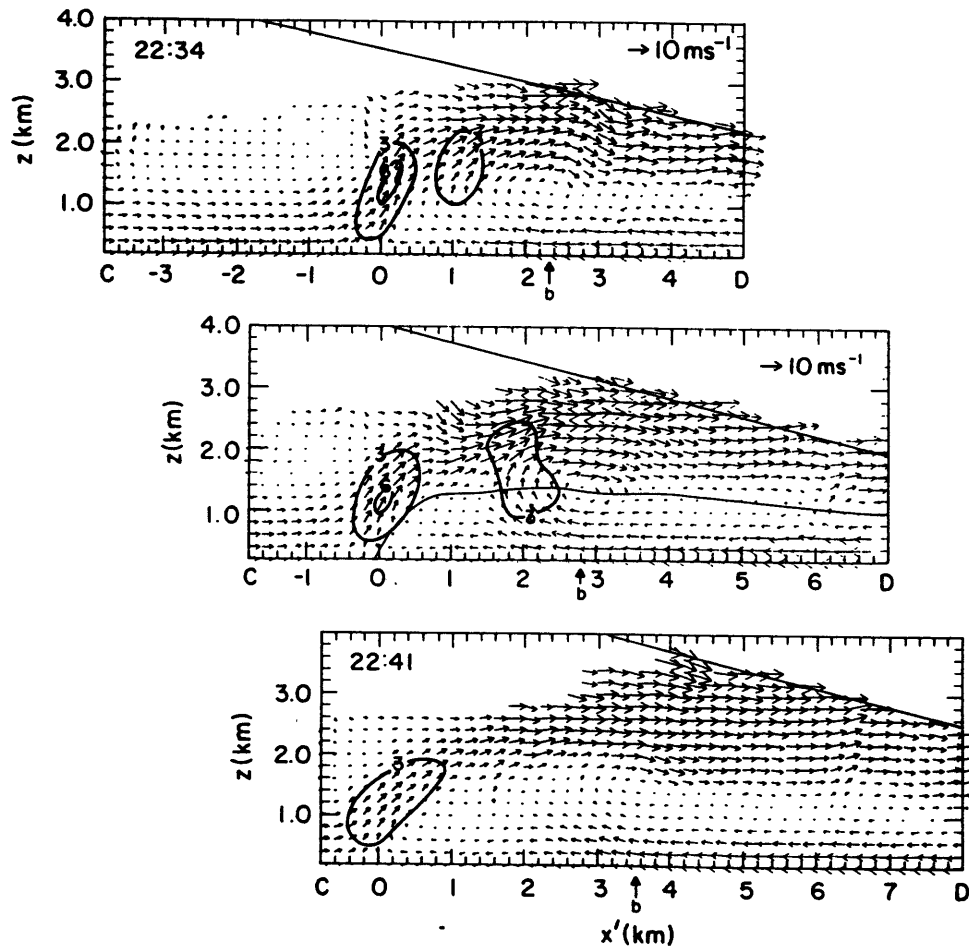


Fig. IV-34. Vertical sections at 2234, 2239, and 2241 through the KHI billow *b*. The cross sections show storm relative wind vectors and vertical velocity in 3 m/s intervals. The thick solid line indicates the top of the scan volume. The sections are aligned relative to the leading edge of the outflow. Taken from Mueller and Carbone (1987).

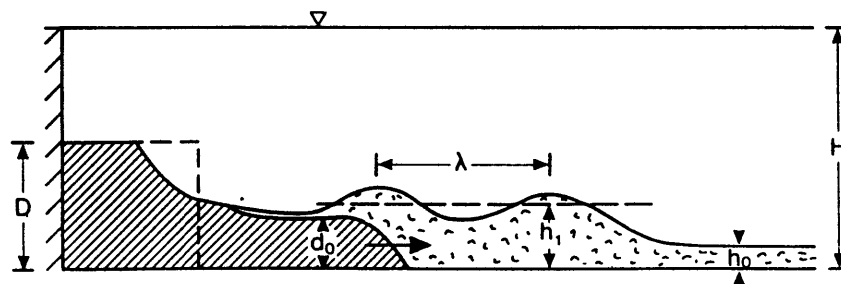


Fig. IV-35. Experimental generation of an internal bore by an advancing gravity current. Taken from Simpson (1987).

flow evolution. They did note that the inversion at 3.3 km acted as a cap for the KH billows; Droegemeier and Wilhelmson (1986) showed that the suppression of KH billow amplitude by a capping stable layer can be considerable. Given the environmental conditions, it becomes debatable whether a vortex occupying the full depth of the gravity current (billow **b** in Fig. IV-34) could be a KH billow, despite the apparent agreement with the most unstable wavelength predicted by linear theory.

Figure IV-35 shows schematically how an advancing gravity current can generate an internal bore. When the gravity current depth is greater than the dense layer ahead, a smooth hump forms which envelops the head of the gravity current. This hump moves forward along the interface, leaving most of the dense fluid of the gravity current behind. A new gravity current head forms, a new hump forms above it, and the process is repeated (Simpson 1987). As each nonlinear wave moves ahead of the current, it may trap some of the cold outflow within its recirculating flow. One way to differentiate between an advancing bore and an advancing gravity current is by examining the relative flow in a reference frame moving with the leading edge; in a gravity current there will be strong flow toward the leading edge near the surface and strong return flow aloft, while in an undular bore there will be *no* flow toward the leading edge. There may be a very weak flow in an undular bore generated by a gravity current if some of the colder fluid remains trapped near the surface in the wave.

Notice in Fig. IV-34 there is strong relative flow toward the leading edge of the gravity current until a point roughly 1 km ahead of billow **b**; from there up to the leading edge of the gravity current (marked as the origin), there is very little forward flow. The circulation thought to be billow **b** may actually be the leading edge of the gravity current, and what is thought to be the leading edge of the gravity current may actually be a bore propagating out ahead. Fulton et al. (1986) effectively used mesonet data to show how the pressure jump, wind shift, and wind gust characteristic of the leading edge of a gust front were actually indicative of an undular bore that was at first coincident with, but later moved out ahead of, the cold airflow of the density current itself. Mesonet data was available for the Mueller and Carbone case, but it was presented at only one time for their large network, and only as an average over all of the stations for their smaller network. Even in averaged form, the pressure trace showed a number of wavelike oscillations behind and within the analyzed frontal region. Examination of the large network dataset may shed light on this alternative interpretation for at least one of the vortices in this case.

Mahoney (1988) suggested that KHI may be responsible for the downdraft 2–3 km behind the leading edge of a Colorado gust front observed with Doppler radars (Fig. IV–36). He cites the Mueller and Carbone (1987) study as evidence that KHI occurs on this scale, and the Droegemeier and Wilhelmson (1987) study, with the anisotropic mixing coefficients, as evidence that downdraft magnitudes associated with KHI could exceed 12 m/s and easily reach the surface. The preceding discussion casts doubt on the identification of this feature with KHI. However, the point Mahoney is making, that the narrow, powerful downdraft portion of this “vortex” could produce a strong, small scale surface divergent signature that qualifies as a microburst, is compatible with the hypothesis put forth in this work. Not enough information is given by Mahoney to determine the stability characteristics of the environment into which the quasi–two dimensional gust front was propagating, or to rule out the possibility that a separate low reflectivity downdraft descended well behind the gust front (and center of rotation X_1) and caused the circular patch of divergence. Kessinger et al. (1988) discuss at least four large horizontal vortex circulations observed at different times within the outflow of one main cell, and suggest that they may be due to KHI on the interface between the outflow edge and the ambient air. In their case, however, the vortices were clearly embedded in a thin layer of cold outflow so an alternative explanation in terms of finite amplitude gravity waves is more likely correct (Chapter V).

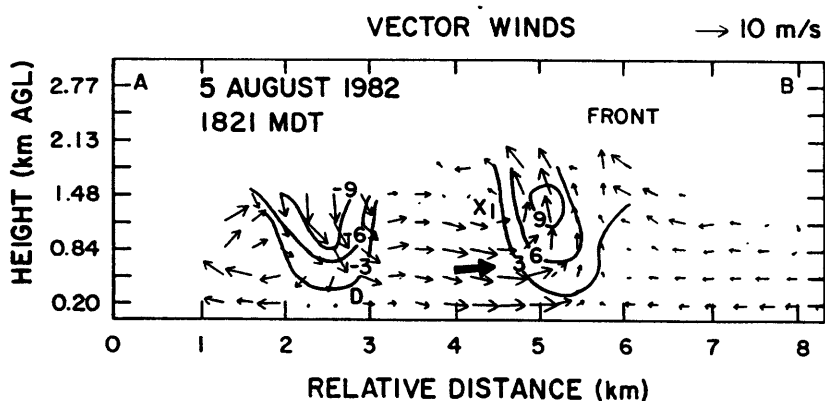


Fig. IV–36. Vertical cross section of vector winds through a gust front on 5 August 1982 near Denver, Colorado. The vertical resolution is 0.3 km, and vertical velocities are contoured each 3 m/s. “ X_1 ” marks the center of rotation and “D” is the center of surface divergence under the downdraft portion of the circulation. Taken from Mahoney (1988).

Linden and Simpson (1985) identified the large leading and secondary vortices that developed in their axisymmetric tank experiments as finite amplitude KH billows. It has already been shown in preceding sections that these vortices are actually the result of the coalescence of nonlinear internal gravity waves, and the formation of interior "fronts". They are not individual finite amplitude KH billows, although KHI is present and contributing to vigorous mixing at the top and rear of the vortices.

On a quite different scale, Kelvin-Helmholtz billows have been suggested as the identity of the amplifying oscillations observed in the wind data from a 440 m tall tower in Oklahoma. Doviak and Chen (1988) found the amplitude of these waves was largest in the high shear zone created at the surface (7 m agl) during the passage of a large internal gravity wave propagating in a layer of stable air created by earlier storms, and decreased upward until it was hardly detectable at the top of the tower (Fig. IV-37). The amplitude of the waves was between 300 and 400 m, and the wavelength between 1.0 and 1.5 km, giving a KH billow amplitude to wavelength ratio between 0.2 and 0.4. This value is comparable to the values confirmed for other atmospheric KH billows. These KH waves grew in the intensified surface boundary layer shear zone created by the passage of a finite amplitude gravity wave in which cold thunderstorm outflow air was trapped. They were not embedded in the shear layer atop the wave. Whether or not the KH waves were more pronounced than they otherwise would have been because of the preexisting layer of stable outflow air (which provided the waveguide) was not discussed.

Rottman and Simpson (1989) have recently reinterpreted five previously published case studies of thunderstorm gust fronts and sea breeze fronts with large embedded "vortices" according to an idealized model of internal bore formation in the atmosphere, based on their laboratory investigations. At least one of these cases was previously attributed to KHI. It is clear that there is a need for more research into the correct interpretation of various observed vortices, secondary surges, and "rotors" in many previously published outflow case studies. Some of these cases are examined in the following chapter.

F. Horizontal Shear Instabilities

Horizontal wave inflections along the leading edge of an outflow, such as those found by Carbone (1982; Fig. IV-38) and Mueller and Carbone (1987), are created by the strong horizontal shearing forces there. At least two of these inflections developed into closed vertical vortices as they dissipated in Mueller and Carbone's case. They found the convergence at the leading edge of

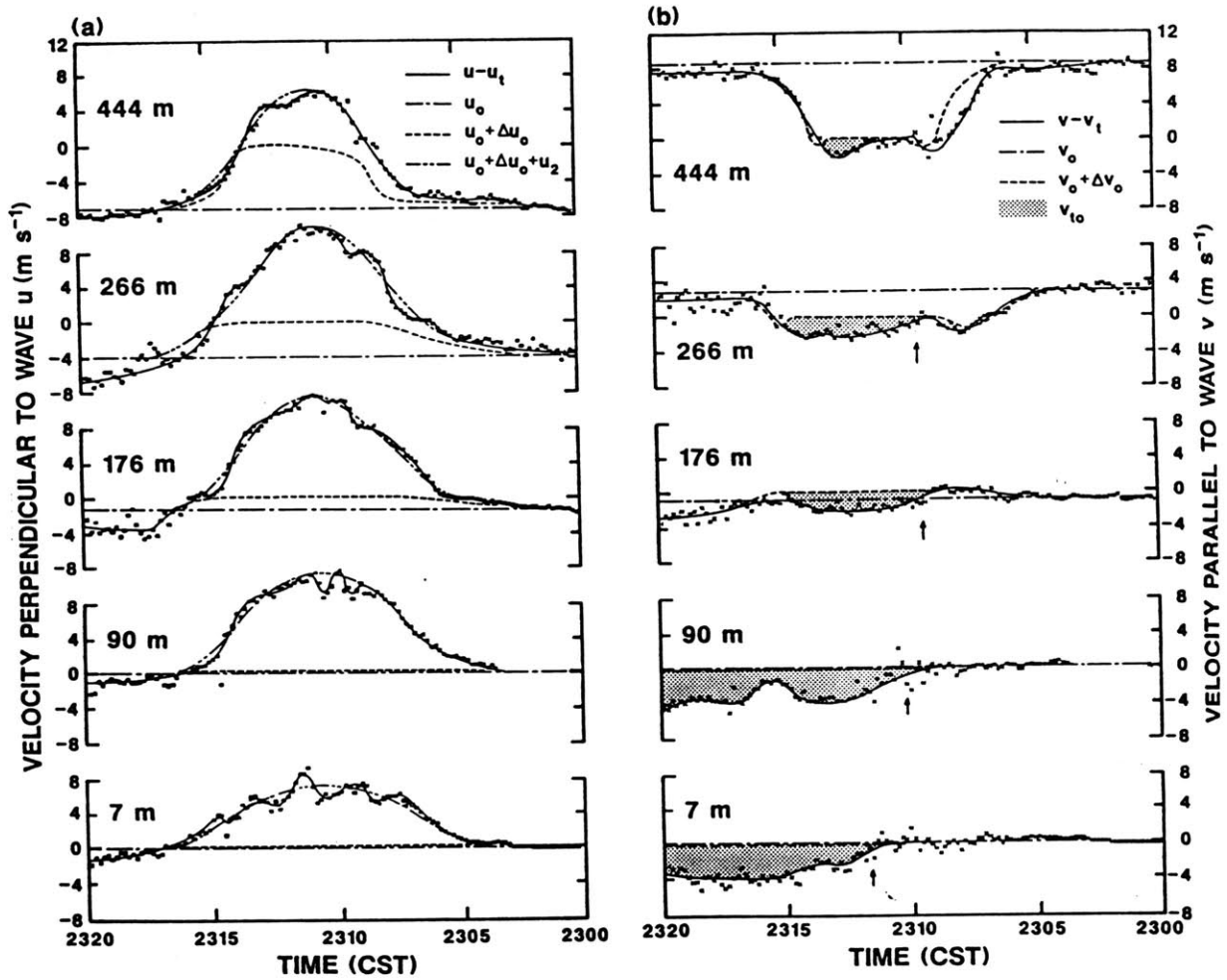


Fig. IV-37. Dots are observations of velocity components (a) perpendicular, and (b) parallel to the solitary wave front, as observed at 5 tower levels. Refer to Doviak and Chen (1988) for explanation of the various curves. The large "hump" in the perpendicular flow is the solitary wave, and it is hypothesized that the smaller sinusoidal variations are manifestations of KHI. Taken from Doviak and Chen (1988).

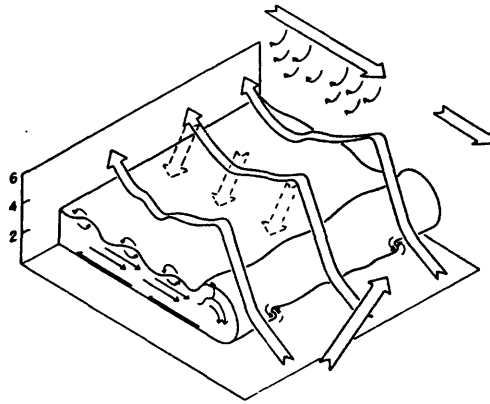


Fig. IV-38. Schematic representation of storm kinematic structure. Taken from Carbone (1982).

the gust front was stronger in this region than it was elsewhere, as was the updraft. A small downdraft 200–400 m in diameter developed along the axis of maximum vertical vorticity and split the updraft into two centers on either side of the downdraft. In the mature stage of the vortex, the downdraft speed reached 7 m/s, the diameter expanded to 500 m, and it extended vertically from 1.0 to 2.2 km agl. The axis of maximum vertical vorticity shifted to the region between the downdraft and the updraft cores (Fig. IV-39), suggesting that the forcing for this vorticity may have come from the downdraft spreading at the surface.

This small downdraft has been called an “occlusion downdraft” by Klemp and Rotunno (1983), who performed a numerical simulation of a tornado parent vortex region. Carbone (1983) found a striking similarity between those numerical simulations and his observations of the vortex circulation at the leading edge of the frontal rainband shown schematically in Fig. IV-38. Wolfson (1983) suggested a hypothesis for the microburst winds observed in the 13 April 1981 Oklahoma case [also studied by DiStefano (1983)] that involved this same type of occlusion downdraft developing in a region of horizontal shear and vertical vorticity generation at the leading edge of a strong squall line outflow. A schematic illustration of the proposed circulation and small scale downdraft is shown in Fig. IV-40. This type of downdraft may indeed have been present, but it cannot account entirely for the damaging outflow winds observed in that case. The vorticity generated by horizontal shear instability at outflow fronts may become strong enough to spawn non-supercell tornadoes (Wakimoto and Wilson 1989).

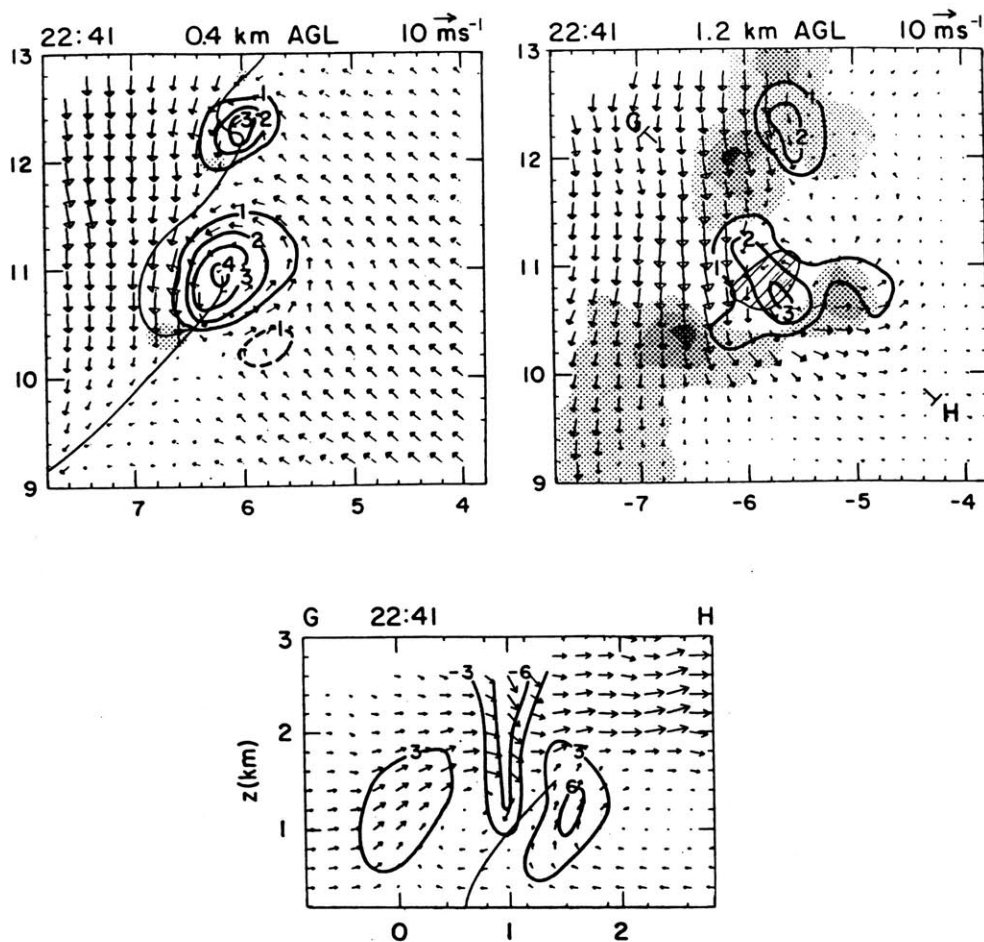


Fig. IV-39. (Top) The 0.4 and 1.2 km agl storm relative flow (plan view) in the region of the northern most closed vortex is shown at 2241. The shaded areas indicate updrafts > 3 m/s with darker areas indicating cores ≥ 6 m/s. The downdraft, ≥ 3 m/s, is hatched. Contours of vertical vorticity an intervals of 10.0 m/s per km are shown in black. At 0.4 km a subjective gust front line is indicated. The location of the vertical cross section shown below is indicated with the letters G,H at 1.2 km. (Bottom) Cross section through the vortex, indicated above by G,H. Contours of vertical velocity with intervals of 3 m/s are shown. The axis of maximum vertical vorticity is marked with a black solid line. Labelled ticks on the horizontal axis are 1 km apart. Taken from Mueller and Carbone (1987).

While I do not suggest calling these small scale features “microbursts”, they may well account for many of the “twisting microburst” ground damage patterns described by Fujita (1985). In fact, it was during an aerial survey of tornado damage that Fujita first found the very small (< 1 km) “starburst” patterns of fallen trees, located inside and outside the tornado damage paths, suggesting to him the then controversial concept of a “strong downdraft which induces an outburst of damaging winds on or near the ground”, i.e., the downburst. The small scale occlusion downdraft within a tornado parent vortex, dynamically driven by strong rotation at low levels, may be

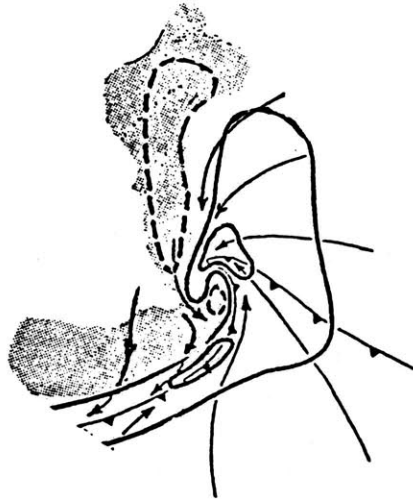


Fig. IV-40. Proposed circulation inducing a microburst at the leading edge of a squall line outflow, adapted from Klemp and Rotunno (1983). Dashed contours indicate downdrafts, solid contours indicate updrafts. The stippled area represents reflectivity greater than 30 dBZ. The small scale downdraft in the "spearhead" shaped reflectivity region is the microburst. Streamlines indicate storm relative flow. In this scenario, it is the mesoscale circulation which distorts the radar echo and induces the microburst, not vice versa. Taken from Wolfson (1983).

the cause of these starburst and straight line wind damage patterns. This type of downdraft does not appear to be related to the first publicized downburst leading to the aircraft crash at JFK 1975, or to the other thunderstorm downdrafts and horizontal vortices called microbursts.

G. Summary

Low altitude downdrafts associated with horizontal vortices in thunderstorm outflows and with vertical vortices at the leading edge of some outflows have been identified in some cases as microbursts or part of microbursts. Interest in horizontal vortices as part of the low altitude wind shear problem was heightened when analyses of the storm in which Delta 191 crashed at Dallas/Ft. Worth airport in 1985 showed three vortices embedded in the outflow. A number of hypotheses were put forth to explain them.

One hypothesis involved the formation of multiple discrete vortex rings around the descending downdraft before it reaches the ground and begins spreading into outflow. It was shown that while a single vortex can form at the leading edge of some virga downdrafts descending from high based cumulus clouds through deep neutral layers, no vortices form in the heavy rain thunderstorm downdrafts typical of the DFW case. In the virga cases, the air temperature inside the vortex

is often very close to that in the ambient environment, so the vortices quickly decay after reaching the ground.

Another hypothesis for the horizontal vortices involved a conservation of angular momentum argument for spin up of a constant volume vortex tube as the circular outflow expanded. The phenomenon of the build up of a leading edge vortex in axisymmetric dense outflows was explained, and it was shown that this vortex tube stretching argument is incorrect. The vortex volume steadily increases with time as the dense fluid accumulates there. It was shown that the characteristic ring formation “requires reflection of downstream propagating internal waves off the leading front to form upstream propagating waves whose absolute wave speeds ($u - c$) increase with radial distance, because of continued plume spreading. This radial gradient in wave speed results in wave coalescence with subsequent ring and interior bore formation” (Garvine 1984). The strongest surface winds in an evolving circular thunderstorm outflow will be associated with this leading ring. Since the ring is also fairly narrow, the wind shear at low altitudes can become very large. This build up of a leading vortex ring does not occur at the leading edge of two dimensional outflows, so slab symmetric gust fronts will contain weaker circulations, and thus weaker embedded downdrafts at low altitudes and less divergent horizontal wind shear than their equivalent circular counterparts. However, the leading updrafts will be just as strong.

The possibility of multiple interior vortex ring formation was also investigated. The formation mechanism is essentially the same as for the leading ring. Mixing and turbulence erode the flow behind the leading ring to the point where separation occurs, and a new “leading” ring can form. This process presumably can repeat itself if the outflow remains continuous. An axisymmetric numerical simulation appropriate for modelling the DFW outflow in a neutral boundary layer showed a periodic breakdown of the leading vortex ring, after about 15 simulated minutes, that could possibly be interpreted as multiple front development. However, no multiple fronts remained, and the ring breakdown occurred far too late in the simulation to be comparable to the embedded DFW vortices.

Another hypothesis for the vortices found within the DFW outflow held that they were finite amplitude Kelvin–Helmholtz (KH) billows, created as the outflow became unstable to this shear instability. The evidence for KH billows in thunderstorm outflows was reviewed. It was concluded that the key numerical simulations upon which a number of observational papers have relied for evidence that the large, persistent vortices in outflows are KH billows, were unrealistic and mis-

leading. The simulations were performed with a model that was dynamically inconsistent because anisotropic diffusion coefficients were used. Many of the observed vortices, roughly equal in depth to the outflows in which they form, have alternative interpretations in terms of finite amplitude gravity waves. As Smith and Reeder (1988) note, “there does not seem to be a widespread awareness of this possibility.” This is explored in the following chapter.

The remaining hypothesis for the DFW vortices suggested that three concentric downdrafts were occurring simultaneously, and that the vortices observed were the leading vortices of each separate, but embedded outflow (Fujita 1986). Since each new dense outflow spreads into old, the stratification of the boundary layer must be taken into consideration. This hypothesis is examined in the following chapter.

Almost every kind of low altitude downdraft described in this chapter has been given the name “microburst” in one publication or another, including the occlusion downdrafts associated with the *vertical* vortices that can develop from dissipating horizontal shear instabilities at the leading edge of an outflow. A number of misconceptions about horizontal vortices in thunderstorm outflows have persisted, and these have been detrimental to understanding and predicting the situations in which the truly hazardous conditions to low altitude aviation operations can be expected to exist. In this chapter, the various flow patterns that can be expected to form in dense thunderstorm air spreading in neutrally stable boundary layer have been explained. A key difference between the hazard posed by slab symmetric and axisymmetric gust fronts was also noted.

V. LOW ALTITUDE DOWNDRAFTS IN THUNDERSTORM OUTFLOWS: STRATIFIED BOUNDARY LAYER

When the environment into which a dense outflow is propagating is stably stratified, the possibility of gravity wave initiation and undular bore formation arises. In the atmosphere, the stratified surface layer providing the gravity wave duct could be a thin layer of cold thunderstorm outflow air or a shallow nocturnal inversion, so disturbances of even limited energy can create nonlinear waves. As these nonlinear waves increase in amplitude, they can form an internal closed “vortex” circulation. It is my hypothesis that these unusually stable propagating “solitary” vortices, which tend to narrow and sharpen as they increase in amplitude, are the identity of some of the very short lived, very high speed surface wind “spikes” and powerful low altitude downdrafts called microbursts. This is an unexplored mechanism for realizing larger surface wind speeds and greater elevated wind shear hazards than could otherwise be expected, especially at large distances from the downdraft.

It is also my hypothesis that the stable layer will influence the newly forming outflow. As the thunderstorm downdraft is approaching the ground, it encounters first the increased stratification of the boundary layer, where it begins to decelerate. Some downdraft air will begin spreading at this level, but most of it will penetrate to the surface and spread there. The overturning that takes place as the cold downdraft air spreads over and under the boundary layer air causes turbulence within the outflow. The overspreading air is advected more rapidly than outflow air in the neutral case, because it encounters a nearly friction free “surface”. Otherwise, there is little difference in the early stages between the thunderstorm outflow spreading in the neutrally stratified versus the stably stratified boundary layer.

In this chapter, I first present an introduction to nonlinear and solitary gravity waves and review some of the observations that have been published. With this background, I then review some “rotor” microburst cases which may be manifestations of gravity waves. In this chapter it is also appropriate to investigate Fujita’s hypothesis for the embedded vortices in the DFW thunderstorm outflow. This is done in the larger context of pulsating downdrafts, and sudden increases in the flow rate of downdraft air into the outflow. In these cases, outflow air that formed earlier provides the stratified fluid into which the newer downdraft air flows.

A. Nonlinear Gravity Waves

Internal waves of finite amplitude that occurred in temperature inversion layers above the surface (200 – 1000 m agl) have been investigated by Gossard and Munk (1954). Using shallow water theory, they found the observed nonlinear periodic oscillations to be the fundamental trapped atmospheric gravity waves modes of low frequency and long wavelength, as would be expected if they were excited by a large initial disturbance and had persisted for some time. Gossard et al. (1970) showed that when the temperature inversion in the atmosphere is near the ground, the wave peaks become sharper and the troughs broader, indicating nonlinear effects are important (Fig. V-1). Gossard and Richter (1970) compared these observations with theoretical predictions of the shape of nonlinear internal gravity waves for a two layer fluid in which the upper layer is infinite, and found good agreement. Gossard (1983) noted that the elevated gravity wave events could represent an unusual fair weather low altitude wind shear hazard to aircraft.

B. Solitary Waves

In ground based inversion layers, the wave sharpening effects of nonlinearity become large enough to balance the frequency dispersion which characterizes these internal gravity waves. As a consequence, solitary waves can exist. They can be thought of as the limiting case of the nonlinear periodic wave train shown in the bottom panel of Fig. V-1, as the peaks become sharper and the troughs become so broad that the waves are "solitary".

A classical solitary wave is defined as a wave of single elevation which propagates at uniform velocity without change of form. In the case of solitary waves, momentum imparted to the fluid remains localized in a stable propagating wave which passes over the fluid and leaves it as it was before the wave arrived (Fig. V-2), instead of spreading over the whole surface of the water in a more typical rippling wave motion. They were first observed and given their name by a Scottish scientist named John Scott Russell (1845). His eyewitness description of a particular solitary wave, which originated when a moving barge came abruptly to a stop in a canal, and which he followed on horseback along the canal for a couple of miles, has now become famous. The description is included in the review of solitary waves in fluid systems by Miles (1980).

Solitary waves were not appreciated for their importance and broad significance until around twenty five years ago, when it was discovered that they can be viewed as the stable asymptotic state of some canonical nonlinear systems, produced by very general initial conditions. The waves are

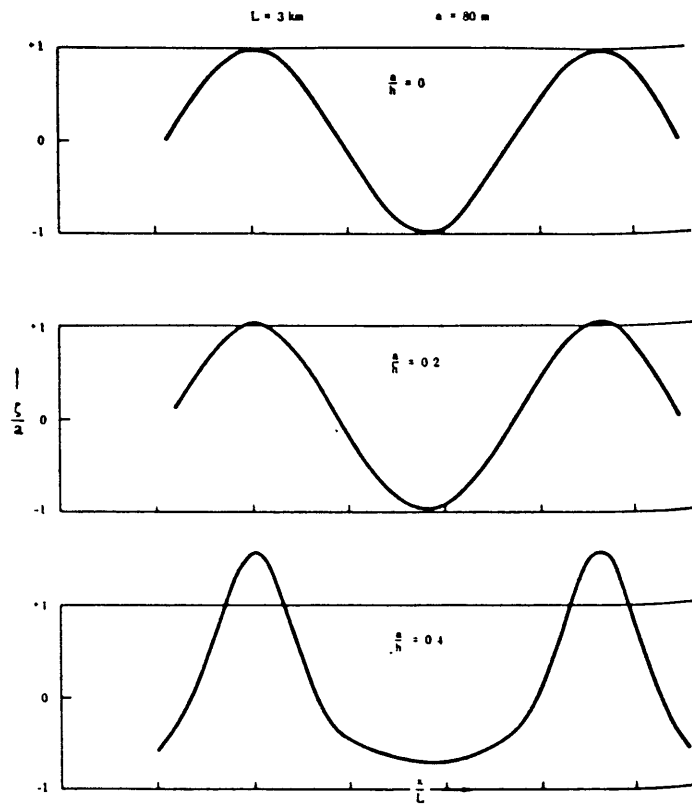


Fig. V-1. Calculated shape of waves of finite amplitude for three thicknesses of lower layer. Vertical scale is ratio of displacement to corresponding "small-amplitude" displacement. Taken from Gossard and Richter (1970).

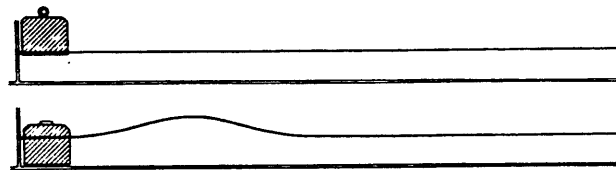


Fig. V-2. Russell's (1845) observation of the evolution of a solitary wave in a wave tank, reproduced from the original drawing by Miles (1980).

unchanged in nonlinear interactions and collisions, except for small phase shifts in some cases. Zabusky and Kruskal (1965) coined the term *solitons* to describe these particle-like waves. Since then, solitary waves have been studied intensively in many different disciplines, including particle physics, ion plasma physics, nonlinear optics, laser physics, and applied mathematics, as well as geophysical fluid dynamics (Scott et al. 1973; Dodd et al. 1982). Planetary solitary waves have been reviewed by Malonotte-Rizzoli (1982), and nonlinear models of isolated eddies (solitons) in geophysics have been reviewed by Flierl (1987). A number of laboratory tank experiments have been performed by Maxworthy (1980) who found: "Quite general and uncontrolled mixing events create solitary wave trains and lead us to suspect that they should be excited under many circumstances in natural systems." He suggests that "...solitary waves are ubiquitous. By which we mean that if a given physical system is capable of supporting solitary wave motions then such motions will invariably arise from quite general excitations."

The first convincing evidence of long nonlinear waves in the lower atmosphere was presented by Christie et al. (1978). They showed that the deep fluid theory of Benjamin (1967), Davis and Acrivos (1967), and Ono (1975) was better for describing solitary wave phenomena in ground based wave guides than the "classical" shallow fluid solitary wave theory of Boussinesq (1872) and Korteweg and deVries (1895). Microbarograph records of atmospheric gravity wave events propagating on the nocturnal inversion in Tennant Creek, Australia, revealed evidence of isolated solitary waves of elevation, and groups of waves consisting of well separated individual solitons. The authors noted that these solitary waves appeared to be closely related to the frequently occurring, sudden, near dawn squall known as the "morning glory" in Australia. Clarke (1972) has explained the "morning glory" as the undular leading edge of an atmospheric bore created by nocturnal surface drainage flow moving onto a plain under conditions of a stable radiation inversion. Smith (1988) provides a review of the work that has been done since on the "morning glory" phenomenon. Pointing out the possibility that large amplitude undulations or individual solitary waves can be created by the "direct impulsive interaction of an advancing gravity current on an established inversion", whether the gravity current was the result of katabatic flow or created by newly formed thunderstorm outflow, was the essential contribution of Christie et al. (1978).

Christie and Muirhead (1983a,b; 1985) and Doviak and Christie (1989) have stressed the potentially serious hazard to aviation created by solitary waves. Because they are stable and long lived, they pose a low altitude wind shear hazard in areas far removed from thunderstorm activity.

This sudden clear air hazard, often more complicated than that encountered at the leading edge of a gravity current because more than one wave can be present, was emphasized as the primary concern. Christie and Muirhead (1983b) note that “the performance of an aircraft during a head-on encounter on final approach with a solitary wave (Fig. V-3) is remarkably similar to the behavior of an aircraft during an unexpected encounter with a microburst.”

The recent theoretical work on long nonlinear waves in the lower atmosphere by Christie (1989) provides a thorough review of the nonlinear wave theory governing the time evolution of these disturbances and of many well documented examples of atmospheric solitary waves and bores. The characteristic behavior of the solutions to the BDO equation is summarized in Appendix B. A version of the BDO equation appropriate for cylindrical geometry has not been previously derived. Yet this is the required geometry to describe the waves created as an isolated thunderstorm outflow spreads at the surface in a stably stratified boundary layer. The cylindrical BDO

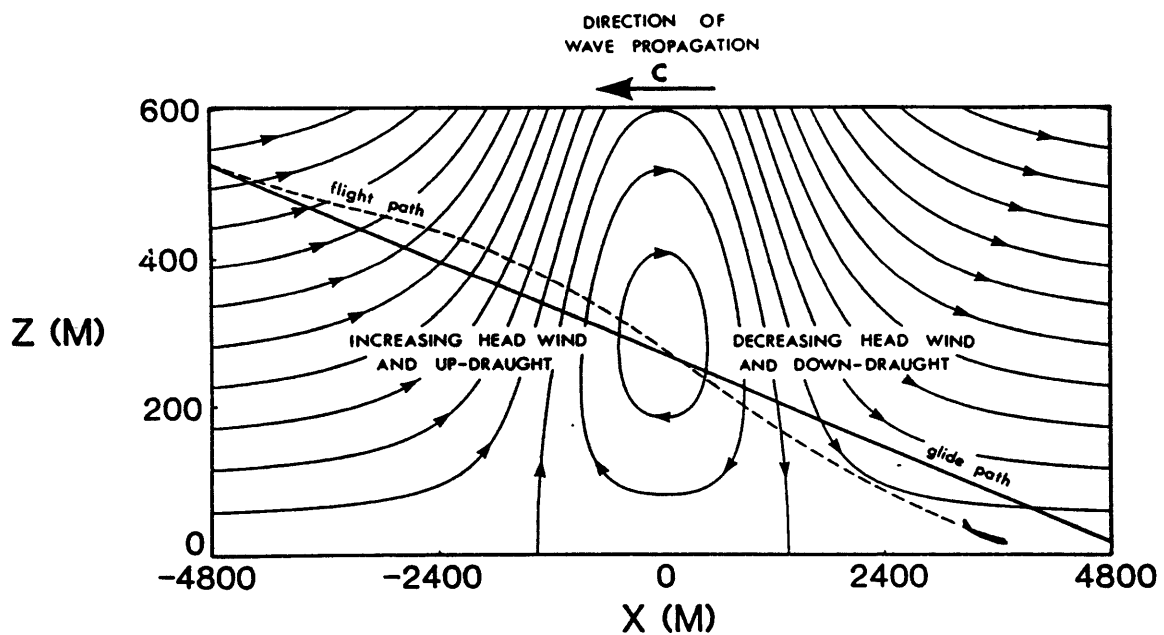


Fig. V-3. Schematic illustration of the undershoot behavior of an aircraft during a hypothetical head-on encounter with a solitary wave on final approach to the runway. Taken from Christie and Muirhead (1983b).

(CBDO) equation is derived in Appendix C and its behavior is compared in some detail to that of the BDO equation in the second part of Appendix B.

The key difference between the planar and cylindrical solitary waves is the amplitude damping caused by the expansion of the wave front in the cylindrical case. This is illustrated in Fig. V-4, where the results of numerically integrating the BDO (top) and the CBDO (bottom) equations are shown. The coordinate system is moving at the long linear gravity wave speed, so the waves moving to the right are the supercritical solitary waves and those moving to the left are part of the subcritical dispersive wave train. In the BDO integration, the initial disturbance with an amplitude of 1 has evolved primarily into solitary waves, the largest of which has reached an amplitude of 2.2. In contrast, the CBDO solitary wave amplitudes increase at first, but soon they begin to decay because of the geometrical distortion. Thus, atmospheric solitary waves with a more slab symmetric geometry, perhaps generated by a line storm or created as the energy of a cylindrical wave is preferentially trapped primarily in one direction, will retain their magnitude and may even amplify over long periods of time. Purely cylindrical solitary waves, however, will decay in amplitude with time.

C. Observations of Thunderstorm Generated Solitary Waves

As Smith (1988) notes, "the last ten years have seen a burgeoning interest in large amplitude waves and bores generated on a stably-stratified layer in the lower atmosphere". Some of the cases of solitary waves triggered by thunderstorms are reviewed in this section. Haase and Smith (1989b) review other atmospheric situations where the study of gravity currents moving into low level stable layers is applicable.

Observations of two pressure jump lines (1.2–1.8 mb jumps) that passed through the St. Louis area at night in August, 1976 were presented by Shreffler and Binkowski (1981; Fig. V-5). They suggested that strong afternoon thunderstorms in Iowa were the source of the lines, which they estimated moved at 13–14 m/s through the nocturnal boundary layer. Pressure perturbations were detected as far as 500 km from their origins. Doviak et al. (1990) suggest that the observed step increase in temperature that accompanied these pressure jump lines was caused by downward mixing through the shallow inversion below the nocturnal low level jet. They also suggest the double peaked wind speed signature, seen in the wind speed trace shown in Fig. V-5, is indicative of the recirculation that occurs within strongly nonlinear solitary waves (e.g., Tung et al. 1982).

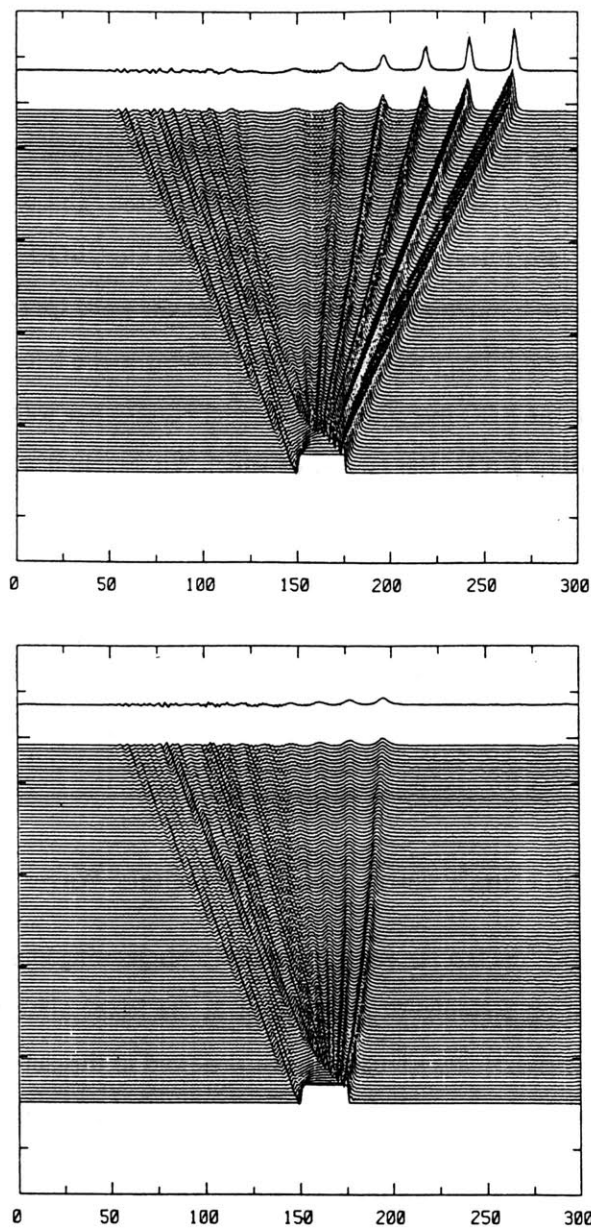


Fig. V-4. Numerical integration for 100 nondimensional time units (one trace for each) of (Top) BDO equation and (Bottom) CBDO equation, for an initial finite wave of elevation (amplitude of 1). The horizontal axis is the nondimensional space coordinate moving at the linear long wave speed. In the cylindrical problem, the initial time τ_0 was 5. The values of α and δ used for both equations were 1.5 and 0.48, respectively.

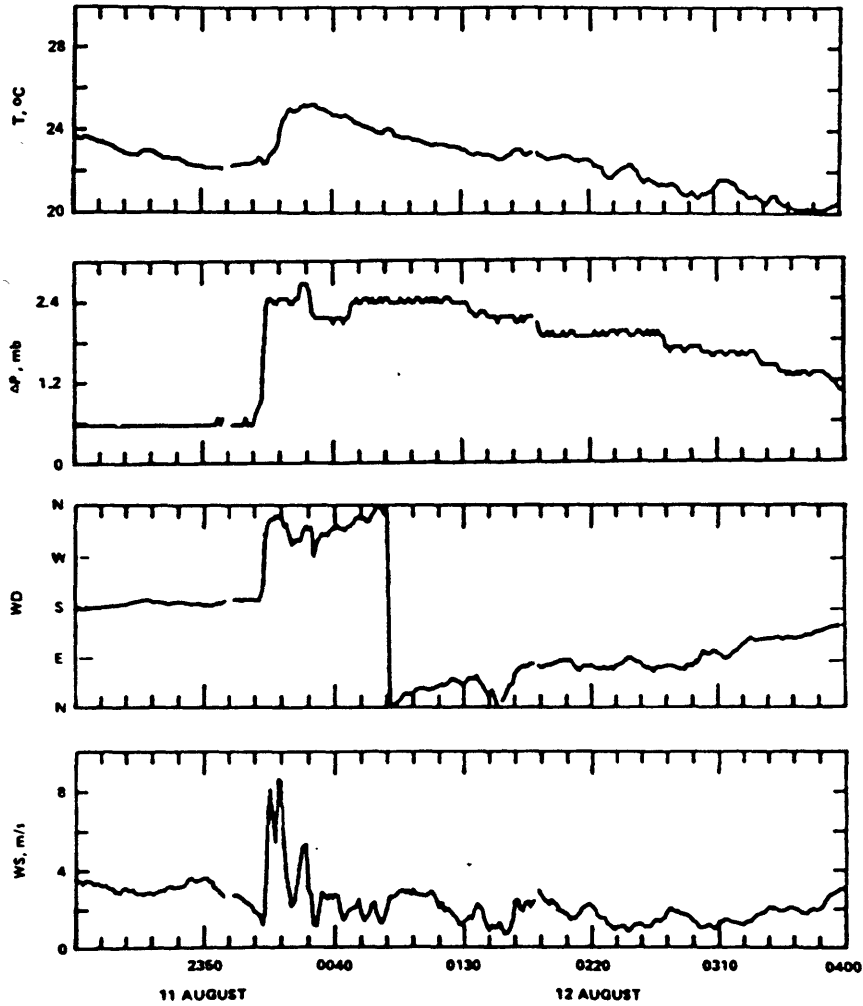


Fig. V-5. Time series of temperature (T), pressure (P), wind direction (WD) and wind speed (WS) for the passage of a pressure jump line ($PJ2$) at the Regional Air Monitoring System station No. 122. Adapted from Shreffler and Binkowski (1981).

Haase and Smith (1984) presented a case study of a morning glory-like system of travelling cloud lines that occurred in Oklahoma. The waves appeared to emanate from an area of rapidly growing intense thunderstorms 400 km away. Up to eight cloud lines could be seen encircling the southern and eastern edges of the parent thunderstorm complex in the visible satellite imagery presented. Wavelike perturbations were found in the measured wind, temperature, and pressure fields for the time period of disturbance passage. Erickson and Whitney (1973) presented satellite imagery of what appears to have been a similar phenomenon.

Doviak and Ge (1984), Doviak and Chen (1988), Doviak and Christie (1989) and Doviak et al. (1990) have all discussed a thunderstorm generated solitary wave detected with Doppler radar, mesonet, and a tall tower in Oklahoma on 11 May 1980. Large thunderstorms passed along the same storm track two hours earlier, generating a current of cool air that established a sufficiently strong surface based inversion so that the outflow from the subsequent storm could generate solitary waves. This may be the first documented case in which outflow from earlier storms provides the waveguide for nonlinear gravity waves. The measured winds and potential temperature structure in the largest solitary wave, and a schematic illustration of the hypothesized generation and evolution of the wave are presented in Fig. V-6. This feature could clearly be identified as a horizontal vortex or "rotor" propagating in old thunderstorm outflow. The cold core of air within the vortex is thought to be trapped outflow air from the generating thunderstorm.

Doviak et al. (1990) compared these observations with characteristics predicted by weakly nonlinear BDO theory, and found that while their model gave a fairly good description of the principal features in the time evolution of this disturbance, it failed to account for the observed decrease in propagation speed and amplitude with time as the waves propagated away from the source region. They attribute these discrepancies to losses due to frictional dissipation, leaking of trapped outflow air in the highly nonlinear waves, and possibly radiation of gravity wave energy into the upper atmosphere. They did account for the rapid storm translational motion in their model, but they failed to take into consideration the circular geometry of the originally generated waves. In Appendix B, I showed that this can have a significant damping effect on the wave amplitude and thus speed. The cylindrical geometry may also account for the asymmetric wave shape, with a steeper interface slope on the backside, and for the depressed outflow layer behind the leading wave (compare Fig. V-6 with Fig. B-6). In comparing the steady state structure of the wave, they found that because of the trapped outflow air in the recirculation region, weakly non-

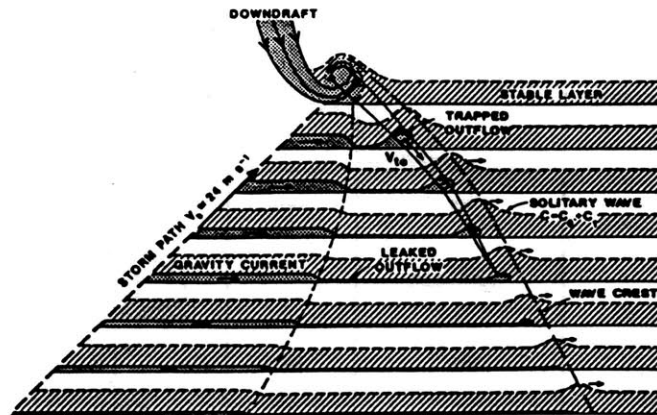
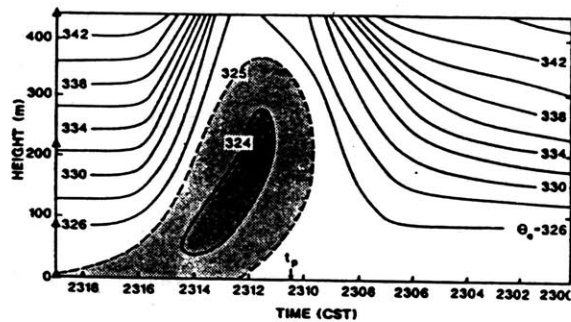
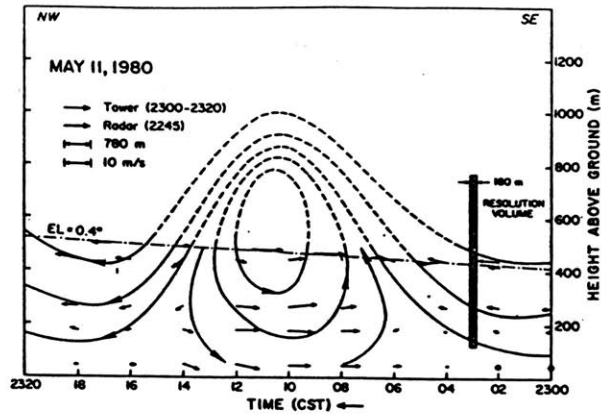


Fig. V-6. (Top) Samples of winds (lightly traced arrows) measured at NSSL tower in central Oklahoma at four levels in the NW-SE cross section of the gust for the time period 2300-2320 CST on 11 May 1980. The velocity scale is listed in the upper left corner and applies to both the horizontal and vertical speeds. Bold arrows are Doppler radar estimates of wind at 2245 projected onto this cross section. The dashed streamlines are subjectively estimated in the data void region between 500 and 1000 m. Taken from Doviak and Ge (1984). (Middle) Equivalent potential temperature in K (t_p is the time of the peak in the cross-wave wind component). (Bottom) Scenario for the evolution of the thunderstorm generated solitary wave. Taken from Doviak and Christie (1989).

linear theory could not account for the observed wave width, which was wider than predicted. The observed wave widths were in reasonable accord with the predictions made using the full nonlinear theory of Tung et al. (1982).

The characteristics of internal gravity waves propagating on a layer of high stratification near the ground, with a deep weakly stratified layer above, were investigated in a numerical study performed by Crook (1988). In this situation gravity waves are not perfectly ducted as they are when the upper atmosphere is unstratified, and some other mechanism is needed to trap gravity wave energy at low levels for waves of significant amplitude to persist. Crook tested the effects of an opposing upper level flow (above 4 km), an opposing lower level flow (jet structure within the stable layer), and an elevated temperature inversion. Figure V-7 summarizes his results for the three thunderstorm generated cases described above. The only energy trapping mechanism present in these three studies was the low level opposing jet-like flow. The curvature in these wind profiles reduces the Scorer parameter [Eq. (B.4)] and can cause it to change sign, creating a region of wave evanescence and substantially trapping wave energy at the lower levels.

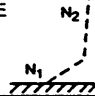
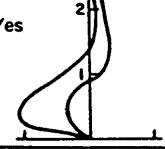
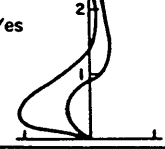
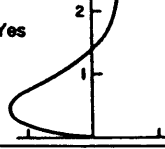
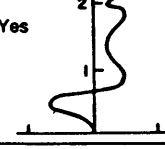
DISTURBANCE	HIGH STRATIFICATION AT GROUND LOW ABOVE 	OPPOSING UPPER LEVEL FLOW	OPPOSING LOW LEVEL FLOW 	INVERSION
MISSOURI DISTURBANCE Shreffler and Binkowski (1981)	Yes $N_2/N_1=0.38$	No	Yes 	No
OKLAHOMA Haase and Smith (1984)	Yes $N_2/N_1=0.45$	No	Yes 	No
OKLAHOMA Doviak and Ge (1984)	Yes $N_2/N_1=0.34$	No	Yes 	Slight 2°/100m at 2.5km

Fig. V-7. Observations of low-level internal gravity waves. Adapted from Crook (1988).

The “burgeoning interest in large amplitude waves” is evidenced by the five very recently completed studies comparing thunderstorm generated bores or solitary waves with the governing nonlinear theory. Doviak et al. (1989) used Doppler radar to map the evolution of a pair of atmospheric solitary waves emanating from a thunderstorm complex in Oklahoma, and hypothesized that the position of these waves was a result of the amplitude dependence predicted by the BDO equation. Fulton et al. (1990) presented perhaps the first direct evidence of a gravity current initiating a solitary wave family. They used Doppler radar, instrumented tower, and especially surface mesonet data collected over an 80 minute period in Oklahoma to show the structure and evolution of this event (Fig. V-8).

Carbone et al. (1990) determined, using data from the PRE-STORM experiment in Kansas, that the observed squall line convection on 26-27 May 1985 was initiated by a gust front generated earlier in the day by a separate mesoscale convective system. The gust front initially propagated as a gravity current, and subsequently as an internal undular bore, into a region of favorable synoptic conditions for convective weather. They note that gravity currents and gravity waves in the nocturnal boundary layer can provide valuable clues for short period convective storm forecasting, and may represent an important form of discrete propagation for mesoscale convective systems.

A unique set of observations of five solitary wave events near Boulder were analyzed by Cheung and Little (1990). The observations included data from an instrumented tower, 2 sodars, and 4 microbarographs, allowing definition of the geometry, thermodynamic characteristics, and propagation speeds of the events. Somewhat surprisingly, they found the wave characteristics were largely consistent with BDO theory even though all of the events contained trapped air from the originating disturbance (an indication of strong nonlinearity).

Lastly, Rottman and Simpson (1989) used a laboratory tank model of density currents interacting with an existing inversion layer to illustrate the types of bores that might be expected to occur in the atmosphere. They identified five previously published gravity current cases and analyzed them according to their two-layer theory. They developed a rule of thumb to predict the structure of the bore as a function of its strength. Referring to Fig. IV-35, “when $1 < h_1/h_0 < 2$, the bore has a smooth undular form, when $2 < h_1/h_0 < 4$, the bore is undular but some mixing, due to shear instability, occurs on the downstream face of the leading undulation, and when $h_1/h_0 > 4$, the bore appears like a gravity current.” Applying this rule of thumb to the Mueller and Carbone (1987) case in which a large KH billow was identified suggests their “bore” should have a smooth

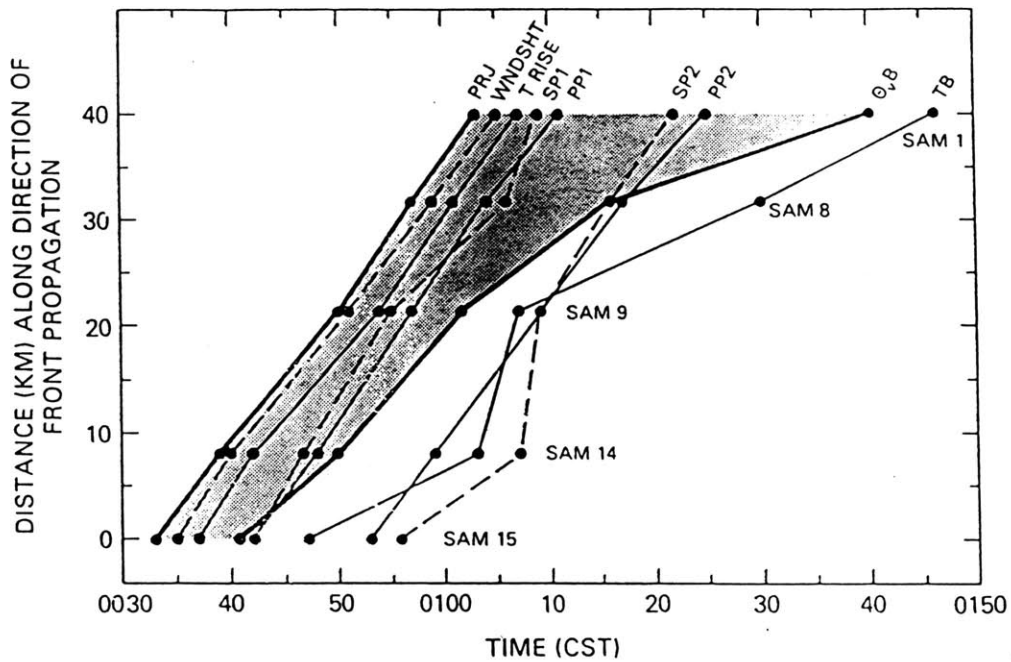
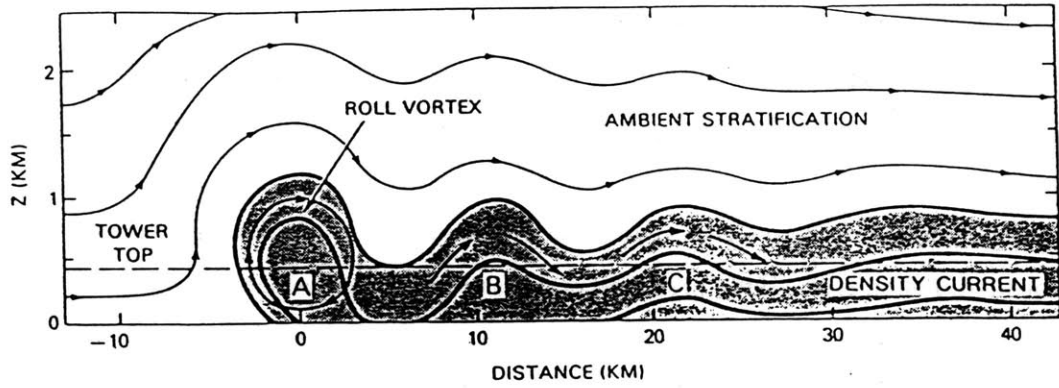


Fig. V-8. (Top) Schematic diagram of the 9 May 1981 cold outflow based on tower and Doppler radar observations. The tower sampled roughly the lower half on the gravity current and the radar provided information on the flow fields higher up. The three wave-like disturbances identified as A, B, and C are still located entirely behind the gravity current front. The streamlines are in a frame of reference translating with the windshift line. (Bottom) Illustration of the passage of significant events at five mesonet (SAM) stations oriented in a line normal to the front. The pressure jump (PRJ) occurs first at all stations followed immediately by the windshift (WINDSHT), the rise in the dry-bulb temperature (T RISE), the first speed peak (SP1) and pressure peak (PP1), and then the second speed peak (SP2) and pressure peak (PP2). The leading edge of the gravity current is delineated by the time when the virtual potential temperature begins to fall (Θ_{vB}). TB defines the time that the dry-bulb temperature falls below the pre-frontal value. Note how all of the events are moving at a nearly constant speed, while the Θ_{vB} curve lags by an ever-increasing amount of time. The shaded region highlights the increasing time between the bore front and the gravity current front. Taken from Fulton (1987).

undular form which is what was observed. Rottman found that, in general, the published atmospheric data compared favorably with their laboratory measurements, and concluded that “there seems little doubt that thunderstorm outflows and sea-breeze fronts can generate internal bores in stable layers”.

Most past gust front studies have not taken into account the stratification of the ambient environment. Since nonlinear gravity waves can propagate faster than gravity currents, estimates of the Froude number (F) in some gust front cases may have been too large, and may have contributed to the wide variation in reported values. Seitter (1986) provided an improved method for determining F , and also showed how observed propagation speeds should be corrected for the influence of ambient winds. Figure V-9 shows these corrected propagation speeds (the numerator of F) versus Seitter’s pressure based denominator of F for a number of studies. It is interesting that at least some of the observations that lie above the best-fit line in Fig. V-9 were cases in which the environment was stably stratified ahead of the gravity current (e.g. Charba 1974; at least 2 from Goff 1975; all 3 from Wakimoto 1982). This raises the possibility that these gravity currents could

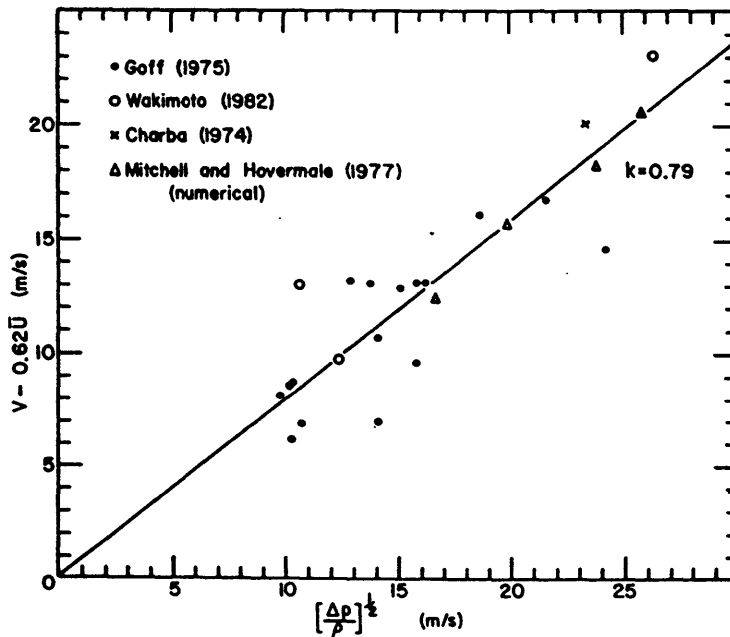


Fig. V-9. Observations of gust front speed versus surface pressure rise. The best-fit line representing the value of F (shown here as k), excluding the numerical data of Mitchell and Hovermale (1977), was found to be 0.79 with a correlation coefficient of 0.84. Taken from Seitter (1986).

be interpreted as developing undular bores or supercritically propagating nonlinear gravity waves that contained trapped cold air. Fulton et al. (1990) reexamined Charba's "classic thunderstorm density current" case in light of their own undular bore observations and concluded that it was "actually a dissipating density current strongly modulated by a developing solitary wave family." The slab symmetric numerical simulations of gravity currents flowing into environments with surface based stable layers by Haase and Smith (1989b) appear to support this.

Smith and Reeder (1988) note that "clearly, there is a need for much more research on the interaction between gravity currents and stable layers and on the structural differences between gravity currents moving into stable layers, internal solitary waves of large amplitude and bores for different stable layer depths and stabilities." This research should include reexamination of case studies already published as well as the analysis of new observations.

However, enough research has been done, as shown in this section, to prove that thunderstorm outflow behavior is definitely *eventually* influenced by the stratification of the boundary layer. But all of these studies examined waves far from the thunderstorms that initiated them. What difference, if any, is caused in the early stages of thunderstorm outflow evolution by the presence of a stably stratified boundary layer? This question is addressed in the following section.

D. Effect of Stratified Boundary Layer on Newly Formed Outflow

1) Laboratory Experiments

Some idea of the difference in behavior of newly formed thunderstorm outflow caused by the ambient stratification can be gotten from the laboratory water tank experiments performed by Maxworthy (1980). He studied the formation of axisymmetric internal waves by allowing a cylindrical region of dense mixed fluid with an excess of potential energy to collapse into a stratified fluid (Fig. V-10). The radial displacement of the leading edge was actually slower at first than the displacement measured with no stratification. Also at these early stages, the dense fluid moved with the solitary wave. Eventually, the supercritical wave separated from the mixed fluid behind; it was just after this time that the radial displacement of the leading edge finally surpassed the neutral case. Even after the wave had separated, fluid remained trapped within and was gradually ejected rearward as long dye streaks.

These experiments were not a good analogy for thunderstorm downdrafts, because the dense mixed fluid had only an excess of potential energy and no momentum when it was initially

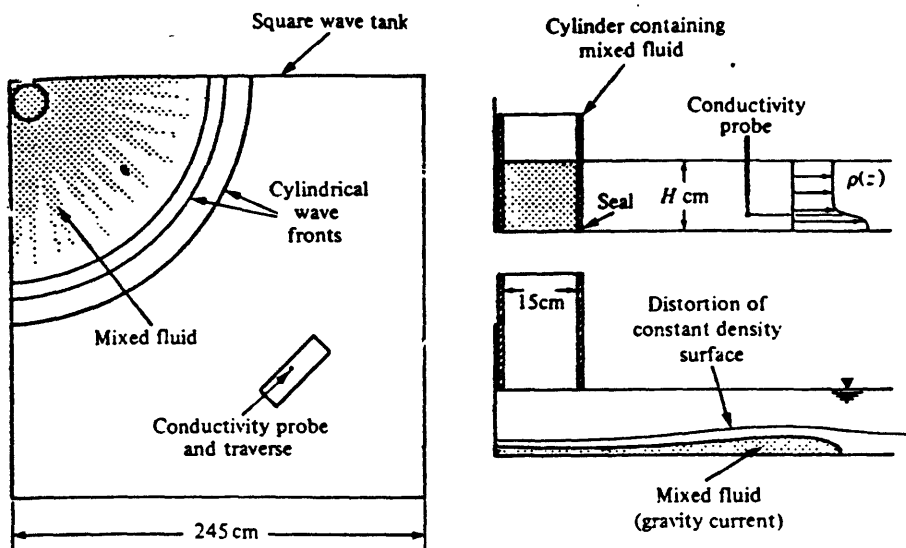


Fig. V-10. Apparatus to study the collapse of a mixed region in an axisymmetric geometry. Showing method of mixed fluid containment, trapping of gravity current within a cylindrical solitary wave and formation of streaky structure as waves leave the mixed region behind. Taken from Maxworthy (1980).

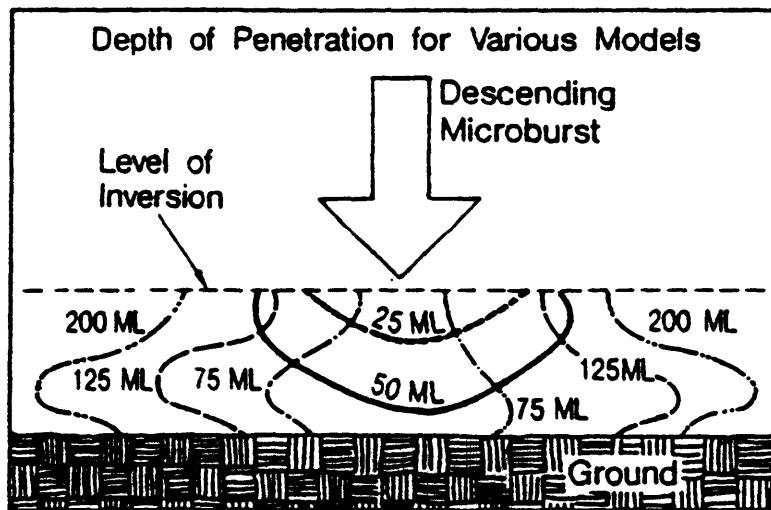


Fig. V-11. Summary of leading edge contours for scale model microbursts of various initial volumes at the time of deepest penetration or largest lateral extent. The larger volumes (indicated in units of ml) produced greater downward momentum, and thus penetrated farther into the stable layer. The downdraft salinity was 5%, and the surface layer was 10% in each case. Taken from Young et al. (1989).

released. Young et al. (1989) used a laboratory water tank to perform experiments designed specifically to model thunderstorm downdrafts impacting surface based inversion layers. In each case they chose a downdraft density intermediate between the ambient fluid and the thin inversion layer, so that penetration through this layer to the surface depended on having enough downdraft momentum (Fig. V-11). Unfortunately, this is not typical of most heavy rain thunderstorm downdraft situations, but may be relevant to some of the virga downdrafts observed in the Denver area. They summarize their results as follows.

1. If the microbursts had insufficient momentum to penetrate to the surface, a "mid-air" microburst occurs. The dyed flow expanded laterally at the [inversion] interface and exhibited roll-up characteristics at the edge of the outflow region. This vortical roll-up then propagated away from the center of the downflow region and diffused into the surrounding medium. A wave also propagated along the inversion interface surface away from the source.
2. If the microbursts had sufficient momentum to penetrate the inversion but insufficient momentum to diverge outward along the surface, the lateral expansion stalled at the inversion interface but the microburst continued down without diverging. The vortical roll-up became very strong and almost immediately broke up. The remains of the roll-up traversed slowly away from the center of the event. A large transverse wave propagated along the inversion interface and locally pushed the inversion up by about 50% of its original height.
3. If microbursts had sufficient momentum to penetrate the inversion layer and to diverge laterally along the bottom, the microbursts essentially overwhelmed the inversion and acted similar to a microburst that encounters no inversion at all. However, the leading edge of the outflow eventually rose off the "ground".

We can anticipate that if the downdraft was more dense than all other ambient fluid, the result (3) would apply except the leading edge of the outflow would not rise as it did in the laboratory experiments. But no experiments have been done that actually reveal how the early stages of cold thunderstorm outflow evolution is influenced by the presence of a stable boundary layer.

2) Numerical Experiments

To answer this question, the axisymmetric numerical model of Anderson (1990) was used* to simulate a downdraft reaching the surface in (a) an environment with a neutral boundary layer and (b) an identical environment except for the inclusion of a thin surface stable layer. Anticipat-

* In performing these experiments, all I did was specify the environmental characteristics for each experiment; Drs. Jerry Straka and John Anderson used their expertise to determine appropriate grid spacing, diffusion coefficients, cooling function magnitudes, and to actually run the models as well. Digital model output data were shipped to me for analysis and display.

ing the development of short wavelength oscillations in the outflow (perhaps like those measured in the DFW aircraft crash), the horizontal and vertical grid resolution was chosen to be 20 m. The time step was 0.1 s, the domain was 500 grid points wide by 350 high, and the eddy diffusion coefficient was 40 m²/s. The environmental lapse rate of potential temperature was based on the profile of virtual potential temperature measured during the DFW crash (Fig. V-12; Doviak, personal communication). The cooling source was Gaussian in shape, with a radius of 1.0 km, and a depth of 4 km, centered at 3.5 km above the surface. The cooling function is shown in Fig. V-13. The cooling rate was chosen so that the downdraft would be approximately 11 K colder than the neutral layer at the surface.

(i) *Model results*

The results of the experiment are shown in Fig. V-14. Temperature perturbations are contoured, and wind vectors representing vertical and radial velocity are drawn every 200 m, to the scale indicated by the maximum vector of 40 m/s. The lowest 3 km and the full 10 km width of the computational domain are shown.

In the first 9 min of the experiment, the flow is remarkably similar in the two experiments, except for the cold air in the stable layer case that has moved out along the top of the stable layer. This creates a situation in which colder air is overlying warm, and an overturning takes place. The differences in the vertical velocities are greatest at min 9 (roughly 5 min after the outflow begins). They can be seen most clearly by examining the contour plots shown in the top panel of Fig. V-15. In the neutral case, the leading vortex has entrained some vorticity of the opposite sense from the boundary layer, and thus shows some shorter wavelength structure at the top. In the stable case, the overhanging "nose" has become convectively unstable, so the low altitude downdraft velocities just ahead of the front are strong. Notice that the downdraft velocities in the core of the storm are stronger than those in the rotor at all altitudes.

As time goes on, the flow structure becomes progressively dissimilar in the neutral and stable cases. The leading vortex maintains its circulation in the neutral case, while the vortex splits in two in the stable case. This causes the overall flow to become more diffuse but not really weaker in the stable layer case (Fig. V-15, bottom). Notice how much faster the cold air "signal" is transmitted in the stable layer case; by min 19 it has reached the far edge of the domain, 2 km ahead of the cold air in the neutral case. This can be interpreted as a wave triggered by the impacting downdraft moving out along the stable layer. This leading wave builds at the expense of the "rotor" until both

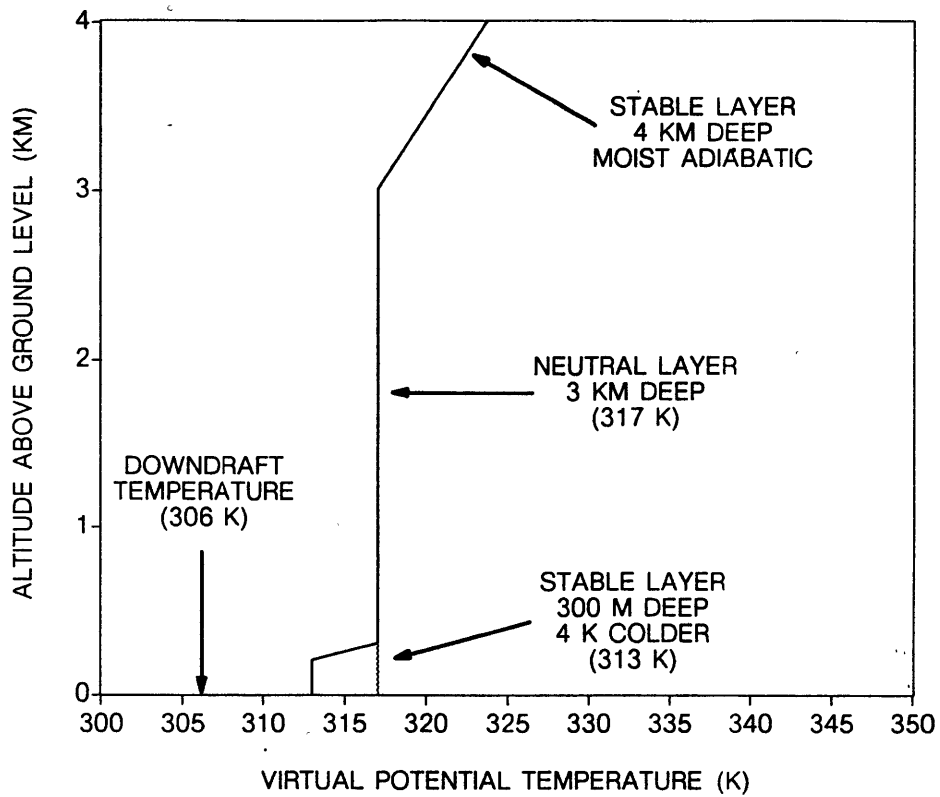


Fig. V-12. Idealized virtual potential temperature profile based on DFW crash observations (Doviak, personal communication), used as potential temperature profile in axisymmetric simulations. Profiles of temperature are identical except 300 m deep stable layer was added at the surface for one experiment.

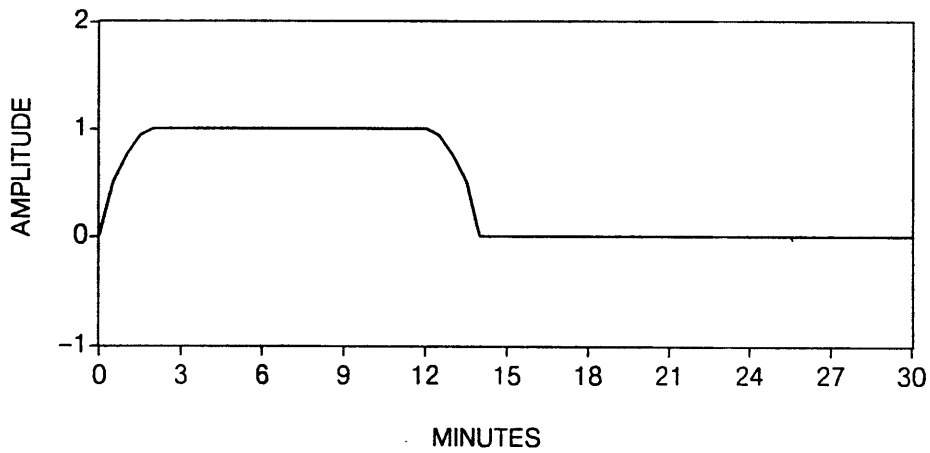


Fig. V-13. The shape of the cooling function for the neutral and stable boundary layer simulations (also doubles as a DFW storm simulation). Base cooling rate was $-0.075 \text{ }^\circ\text{C/s}$.

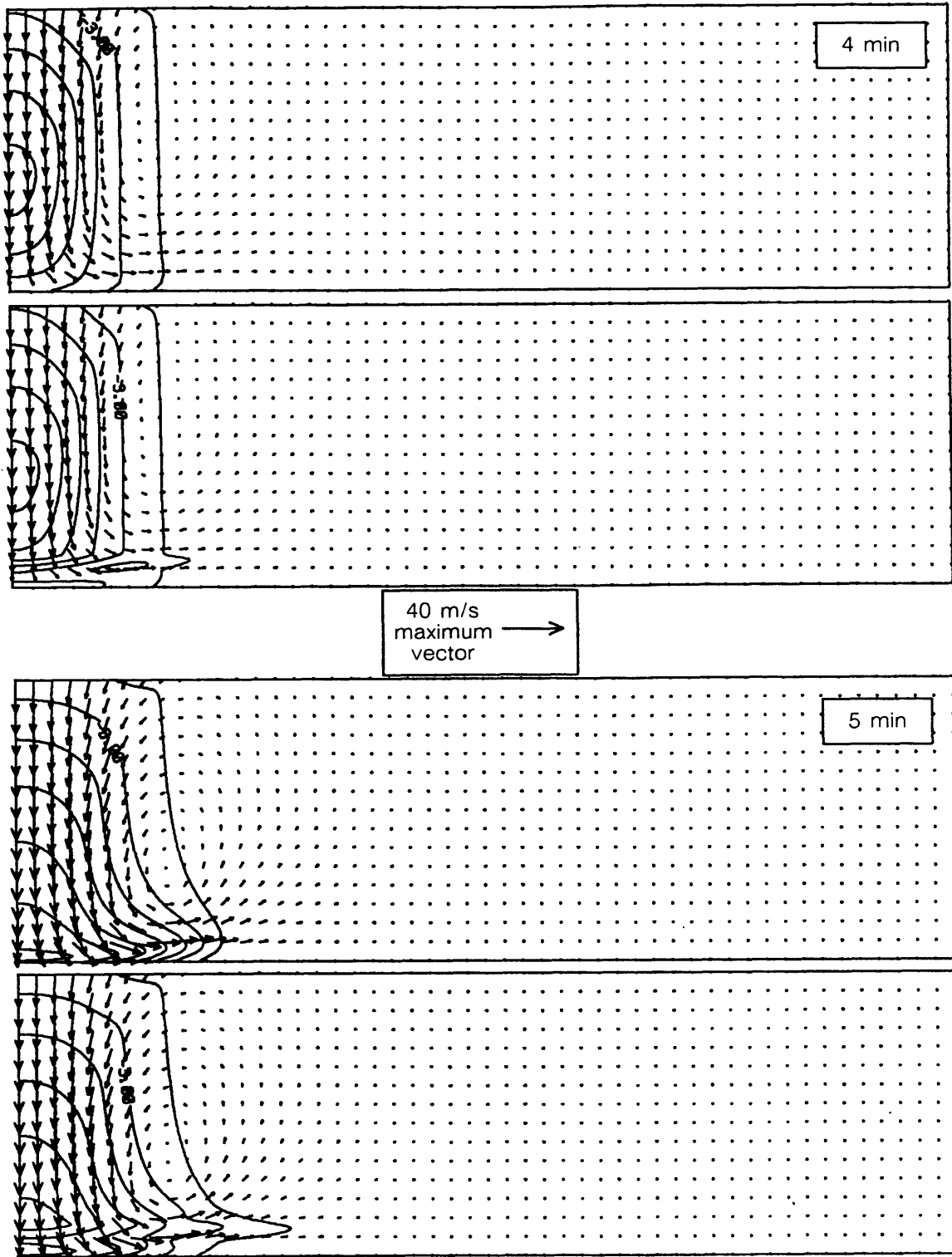


Fig. V-14. Potential temperature perturbation is contoured every 2°C , and wind vectors are drawn to indicated scale every 200 m (10 grid points). Domain shown is 10 km wide and 3 km high. At each minute, the top panel shows the neutral boundary layer run, the bottom, the stable boundary layer. Minutes 4 and 5 of the simulation are shown.

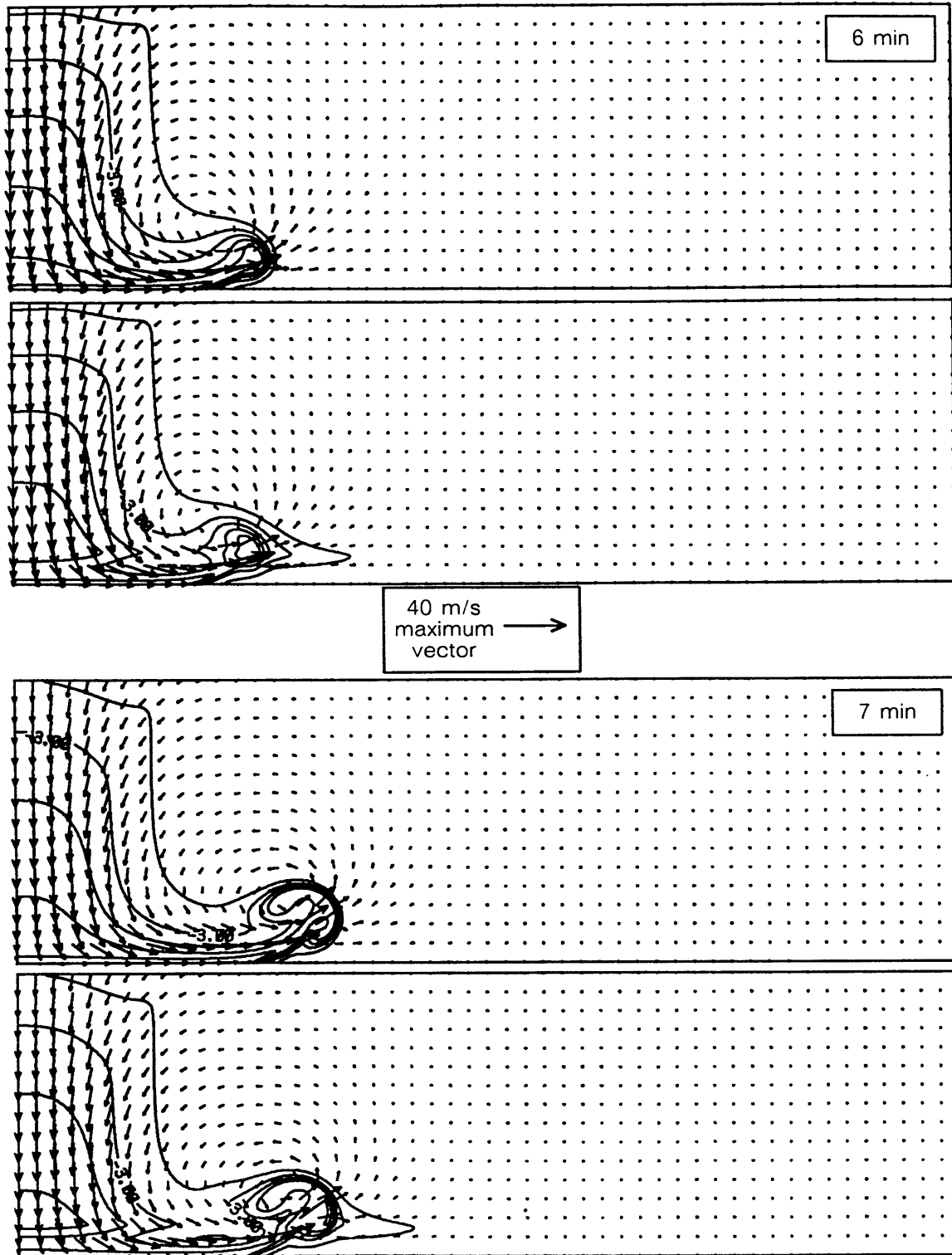


Fig. V-14. (Continued) At each minute, the top panel shows the neutral boundary layer run, the bottom, the stable boundary layer. Minutes 6 and 7 of the simulation are shown.

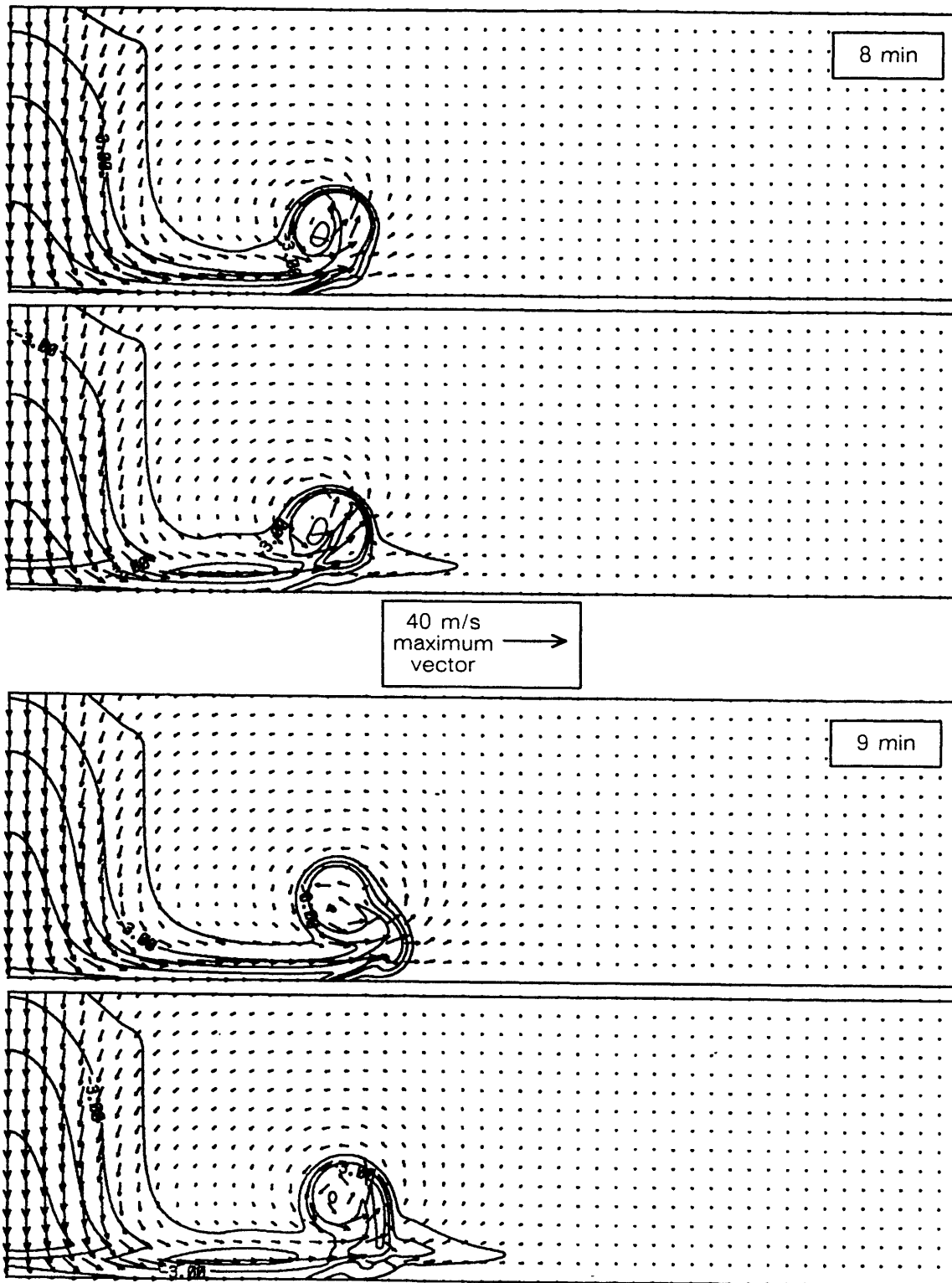


Fig. V-14. (Continued) At each minute, the top panel shows the neutral boundary layer run, the bottom, the stable boundary layer. Minutes 8 and 9 of the simulation are shown.

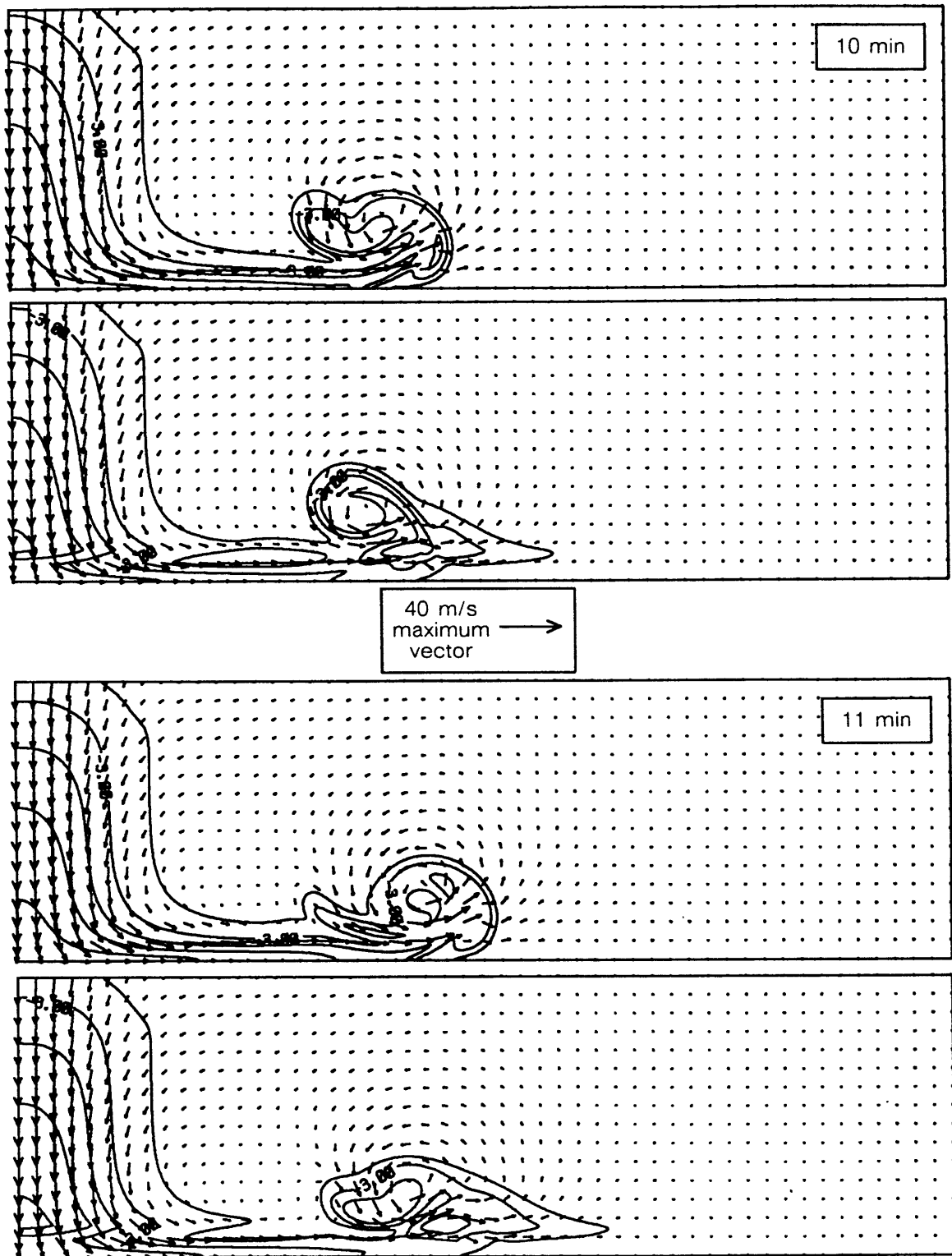


Fig. V-14. (Continued) At each minute, the top panel shows the neutral boundary layer run, the bottom, the stable boundary layer. Minutes 10 and 11 of the simulation are shown.

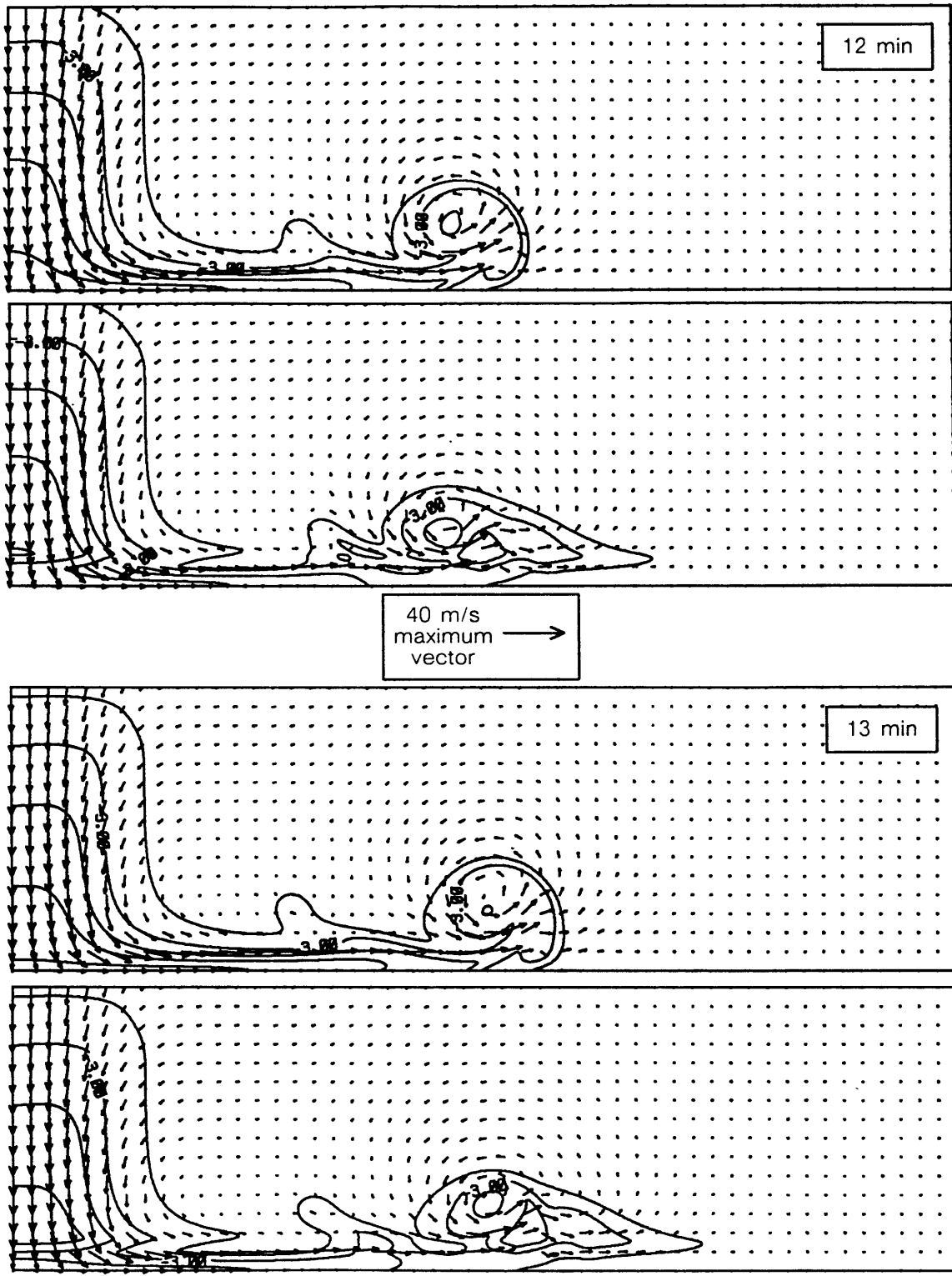


Fig. V-14. (Continued) At each minute, the top panel shows the neutral boundary layer run, the bottom, the stable boundary layer. Minutes 12 and 13 of the simulation are shown.

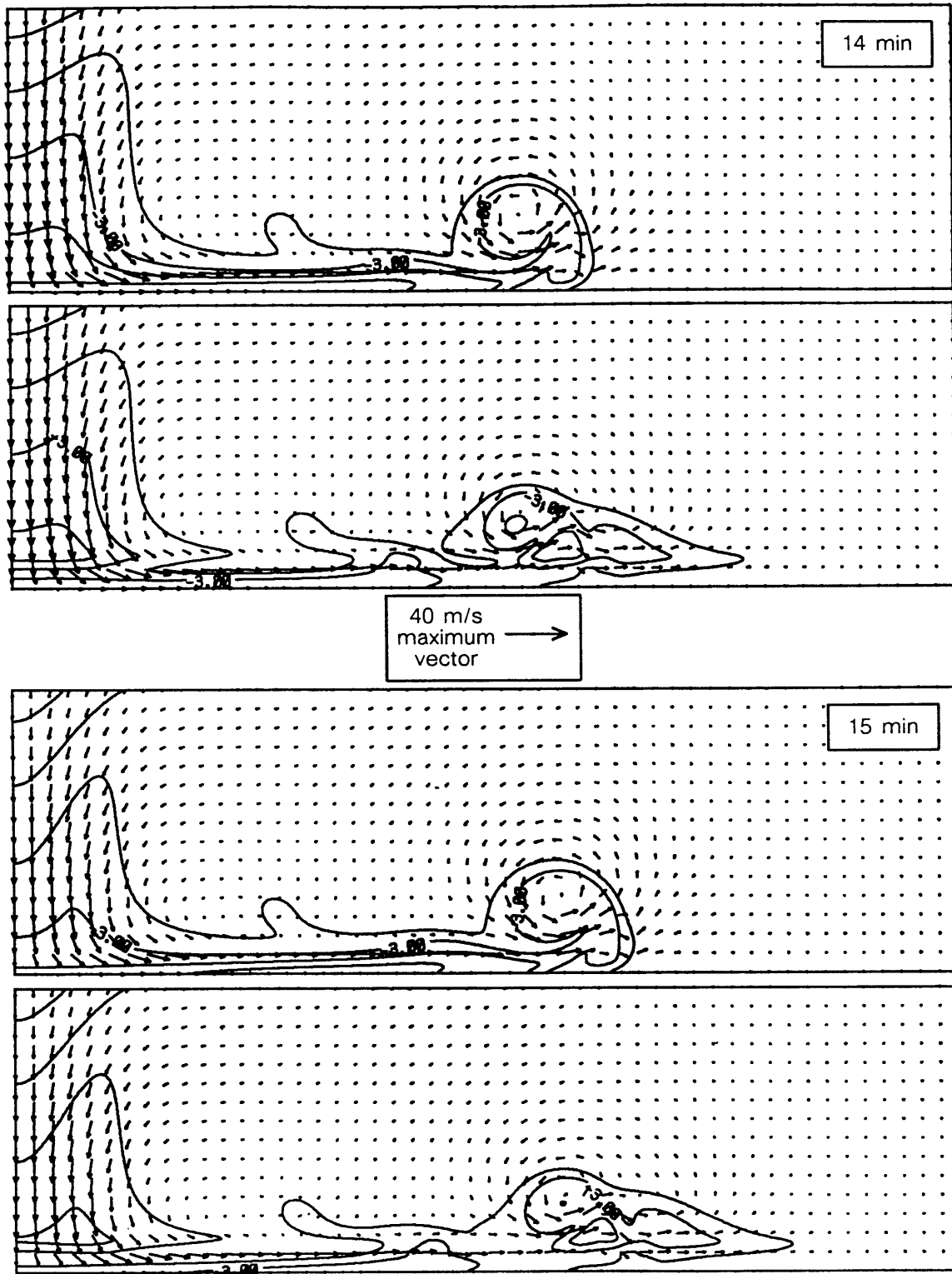


Fig. V-14. (Continued) At each minute, the top panel shows the neutral boundary layer run, the bottom, the stable boundary layer. Minutes 14 and 15 of the simulation are shown.

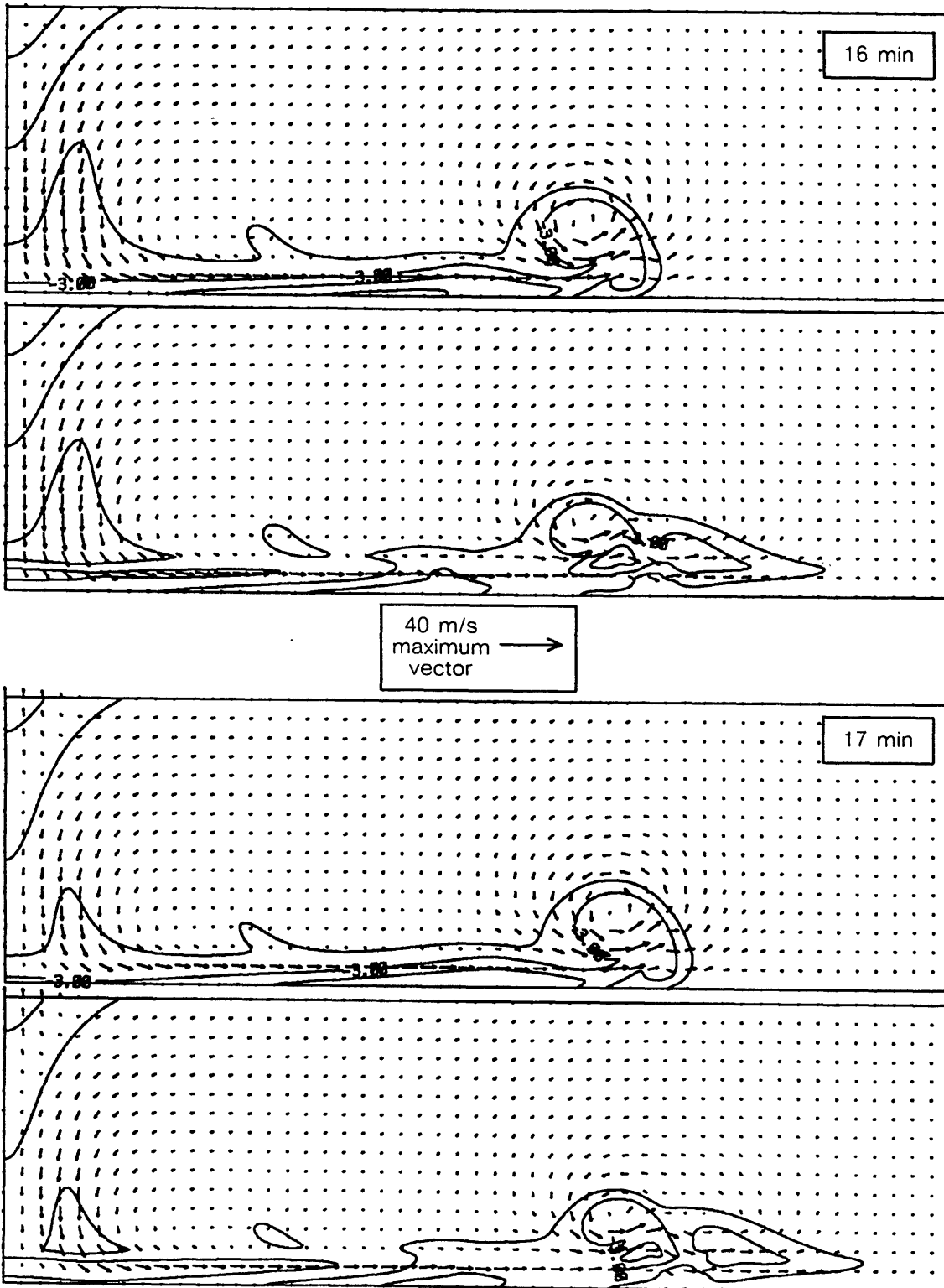


Fig. V-14. (Continued) At each minute, the top panel shows the neutral boundary layer run, the bottom, the stable boundary layer. Minutes 16 and 17 of the simulation are shown.

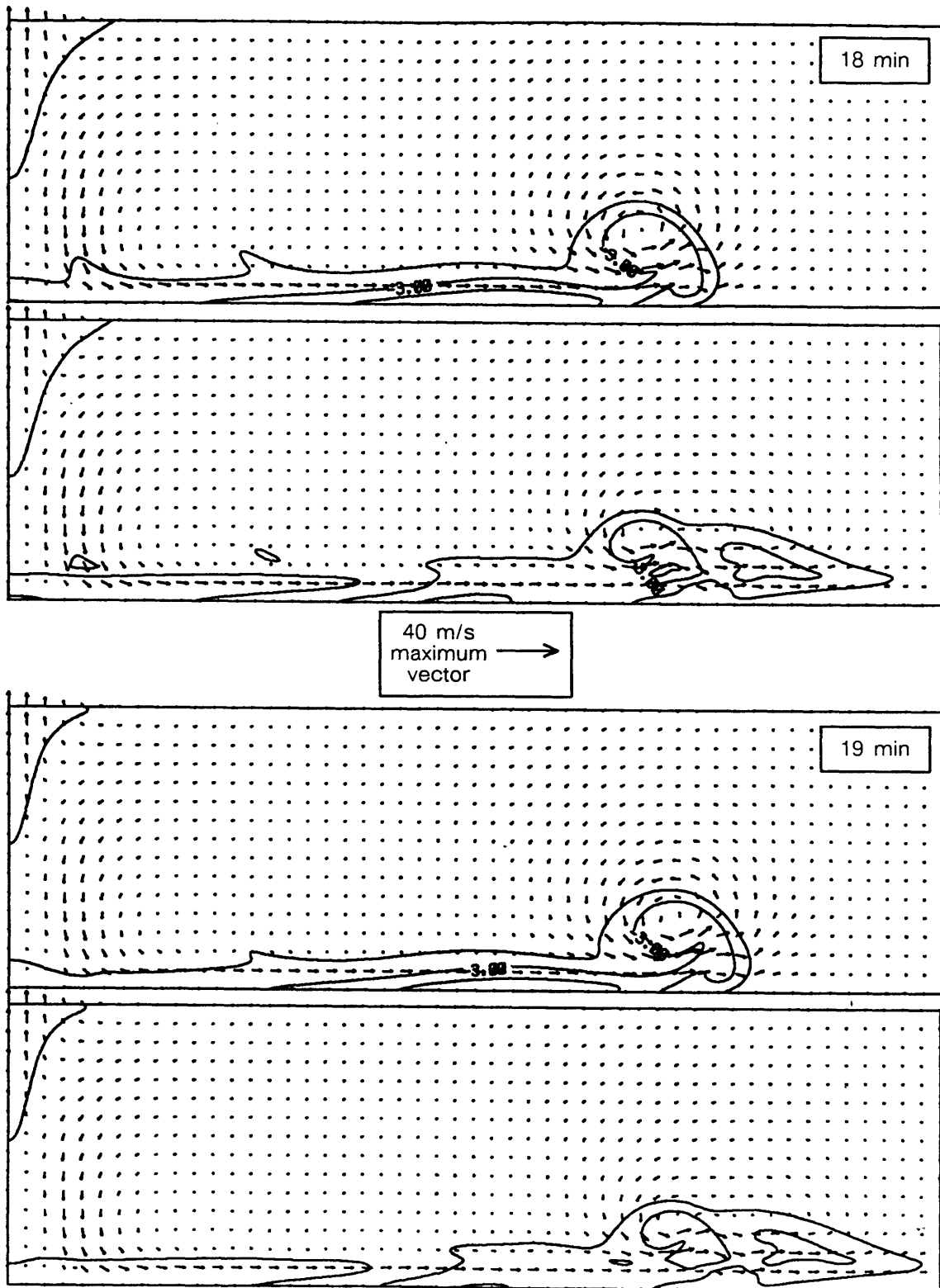


Fig. V-14. (Continued) At each minute, the top panel shows the neutral boundary layer run, the bottom, the stable boundary layer. Minutes 18 and 19 of the simulation are shown.

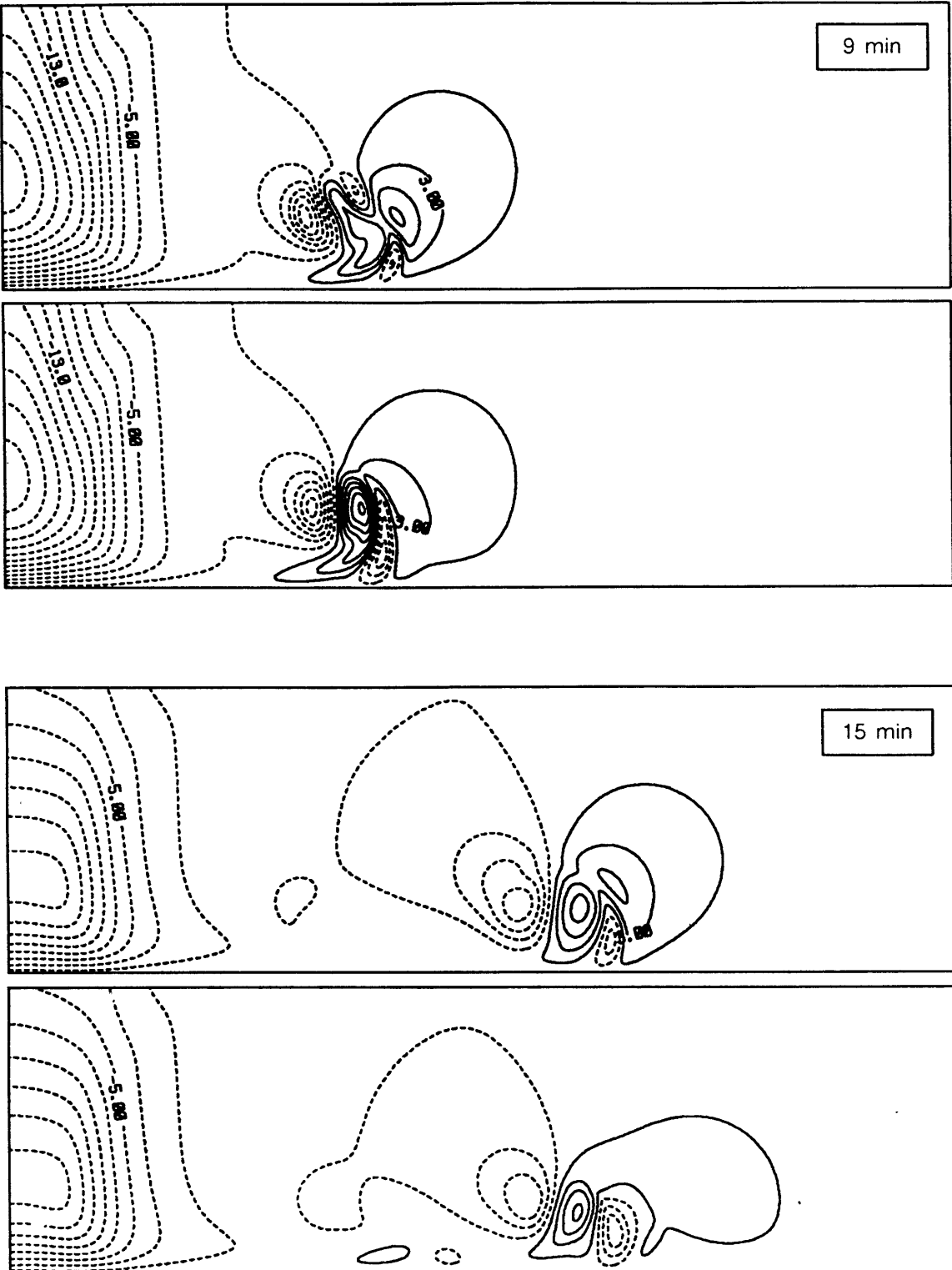


Fig. V-15. Vertical velocity is contoured in 2 m/s increments. Dashed contours indicate negative values. At each minute, the top panel shows the neutral boundary layer run, the bottom, the stable boundary layer. Minutes 9 and 15 of the simulation are shown.

features begin eventually to decay. Since cold air is contained within this feature, perhaps in this early stage it should be called an “undular gravity current”.

(ii) *Quantitative assessment of aircraft hazard*

When the effects of the windfield through which an aircraft is flying change the total specific energy of the aircraft an amount comparable to the excess thrust to weight ratio of the plane, then the windshear becomes a significant factor in the overall aircraft flight performance. A measure of this loss or gain in aircraft available excess thrust-to-weight ratio due to horizontal wind shear and vertical drafts can be expressed as (Targ and Bowles 1988):

$$F = \frac{\frac{DU}{Dt}}{g} - \frac{W}{V}$$

where F is the “F-factor” hazard index, DU/Dt is the Lagrangian derivative following the aircraft itself of the horizontal wind along the flight path (U), g is the gravitational acceleration, W is the vertical wind component and V is the aircraft inertial airspeed. The flight path angle from horizontal is assumed to be small. Positive values of F indicate performance decreasing situations for an aircraft; thus downdrafts and divergent horizontal winds cause a loss of lift. Negative values of F indicate performance increasing wind patterns. However, when the *magnitude* of F is greater than a threshold value, thought to be approximately $|F| = 0.13$ for jet transport, then a hazard exists. Figure I-6 schematically shows the safe operations conditions as a function of F .

This F-factor hazard index was computed for the numerically simulated windfields shown in Fig. V-14. Contour plots of the index are presented in Fig. V-16 for minutes 6-11, for both the neutral and stable boundary layer simulations. Notice that the main downdraft portion always contributes positive values, while large positive and negative values are associated with the leading edge of the outflow, the gust front. These are indicative of strong turbulence, and show dramatically why “roll clouds” pose such an extreme hazard to aircraft (see Chapter I.B). In certain small areas, positive F values are even larger at low altitudes in the gustfront than in the main downdraft.

To compare the relative aircraft hazard of an outflow spreading in a neutral versus a stable boundary layer, the total hazardous area below 500 m was computed as a function of time. The results of this calculation are shown in Fig. V-17. The total performance decreasing area is nearly

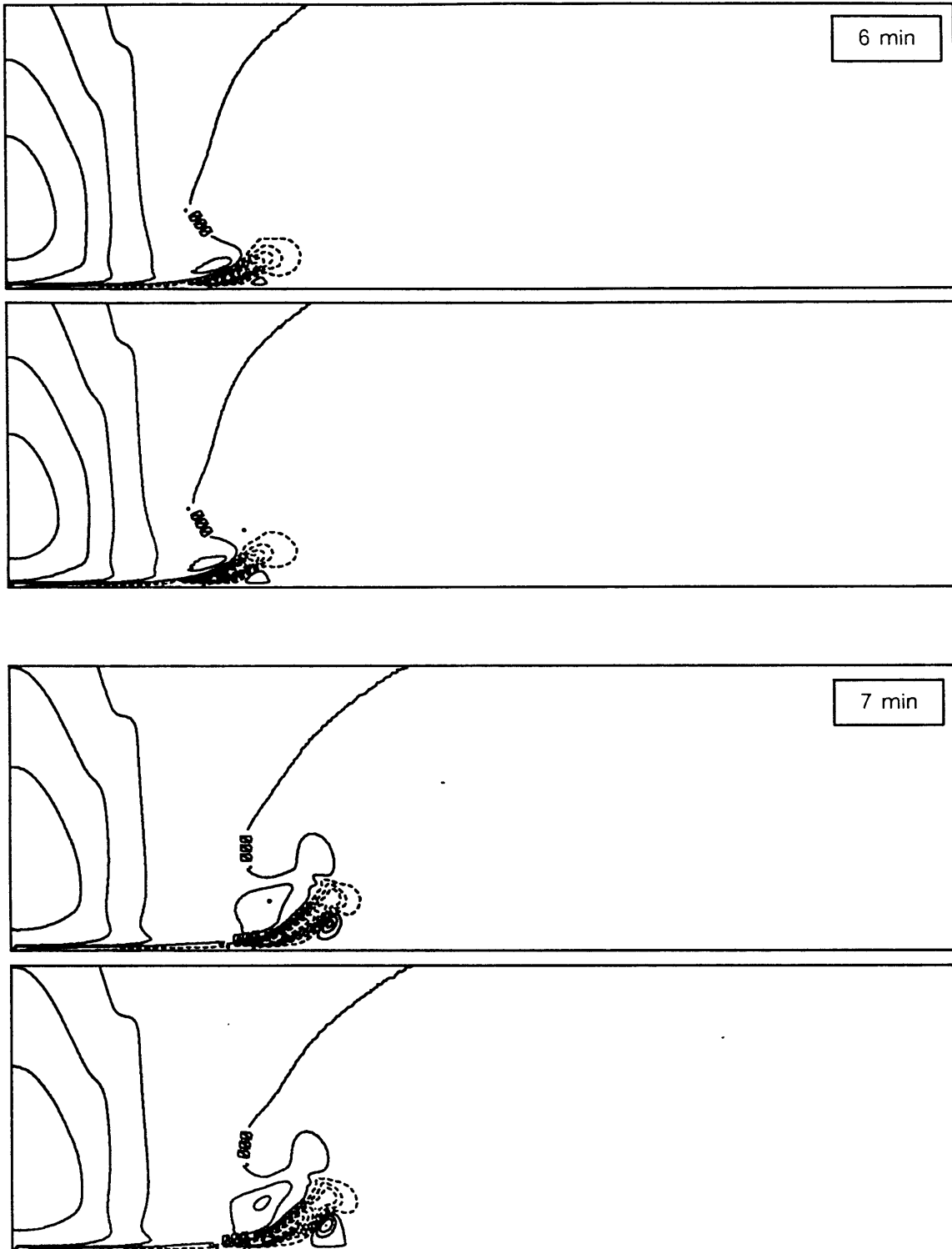


Fig. V-16 F factor calculated for a 3° landing glideslope. Values are contoured in increments of 0.1. Solid contours indicate positive (performance decreasing) values of F ; dashed contours indicate negative values. Domain shown is 10 km wide and 3 km high. At each minute, the top panel shows the neutral boundary layer run, the bottom, the stable boundary layer. Minutes 6 and 7 of the simulation are shown.

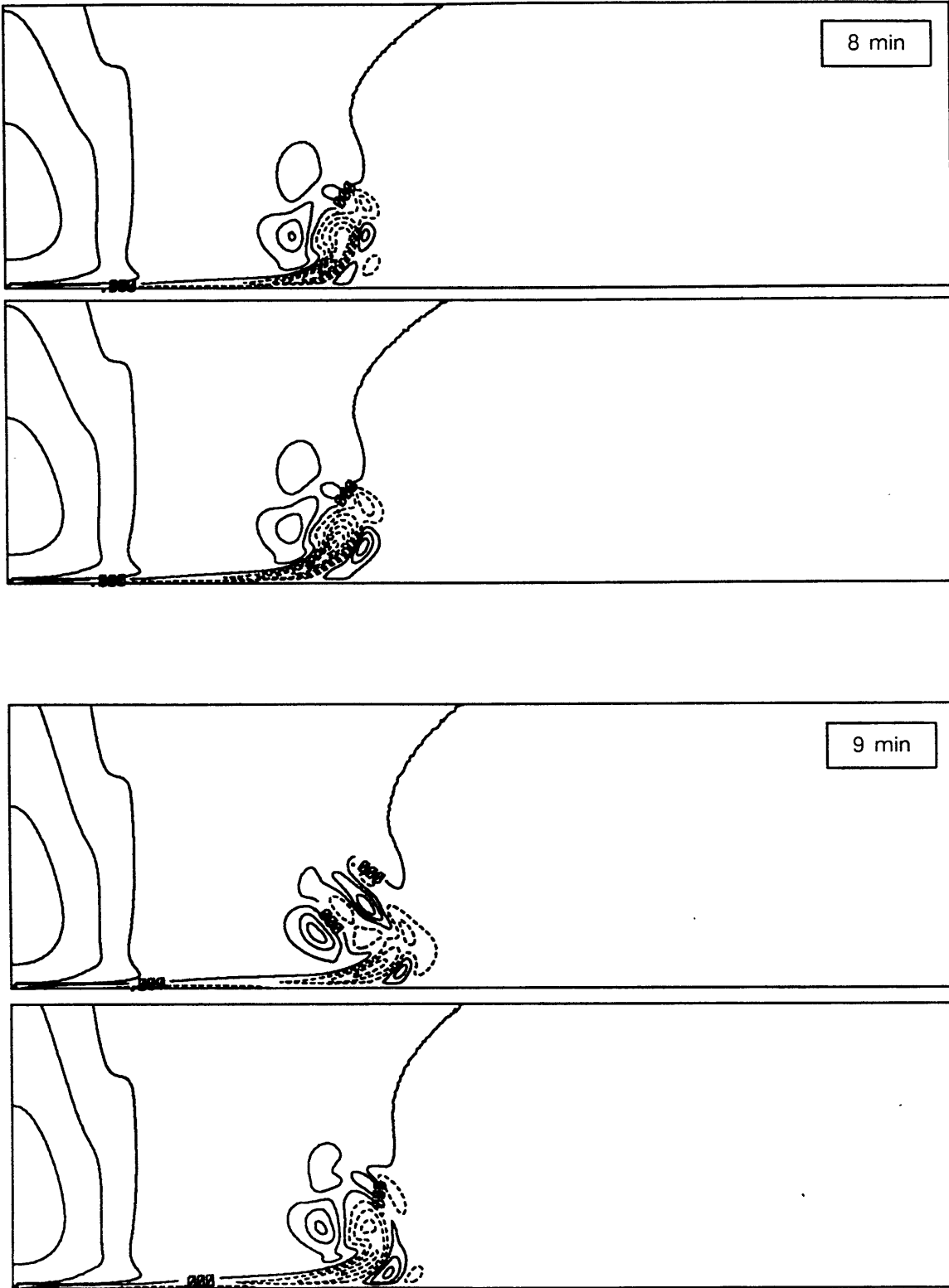


Fig. V-16 (Continued) F factor calculated for a 3° landing glideslope. Values are contoured in increments of 0.1. At each minute, the top panel shows the neutral boundary layer run, the bottom, the stable boundary layer. Minutes 8 and 9 of the simulation are shown.

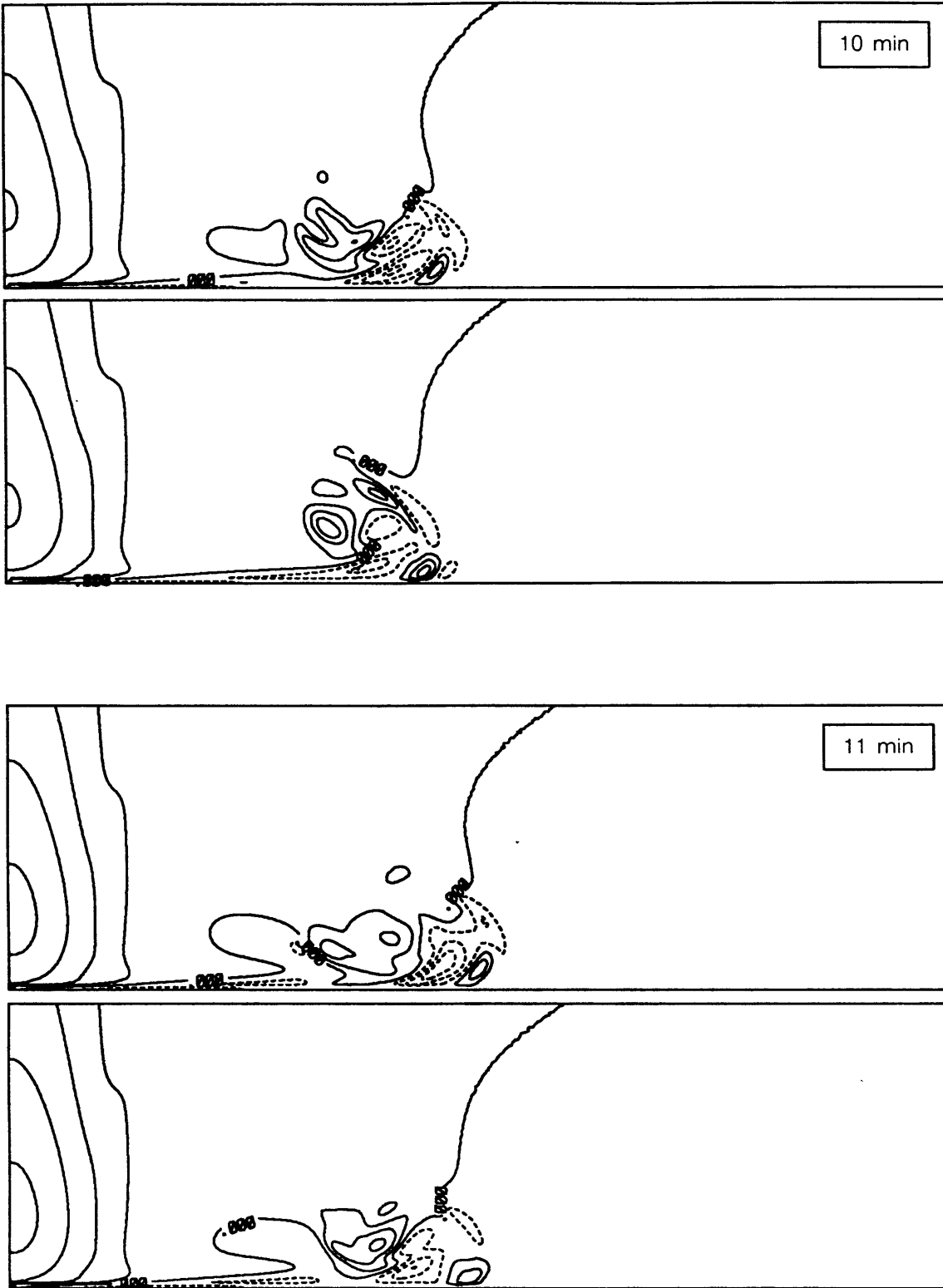


Fig. V-16. (Continued) F factor calculated for a 3° landing glideslope. Values are contoured in increments of 0.1. At each minute, the top panel shows the neutral boundary layer run, the bottom, the stable boundary layer. Minutes 10 and 11 of the simulation are shown.

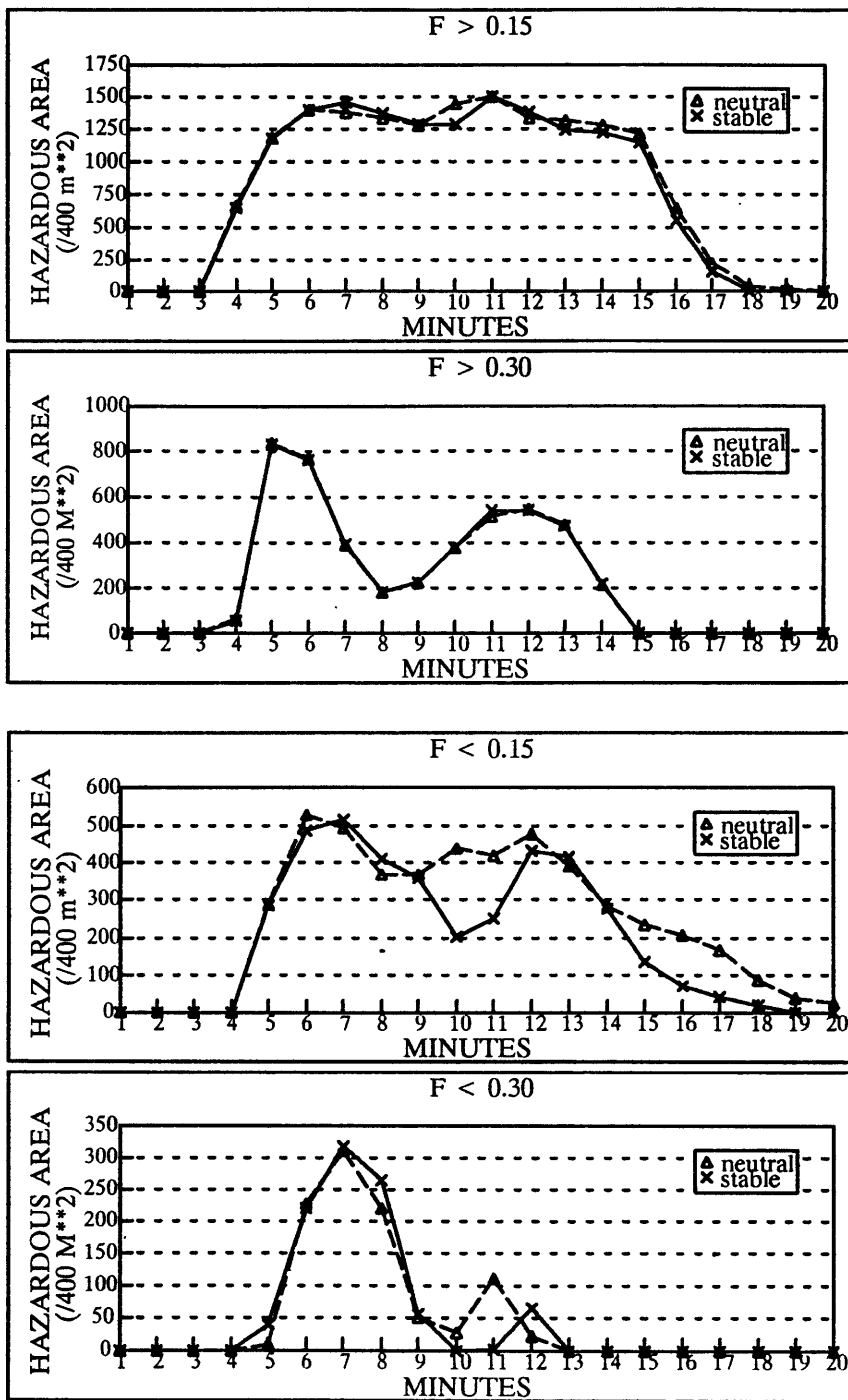


Fig. V-17. Comparison of the hazardous area below 500 m agl in the numerical simulation shown in Fig. V-14. The total cross-sectional area normalized by 400 m² (the area of one model grid point) as a function of model simulation time for positive (performance decreasing) values of F is shown in the top two panels, and for negative (performance increasing) values of F is shown in the lower two panels. The two curves shown in each panel are for the neutral boundary layer and stable boundary layer experiments, as indicated.

identical for the neutral and stable boundary layers. The total performance increasing area (lower two panels) is larger for the neutral boundary layer case because the leading updrafts are stronger, a result of the larger relative temperature contrast across the outflow front.

(iii) Summary

In summary, there is little difference between the flow in the neutral versus the stable layer cases during the first 5 min after thunderstorm downdraft touchdown. During this time the surface winds are strongest and most highly divergent since the outflow diameter is still small. In the later stages, the leading vortex in the neutral case remains in tact, while the stable layer leading vortex splits in two. This could be interpreted as the formation of a multiple ring structure, a phenomenon found not to occur in thunderstorm outflows spreading in neutral boundary layers in Chapter IV.D. The stable layer supports the formation of a nonlinear gravity wave ahead of the outflow and as this wave grows, it draws cold outflow air into its internal closed circulation. In both the stable and neutral boundary layer cases, cold thunderstorm air remains coincident with the leading vortices during the entire simulation. In neither case were short wavelength (~ 350 m) vortices, or any type of flow perturbations similar to those measured in the DFW case, observed apart from the leading vortex formation. A similar experiment performed using a quadrant three dimensional model with the same axisymmetric forcing produced an essentially identical windfield (Anderson and Straka, personal communication). The extra degree of freedom this model provided did not cause any new short wavelength vortices to form within the outflow.

E. Microbursts and Rotors as Solitary Waves

Some of the strongest wind speed measurements attributed to microbursts have been associated with the “rotor” (Fujita 1985). These are identified by short lived bursts of wind (e.g., at a ground anemometer site) suggesting immediately a translating or rapidly evolving phenomenon. Waranauskas (1985) notes that the damage pattern from a “burst swath” within a microburst is sometimes long and narrow, and “is often mistaken as that of a tornado. However, the vector pattern within the swath is uni-directional and divergent, showing few rotational characteristics as found in tornado damage.” Since the structure of these “rotors” is quite similar to that of propagating solitary waves, the past microburst cases attributed to rotor formations are reexamined here to see if propagating waves were involved.

A wind speed measurement over 66 m/s (off the scale) was recorded during the “Andrews Air Force Base” microburst studied by Fujita (1984). From his ground damage survey and the available measurements and eyewitness accounts, Fujita developed the schematic stages of this microburst shown in Fig. IV-17. While the envisioned vortex ring around the “descending microburst” and the explanation for the intensifying vortex ring at the surface were shown to be incorrect in Chapter IV, the presence of very high speed outflow air at the surface at the outer edge of the downdraft and a building vortex ring at the leading edge of the outflow were probably correctly depicted. Figure V-18 shows that expanding outflow air from a previous thunderstorm crossed the air force base approximately 20 minutes before the damaging outflow began. Since temperature was not continuously recorded, the change in temperature associated with this air cannot be confirmed, but it is estimated to have dropped at least 2°C.

The damaging wind event analyzed at Andrews AFB was definitely associated with the outflow from a strong thunderstorm with heavy rain and hail within a multicell storm complex. The most accumulated rainfall was measured 18 km west-southwest of the base, but the center of the cell responsible for the winds at Andrews was estimated by Fujita to be located 5.5 km to the northwest. Estimates of the cell diameter from the radar located over 90 km away ranged from 11 to 22 km but actual values could have been much smaller. If the cell location estimate is correct, then the winds blowing in the opposite direction from the >66 m/s measurement, shown in Fig. V-19, were not associated with the divergent “foot” of the thunderstorm downdraft. However, the sudden increase in winds was accompanied by the onset of heavy rain and some hail. As shown in Fig. II-12, the strongest, most rapidly increasing winds occurred 1.5 km from the storm center for a typical narrow, strong thunderstorm. Radar data showed the Andrews AFB storm complex moving to the northeast at ~25 m/s; if the northwesterly winds of > 65 m/s and the southeasterly winds, 4 min later, of 46 m/s were associated with the divergent foot of the thunderstorm, then the storm radius was between 2 and 3 km. A 30% reduction in wind speed 4 min after the peak winds is consistent with the numerical model results in Fig. II-12. I suggest that the thunderstorm center was located much less than 5.5 km from Andrews AFB; it may well have passed directly over the airport. As discovered in the preceding section, the presence of the thin stable layer at the surface has almost no influence on the windfield at these early stages of outflow development.

A similar outflow vortex caused a boat to capsize on the Tennessee river south of Huntsville on 7 July 1984. As in the previous example, expanding outflow winds from an earlier thunder-

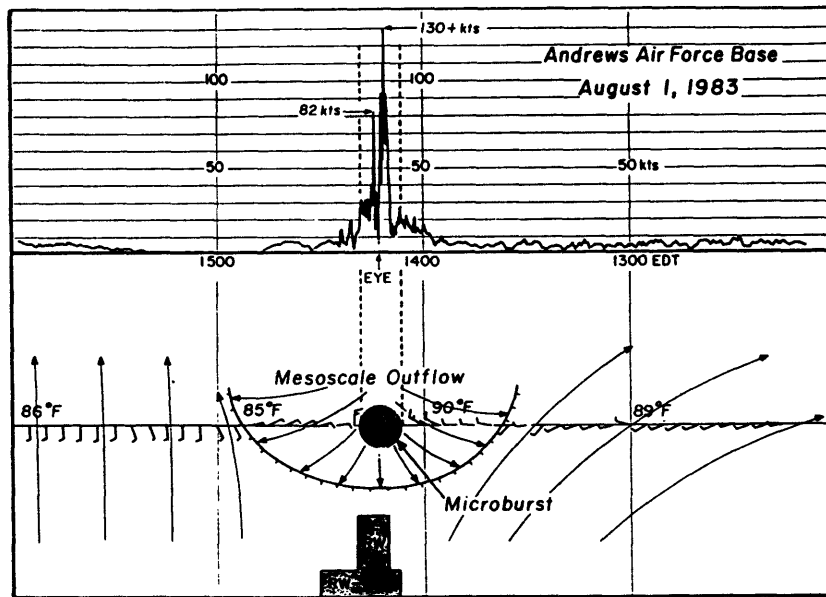


Fig. V-18. Time cross section of meteorological parameters observed at Andrews AFB located just to the south of the rainfall center line. Note that the area of the microburst (black circle) is significantly smaller than the overall area of the mesoscale outflow which affected the air force base. Taken from Fujita (1984).

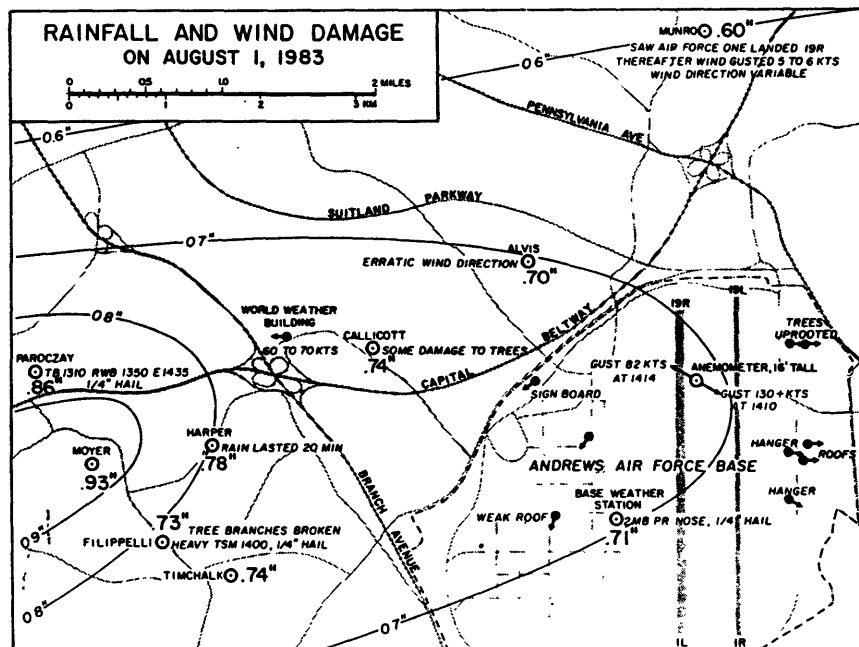


Fig. V-19. Distribution of rainfall and wind damage in and around Andrews AFB caused by the microburst storm on August 1, 1983. Damaging winds are shown by black circles with arrows attached. Rainfalls are in 0.01 inch units. Taken from Fujita (1984).

storm had already spread over the area when a new outflow developed. Fujita's illustration of the storm scenario is shown in Fig. V-20. Rain of an unspecified intensity and a northwest wind began 5 min before the southwest winds capsized the boat. The distance between the storm center and the boat was estimated to be 1 km. As in the previous case, this vortex can not be distinguished from that expected at the leading edge of a cold axisymmetric outflow.

F. Variable Source Strength

Another important mechanism for creating vortices within a density current is the sudden increase or pulsation of the source strength. This could happen in the atmosphere when a single thunderstorm cell produces a second downdraft, or when a new cell in a squall line or multicell storm collapses into the pooled outflow of previously collapsed cells. I believe this is essentially the mechanism hypothesized by Fujita (1986) for the creation of the embedded outflow vortices observed in the DFW accident, although instead of describing the single downdraft as pulsating he envisioned three concentric downdrafts (microbursts) occurring simultaneously, with the central being the coldest and strongest (Fig. IV-1).

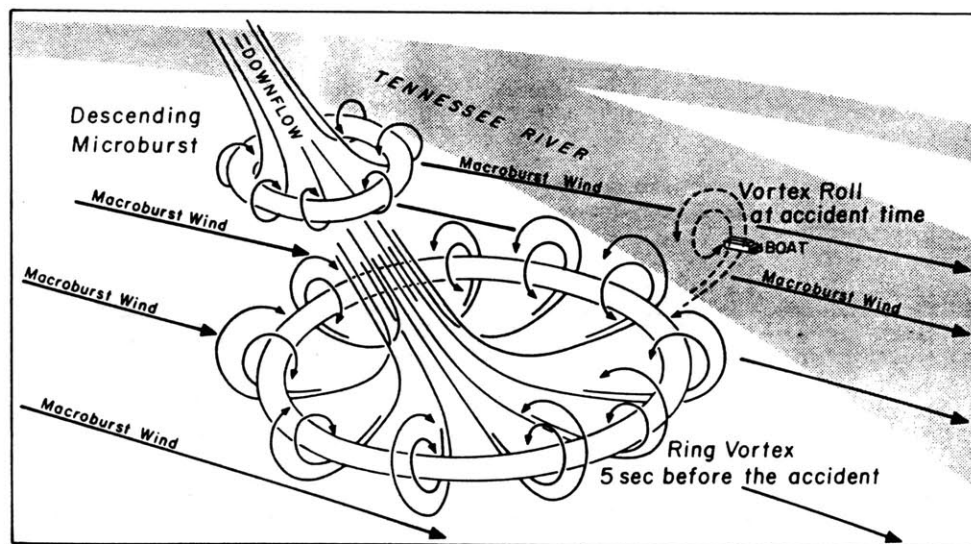


Fig. V-20. A schematic view of the ring vortex which encircles the downflow of a microburst. It is expected that the ring vortex expands rapidly after the touchdown. The boat was hit by south-southwesterly winds as the vortex roll passed by. Taken from Fujita (1985).

1) Observations

Although a number of cases have been reported of multiple consecutive fronts in fjords and river plumes (Chapter IV.D.), a very different type of subfrontal feature was reported by Luketina and Imberger (1987). They studied the tidal outflow from an estuary which forms an unsteady surface buoyant jet or plume in the adjacent bay on each outgoing tide. In one case, the density profile within the plume revealed a "subfrontal feature" 90 m behind the leading edge of the plume. The time series of density profiles (Fig. V-21) shows that the subfront formed behind the main front (a), and then moved toward and into the leading frontal structure (b). The main frontal region then sharpened and strengthened (c). A new subfrontal feature had formed 18 min

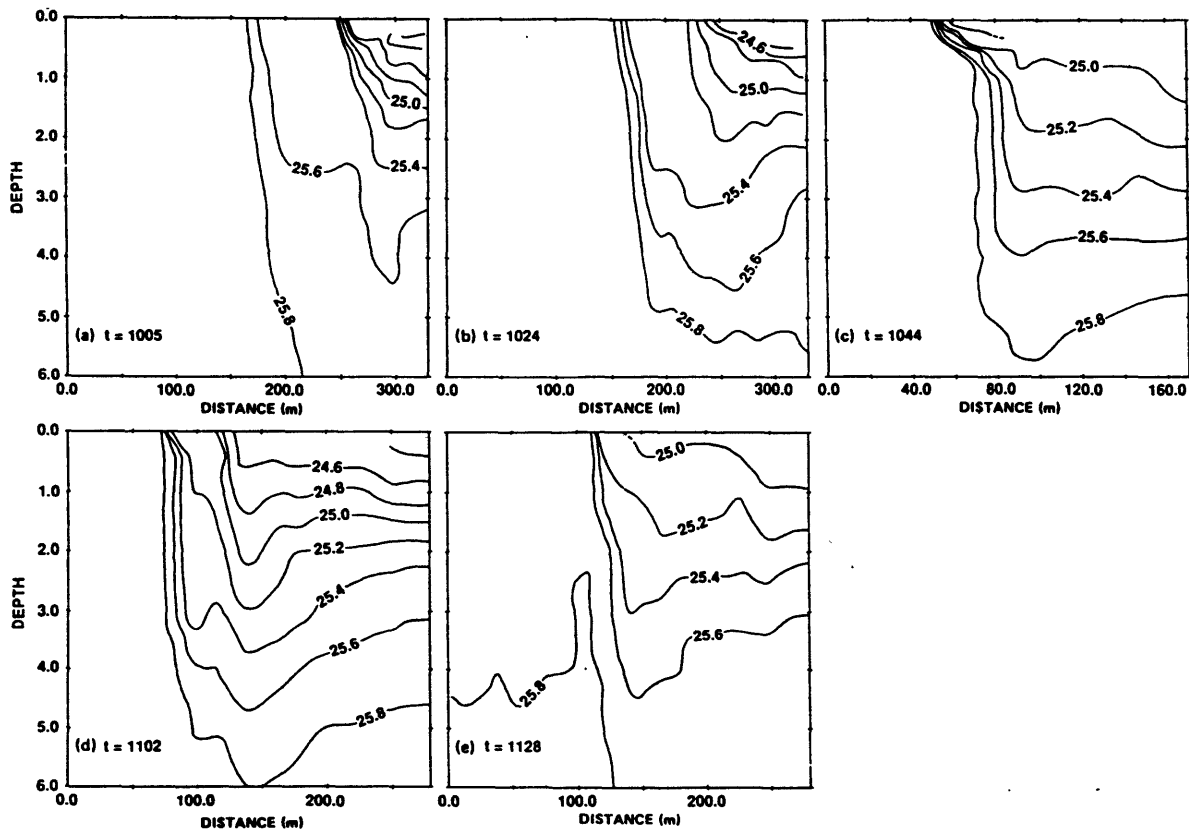


Fig. V-21. A series of density (kg/m^3) sections across the front on September 22, 1984, by the yo-yo method at (a) 10:05 hrs, (b) 10:24 hrs, (c) 10:44 hrs, (d) 11:02 hrs, (e) 11:28 hrs. The maximum data spacing in the horizontal is about 12 m with an average of 6 m, whilst that in the vertical is 0.02 m. Each section took approximately 5 min to collect. Taken from Luketina and Imberger (1987).

later (d), about 50 m behind the main front. Shortly thereafter, a strong gusty wind began and caused vertical mixing that diluted the density differential across the front. As noted by Luketina and Imberger, this behavior is in distinct contrast to the observations of consecutive multifrontal structures described in Chapter IV.D. They hypothesize that short period seiching in the bay created perturbations in the flow which lead to the subfrontal features.

In the atmosphere, these subfrontal features have been called "rotor microbursts" (Fig. I-4). Fujita (1985) states that "some rotor microbursts develop inside macrobursts behind their gust fronts". The horizontal rotor formations in the outflow of a multicell thunderstorm that occurred on 30 June 1982 in the JAWS observation network have been discussed by Waranauskas (1985), Fujita (1985), and Kessinger et al. (1988). In this case, four rotors within a larger, expanding outflow could be identified (Fig. V-22). Surface winds outside the storm cell in the vicinity of the rotors were northwesterly, under the influence of the larger scale outflow. However, at 1.25 km agl, the environmental winds were from exactly the opposite direction. This created a low level opposing flow (Fig. V-7) and probably explains why it is only in this limited direction that the rotors appear to persist. Because of this, the geometry of these waves evolved from circular to more linear as wave energy was preferentially trapped.

Enough data were available to observe the formation of rotors R3 and R4. They were formed as the outflow from the main cell began. R3 was formed first at the leading edge of the outflow, began to separate away as the downflow portion of the vortex developed, and R4 formed immediately behind it. The region of downflow contributing to the formation of R3 as a separate vortex is not clearly distinct from the downdraft of an "outflow cell", shown by a 35 dBZ contour in the bottom panel of Fig. V-22. As R4 separated from the main cell, a linear, parallel patch of strong surface divergence, approximately as strong as that under the main cell downdraft, was created behind it. The rotors R3 and R4 were observed close to the parent cell and were indistinguishable from the expected leading edge vortex formation. The thin layer of dense outflow air covering the surface did not appear to have a significant influence on the new vortex development. No data were available showing the propagation speeds of the vortices, or the surface conditions created as they moved away from the storm.

The tower measured vertical velocities at the leading edge of the squall line outflow case studied by DiStefano (1983) and Wolfson (1983), shown in Fig. V-23, appears to have a similar structure to the undular bore case illustrated in the top panel of Fig. V-8. Yet there was no evi-

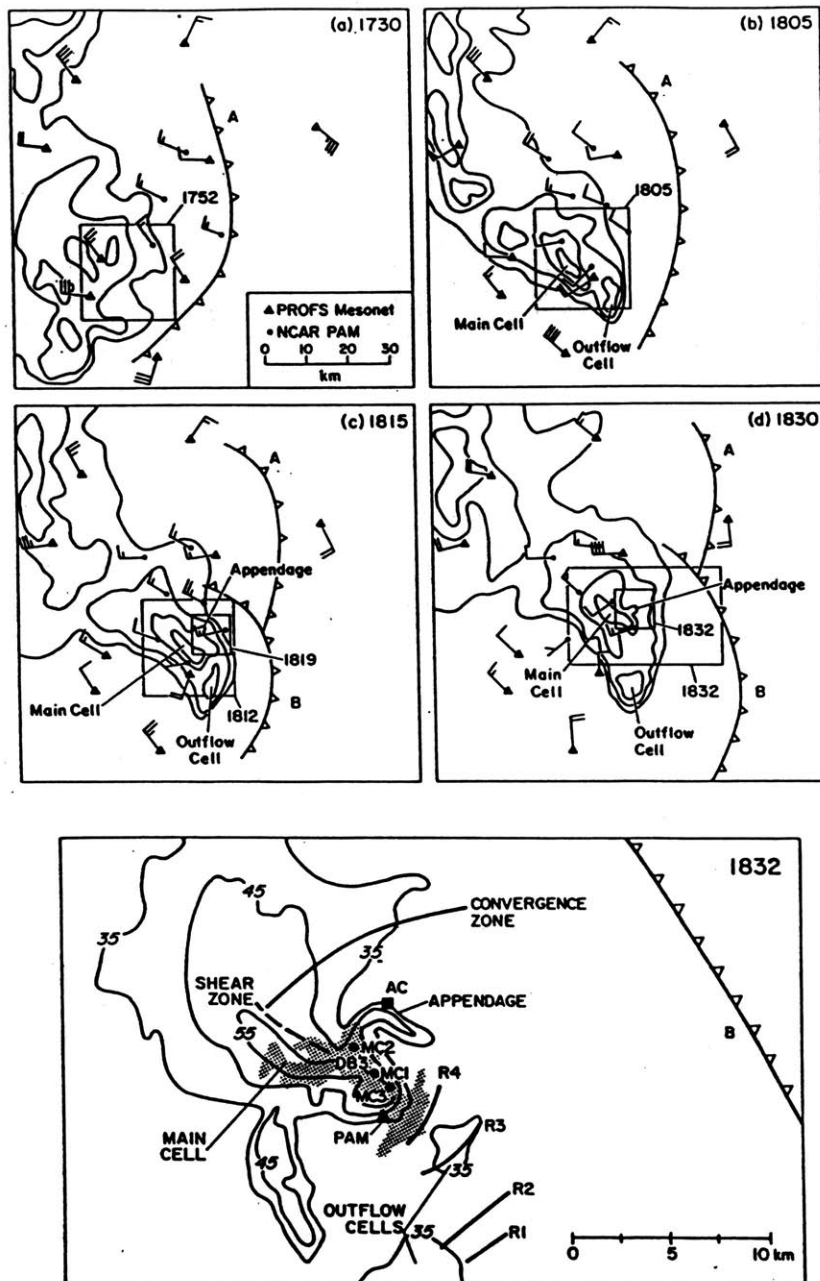


Fig. V-22. (Top) The evolution of the main cell, shown at (a) 1730, (b) 1805, (c) 1815, (d) 1830. Reflectivity at 500 m agl is contoured at 10, 30, 45, and 55 dBZ. Storm features are labelled. Surface mesonet winds are plotted (full barb = 5 m/s). Locations of gust front boundaries A and B are shown. Doppler analysis domains are indicated by boxes labelled with the analysis times. The large box in (d) labelled 1832 is the area covered by the bottom figure. (Bottom) Composite illustration of storm features at 1832. Labelled features are discussed by Kessinger et al. (1988). Of primary interest are the horizontal rotors R1, R2, R3, and R4. The shaded area represents divergence > 5 m/s per km. The location of the PAM station affected by R3 and R4 is shown. Taken from Kessinger et al. (1988).

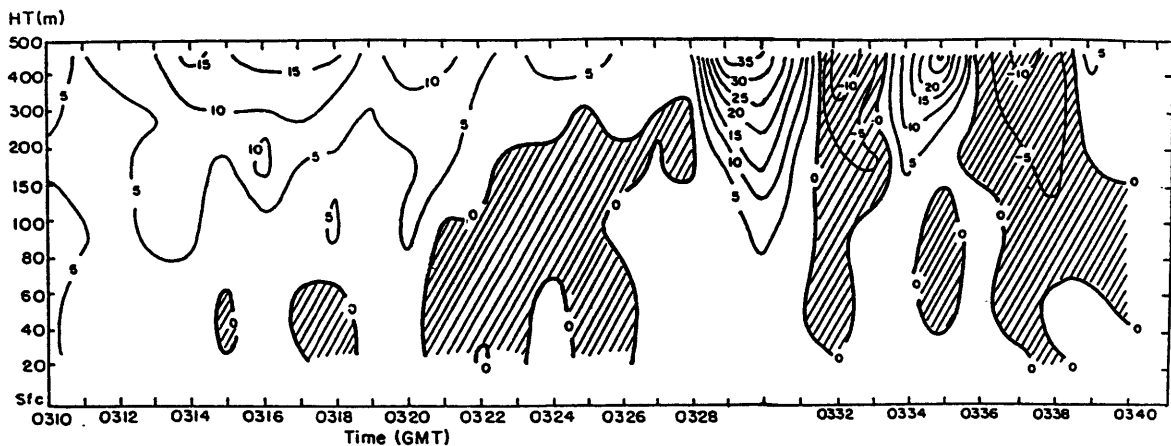


Fig. V-23. Vertical velocity measured by the NSSL 400 m tall tower in Oklahoma on 13 April 1981. The data is contoured in units which, when multiplied by 0.023, equal the vertical wind speed in m/s. The leading edge of the gust front passed the tower at approximately 0328 GMT. Taken from DiStefano (1983).

dence that the boundary layer in advance of the gust front was stratified. The gust front was formed by the pooled outflow from cells in a squall line, and a large cell had recently contributed fresh outflow. This low altitude wave like structure may have been caused by the surge in outflow from this cell. The other possibility is that the boundary layer actually was stratified and the event could be interpreted an undular bore, similar to the Mueller and Carbone (1987) and Fulton et al. (1990) cases. Perhaps reexamination of the data from this case would reveal the correct interpretation of this wave structure.

2) Laboratory Experiments

Maxworthy (1983) performed laboratory experiments in which the flow rate into an advancing submerged gravity current was suddenly changed from a constant value to another much higher value. He found that "a sequence of solitary waves, ordered by amplitude, was formed and these propagated on the interface between the two fluids until they reached the nose. At this point the latter became more bulbous" and the entire gravity current front began propagating more rapidly. Thus, even when a dense outflow is propagating into a neutral environment, finite-amplitude nonlinear, dispersive waves with their closed circulations can still arise within the current if the flow rate is suddenly increased. If the flow rate is gradually increased instead, Maxworthy suspects that dispersion will be less important and that solitary waves will not form.

3) Numerical Experiments

Two axisymmetric numerical experiments were performed, again with Anderson's (1990) model, to determine the influence of variable source strength on the internal outflow structure of an isolated cylindrical thunderstorm. In each experiment, the horizontal and vertical grid resolution was 75 m, the time step 0.5 s, the domain 300 grid points wide by 100 high, and the eddy diffusion coefficient $40 \text{ m}^2/\text{s}$. The environmental lapse rate was dry adiabatic (300 K) up to 5 km agl, and stable above (4 K/km). The cooling source was Gaussian in shape, with a radius of 1.5 km, and a depth of 4 km, centered 3.75 km above the surface. The cooling function for each experiment is shown in Fig. V-24.

The first two cycles of the pulsing experiment (12 min) essentially created the surface outflow. The cold air pulse created by the cooling cycle that peaked at 13.5 min can be followed as it falls into the preexisting outflow and moves toward the front (Fig. V-25). By 20 min, a distinct subfrontal feature has formed, and it is clear from the time evolution that it propagates relative to the surrounding current toward the front. By 22 min into the simulation, another sharpening pulse of cold air from the cooling maximum at 19.5 min can be seen beginning to move out into the current. Each pulse has a horizontal circulation associated with it that is less intense than, but in the same sense as the circulation associated with the gravity current front. By 26 min, the 13.5 min pulse has reached the front. The next panel shows that this colder air undercuts the main part of the leading head and strengthens the temperature gradient at the front. Also by this time, a new cold pulse can be seen flowing toward the front. The overall behavior of this flow suggests that the seiching hypothesis of Luketina and Imberger (1987) may well be the explanation for the transient subfrontal features they analyzed.

In the step cooling experiment, the initial stages are uneventful as the gravity current becomes established. At 12 min, the cooling is increased by a factor of three and then held constant for three minutes. This step increase in actual cooling was 2.4 times larger than the pulses in the previous experiment because the base cooling rate was slightly smaller. A time sequence of the perturbation temperature field is shown in Fig. V-26. By 16 min, the sharpening of the new cool air into a subfrontal feature has taken place. The bulge of cold air continues to sharpen and increase in amplitude until it encounters the downflow in the wake region of the head (18 min). It then "slides under" the head, rapidly increasing the temperature gradient at the leading edge and creating a protruding nose. This overhanging nose at 20–21 min rapidly collapses to the surface

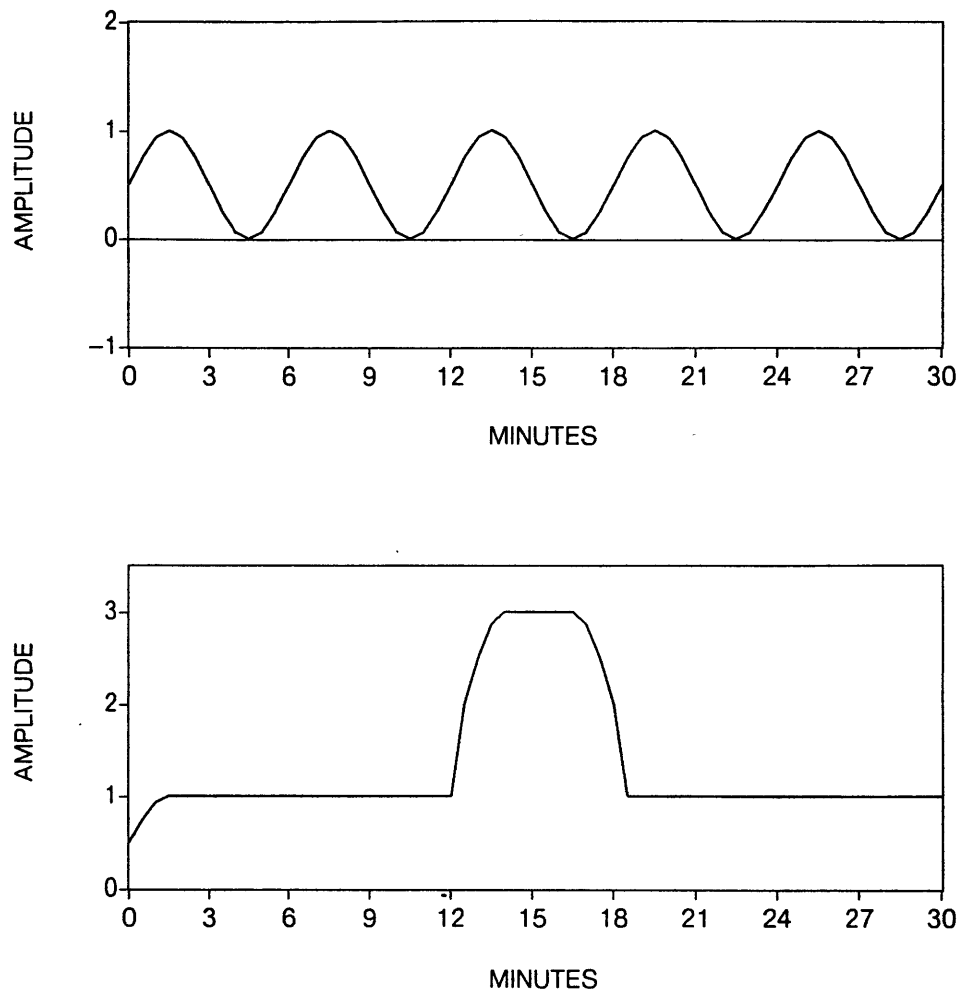


Fig. V-24. The shape of the cooling functions for variable flow rate experiments are shown. (Top) Pulsating cooling function. Base cooling rate was $-0.05\text{ }^{\circ}\text{C/s}$. (Bottom) Step cooling function. Base cooling rate was $-0.04\text{ }^{\circ}\text{C/s}$. The experiments continued for 30 simulated minutes.

because it contains very dense air. This colder air continues to propagate relative to the rest of the current and gradually changes the shape of the leading edge.

The sudden change or pulsation in flow rate appears to be a plausible explanation for certain vortices or secondary surges within thunderstorm outflows. The notion of a pulsating downdraft is one of the most common hypotheses for multiple surges in thunderstorm outflows (e.g., Srivastava 1967; Kessler 1982; Klinge 1987); the surge separation time would be on the order of 20 min if the cause of pulsation was cell redevelopment. With the high frequency pulsating cooling function (indicative of secondary downdraft fronts within the same cell, not cell redevelopment), vortices

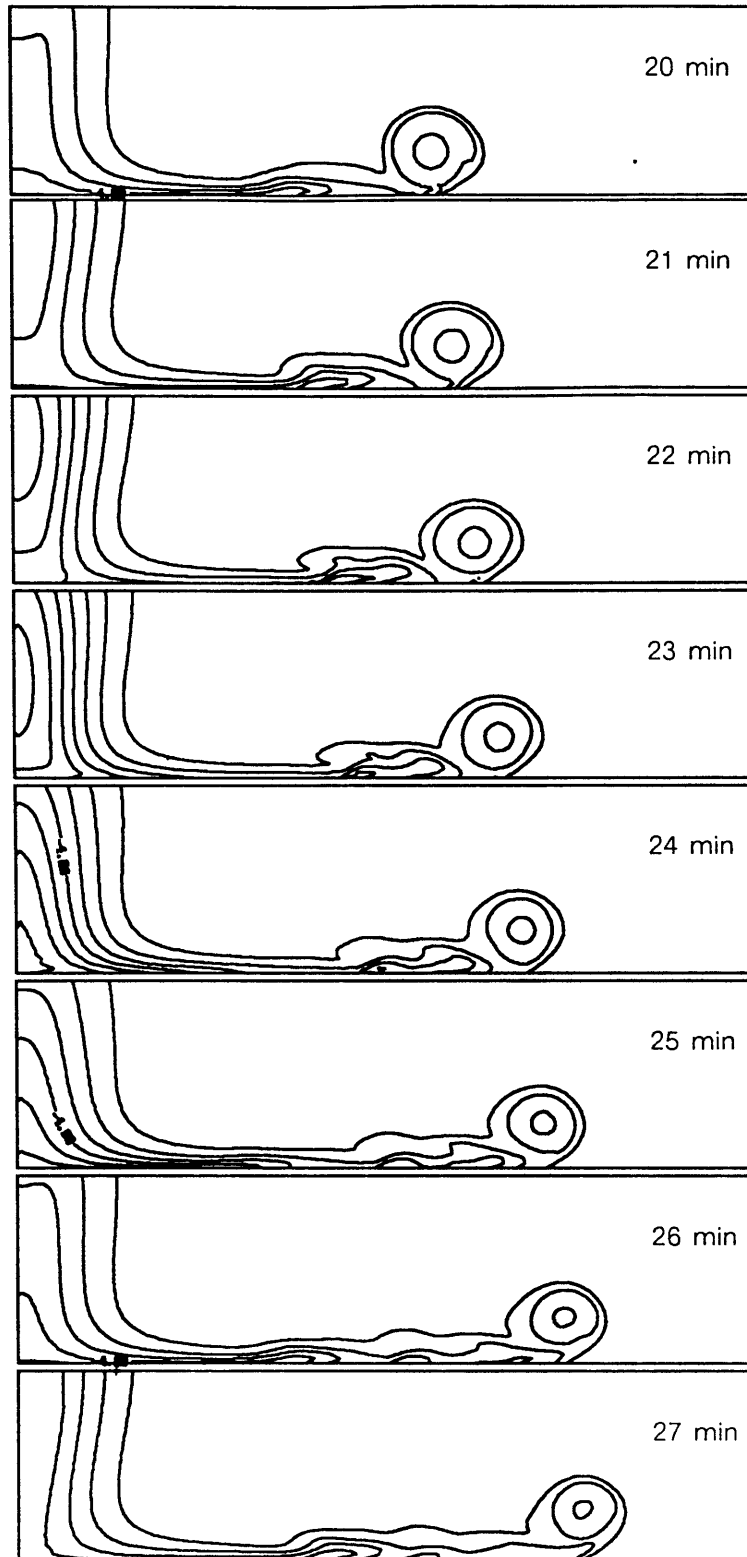


Fig. V-25. Pulsating cooling experiment. The flow is shown every min from 20 min to 27 min into the simulation. Potential temperature perturbation is contoured every 1°C ; coldest contour shown is -7°C at minutes 23 and 24. Domain shown is 12 km wide and 3 km high

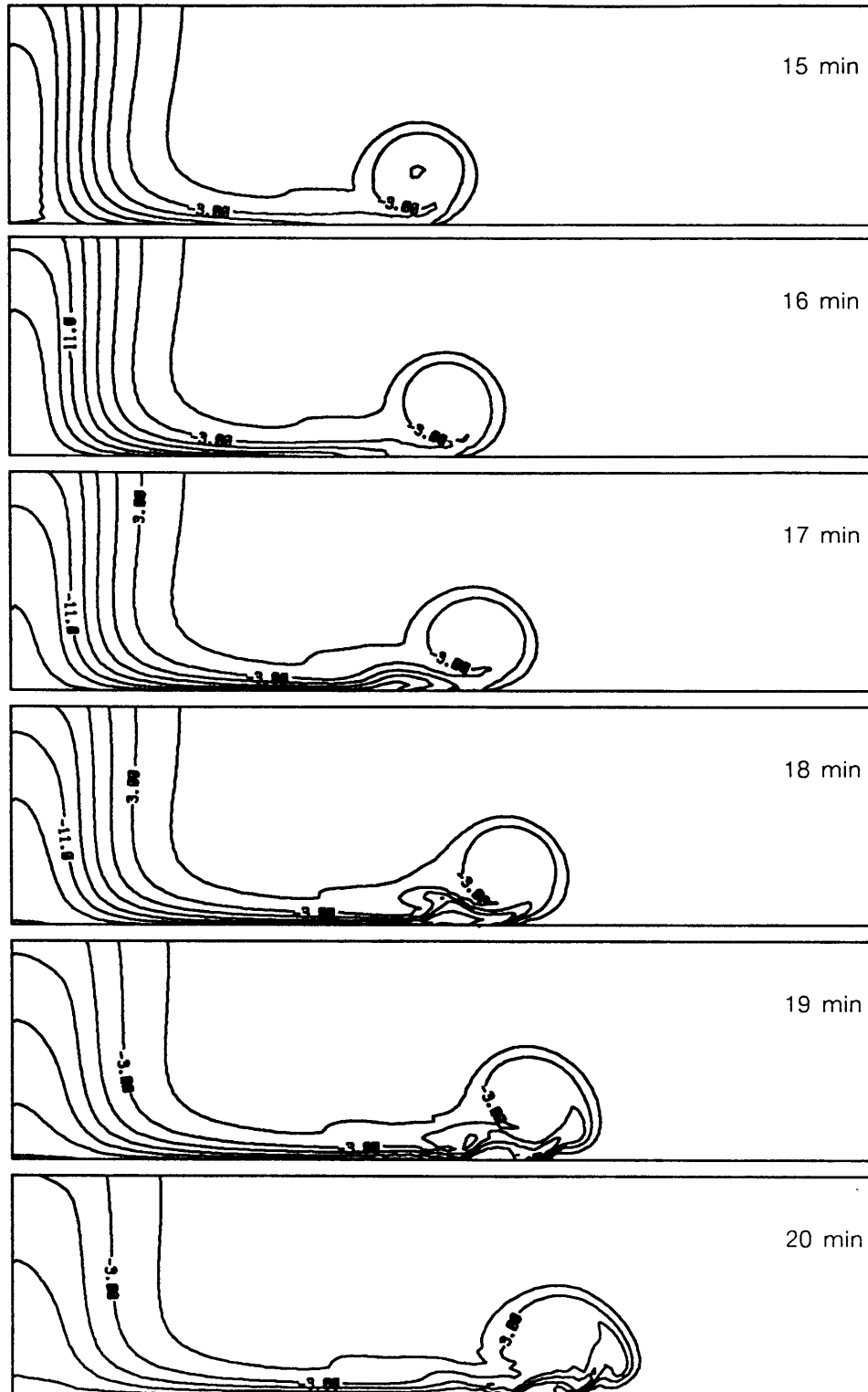


Fig. V-26. Single step cooling experiment. The flow is shown every minute from 15 min to 26 min into the simulation. Potential temperature perturbation is contoured every 2°C ; coldest contour shown is -15°C at minutes 15 and 16. Domain shown is 12 km wide and 3 km high.

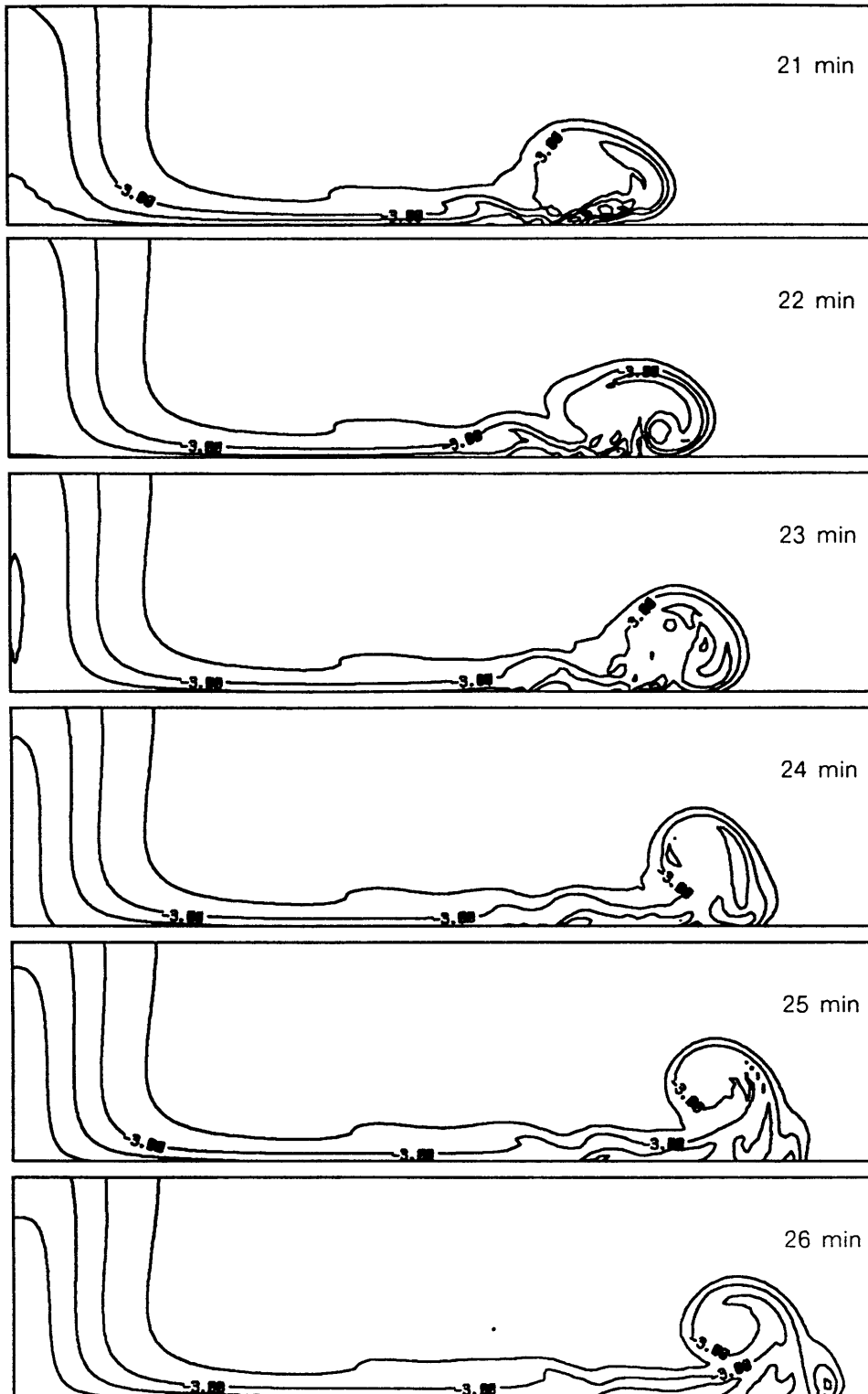


Fig. V-26. Single step cooling experiment (continued). Minutes 21-26 are shown. Potential temperature perturbation is contoured every 2°C . Domain shown is 12 km wide and 3 km high.

were created roughly 2 km apart well away from the downdraft. But the wavelength of the DFW vortices was ~ 350 m, and the waves occurred either within or just beyond the downdraft. It appears as if Fujita's hypothesized concentric downdrafts cannot explain the observed DFW vortices.

One other possibility is that even higher frequency pulsations typically occur in heavy precipitation driven thunderstorm downdrafts. The distribution of recorded precipitation as a function of time was compared with the measured peak wind speed at three stations during a typical "air mass" thunderstorm event (Fig. V-27). If increases in rain rate imply increases in the downdraft speed, then these should translate into increases in horizontal wind speed. There is indeed a correlation between rain rate and wind speed, and the major surges in rain rate appear to come about 4-7 min apart. The DFW raingage data show a strong rain surge at 1825 CDT, then a lull of about 5-6 min, and then a heavier burst of rain (Fig. V-28). Even though these rainfall data were not recorded exactly where the accident took place, they should be representative of the type of rainfall pattern experienced elsewhere. The simulated pulsation frequency in the numerical experiment described here was representative of what typically occurs in isolated airmass thunderstorm cells. Fujita's (1986) hypothesis that three separate but concentric downdrafts occurring nearly simultaneously were the cause of the embedded outflow vortices appears to be incorrect.

G. Summary

In this chapter, meteorological observations of solitary waves and undular bores generated by thunderstorms were reviewed to determine if they could be the identity of some of the low altitude downdrafts and short lived surface wind speeds characteristic of microbursts. All of the published cases examined solitary waves far from the generating thunderstorm, and while a surface wind speed peak remained, these events were *not* particularly noted for causing ground damage. They do represent a significant clear air and elevated wind shear hazard to aviation. Because they are so stable and long lived, they can be found in unexpected places far from thunderstorm activity. The observational evidence showed that linear or one dimensional solitary waves can persist for hours when a mechanism exists for trapping gravity wave energy, in particular a low level opposing jet-like wind structure.

The stratification of the boundary layer influences the structure of gravity currents well before the nonlinear waves have completely moved ahead of the cold air. There are many published studies of gust fronts that have not correctly interpreted the observed structure because no account

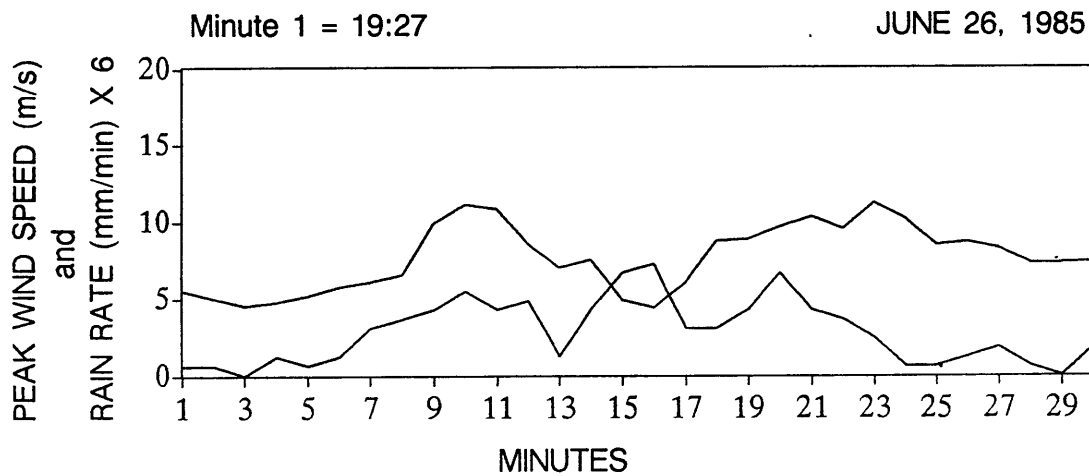
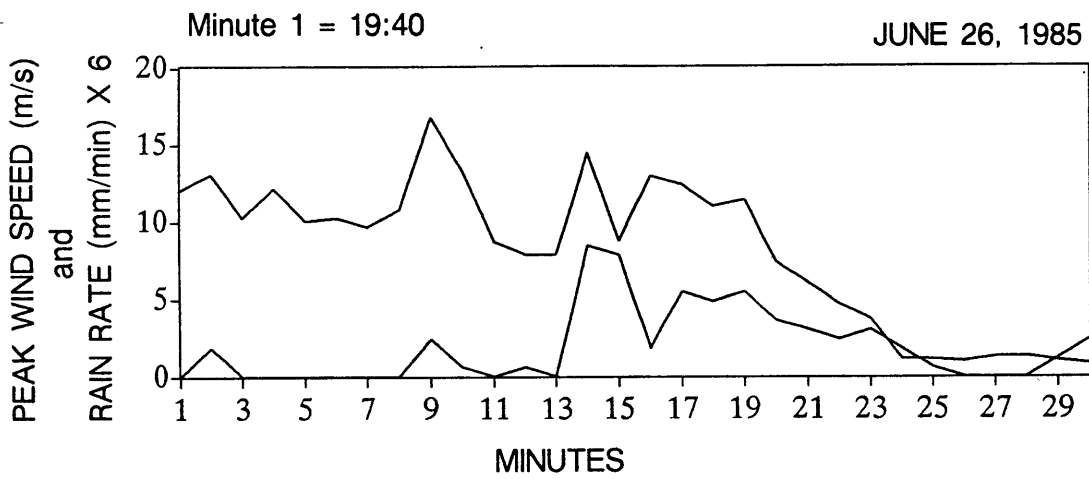
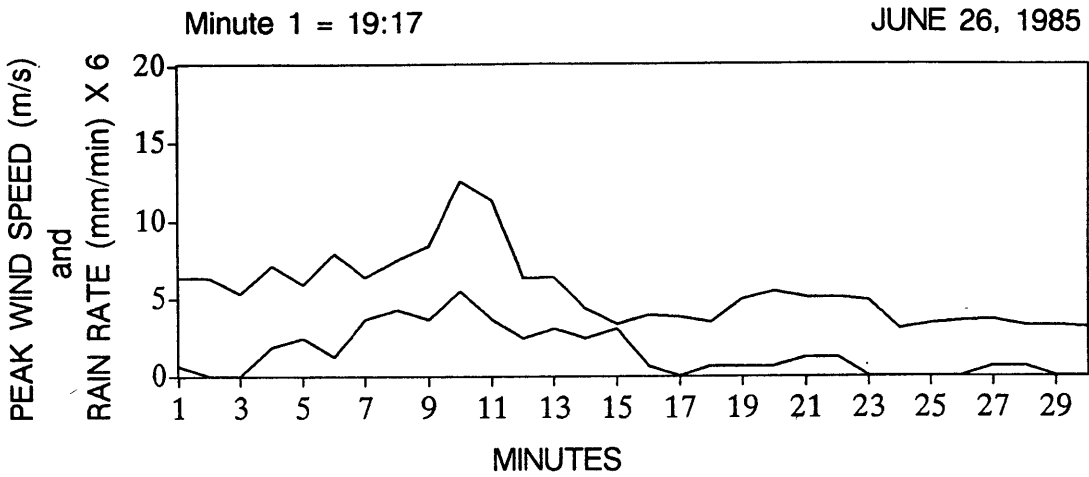


Fig. V-27. Peak wind speed (top curve) and rain rate during three rain and wind events recorded on June 6, 1985 at three different stations in the FLOWS mesonet. These curves illustrate a natural fluctuation within these events of 3-6 min.

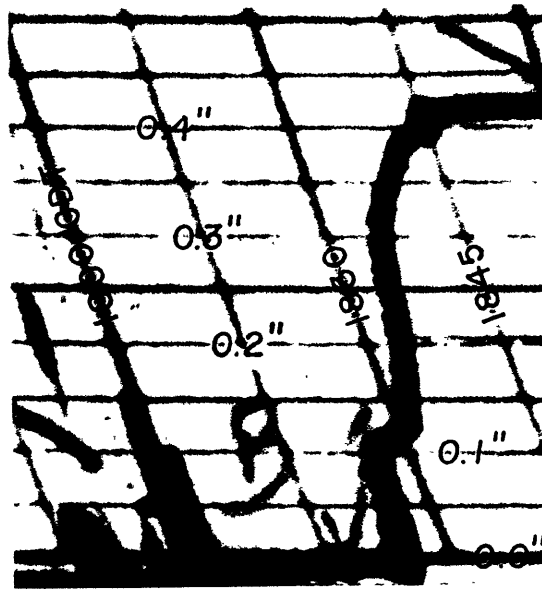


Fig. V-28. Raingage trace from the National Weather Service DFW airport office at the Delta hangar. Taken from Fujita (1986).

was taken of the ambient stratification. These undular gravity currents with secondary surges can have very strong surface winds associated with them; they can be identified with the events sometimes called downbursts or derechos because of their large scale, straight line wind patterns. They can be especially hazardous when they are fed by the pooled outflow of a number of cells that are continually forming new outflows; these surges in source strength cause strong downdrafts at low altitudes and add to the already strong ground relative winds.

The amplitudes of cylindrical solitary waves generated by isolated thunderstorms decay rapidly with time, so it is not expected that they will pose a problem far from their source. This conclusion was based on study of the cylindrical BDO equation, derived here for the first time in Appendix C. Its time dependent behavior was compared with that of the BDO equation and of the CKdV equation in Appendix B.

The numerical simulation of newly formed outflow from axisymmetric thunderstorms showed that during the early stages (first 9 min), there were almost no differences in the flow evolution between the neutral and stable layer cases. Eventually the leading edge vortex formation split into two distinct vortices in the stable layer case, and became more diffuse than the same formation in the neutral boundary layer case. At the same time, the winds were not weaker as might be expected from the smaller temperature contrast across the front. This has been known

for many years, but its significance has not been fully recognized (Fig. V-29). The cold air was advected 15-20% more rapidly in the stable layer case than in the neutral case. In neither case were short wavelength vortices were observed within 3 km of the main storm downdraft; the vortex formation itself was the only feature that had oscillations on a small horizontal scale. This means that the conceptual drawings of the DFW thunderstorm outflow by Fujita (1986; Fig. IV-1), and Caracena et al. (1986; Fig. IV-2) cannot be correct. It was determined that the microbursts attributed to "rotors" were caused by the winds associated with the early stages in the formation of the leading edge vortex ring structure characteristic of axisymmetric outflows, and the presence or absence of a stable layer at the surface made essentially no difference.

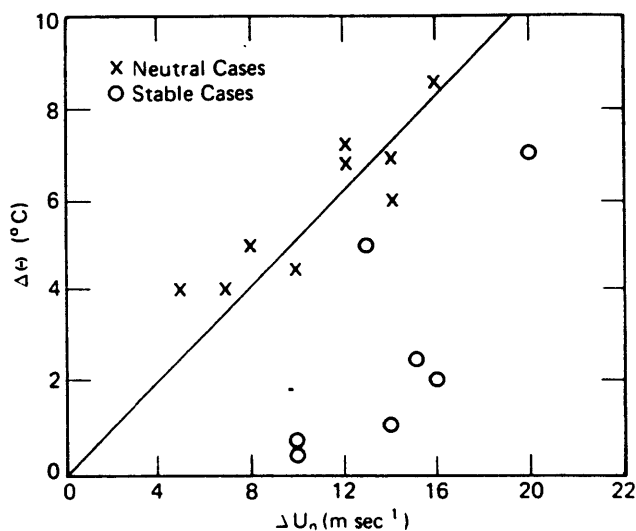


Fig. V-29. Horizontal wind change vs. surface temperature decrease for neutral and stable cases studied by Goff (1975) as determined by Greene et al. (1977).

VI. ANOTHER LOOK AT THE FATAL MICROBURST AIRCRAFT ACCIDENTS

In the preceding chapters, I have discussed a number of dynamically distinct phenomena that have been referred to as microbursts. The precipitation driven thunderstorm downdraft, the penetrative downdraft, the leading edge vortex in axisymmetric outflows, the occlusion downdraft, and the undular gravity current are all causes of strong low altitude downdrafts in or near thunderstorms. The point, however, is not really to explore low altitude downdrafts in general, but to figure out what the meteorological identity of the wind shear that caused the fatal aircraft accidents really was. In this chapter, I take another look at the three accidents in this country attributed specifically to microburst wind shear that have caused all of the fatalities.

A. DFW

The most recent aircraft accident attributed to microburst wind shear was the crash of Delta Flight 191 at Dallas/Ft. Worth airport on August 2, 1985. Summaries of the case have been written by Fujita (1986) and Caracena et al. (1986). Very careful attention was given by Bach and Wingrove (1986) and Wingrove and Bach (1987) to correctly deriving the winds through which the aircraft flew. There was a digital flight data recorder on board the aircraft, so the measured normal, lateral, and longitudinal accelerations, the roll, pitch, heading, and attack angles, the pressure altitude, indicated airspeed, elevator and rudder deflections, and engine thrust were all recorded as a function of time, at frequencies ranging from 4 times per second to once every four seconds. The results of the Bach and Wingrove analysis are shown in Figs. VI-1 and VI-2. The aircraft was flying from the north toward the south to land on runway 17L, the left runway headed toward 170° azimuth.

The conceptual models of the vertical cross section through the DFW windfield drawn by Fujita and Caracena et al. have already been presented in Figs. IV-1 and IV-2. Also presented in Fig. IV-1 is Fujita's conceptual plan view model, with the center of his three concentric downdrafts 0.15 km west of the runway approach, and 3.5 km north. The overall storm radius was 2.1 km. Caracena et al. placed the microburst center 0.5 km west and 3.6 km north of the runway, with a 2 km radius (Fig. VI-3), and Proctor (1988b) placed the microburst center 0.6 km *east* and 3.5 km north of the runway, with a radius of 2 km (Fig. VI-4).

Using his axisymmetric numerical model simulations of an isolated thunderstorm shown in Fig. IV-23, Proctor determined that his model data at 10.5–11.25 min into the simulation best

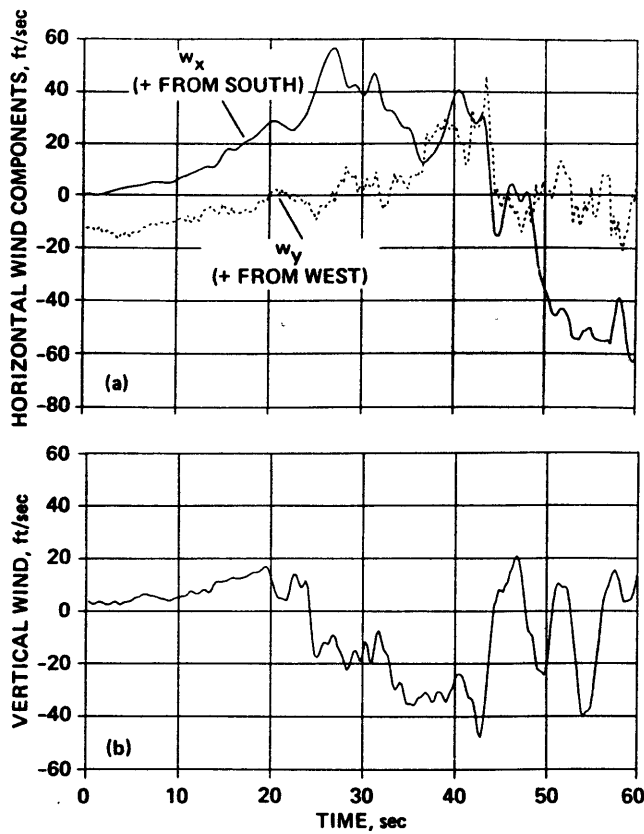


Fig. VI-1. Flight path wind estimates (last 60 s). (a) Horizontal components; (b) vertical component. Taken from Bach and Wingrove (1986).

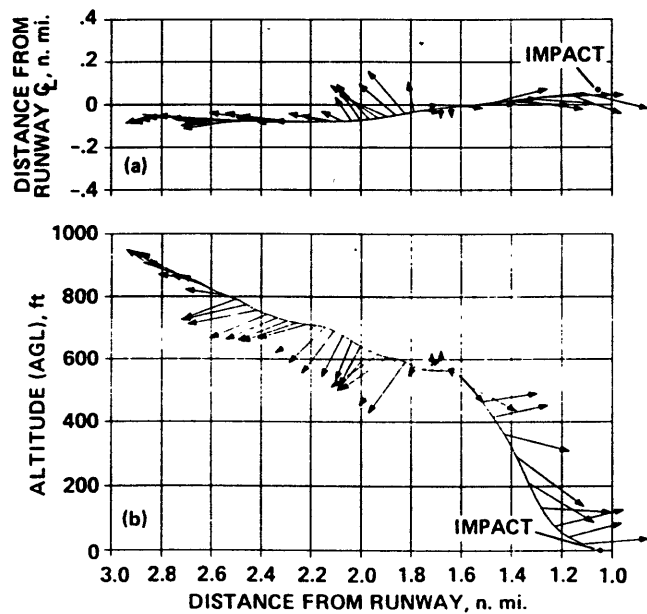


Fig. VI-2. Flight path wind vectors (last 44 s). (a) Seen from above; (b) seen from west. Taken from Bach and Wingrove (1986).

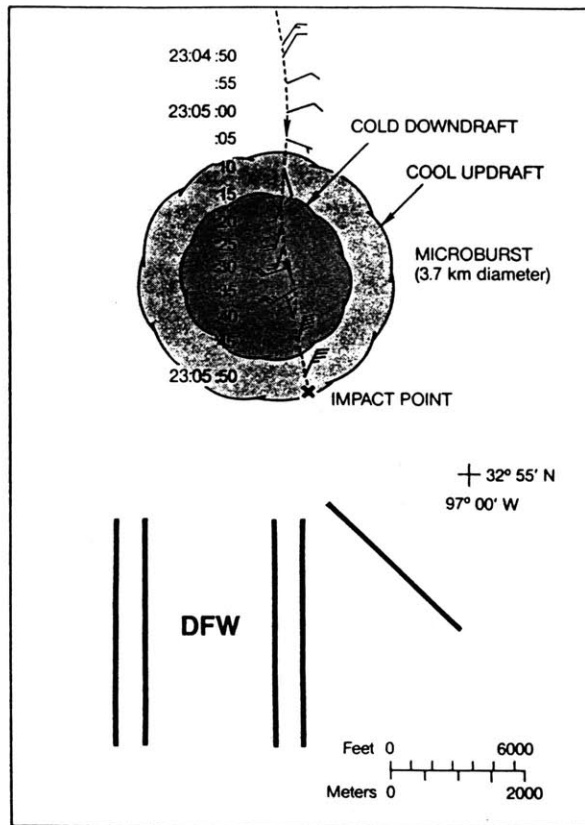


Fig. VI-3. A conceptual model of the horizontal airflow structure in the DFW microburst, based on the analysis of flight recorder data by Bach and Wingrove (1986). Dashed line represents aircraft track. Taken from Caracena et al. (1986).

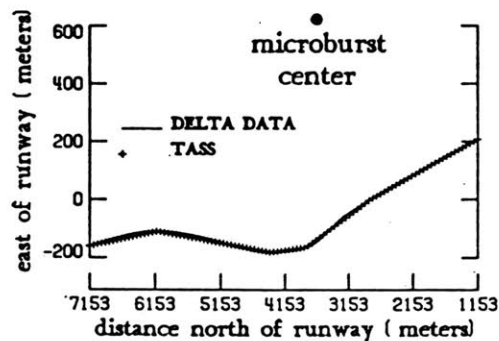


Fig. VI-4. Relative location of the Delta 191 flight path to the runway end and microburst center. TASS is the numerical model data. Adapted from Proctor (1988b).

matched the observations (top panel in that figure). The comparison of the actual data profiles and Proctor's model profiles are presented in Fig. VI-5. Notice however, that short wavelength fluctuations, the famous "vortices", were completely missed. Also, the east-west wind components are not plotted with the others, probably because with the hypothesized microburst center to the east of the runway, the model data and the aircraft data show opposite trends.

I have shown that none of the hypothesized conceptual models or the numerical simulations can account for the observed DFW vortices. I have also shown, through the numerical simulations performed in Chapter V.D., that short wavelength vortices are not found within the strong outflow winds of a newly formed outflow, even when that outflow impacts and propagates through a thin surface stable layer. The quadrant model simulation (Anderson and Straka, personal communication) showed that the missing coordinate in the axisymmetric model was not the reason vortices were not found. What, then, is the explanation for the measured DFW wind and temperature fields?

The answer may be that Delta 191 flight encountered *two* thunderstorm outflows during the last 90 s of its flight! One storm was located 1 km west and 3.4 km north of the DFW runway, and had a 2 km radius. This is the storm thought to be the only storm present by all other researchers. The second storm was 6 min older, and was located 7.2 km north and 2.1 km east of the DFW runway, and had a 4.75 km radius to the leading edge updraft. The radius to the downdraft at the back of the leading vortex was 4.0 km.

To prove that this could indeed be the resolution of the "vortices" mystery, the numerical simulations performed in Chapter V.D. are compared with the Delta data in Fig. VI-6. The 4K stable layer found to be present based on the air temperatures encountered by Delta 191 was actually the outflow from the second, older storm. Thus, while the older storm may have fallen into a weak stable layer, it did not fall into a stable layer 4K colder than the neutral boundary layer air above. For that reason, the neutral boundary layer model simulation was used for the older, distant storm (11 min simulation), and the stable layer model simulation for the newer, closer storm (5 min simulation; see Fig. V-14). The distant storm provides the oscillations in vertical velocity and temperature, and a sizable downdraft and increase in tailwind (V negative). The closer, younger storm provides the strong downdraft and tailwind, plus the cross wind blowing from west to east. The plotted dataset from Delta 191 ends at the last wind measurements, but the

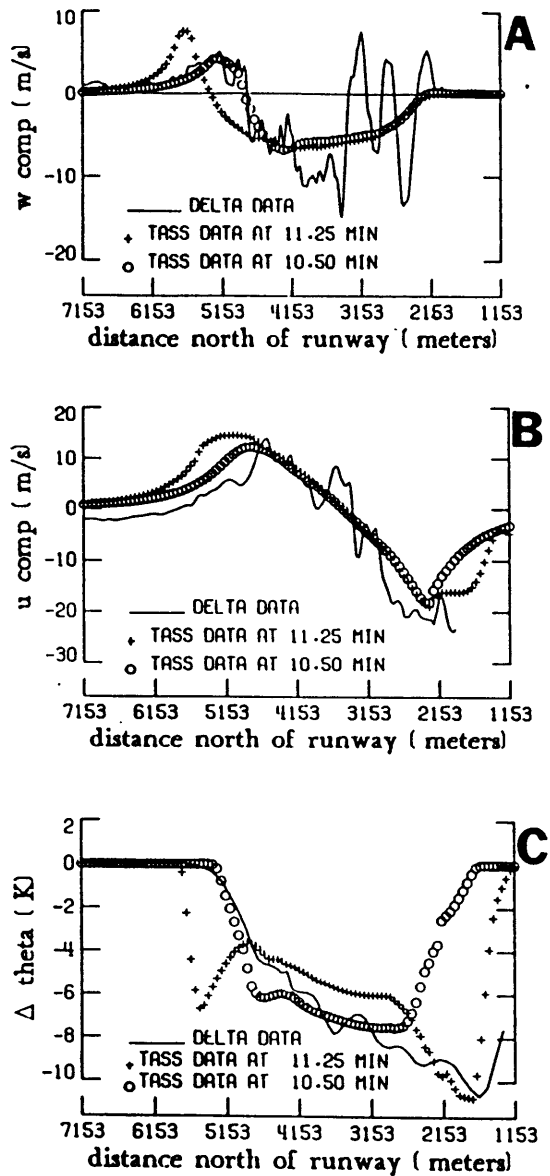


Fig. VI-5. Comparison of the model simulated profiles and the actual profiles derived from the Delta 191 flight recorder data. The plots are (a) vertical velocity, (b) southern wind component, and (c) potential temperature deviation from 700 mb ambient potential temperature. Taken from Proctor (1988b).

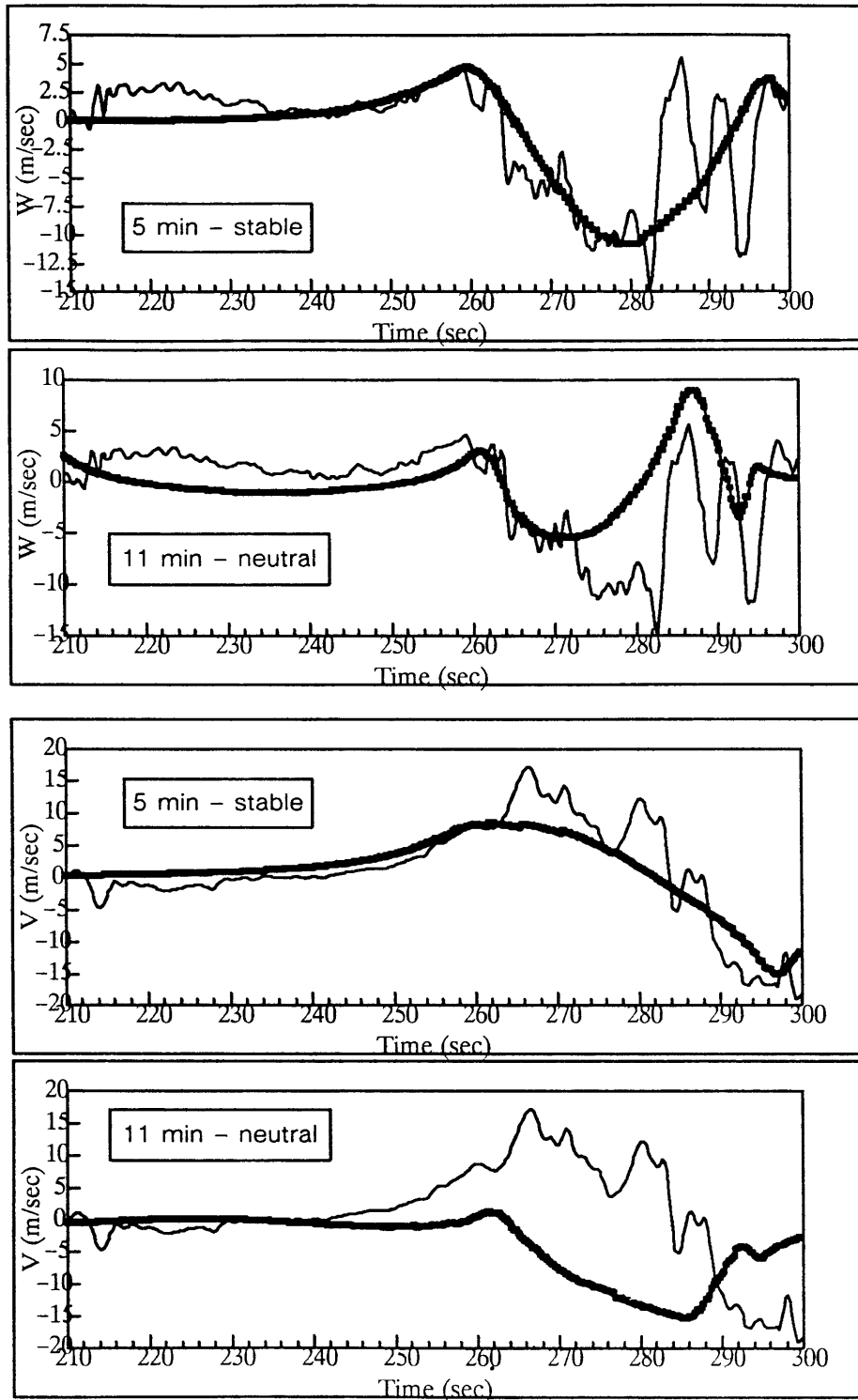


Fig. VI-6. (Top) Vertical velocity (W) and (Bottom) North-south wind component (V) from axisymmetric numerical model data compared with Delta 191 data supplied by Wingrove. The top panel shows the data encountered from the closer, younger thunderstorm outflow, and the bottom panel shows those encountered from the more distant, older outflow.

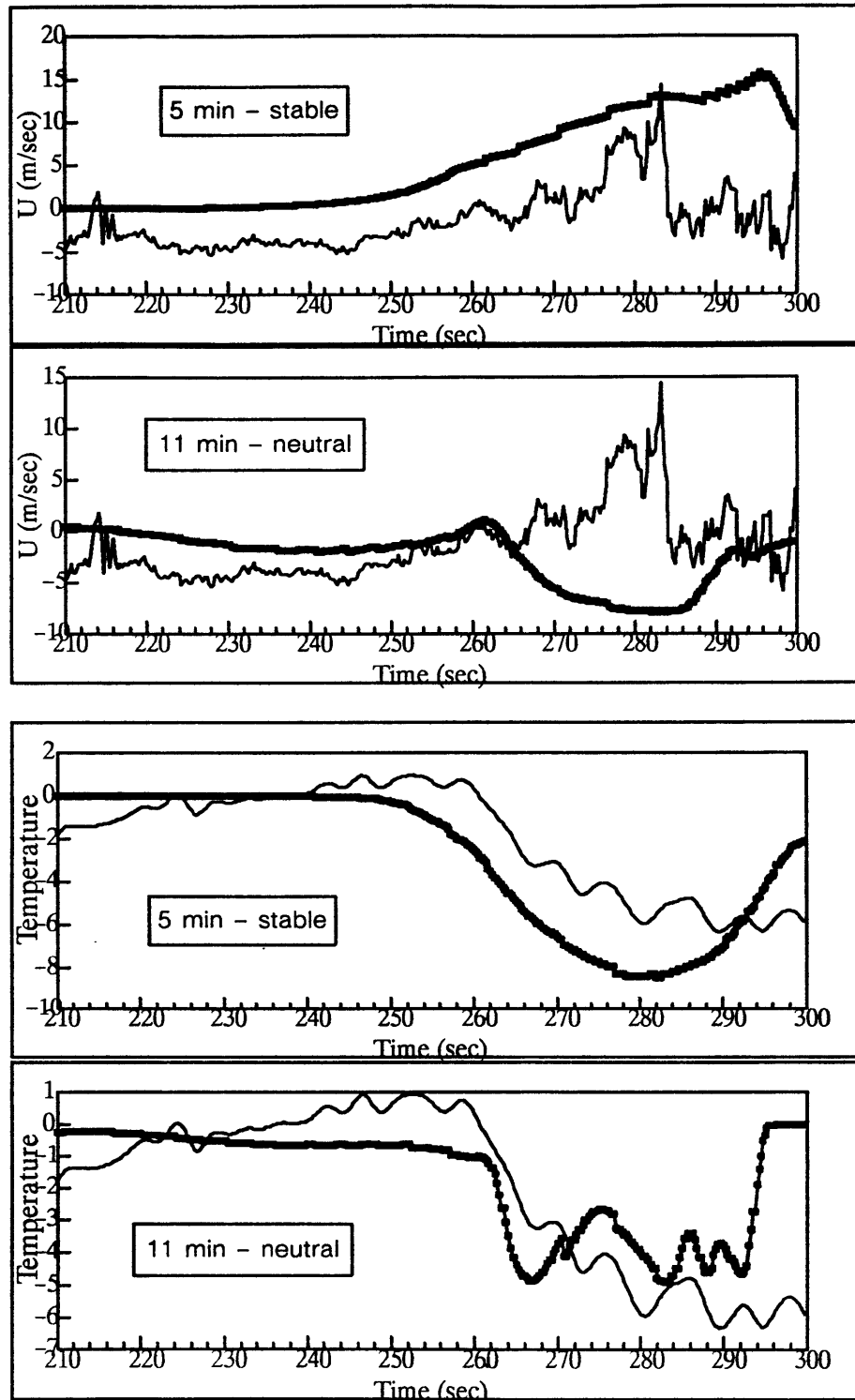


Fig. VI-6. (continued) (Top) East-west wind component (U), and (Bottom) Temperature perturbation (mean of 34.9 C has been removed) from axisymmetric numerical model data compared with Delta 191 data supplied by Wingrove. The top panel shows the data encountered from the closer, younger thunderstorm outflow, and the bottom panel shows those encountered from the more distant, older outflow.

temperature was available for a short time afterward. As can be seen in Fig. VI-5 (c), the temperature does increase afterward, as the numerical simulations indicate.

Admittedly, not every wiggle is simulated through these two axisymmetric storm models at these times in these locations. However, certain spatial compression and skewing of the wind features would be expected to result from the interaction of the two outflows. A plan view of the suggested scenario is presented in Fig. VI-7. The vortices encountered by Delta 191 were part of the actual wind pattern inside the gust front from an axisymmetric thunderstorm. In these early stages of thunderstorm outflow, the gust front portion of the outflow is at least as hazardous as the more laminar central downdraft.

The Stephenville radar 140 km away shows the DFW "cell" to have achieved VIP level 3 at least by 2256 GMT. By the time the accident occurred at 2305-2306, VIP level 4 was observed. I suggest both downdrafts encountered by Delta 191 came from this same radar cell; perhaps at higher resolution the individual cell components could have been identified. The same radar "cell" (different downdraft within) produced 35 m/s winds over the airport 20 min after the crash. The NSSL lightning detector observed a lightning strike about 15 min before the accident north-northeast of DFW. At this same time, observers also reported a cumulonimbus cloud north-northeast of the airport. Caracena's report suggests that the outflow from a cell 20 km north-northeast of the airport contributed to the forcing for the DFW cell. This storm formed 20-30 min before the accident, and was visible on the Stephenville radar display. I think another, closer storm must have formed because of the observed strength of the vortices (gust front) and the cold temperature of the air.

Observations of the onboard weather radar of another flight airborne at the time of the crash indicated a "solid red contour (the highest contoured reflectivity) with no visible reflectivity gradients on a plan view scan. He notes having seen a green hook shaped echo (the lowest contoured reflectivity) protruding from a microburst cell over DFW airport seconds before another crew member sighted the fireball produced by Delta 191." (Caracena et al. 1986). This green thin line echo is the signature of a gust front, but it could not be the gust front from the new cell that Delta 191 encountered for two reasons. First, the gust front (leading vortex ring) would not have separated from that storm for another 2 min at least (refer to Fig. V-14), and second, even if the gust front had separated it would have been concentric with the cell not "protruding". Yet this protruding gust front separated from its parent storm is exactly what would have been seen if something

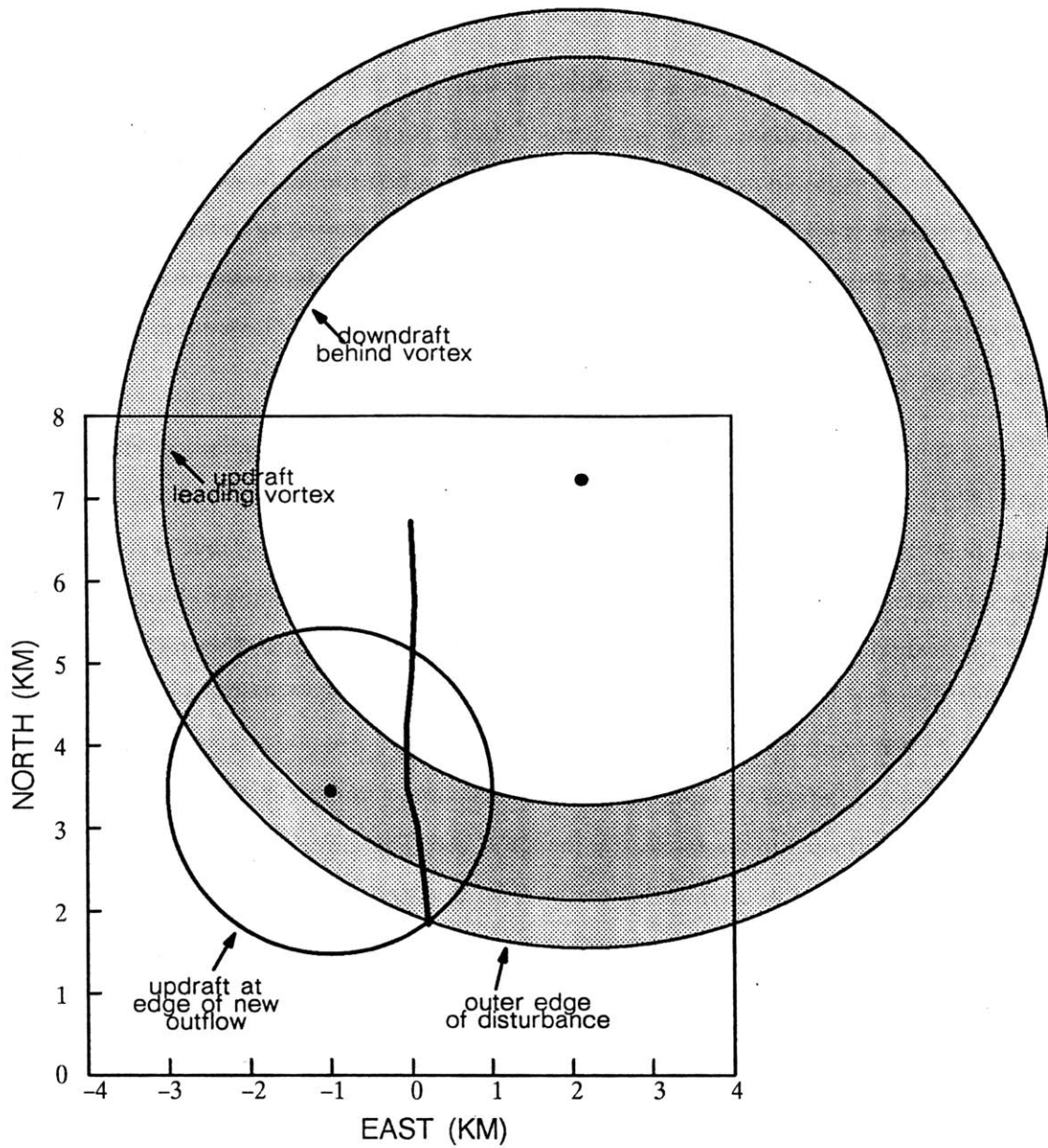


Fig. VI-7. Proposed meteorological scenario during DFW crash. The spots indicate thunderstorm downdraft centers. The thick black line is the Delta 191 flight path during the last 90 s of flight. Runway is located at (0,0).

like the scenario in Fig. VI-7 is correct. This provides additional support to the argument that Delta 191 encountered two outflows during its last 90 s of flight.

Assuming this hypothesis is correct, the relative contributions to the aircraft hazard of the new storm and the older gust front can be calculated using the F-factor hazard index (Targ and Bowles 1988). Figure VI-8 shows the results of this calculation for the actual aircraft data, and for the appropriate model simulations. The bulk of the performance decreasing hazard is coming from the downdraft and outflow from the new, closer storm (top panel). However, if that were the only storm present the F-factor would have increased and decreased relatively smoothly. Notice that F surpasses the conservative threshold of 0.1 for only about 10 s. The gust front contributes smaller values of F (bottom panel), but they change rapidly from 0.1 to below -0.1. It is difficult to estimate what effect this "turbulence" might have had on the control of the aircraft. When Proctor's model simulation for the DFW storm without the vortices was fed into a flight simulator, a pilot was able to "land" the plane safely (Stevens, personal communication). The Delta 191 pilots knew the storm was present and were preparing to handle the anticipated downdraft and outflow. It may be that the presence of the vortices, the hypothesized gust front, was the added ingredient that prevented the safe landing of the aircraft.

B. New Orleans

The next most recent microburst aircraft accident was the crash of Pan American Flight 759 at New Orleans International airport on July 9, 1982. Not nearly as much information is available on this crash; unambiguous reconstruction of the wind field was not possible. However, from Fujita's (1983) analysis, it is fairly definite that a newly formed thunderstorm downdraft and outflow occurred almost directly over the runway. It also appears that this downdraft landed just behind a gust front that had recently crossed the airport (Figs. VI-9 and VI-10). The significance of encountering an old gust front just when the aircraft was emerging from the new downdraft is not known, but by analogy with the DFW case, this could well have contributed to the overall hazard. Also, this crash occurred on takeoff, when the F-factor is larger because of the positive vertical wind shear and upward aircraft motion. Fujita's report discussed the "lifesaving" increase in headwinds for one of the other flights near the time of the Pan Am crash, attributed to a gust front crossing the airport. But the performance effects on aircraft of gust frontal wind shear depend strongly on the flight altitude. In some cases gust fronts are even more hazardous than microbursts; certainly "fresh" gust fronts are the most hazardous.

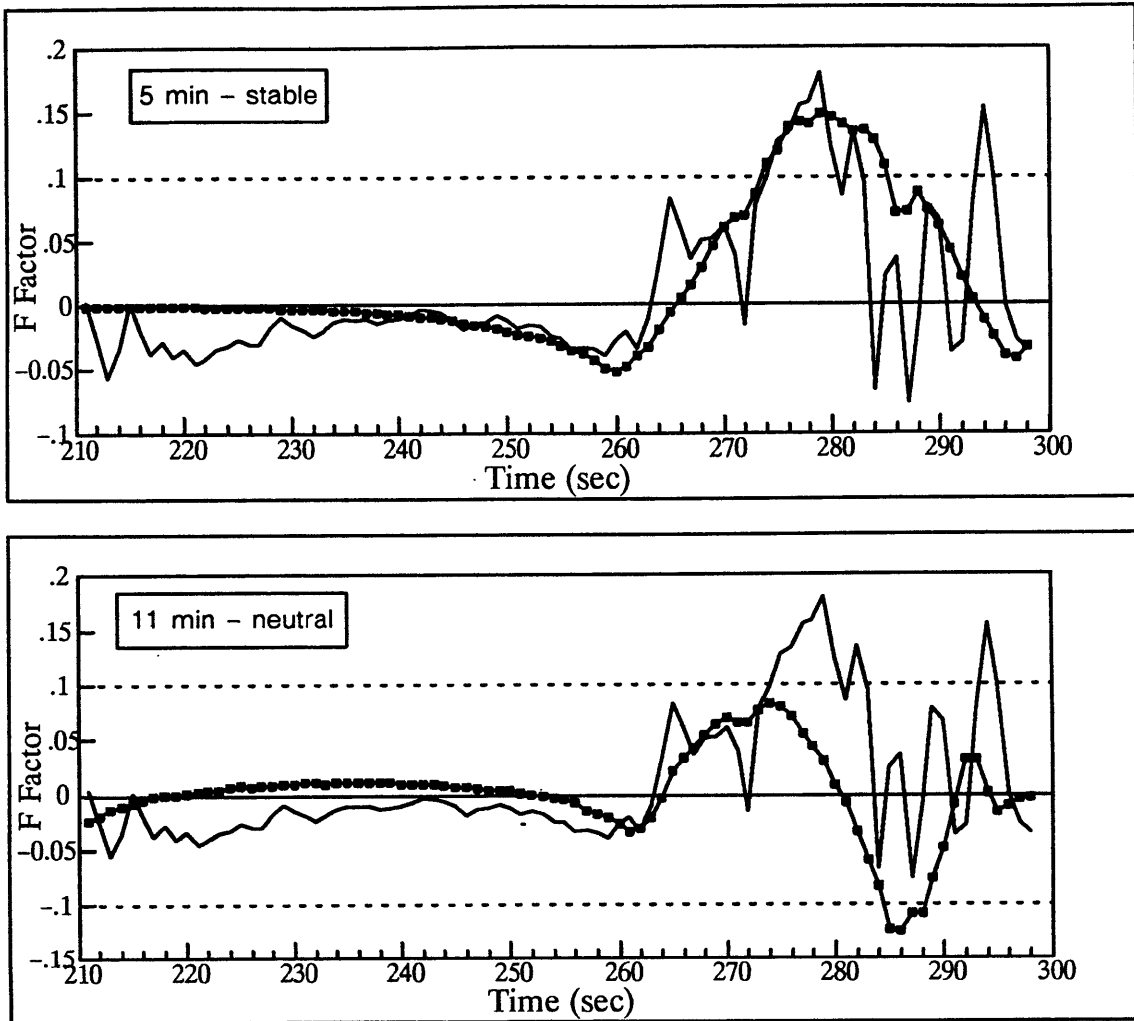


Fig. VI-8. *F-factor calculations for the last 90 s of the Delta 191 flight that crashed at DFW. In each panel the solid curve shows the actual F-factor from the flight data, and the dotted curve shows F calculated from the numerical simulation. The top panel shows the model data from the close storm, and the bottom panel, data from the distant, older storm.*

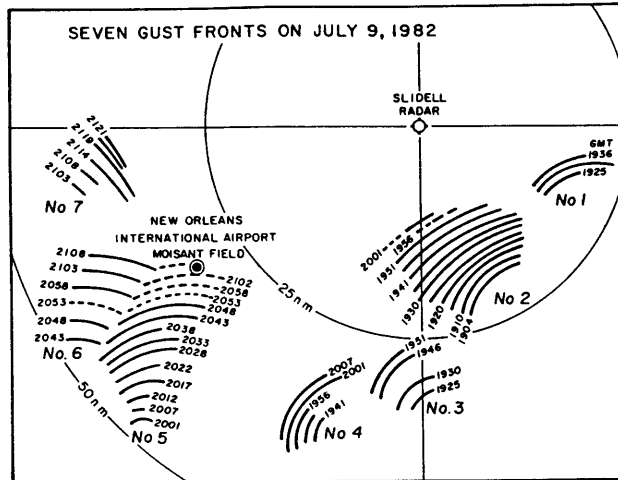


Fig. VI-9. Seven gust fronts on July 9, 1982 determined as based on the radar film from the National Weather Service Office, Slidell, LA. Location and movement were obtained by time-motion analyzer at the University of Chicago. Taken from Fujita (1983).

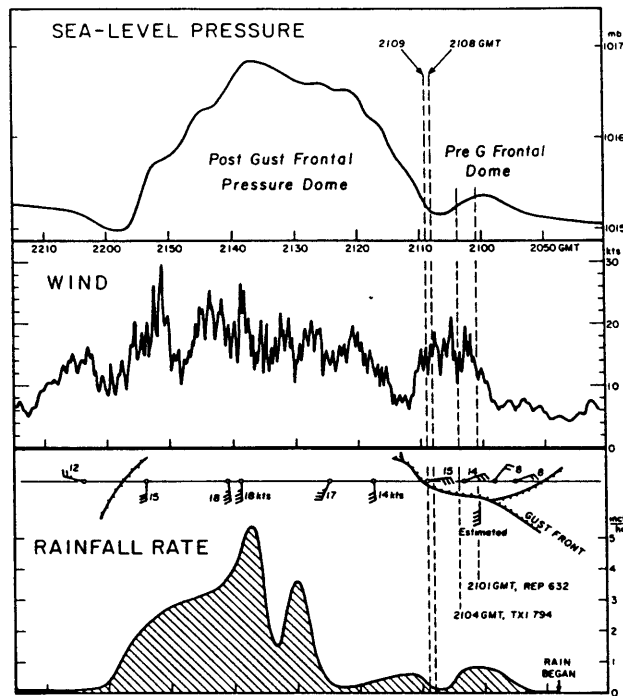


Fig. VI-10. Enlarged traces of pressure, wind, and rainfall rate at Moisant Airport (New Orleans International) between 2040 and 2215 GMT on July 9, 1982. The airport was under the influence of ENE to NE winds during the pre-gust frontal dome period. After the passage of gust front Nos. 5 and 7, up to 30 kt gusts from the southerly direction dominated the airport area. Republic 632 was saved by the gust front while Texas International 794 reported no wind shear PAA 759 released brakes at 2107:56 and made the first contact with trees at 2109:00. Taken from Fujita (1983).

C. JFK

Finally, we can reexamine the very first accident ever attributed to microburst wind shear, the crash of Eastern Flight 66 at JFK airport in New York on June 24, 1975. This was the accident that led to the development of the new burst terminology. Was this new downburst (later redefined as a microburst) anything other than a thunderstorm downdraft?

I suggest that the presence of the sea breeze front made a fundamental difference on the evolution of the outflow pushing southward and eastward from scattered thunderstorms over the land. The winds from the sea breeze, perhaps augmented by the environmental winds, opposed the southward advancement of the thunderstorm air. Along this boundary an arc cloud developed that was visible in the satellite imagery (Fig. VI-11); this indicated convergence and an updraft strong enough to raise surface air to the condensation level. The sea breeze itself is a dense current and provides a thin stratified surface layer. The wind pattern of an opposing sea breeze has the curvature required to “trap” the gravity wave energy in the boundary layer, as shown in Chapter V. In addition, three separate downdraft cells occurred nearly in place at 6–8 min intervals (Fig. VI-12); it was the third downdraft that caused the accident. As was also shown in Chapter V, the pulsation of the downdraft source strength contributes to the complexity and shear of the outflow front.

My hypothesized scenario for the JFK accident is shown in Fig. VI-13. As in the other two microburst accidents, the thunderstorm downdraft landed just behind a gust front. In this case, the gust front may have been an undular gravity current that was “propagating” relative to the sea breeze flow, even though it was roughly stationary relative to the surface. The increased flow from two preceding downdrafts, in almost the same place as the third accident causing downdraft, added to the circulation about the leading edge and probably enhanced the wind shear. Judging from the DFW accident case, it is likely that the fluctuations in vertical velocity were far stronger than those depicted in Fujita’s analysis. The narrow scale of the powerful low altitude downdraft was probably the region of combined flow from the gust front and the thunderstorm.

D. Summary

If the hazardous low altitude wind shear events that have caused the fatal aircraft accidents attributed to microbursts are used to define what a microburst actually *is*, then one would have to conclude that a microburst is a *combination* of things. It involves the precipitation driven down-

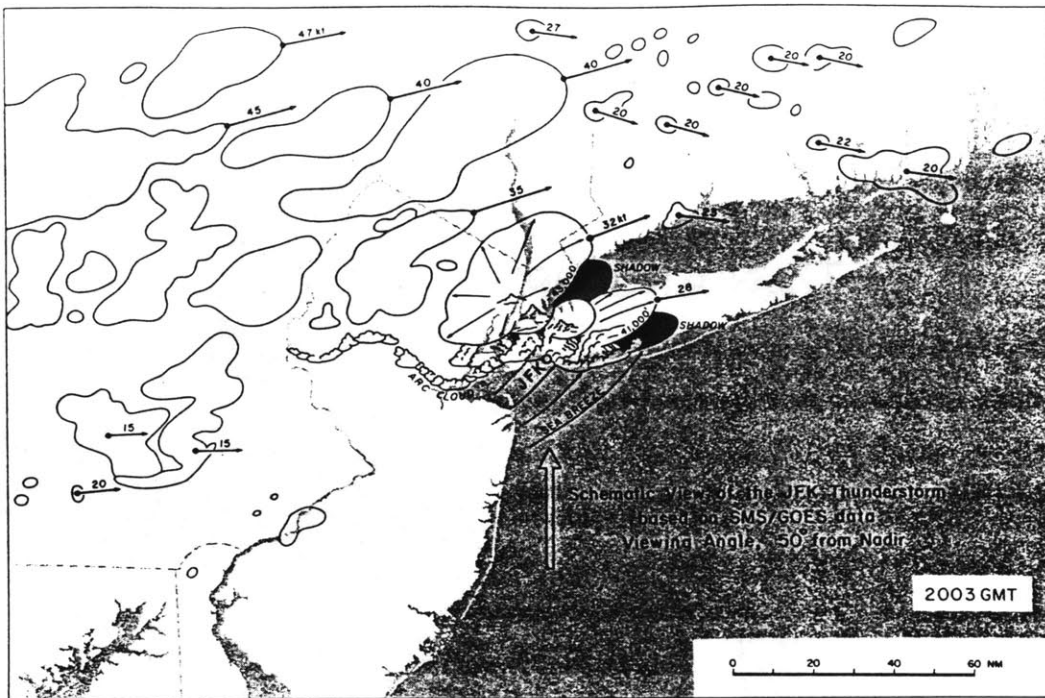


Fig. VI-11. Schematic view of the JFK thunderstorm drawn on the basis of the geostationary satellite data. The circle identified as JFK is the location of the airport. An arc cloud is seen just to the south of the thunderstorm activity. Its southward advancement is prevented by the sea breeze. The arrowhead vectors denote the cloud motion in knots. Taken from Fujita (1976).

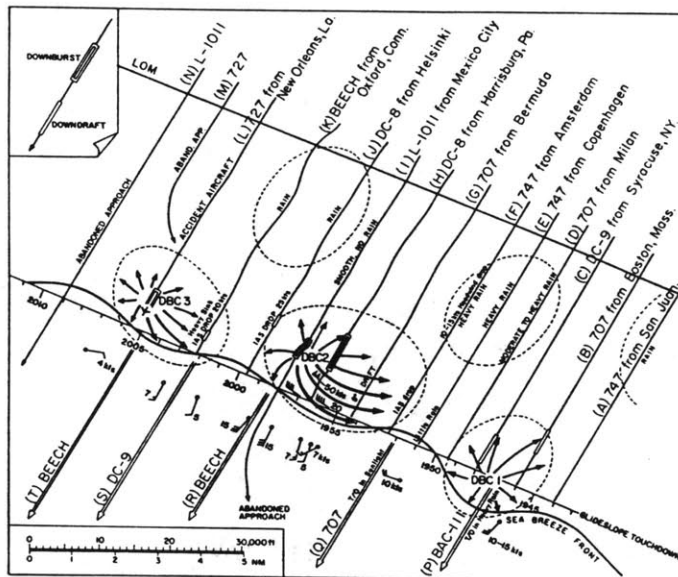


Fig. VI-12. Three downburst cells (DBC) depicted on time-space coordinates. DBC 1 was on the runway threshold and DBC 2 affected seriously the approach effort of aircraft "H" and "I". DBC 3 blew aircraft "L" down to the ground, 2000 ft short of runway 22-L. Most of the airport was under the influence of sea breeze. The outflow from the downburst cells was distorted by the sea breeze front, resulting in the strong outflow winds to the north of the front. Taken from Fujita (1976).

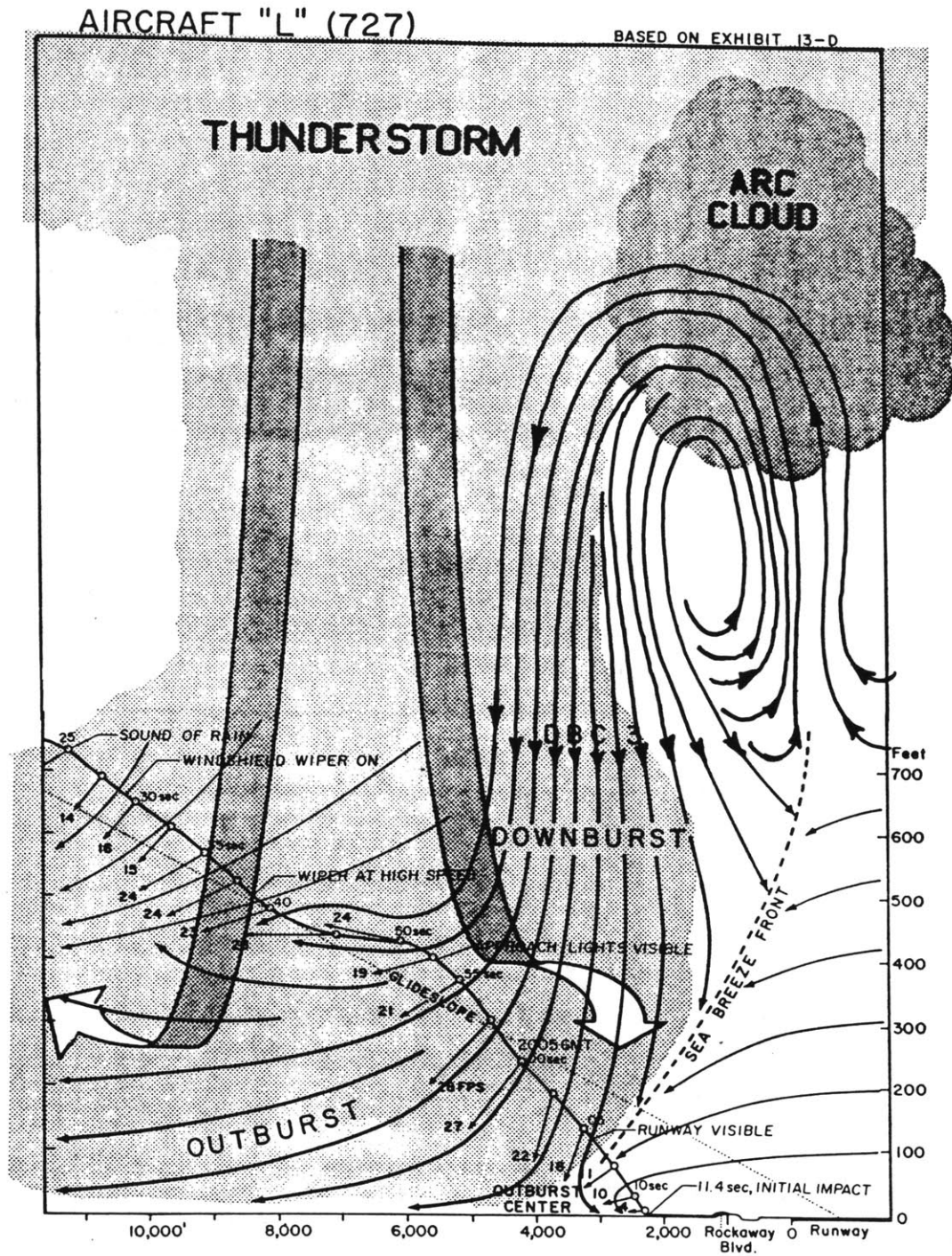


Fig. VI-13. Proposed scenario for JFK crash. The "microburst" was a thunderstorm down-draft coincident with the downdraft behind the leading circulation of an undular gravity current. Both features contributed to the accident. The depicted arc cloud was visible on satellite imagery. Adapted from drawing by Fujita (1976).

draft from a thunderstorm landing within the outflow of another thunderstorm, very near or essentially on top of the leading gust front. The "fresher" that gust front, the greater the aircraft hazard. In an isolated storm, the gust front has moved far enough from the main storm downdraft by the time it has built into a strong horizontal vortex to physically separate the two hazardous regions. The most dangerous combination appears to include a strong downdraft about 2 min after reaching the surface, landing on top of the leading vortex of a circular gust front formed no more than about 10 min previously. In this way, the turbulent hazard of the gust front is brought into the same area as the performance decreasing downdraft and divergent wind shear of the precipitation driven thunderstorm downdraft.

VII. CONCLUSIONS

The primary conclusion of this work is that the fatal aircraft accidents attributed to microbursts, including the first accident for which the microburst terminology was developed, all involved the *combination* of a precipitation driven downdraft and the narrow, low altitude downdraft and turbulent region associated with a gust front, or the leading edge of an undular gravity current. The unusually powerful downdraft at very low altitudes identified as the microburst came from this combined downflow and turbulence.

The first part of predicting microbursts, then, is predicting the strength of the precipitation driven thunderstorm downdraft. A number of apparent mysteries involved in the prediction of outflow strength based on Doppler radar detection of thunderstorm reflectivity cells are explained. Using numerical modelling results as “data”, I show that the thunderstorm downdraft maximum can occur much closer to the surface (~ 1 km agl) than was previously thought. A quantitative heuristic model is developed based on the vertical momentum and continuity equations that predicts the eventual maximum downdraft and outflow strength of a thunderstorm given the storm geometry, peak water content, downdraft depth, and mean environmental temperature lapse rate from the surface to the freezing level. Suggestions are made as to how these parameters should be estimated from Doppler radar data and surface temperature measurements.

Observations of a cloud edge downdraft that may be a manifestation of the penetrative downdraft are presented. In this case, air of very low equivalent potential temperature was transported to the surface, and a short lived wind gust of just under 20 m/s was measured. The small spatial scale and strong surface winds caused by this event qualify it as a microburst, yet it is a distinctly different phenomenon than the precipitation driven downdraft. I conclude that events of this strength are rare, and that the hazard posed to the safe flight of aircraft by these cloud edge downdrafts is not significant.

Attention is then turned to low altitude thunderstorm outflow structure, to investigate my basic hypothesis that a low altitude downdraft apart from the main precipitation driven downdraft could be the identity of some microbursts. I found that axisymmetric storm geometry causes a deep circulating flow to form at the leading edge of cold outflow; this consistent formation is explained for the first time based on the work of Garvine (1984). It is shown that the popular explanation of “spin up” caused by vortex tube stretching under the constraint of angular momentum conservation is incorrect. This build up of a leading vortex does not occur at the leading edge

of two dimensional, slab symmetric outflows. The possibility of multiple interior vortex ring formation was also investigated for axisymmetric outflows typical of those involved in the fatal microburst aircraft accidents. I found that more than multiple interior fronts occur only when the downdraft “pulses” in strength.

Kelvin–Helmholtz instability has been cited as the cause of large vortices or “billows” at the leading edges of, or embedded within the full depth of thunderstorm outflows. I show that the primary evidence on which this conclusion is based is misleading, and the published observations purporting to show this instability may have the alternative interpretation of an undular gravity current strongly influenced by the stable boundary layer stratification.

To investigate the possibility that solitary waves emanating from a newly formed thunderstorm outflow propagating into a thin stable layer could be related to microbursts, a cylindrical version of the Benjamin–Davis–Ono equation governing weakly nonlinear, dispersive waves in infinitely deep fluids is developed. The behavior of this equation is contrasted with the BDO equation for plane waves, and with the cylindrical version of the Korteweg–deVries equation governing surface waves. The cylindrical geometry causes the BDO wave amplitude to decay with range at a slightly greater rate than cylindrical linear or KdV waves. This decay prevents large wind speeds from persisting in cylindrical waves.

Numerical simulations performed with the axisymmetric numerical model developed by Anderson (1990) at the University of Wisconsin are used to show that the *early* outflow evolution from a strong thunderstorm is influenced very little by the presence of a thin stratified boundary layer. Nonlinear gravity wave phenomena become increasingly important as the flow evolves. Geometrical considerations dictate that waves must have small curvature to persist with large amplitudes. An opposing jet like flow often preferentially traps gravity wave energy from a circular storm leaving a slab symmetric wave or “rotor”. A review of the literature describing thunderstorm generated solitary waves revealed that the cases studied were all far from the parent storm, roughly slab symmetric, and had a noticeable but not dangerous increase in wind speed associated with them. I examine other case studies in which very high speed wind spikes were recorded and attributed to “rotor” microbursts, but in every case the surface wind measurement was made close to the main precipitation driven downdraft of the parent thunderstorm.

Finally, the three major aircraft accidents attributed to microburst wind shear are investigated. Taken as a whole, these actually define microbursts. It is shown that in every case, the

outflow from more than one thunderstorm was probably encountered. In the most recent crash of Delta 191 at Dallas/Ft. Worth airport in 1985, short wavelength vortices were observed. I suggest these were caused by traversing the leading vortex front of the outflow from an older thunderstorm located to the northeast immediately after passing through a newly developed thunderstorm downdraft centered slightly to the west. This is a possibility unrecognized in all previous research on this accident. Pan American 759 that crashed at New Orleans in 1982 also encountered both thunderstorm downdraft and gust front, although the ambient winds through which the plane flew could not be recovered unambiguously. The crash of Eastern 66 at JFK in 1975 (the one for which the downburst/microburst terminology was developed) was probably caused by both a thunderstorm downdraft, and the powerful small scale downdraft behind the leading vortex of an undular gravity current or "roll cloud".

Thus the second part of predicting microbursts involves tracking the gust fronts from previously formed thunderstorm outflows. The presence of a relatively fresh gust front appears to greatly increase the aviation hazard of flying through a newly formed thunderstorm outflow. The gust front flow pattern is experienced as intense turbulence rather than a systematic divergent horizontal wind shear.

Through examination of low altitude downdrafts in and near thunderstorms, it has been shown that a number of dynamically distinct phenomena meet the arbitrary definition of a microburst. Understanding these downdrafts and how they form allowed a fruitful reexamination of the three major fatal microburst aircraft accidents. The work in this thesis shows that, if whatever meteorological event caused these aircraft accidents is used to *define* the microburst, then the microburst is actually a combination of a precipitation driven thunderstorm downdraft and what would commonly be called a gust front.

APPENDIX A. Derivation of Prediction Equations

In this appendix, the details of the derivation of prediction equations for the maximum downdraft and outflow speeds from a thunderstorm downdraft are given. An overview of the derivation was given in Chapter II. The vertical momentum equation [Eq. (II.1)] was used as a framework, and each forcing term was related to observable environmental parameters such as the mean temperature lapse rate, or observable storm characteristics such as the aspect ratio of the precipitation core.

Here, I use the published axisymmetric numerical model output of Proctor (1989; referred to below as P89), Krueger and Wakimoto (1985, referred to below as KW), and Droegemeier and Babcock (1989; referred to below as DB) to show that expected physical relationships are indeed consistently observed. The characteristics of these models are given in Table A-1. Each model was initiated with a precipitation distribution and an environmental profile of temperature, and allowed to evolve. The modelers systematically varied certain parameters such as the radius of the rain core, or the precipitation water content, and examined the resulting downdraft and outflow speeds. In the sections that follow, the dependence of the downdraft and outflow velocity on each parameter is anticipated from physical principles and compared with the numerical model results.

1) Physical Explanations for Numerical Modelling Results

(i) *Radius of the rain core*

Both P89 and KW test the effects of increasing precipitation radius on the maximum downdraft speeds in their models. The dependence of vertical velocity on radius is shown in Fig. A-1, where the results of both model simulations have been combined. The expected dependence can be deduced from the vertical momentum equation; if the forcing of the vertical acceleration comes from the pressure term only, a version of Bernoulli's equation can be derived (assume the density is constant):

$$\left(\frac{w^2}{2}\right)_z \sim - \left(\frac{P'}{\rho_0}\right)_z$$

or,

$$\left(\frac{w^2}{2}\right) + \left(\frac{P'}{\rho_0}\right) = \text{constant}$$

Table A-1. Comparison of numerical model characteristics from P89 (Proctor 1989), KW (Krueger and Wakimoto 1985), and DB (Droegemeier and Babcock 1989).

MODEL CHARACTERISTICS	P89	KW	DB
form of precipitation	hail	rain	rain
radial distribution of precipitation	cosine of reflectivity	Gaussian rainwater	Gaussian rainwater
diameter of precipitation (km)	6	4	4
depth of precipitation (km)	∞ duration	4	2
aspect ratio of precipitation	~ 1	1	0.5
source height of precipitation (km)	5	4	4
height of melting level (km)	3.33	3.4	?
height of transition level (km)	3.33	3.7	N/A
precipitation mixing ratio (g/Kg) (nominal value used for baseline)	4.27	2	8
mean temperature lapse rate (K/km) between ground and melting level	8.47	9.75	9.75

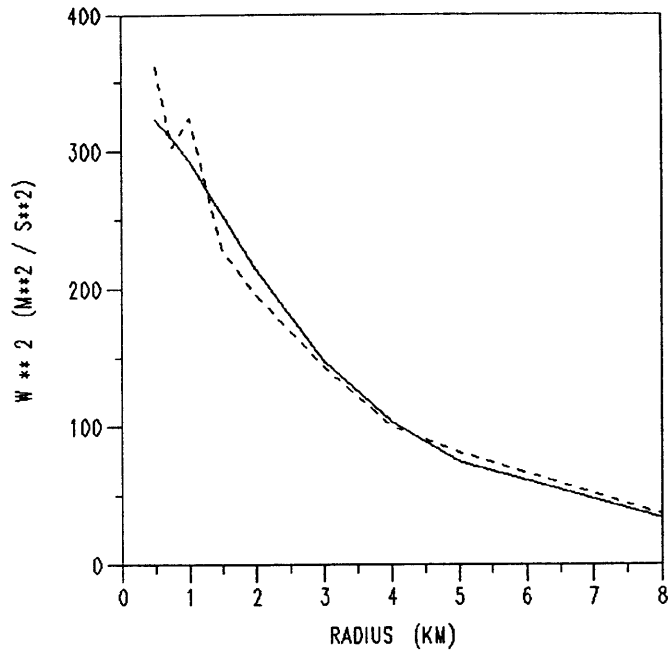


Fig. A-1. Plot of the square of the vertical velocity (w) vs the radius of the downdraft core (R), from the model results of P89 and KW (dashed curve). The predicted dependence, shown as the solid curve, was found to be $w^2 = 167 / (0.5 + 0.07 R^2)$. [See below.]

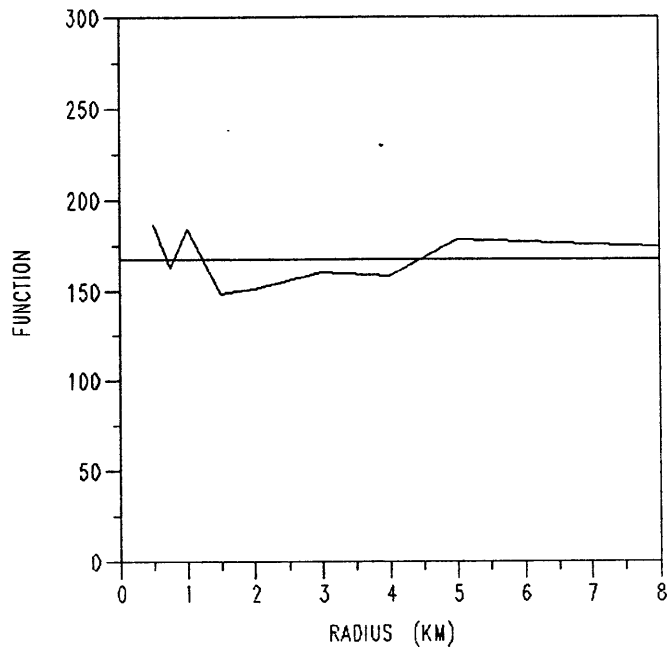


Fig. A-2. Plot of "FUNCTION" = $w^2/2 + 0.07 w^2 R^2$, for the data shown in fig. A-1. The function should equal 167 for a perfect fit to the predicted dependence based on Bernoulli's equation.

Fujita (1963) derived the following expression relating the nonhydrostatic pressure at the surface in the center of a cylindrical downdraft to the radius of the downdraft:

$$P' = \frac{1}{8} \rho (\nabla \cdot \mathbf{u})_{\text{horiz}}^2 R^2$$

where \mathbf{u} is the velocity vector and the other variables have been previously defined. This expression was derived from the equation for an ideal fluid striking a perpendicular plate by subtracting off the hydrostatic component. The continuity equation relates the horizontal divergence to the vertical gradient of the vertical velocity. Assuming that the horizontal divergence is proportional to w itself (discussed in the following paragraph); the pressure perturbation can be modeled as being proportional to $w^2 R^2$. The best match to this derived dependence is $[w^2/2 + 0.07 w^2 R^2 = 167]$, shown as the solid curve in Fig. A-1 and compared with the constant value of 167 in Fig. A-2. The fit is not terribly good at small radii, perhaps because the vertical acceleration is not dominated by pressure forces until the downdraft becomes large.

Both P89 and KW also test the effects of increasing precipitation radius on the ratio of the maximum outflow speed (U) to maximum downdraft speed (W); neither of these studies mentioned that the dependence of U/W on radius was almost exactly linear. To see why this should be the case, first make the simplifying assumptions that

$$w_z = K \cdot w$$

where K is a constant of proportionality, and that

$$\begin{aligned} w &= -W & \text{for } 0 < r \leq R \\ w &= 0 & \text{for } r > R \end{aligned}$$

where W is a constant value. The cylindrical equation of continuity for an incompressible fluid can then be integrated to give:

$$\int_0^R (u r)_r dr = K W \int_0^R r dr$$

$$u r \Big|_0^R = K \frac{W}{2} r^2 \Big|_0^R$$

$$\frac{U}{W} = \frac{K}{2} R$$

The ratio of the maximum surface outflow speed to the maximum downdraft speed will be a linear function of the radius of the water mass accelerating the vertical flow. A slab-symmetric model would give the same result without the factor of 1/2, thus predicting a similar linear, though doubly steep, dependence of U/W on radius (half width). Although the cited papers use more complicated radial profiles of vertical velocity (cosine or Gaussian), both sets of results show this anticipated linear dependence (Fig. A-3). The preceding paragraph discussed the relationship between W itself on the downdraft radius. At large values of R , $W \sim 1/R$ and $U \sim \text{constant}$ with respect to R , while at small values of R , both U and W depend somewhat on R . However, the ratio U/W depends linearly on R over the entire range of values tested.

(ii) *Liquid water mixing ratio*

Both KW and DB test the influence of increasing water mixing ratio on the maximum resulting downdraft speeds but the results were not interpreted in terms of what physically might be expected. Based on the vertical momentum equation, the dependence of w on liquid water mixing ratio might be:

$$\left(\frac{w^2}{2}\right)_z \sim -g l$$

Integrating in height,

$$w^2 = K l \Delta z \tag{A.1}$$

where K is a constant of proportionality. The reported results do show this anticipated dependence, but the slopes for KW and DB are significantly different (Fig. A-4). Both studies use a neutral environmental lapse rate, and both start with a 2 km radius Gaussian rainwater region at 4 km agl. The difference is that KW use a 4 km deep water mass centered at this height, whereas DB use a 2 km deep region. This explains why the former predict stronger vertical velocities for a given liquid water content than the latter, and why the slopes differ by roughly a factor of two.

This result emphasizes that the vertical distribution of water in the thunderstorm core, or equivalently the duration of the rain event (given the descent rate of the water mass), is important

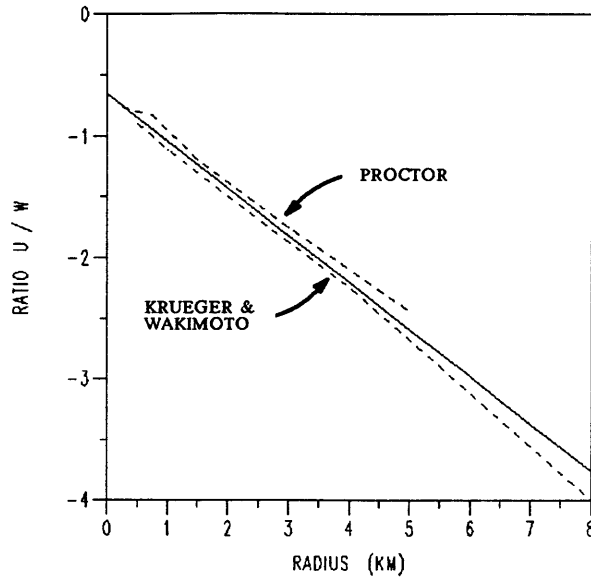


Fig. A-3. Plot of the ratio of the maximum outflow speed to the maximum downdraft speed (U/W) vs radius of the precipitation core, from the numerical simulations by P89 and KW (dashed lines). The solid line, $U/W = -0.39 R - 0.65$, is the best approximation to both datasets.

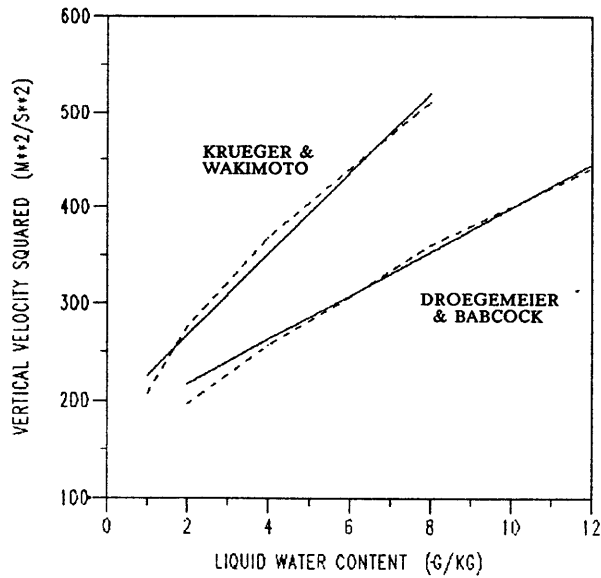


Fig. A-4. Plot of the square of the vertical velocity (w) vs liquid water content (L), from the numerical simulations by KW and DB (dashed lines). The solid lines represent the least squares linear fit to each dataset: $w^2 = 42.1 L + 183$ (KW) and $w^2 = 22.8 L + 171$ (DB).

in determining the intensity of the downdraft and the resultant outflow speed. Proctor (1989) specifically investigates the sensitivity of downdraft and outflow speeds to the duration of precipitation at the top of the model. (He does not use a vertical extent.) He found that speeds increased with increasing duration up to about 5 min, after which the peak intensity was close to his baseline case with infinite precipitation duration. For a nominal descent rate of 20 m/s, this is equivalent to a rain core depth of 6 km, equal to the value prescribed for his core width.

Although the dependence of vertical velocity on rainwater mixing ratio is quite strong, U/W is nearly constant with respect to increasing mixing ratio above ~ 3 g/Kg (Fig. A-5). The KW and DB data show that for a rainwater region of a given horizontal extent and a given subcloud lapse rate, the deeper the rain core the closer U/W will be to unity. This suggests that it is the *aspect ratio* of the rainwater core that is important in governing U/W , a reflection of the decelerating effects of pressure perturbations set up as the core descends. (This might also be anticipated from dimensional reasoning.) Das (1979) used a perturbation analysis to show that the vertical gradient of the pressure perturbation will be small compared to buoyancy when the aspect ratio of the system is large, i.e. when the vertical extent of the system is much larger than the horizontal [see also Yau (1979)]. As long as the forcing for the vertical acceleration of the downdraft is dominated by

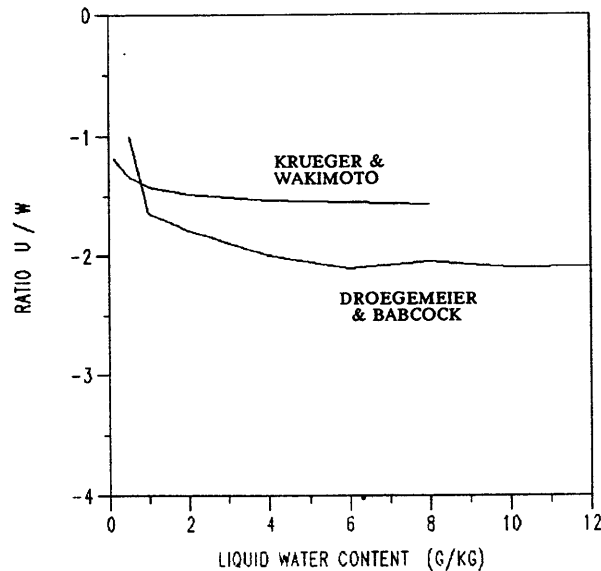


Fig. A-5. Plot of the ratio of the maximum outflow speed to the maximum downdraft speed (U/W) vs liquid water content, from the numerical simulations by KW and DB.

buoyancy, as it is when the mixing ratio is large, U/W should remain approximately constant with respect to further increases in this variable.

(iii) *Environmental lapse rate*

For a given mixing ratio, the downdraft velocity will increase as the lapse rate in the subcloud environment increases from stable values toward neutral. KW (1985) tested their model with six different lapse rates from 7.4 K/km to 9.6 K/km with varying rainwater mixing ratios, to examine the dependence of the resultant downdraft and outflow speeds.

Srivastava (1985) calculated the temperature excess of descending air parcels over their ambient environment for various subcloud lapse rates and liquid water mixing ratios, using a model based on evolution equations for raindrop mass and size distribution, thermodynamic energy, water substance, and vertical velocity. His tabulated data show a quadratic dependence of this temperature difference on lapse rate for a given liquid water mixing ratio (Fig. A-6). Using this, and referring again to the vertical momentum equation, we can anticipate a linear dependence of the vertical velocity on the lapse rate from the form of the temperature buoyancy term:

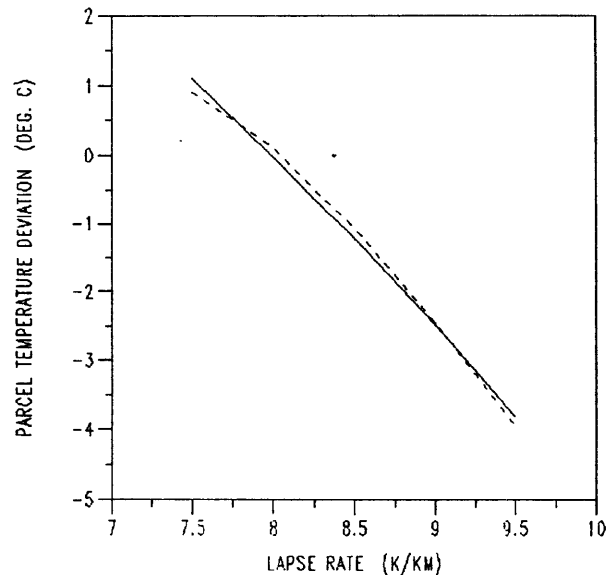


Fig. A-6. Plot of a one-dimensional air parcel's temperature deviation (ΔT) from the environment vs the environmental lapse rate (Γ), for an initial rainwater mixing ratio of ~ 7 g/Kg (dashed line). The data were taken from Srivastava (1985), Fig 5.b, rightmost column. The solid line is the least squares nonlinear fit to the data: $\Delta T = -0.145 \Gamma^2 + 9.23$.

$$w^2 \sim K \cdot \Delta T \cdot \Delta z$$

or,

$$w = K' \Gamma \sqrt{\Delta z} \quad (\text{A.2})$$

where Γ is the temperature lapse rate, and K and K' are constants of proportionality. Based on the results of KW, Fig. A-7 shows that the vertical velocity is indeed linearly related to the environmental lapse rate, and that the slope is approximately identical for liquid water concentrations of 2, 4, and 8 g/Kg. Moreover, it appears as if the intercept of these curves can be related to the liquid water content.

Once again, although the dependence of vertical velocity on lapse rate is quite strong and additionally dependent on the liquid water mixing ratio, the ratio U/W is roughly constant. Figure A-8 shows U/W predicted by the KW model, versus lapse rate, for liquid water mixing ratios of 2, 4, and 8 g/Kg. The magnitude of U/W does increase slightly, from 1 to 1.5 as the environmental lapse rate increases from 7.5 to 9.5 K/km, reflecting the additional dependence of outflow speeds on the resulting temperature difference between the outflow and surface air. This confirms that while the vertical velocity is strongly dependent on the factors that influence the buoyancy of the downdraft, the ratio U/W is strongly dependent only on the aspect ratio (radius) of the rainwater core.

(iv) Height of the transition level (melting level)

Proctor (1989) developed an index for “wet microbursts” (strong thunderstorm precipitation driven downdrafts) that depends on the height of the melting level, the mean temperature lapse rate between the surface and melting level, and the water vapor mixing ratio at 1 km and at the melting level. The value of the index is interpreted as the predicted differential outflow velocity under the collapsed thunderstorms, given that convection does develop that day. It reflects his finding that the strength of the downdraft is sensitive to the height of the melting layer. Knupp (1987) emphasizes the transition level of the sounding, rather than the melting level, as the “zone separating potentially strong downdrafts below from potentially weak downdrafts above”. Figure A-9 shows the relationship between both Knupp’s and Proctor’s simulated maximum downdraft speeds and the appropriate sounding transition level. Given that Knupp predicts the entire three

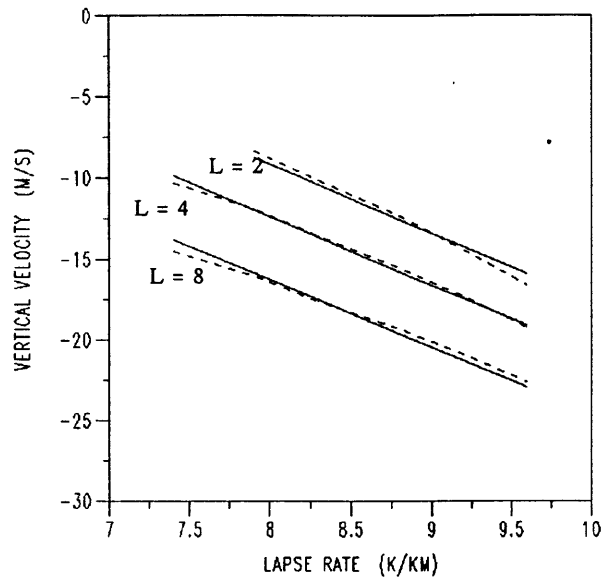


Fig. A-7. Plot of the vertical velocity (w) vs the environmental lapse rate (Γ) from the numerical simulations by KW, for liquid water mixing ratios (L) of 2, 4, and 8 g/Kg (dashed lines). The solid lines represent the best fit for each mixing ratio using the mean of the slopes derived from the least squares linear fit for each mixing ratio curve individually: $w_2 = -4.175 \Gamma + 24.19$; $w_4 = -4.175 \Gamma + 20.99$; $w_8 = -4.175 \Gamma + 17.14$.

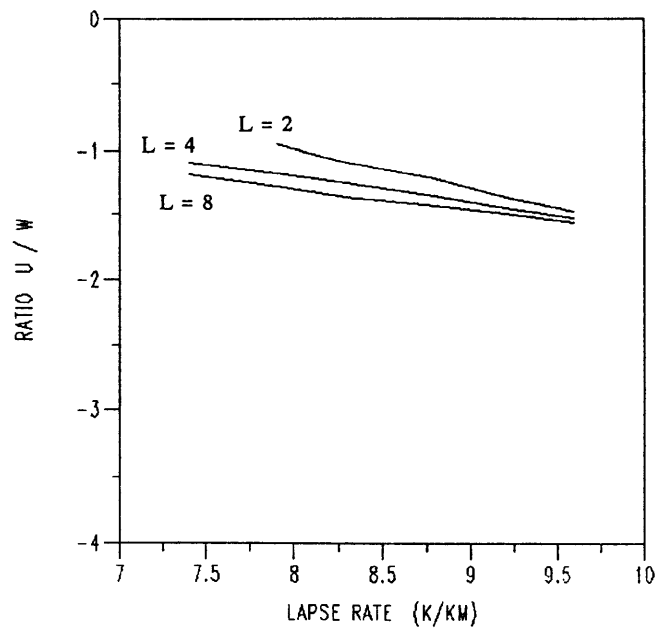


Fig. A-8. Plot of the ratio of the maximum outflow speed to the maximum downdraft speed (U/W) vs environmental lapse rate, for liquid water mixing ratios (L) of 2, 4, and 8 g/Kg.

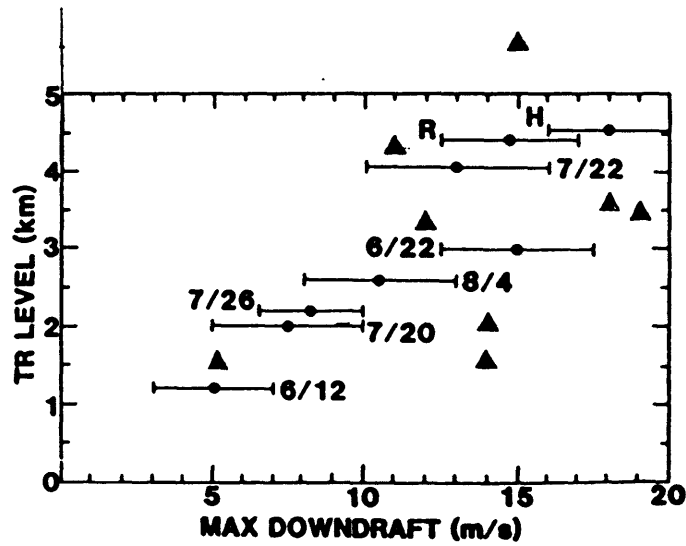


Fig. A-9. Plot of analyzed maximum downdraft as a function of height of the transition level (TR, defined as the level at which the lapse rate changes from roughly dry adiabatic or conditionally unstable to approximately moist adiabatic or absolutely stable). Error bars indicate the uncertainty in vertical motion estimates. The bars labeled R and H are data taken from Rodi et al. (1983) and Hjelmfelt (1984), respectively. The solid triangles represent the transition levels, and the simulated downdraft speeds for the cases presented by Proctor (1989). The base figure, without the triangles, was taken from Knupp (1987).

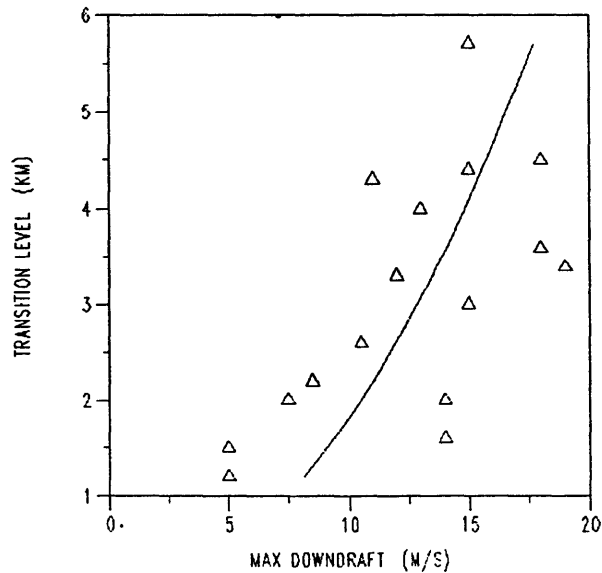


Fig. A-10. Plot of analyzed maximum downdraft as a function of height of the transition level from fig. A-9 (triangles), with least squares nonlinear fit superimposed (solid line). The equation for this curve is $W = 7.41 \sqrt{TR}$ where W is the maximum downdraft speed and TR is the transition level.

dimensional storm life cycle from the sounding, including the water mass that condenses, whereas Proctor specifies an axisymmetric water mass and allows it to fall through the lowest 5 km of the thermodynamic sounding, the data appear quite comparable. Both authors do stress that downdraft strength is also strongly dependent on other environmental factors.

Integrating the vertical momentum equation over height, we can anticipate the dependence of vertical velocity on the height of the transition level to be:

$$w = K \sqrt{\Delta z}$$

Addis (1984) showed a similar dependence of the vertical velocity on the height of the downdraft column in his convective storm outflow modelling work. Using the data shown in Fig. A-9, a least squares nonlinear fit was performed to determine the actual dependence; the exponent of the transition level (ΔZ) was found to be 0.46 ± 0.16 , very close to the predicted value. The solid curve plotted in Fig. A-10 was derived by setting the exponent to 0.5, and again performing the least squares nonlinear fit.

2) Prediction Equations

Although the final prediction equations were stated in Chapter II, they are repeated here for convenience. A comparison between these predictions and the numerical model results is presented in the following section.

(i) Vertical velocity

The dependence of vertical velocity on the radius and depth of the precipitation core, the precipitation mixing ratio, the environmental temperature lapse rate, and the height of the transition level was investigated using axisymmetric numerical model output. These results were combined into one predictive equation for the maximum vertical velocity:

$$W^2 = [7.3 \Gamma^2 + 9.75 L D - 480] \frac{T_r}{3.3} \quad (\text{A.3})$$

where W is the maximum downdraft velocity in m/s, Γ is the temperature lapse rate in K/km, L is the precipitation mixing ratio in g/Kg, D is the depth of the precipitation core in km, and T_r is the transition level of the sounding in km. The assumption has been made that the pressure perturba-

tion term in the vertical momentum equation is negligible; were it to be included, an additional function proportional to $1/R^2$ would appear multiplying the right hand side of Eq. (A.3). However, remember that the effect of the pressure perturbation was captured in the dependence of the ratio of U/W on R , discussed below. The new variable L has been used for the mixing ratio instead of l or i defined in Eq. (II.1) because no account is taken in Eq. (A.3) of the phase of the water mass present. If evaluating the terms on the right hand side of Eq. (A.3) produces a negative number, W should be interpreted as negligibly small.

(ii) *Outflow velocity*

The dependence of the ratio of the maximum outflow speeds (U) to the maximum downdraft speeds (W) was found to depend strongly only on the aspect ratio (A) of the precipitation core (i.e. ratio of vertical to horizontal extent), with a weak dependence on the environmental lapse rate (temperature of outflow air). These results were combined into a predictive equation for the ratio U/W which, when combined with Eq. (A.3), provides a predictive equation for U alone:

$$\frac{U}{W} = \left(\frac{.75}{A} + .65 \right) \frac{\Gamma}{9} \quad (\text{A.4})$$

where all of the variables have been defined above. If the predicted value of U/W is less than 1.0, the value should be set equal to 1.0. For example, when the lapse rate is dry adiabatic, $U/W = 1$ for aspect ratios ≥ 2.75 .

3) *Comparison of Predictions with Numerical Model Results*

Eqs. (A.3) and (A.4) were tested by comparing the predicted results with the actual results from the numerical models used in their derivation. Figure A-11 shows the predicted and actual (from KW) dependence of both W and U on variations in the environmental lapse rate, for rain-water mixing ratios of 2, 4, and 8 g/Kg. The prediction is worst for the outflow velocity at the lowest mixing ratio, reflecting the region in Fig. A-5 where U/W is not constant; however, the error is less than 3 m/s.

Figure A-12 shows the predicted and actual dependence of W and U on variations in the liquid water content of the raincore from KW (a) and DB (b and c). The KW results are matched to within ~ 1 m/s above a mixing ratio of 3 g/Kg, and the DB results match to within ~ 3 m/s above

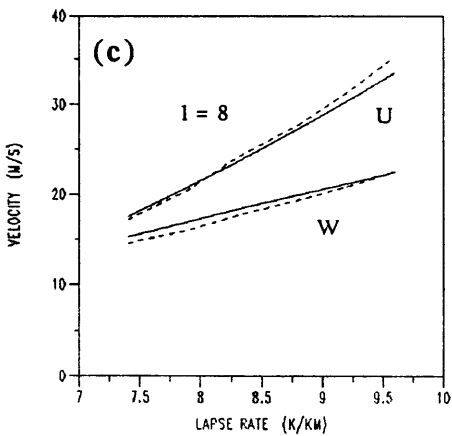
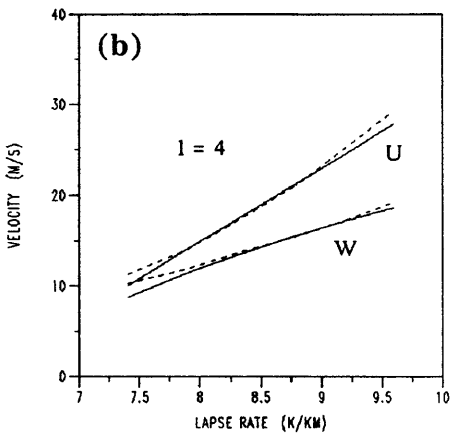
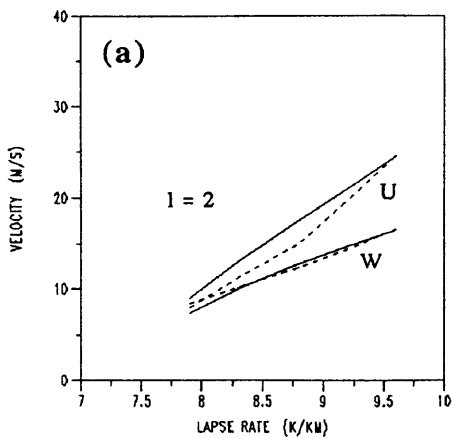


Fig. A-11. Plots of numerical model output (dashed; from KW) and predicted values (solid) of maximum outflow velocity (U) and maximum downdraft velocity (W) vs environmental temperature lapse rate, for liquid water mixing ratios of 2 g/Kg (a), 4 g/Kg (b), and 8 g/Kg (c).

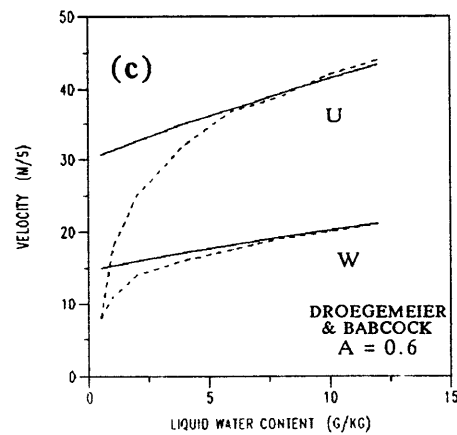
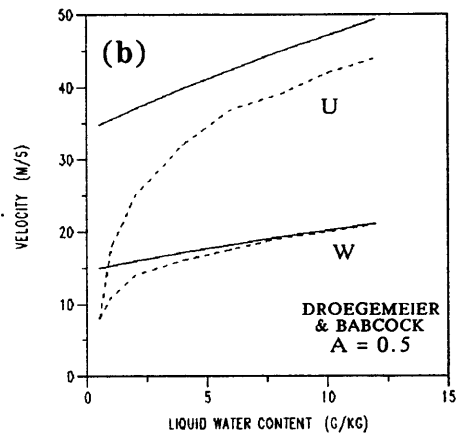
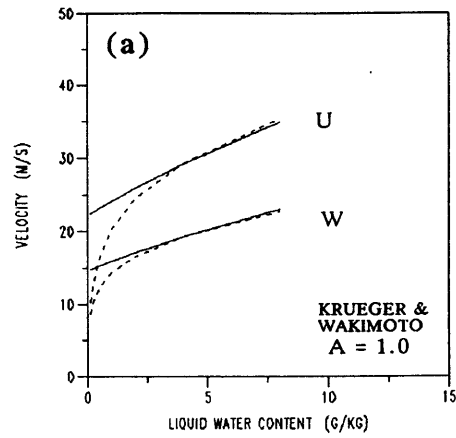


Fig. A-12. Plots of numerical model output (dashed; from indicated model) and predicted values (solid) of maximum outflow velocity (U) and maximum downdraft velocity (W) vs liquid water mixing ratio. The aspect ratio used in the prediction is 1.0 in (a), 0.5 in (b) and 0.6 in (c).

a mixing ratio of 5 g/Kg, if an aspect ratio of 0.6 instead of the actual initial value of 0.5 is used. While it is possible that the rainwater core in the DB model experienced some elongation as the run evolved, this discrepancy between the predicted and modelled U/W highlights the extreme sensitivity of Eq. (A.4) to the aspect ratio. Considerable uncertainty stems from the lack of clear choice of aspect ratio to assign to the P89 infinite precipitation duration experiments, which were equally weighted with the KW data in deriving Eq. (A.4).

At low mixing ratio, the predictions in Fig. A-12 do not match either dataset because of the observation, based on Fig. A-5, that U/W was approximately independent of this quantity. In both cases the vertical velocity itself matches quite well down to ~ 3 g/Kg, and the dependence of U/W on low mixing ratio is similar in both cases. It appears that Eq. (A.4) could easily be made more accurate by including an increasing function of the water content that caused the ratio of U/W to equal unity at values approaching 0 g/Kg, and to equal its current predictions at values greater than ~ 5 g/Kg.

However, the variation of U/W at low mixing ratio may actually reflect changes in the aspect ratio of the precipitation core. If so, no correction to Eq. (A.4) would be necessary if the aspect ratio was measured after the downdraft formed instead of being specified from the initial precipitation distribution. Proctor (1989) has shown that when the mixing ratio is low and the precipitation is in the form of small frozen particles (snow), rapid formation and acceleration of the downdraft takes place, causing the precipitation distribution to narrow and become elongated because of the compensating convergence. The examples shown in Figs. II-6 and II-7 suggest that a core aspect ratio ~ 2 is typically observed in these cases; for a dry adiabatic lapse rate this would give $U/W \sim 1.1$, close to the numerical results of both KW and DB. In cases of higher initial mixing ratios, the aspect ratio of the core does not change as dramatically from its specified value, so the timing of its measurement from numerical model data is not as critical.

Figure A-13 shows the predicted and actual ratio of U/W versus radius for the model results of P89 and KW. The lapse rate dependence in Eq. (A.4) has compensated for the observed differences in the linear slopes from these two experiments. The maximum error in the ratio U/W is only ~ 0.1 .

Equations (A.3) and (A.4) are meant only to suggest that the modeled dependencies can account for the observed thunderstorm downdraft and outflow speeds, and to encourage focused observational research and systematic numerical experimentation. In deriving these equations,

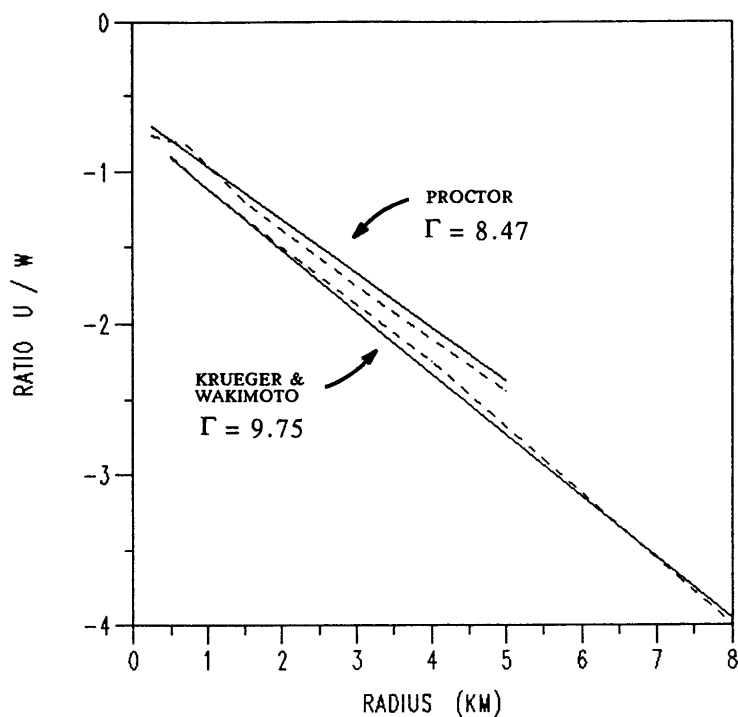


Fig. A-13. Plot of numerical model output (dashed; from indicated model) and predicted values (solid) of the ratio of maximum outflow velocity to maximum downdraft velocity (U/W) vs the radius of the precipitation core. The aspect ratio was ~ 1.0 in both models (but see Table A-1).

many of the data had to be estimated from published graphs and thus contain inaccuracies. Also, although the agreement between the different models is encouraging, the different methods of specifying the vertical distribution of precipitation (equivalent to duration of precipitation) lead to an additional lack of confidence in the aspect ratio dependency. The maximum liquid water content used in the numerical experiments was 12 g/Kg, but this value could easily double in high reflectivity thunderstorms. Ideally, numerical modelers should run experiments over a wide range of aspect ratios, lapse rates, mixing ratios, and transition levels to allow derivation of more accurate equations, with estimates of error bars on all of the coefficients. But the form of the equations, based on the vertical momentum equation and the equation of continuity, is not likely to change.

Omitted from the predictive equations for W and U derived here are any dependencies on the phase or particle size distribution of the precipitation, or the environmental humidity distribution. These factors are known to influence the ultimate downdraft development but all numerical modelling results have shown them to be of secondary importance compared to the factors that

were included. For example, Krueger et al. (1986) showed that the variations caused by different cloud base precipitation rates are much greater than the small variations between condensate of different phases (rain, snow, and graupel) at a given cloud base precipitation rate, at least when the subcloud lapse rate is nearly dry adiabatic (Table II-1). This was confirmed by Srivastava (1987), who showed that the presence of ice became more important in driving intense downdrafts as the subcloud lapse rate became more stable. He showed, for a nominal lapse rate of 7 K/km, that the difference in vertical velocity between the rain and ice cases was largest aloft where most of the melting occurred, but that the downdraft speeds differed by only 20% at lower levels. When the entire storm life cycle is simulated, the exclusion of ice microphysics produces a slightly weaker; less massive, and more slowly evolving storm (15–25% differences; Chen 1986; Straka 1989). The inclusion of precipitation phase, particle size distribution, environmental humidity, as well as the vertical shear of the horizontal wind, will be left as refinements to the quantitative model developed here.

4) Estimating Parameters in Prediction Equations

One goal in developing these predictive equations, in addition to verifying the hypothesized parameter dependencies of downdraft and outflow speeds, is to use them as part of a Doppler radar system to detect collapsing thunderstorms, and to predict the surface outflow speeds well before they are realized. Estimates of the temperature lapse rate are not possible from radar, and it must be assumed that sounding data will not be available. However, if 1-min averaged measurements of the surface temperature (or better, virtual temperature) were available, the average (virtual) temperature lapse rate between the surface and the melting level could be estimated. The height of the melting level changes very little; it could, for example, be estimated from the morning sounding, or from climatological data and adjusted slightly depending on the departure of the current diurnal minimum temperature from the climatological norm. In some cases, the melting level is revealed quite clearly by the “bright band” in the radar returns from stratiform rain regions. This is caused in part by the enhancement of reflectivity that takes place as the frozen particles melt (Wexler, 1955). Even if no bright *band* is present, it may well be that the height at which the peak storm core reflectivity occurs indicates the melting level for the same reason (Fig. A-14).

Estimates of the other parameters needed for predicting U and W are possible from Doppler radar data. Since the sounding transition level is the upper limit of the precipitation driven

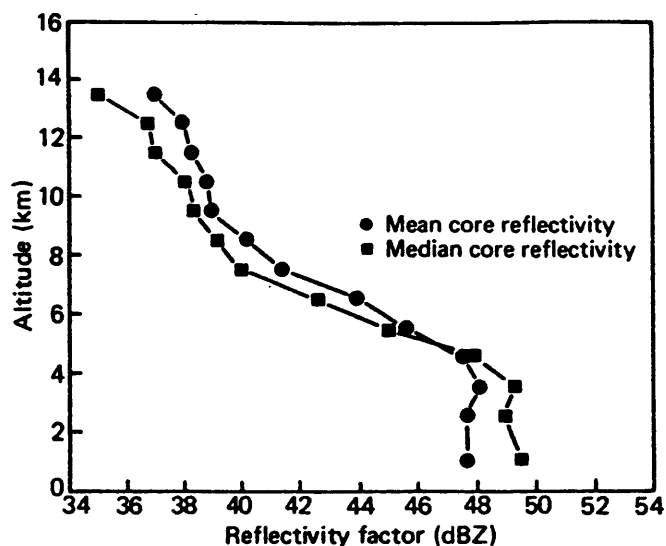


Fig. A-14. Profiles of mean and median core reflectivity for all cells observed during Wallops Island summer data collection (see caption for Fig. II-19). The height of the peak in mean core reflectivity may indicate the average height of the melting level. Taken from Konrad (1978).

downdraft, the uppermost level of the convergence into the storm core gives this parameter. The height and width (and aspect ratio) of the precipitation core can be estimated from the storm reflectivity, but research is needed to determine exactly how this should be done to provide consistent results. Statistically fitting the observed cell shapes to idealized mixing ratio distributions (such as the Gaussian) would allow the parametric specification of these dimensions and the relevant comparison with numerical models initialized with similar precipitation distributions. Also, since the conversion equation relating reflectivity to precipitation mixing ratio ultimately depends on an estimate of the particle drop size distribution and phase of the water present, parameterizing this conversion effectively must also be a priority. For example, it may be possible to correlate the precipitation phase and drop size distribution with the reflectivity and height of first echo formation.

Care must be taken to check that the axisymmetric approximation to the storm geometry is valid. As isolated storm cells merge, their overall geometry will become more linear, and a slab-symmetric approximation may become more appropriate. Quasi-linear storm formations are at least as likely as axisymmetric storms to produce hazardous outflows but they are longer lived and thus easier to predict; they have been called "derechos" (Hinrichs 1888; Johns and Hirt 1983; Przybylinski and DeCaire 1985), "line echo wave patterns" (Nolen 1959; Hamilton 1970), "bow

echoes”, “macrobursts”, “downbursts” (Fujita 1981; Forbes and Wakimoto 1983; Knupp and Jorgensen 1985; Eilts and Doviak 1987; Lee 1988), “microburst lines” (Hjelmfelt and Roberts 1985; Hjelmfelt 1988; Hjelmfelt et al. 1989), as well as “squall lines” (Talman 1907), “instability lines” (Fulks 1951), and “linearly oriented mesoscale convective systems” (Maddox 1980; Bluestein and Jain 1985). Simple arguments based on continuity showed that U/W would be larger for the slab geometry, but the factor of two suggested previously is too large because multicell storms are still made up of cylindrical cells, not all collapsing simultaneously. On the other hand, the DB numerical results showed the opposite trend: $(U/W)_{\text{slab}} = 2/3 (U/W)_{\text{axi}}$. Apparently the axisymmetric case had a much stronger vortex at the leading edge of the outflow, with 65% stronger surface winds for roughly the same vertical velocity (but that model had a free slip boundary condition). The vertical velocity in the slab symmetric geometry was close to that in the axisymmetric geometry [$(W)_{\text{slab}}/(W)_{\text{axi}} \sim 0.9$ regardless of precipitation content], suggesting that Eq. (A.3) for predicting W can be used without modification. Three dimensional numerical modelling results might provide some indication of the correct U/W formula for more linear storm geometries.

5) Predicting Other Downdraft and Outflow Parameters

Equations for predicting other parameters of interest for downdrafts and outflows can be easily derived from numerical model output. For example, the depth of the outflow essentially depends only on the radius of the precipitation core [$\text{Depth (m)} \approx 85 R \text{ (km)} + 170$]. This is also true of the height of the wind speed maximum within the outflow, although the variation is small, from 75 – 100 m agl for radii from 1.0 to 5.0 km. However, these may both depend on the stability of the boundary layer and temperature of the outflow air; if the boundary layer is neutral and the outflow temperature is close to that in the environment, there will be no restoring force and deeper outflows in general are possible.

More important perhaps for outflow prediction is the time from initial core descent to maximum surface divergence. The DB model results suggest that this is a linear function of precipitation mixing ratio for axisymmetric storms [$\text{Time (sec)} \approx 648 - 24 L \text{ (g/Kg)}$ for a rain core centered at 4 km agl, falling in a dry adiabatic environment, with $L \leq 12 \text{ g/Kg}$]. Knupp (1989) has shown, through three-dimensional numerical simulations of two storms in different environments that produced the same maximum downdraft speeds, that the development time for the downdrafts depended critically on the ambient humidity distribution. Parsons and Kropfli (1990)

have shown that the effect of environmental wind shear, tilted reflectivity cores, and cell translation may be for the cell to "leave behind" its outflow, causing an offset between the location of the cell and the divergent outflow. Accurate predictions of the dependencies of both outflow structure and downdraft development time, on observable environmental and storm related parameters, will probably depend on systematic numerical experimentation to provide additional insights.

6) Other Prediction Approaches

A fair amount of recent observational work on thunderstorms has focussed on finding reliable precursors to the hazardous outflows from precipitation driven downdrafts, especially for the development of automated computer algorithms (e.g., Campbell and Isaminger 1989). This work has largely followed in the historical tradition of heuristically associating specific radar signatures of severe thunderstorms with their observed surface wind patterns (e.g., Fujita and Brown 1958; Donaldson 1965; Hiser et al. 1970; Fujita 1981; Przybylinski and DeCaire 1985).

One obvious precursor is the descent of the reflectivity core itself. This was observed in almost 100% of high reflectivity storm cases from Huntsville and Denver, but in only 10–20% of low reflectivity storms that produced strong outflows (Biron and Isaminger 1989). However, Mahoney and Elmore (1989) describe a high reflectivity storm that showed no clear sign of a descending reflectivity core. And even in the high reflectivity cases, the capability of estimating the downdraft speeds based on the descent rate of the core has not been demonstrated. The coincidence of the start of surface outflow with the arrival of rain at the ground in these cases has been demonstrated, so predicting this timing may be the most fruitful application of the core descent rate.

Biron and Isaminger (1989) found that "mid-level" (1 – 7 km a_{gl}) rotation and convergence were present in roughly half of all storms that produced strong outflows in both Huntsville and Denver. The convergence is the quantity physically related to the downdraft and subsequent outflow; the rotation is produced as a result of stretching of ambient vorticity and must be associated with convergence of some strength. The amount of vertical vorticity and its sense will strongly depend on the vertical shear of the horizontal wind on a given day and on other factors such as the local orographic variations (e.g. Peterson 1985). Proctor (1989) found that strong rotation may actually inhibit strong downdrafts because of the responsive dynamic pressure perturbations that occur. This is a well known effect (e.g., Chandrasekhar 1961).

Biron and Isaminger (1989) also found positive correlations between the surface outflow velocity and both maximum echo top height and echo top divergence. The correlation between the height of the radar echo top and the severity of the storm has been well verified; Donaldson (1965) notes that “the height of echo tops was recognized as an indicator of the intensity of convection from the very earliest days of radar meteorology”. Both echo tops and divergence may well be indicative of the convective available potential energy and perhaps the amount of ice that formed in the precipitation core. If so, this suggests two radar observable parameters that would allow the inclusion of these quantities in the current prediction equations. Both echo top height and divergence are observable long before the downdraft forms, and thus could be particularly valuable in early predictions of outflow strength.

Unfortunately, an operationally scanning radar system that requires a high update rate at low altitudes would probably not be able to scan routinely above ~ 6 km. However, Donaldson (1965) showed that the presence of a peak in reflectivity 1.5 km or higher above the freezing level was a strong indicator of severe weather. The presence of a peak in reflectivity around 6 km agl would be easier to detect accurately than the fraction of the storm mass above the freezing level suggested by Goodman et al. (1989). Hiser et al. (1970) found that the cells with lifetimes in excess of one hour were correlated with damaging winds in southern Florida (as well as cells with high maximum cloud tops and reflectivity levels). This suggests a direction for future research, since cell lifetime could easily be monitored in an operational radar system.

Historically, the predicted temperature difference between the thunderstorm outflow and the ambient environment has been used to estimate the resulting outflow speeds. Fawbush and Miller (1954) derived a cubic dependence of the surface wind speeds on this temperature difference, based on the discovery by Brancato (1942) that the surface temperature of thunderstorm downdrafts is approximately equal to the surface temperature of the moist adiabat that joins the intersection of the environmental wet bulb temperature curve and the zero degree isotherm. Proctor (1988b) derived a linear relationship that gave similar results. Results based on the theory of density currents indicate a square root dependence, at least in regions away from the source. These equations are most appropriate for heavy precipitation driven downdrafts, and would not apply to typical cases observed in Denver where the surface temperature of the downdraft air does not differ substantially from that of the environment. Also, any relationship between the surface

wind change and the temperature decrease must also take into account the stratification of the surface layer (e.g., Greene et al. 1977; Frank and Moninger 1977).

APPENDIX B. BDO Theory and the Cylindrical BDO Equation

The recent theoretical work on long nonlinear waves in the lower atmosphere by Christie (1989) provides a thorough review of the nonlinear wave theory governing the time evolution of these disturbances, and many well documented examples of atmospheric solitary waves and bores. The time dependent behavior of the Korteweg–deVries (KdV) equation and the Benjamin–Davis–Ono (BDO) equation are detailed and contrasted. Although they are quite similar, the BDO equation is appropriate for a surface based wave guide in an infinitely deep fluid and is thus most appropriate to the atmospheric boundary layer problem. The characteristic behavior of the solutions to the BDO equation is briefly summarized below. In the second section, the behavior of a modified BDO equation appropriate for cylindrical waves (the CBDO equation) is discussed and contrasted with that of the standard BDO equation, and with the cylindrical KdV equation. Some remarks on solitary waves versus undular bores are included in section 3.

1) BDO Theory

Following the notation of Christie (1989), the BDO equation can be written as

$$A_t + c_0 A_x + \alpha A A_x + \delta [\mathfrak{H}(A)]_{xx} = 0, \quad (\text{B.1})$$

where $A(x, t)$ multiplied by a vertical structure function determines the streamfunction at any point in the two dimensional fluid, x is the horizontal coordinate in the direction of propagation, t is time, subscripts x and t denote partial differentiation with respect to those variables, c_0 is the linear long wave phase speed, α and δ are the coefficients of the nonlinear and dispersive terms, respectively, which depend on the waveguide characteristics [see Christie (1989) or Eqs. (C.19) and (C.20)], and $\mathfrak{H}(A)$ is the Hilbert transform defined as

$$\mathfrak{H}(A(x)) = \frac{1}{\pi} \int_{-\infty}^{\infty} \frac{A(x')}{x' - x} dx', \quad (\text{B.2})$$

where the bar across the integral sign denotes the Cauchy principal value of the integral*. Often the $c_0 A_x$ term is eliminated by transforming to a coordinate system moving at c_0 .

The vertical structure function itself (ϕ) satisfies an eigenfunction equation that, in the Boussinesq approximation, simplifies to the Taylor–Goldstein equation:

$$\frac{d^2 \phi}{dz^2} + l^2 \phi = 0, \quad (\text{B.3})$$

where

$$l^2 = \frac{N^2}{(u_0 - c_0)^2} - \frac{\frac{d^2 u_0}{dz^2}}{(u_0 - c_0)}, \quad (\text{B.4})$$

z is the vertical coordinate, N^2 is the Brunt–Vaisala which depends on the vertical profile of virtual potential temperature in the environment, and u_0 is the horizontal wind that varies only with height. The vertical profile of the parameter l , the Scorer parameter, determines the conditions under which gravity wave energy can be trapped in the highly stratified surface layer (e.g., Crook 1986; 1988).

The important characteristics of the solution to the BDO equation can be summarized as follows [any quotes below are from Christie (1989) unless otherwise noted]:

1. “Arbitrary initial disturbances of finite volume evolve asymptotically into a finite number of permanent solitary waves followed by a dispersive oscillatory wave train.” An example of this is shown in Fig. B-1, where an initial (rounded) square pulse is shown evolving for 4.8 nondimensional time units, in a coordinate system moving with the linear phase speed c_0 . The dispersive wave train moves to the left (subcritical speed), and the solitary waves move

* The Hilbert transform can be interpreted as a convolution of the function to be transformed with $(-1/\pi x)$. It represents a kind of quadrature filter, where the amplitudes of the spectral components are left unchanged, but their phases are altered by $\pi/2$, positively or negatively depending on the sign of the spectral wavenumber (Bracewell 1986). This property allows a very efficient Hilbert transform package to be implemented on a computer through the use of fast Fourier transforms (Melville 1983; Chereskin and Mollo–Christensen 1985). The output of the Hilbert transform will be real when the input is real, and two successive applications of the transform will give back the negative of the original function. For example, the Hilbert transform of $[\cos x]$ is $[-\sin x]$, and the Hilbert transform of $[\sin x]$ is $[\cos x]$.

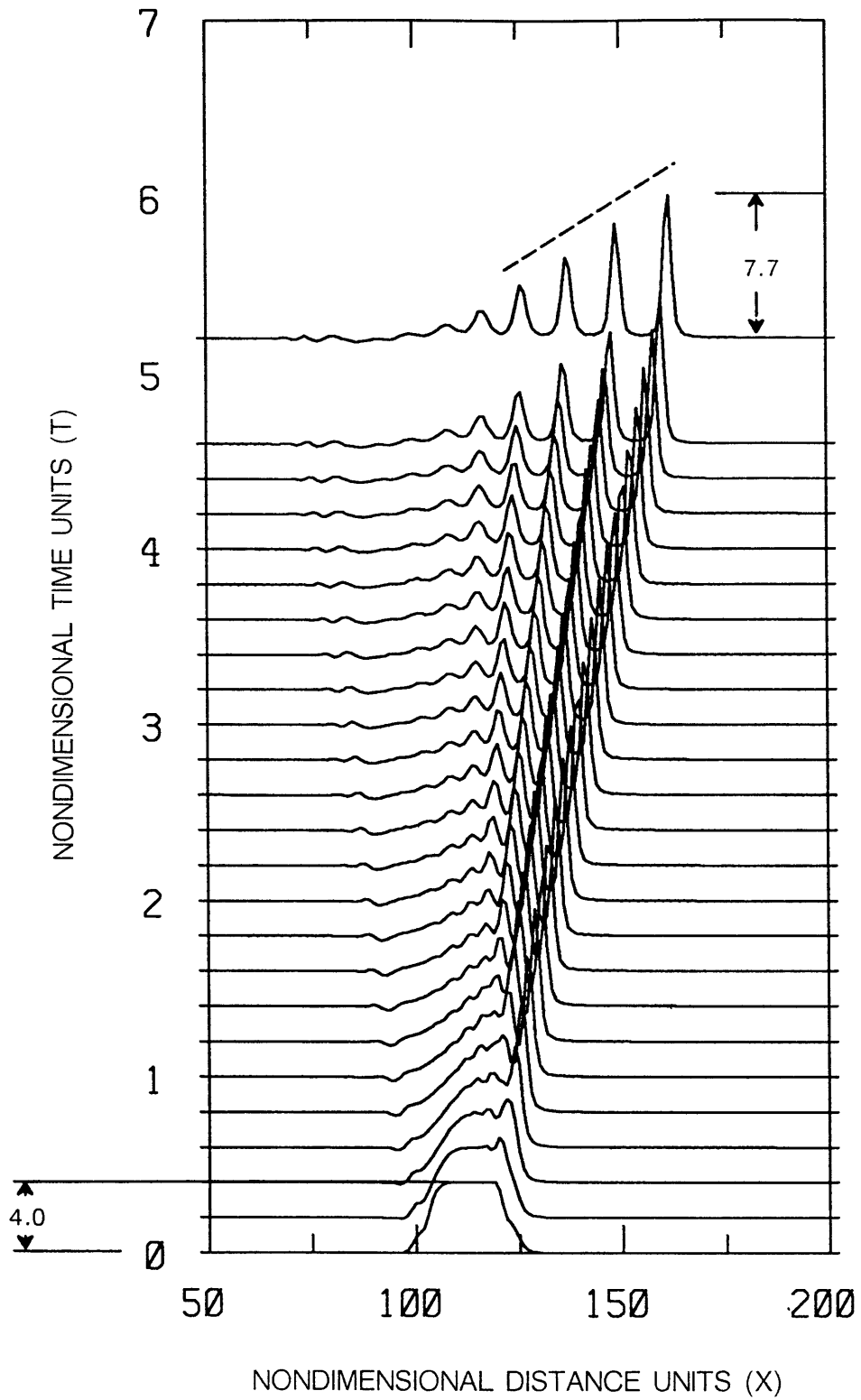


Fig. B-1. Illustration of an arbitrary initial disturbance evolving into BDO solitary waves.

to the right (supercritical speed). The BDO equation is formulated so as to admit only the right-moving solitary waves.

2. "Most of the energy in initial waves of elevation is focussed into the solitary wave component. As a rule, initial disturbances of this type with large positive volume produce only very minor dispersive wave components." The example shown in Fig. B-1 has a very weak dispersive wave train. Had the initial square pulse disturbance not been rounded, the dispersive components would have been larger.
3. "The speed of the solitary wave components exceeds the linear phase speed, c_0 , by an amount proportional to the wave amplitude." This relationship can be expressed, for the exact time-independent solution to the BDO equation [$A = f(x-ct)$; see 4. below], as

$$c - c_0 = \frac{\alpha}{4} a = \frac{\delta}{\lambda} , \quad (\text{B.5})$$

where c is the solitary wave speed, a is the wave amplitude, λ is the wave half width at half maximum amplitude, and the other variables have been previously defined. The first equation shows that the solitary wave speed excess over the linear wave speed is indeed linearly proportional to the amplitude. "The asymptotic solution therefore consists only of a family of amplitude ordered solitary waves." This is illustrated by the last, offset trace in Fig. B-1, where it is clear that the largest wave has moved the farthest.

4. The second part of Eq. (B.5) shows that the horizontal wavelength of the solitary wave is inversely proportional to the wave amplitude. As the solitary wave evolves and increases in amplitude, its horizontal dimension becomes narrower. In the asymptotic limit, each solitary wave has the characteristic Lorentzian shape given by

$$A(x, t) = \frac{a \lambda^2}{(x - ct)^2 + \lambda^2} . \quad (\text{B.6})$$

This is the exact solution to the time-independent BDO equation first found by Benjamin (1967). With the relationships specified by Eqs. (B.5) and (B.6), it is clear that the complete time-independent solitary wave shape and speed are determined once the amplitude and waveguide characteristics are specified.

5. The number of solitons created depends upon the volume of the initial disturbance, with larger initial volumes creating more waves. The solitary wave creation process is quantized; in fact there is a direct analogy between KdV solitons produced from an arbitrary initial disturbance and the eigenvalues of the Schrodinger equation of quantum physics, with the profile of the initial disturbance providing the scattering potential (Gardner et al. 1967; Whitham 1974; Drazin and Johnson 1989). There is no known exact solution for the number of solitons created in the evolution of a disturbance governed by the BDO equation. Matsuno (1984) showed that in the limit of zero dispersion, the number of solitary waves created increases without bound. Christie (1989) found an approximate expression for the number of solitons created from an arbitrary disturbance in the BDO system with finite dispersion

$$N = \frac{1}{4\pi} \int_{-\infty}^{\infty} U(X,0) dX, \quad (\text{B.7})$$

where N is the number of solitons and U is a nondimensionalized version of the amplitude structure function A . This dependence on the initial conditions is illustrated in Fig. B-2, where the evolution of an initial (rounded) square pulse (as in Fig. B-1), is examined for initial pulse amplitudes of 1, 2, and 3 (2, 3, and 4 times the depth of the inversion layer). The early time evolution is shown, and the differences are quite apparent. More waves evolve with larger initial conditions.

6. The amplitude of the evolving waves, as well as the number, increases with increasing amplitude of the initial disturbance. Matsuno (1984) showed that in the limit of zero dispersion, the maximum solitary wave amplitude was limited to four times the maximum amplitude of the initial condition. Christie (1989) found that the same condition applies with finite dispersion. This is an important difference between the classical shallow fluid solitary waves, governed by the KdV equation, and the deep fluid solitary waves governed by the BDO equation; the maximum amplitude of KdV solitary waves is limited to only two times the maximum amplitude of the initial condition. The consequence of this and Eq. (B.7) is that the amplitudes of the solitary waves in the asymptotic limit will not only be ordered, with the largest fastest wave leading, but their amplitudes will be linearly related as they are in the

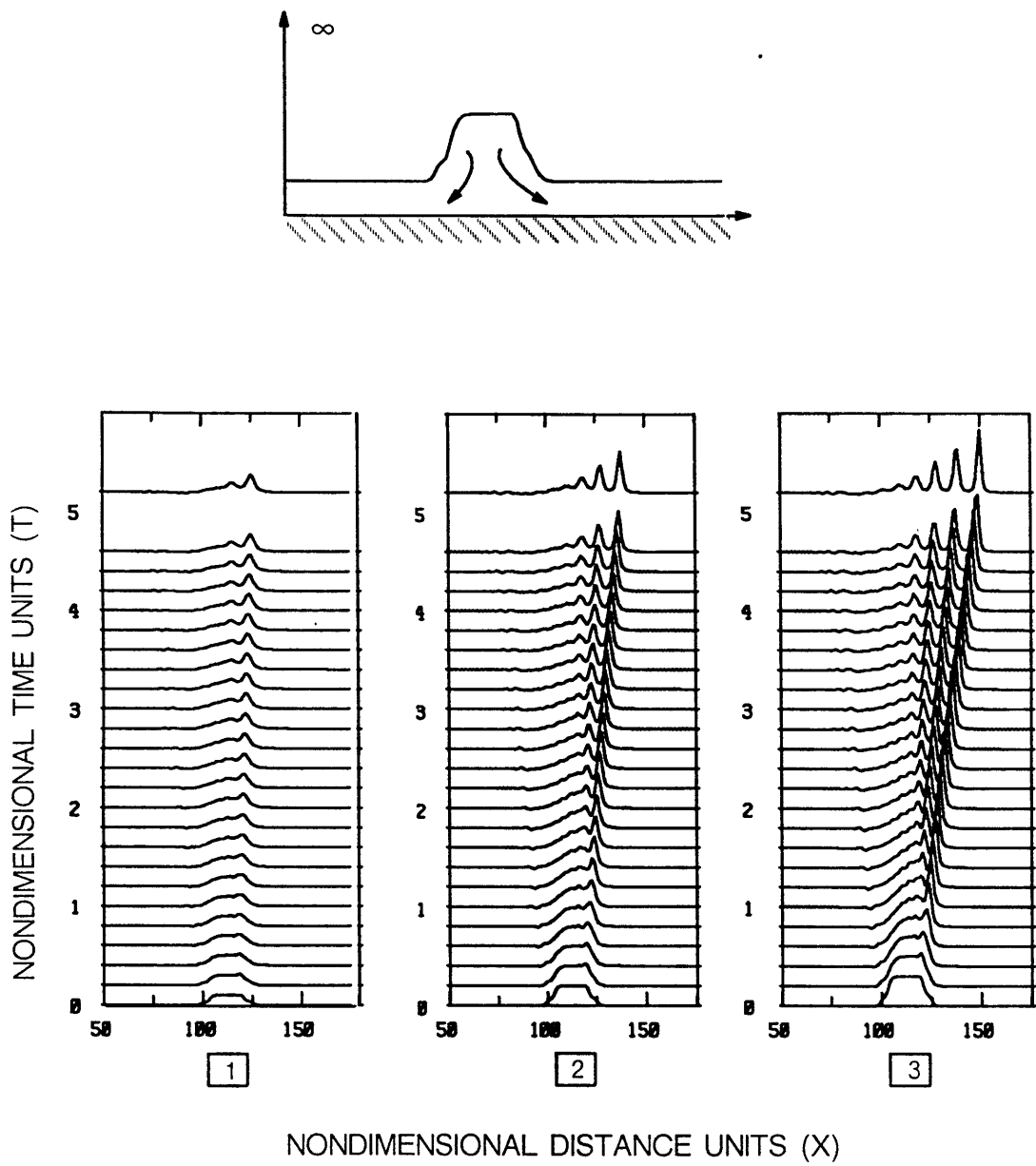


Fig. B-2. Inversion height is initially increased locally to a height two times the inversion depth ("1"), three times the inversion depth ("2"), and 4 times the inversion depth ("3") as illustrated in the uppermost figure. The flow is allowed to evolve for 4.8 T (nondimensional time) units. The larger the initial condition, the more solitons evolve, and the larger they can become.

KdV system (Whitham 1974). This is illustrated by the dashed curve above the wave peaks in Fig. B-1.

7. The BDO equation governs weakly nonlinear disturbances. If h is the effective depth of the deep fluid waveguide, then observed waves with amplitudes up to $a/h = 0.5$ should be described accurately. Tung et al. (1982) found that as wave amplitude increases above $a/h = 0.5$, the agreement between the predictions of the full nonlinear theory and those of the weakly nonlinear BDO theory begins to deteriorate. They note that "at $a/h \sim 1$ recirculation regions appear in the flow domain and some of the predictions of the weakly nonlinear theories become not even qualitatively correct. For example, the contraction in half-widths with increasing amplitudes predicted by the weakly nonlinear theories ceases to be correct for $a/h \geq 1$ as recirculation regions seem to bring about an expansion in wave widths for increasing amplitudes." An illustration of the relative streamline pattern in an amplitude ordered solitary wave family, in which the first (largest) wave has a recirculating flow, is given in Fig. B-3.

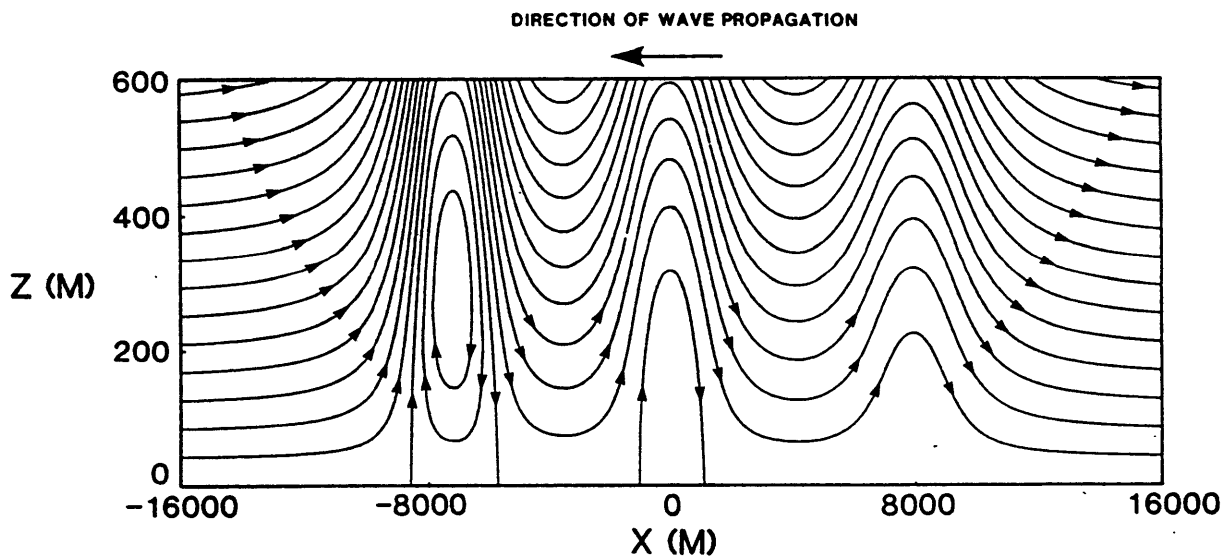


Fig. B-3. Model calculation of the relative streamline pattern for a well-resolved amplitude ordered solitary wave family propagating in an inversion waveguide of effective depth of 400 m. Taken from Christie and Muirhead (1983b).

2) The Cylindrical BDO Equation

In a cylindrical geometry appropriate for the waves generated in a stably stratified boundary layer by the outflow from an isolated axisymmetric thunderstorm, the effects of geometrical distortion are equally important to the resulting waveform evolution as are nonlinearity and dispersion. The cylindrical BDO (CBDO) equation, derived in Appendix C [Eq. (C.18)], is

$$A_{\tau} + \boxed{\frac{A}{2\tau}} + \alpha A A_{\xi} - \delta [3\epsilon(A)]_{\xi\xi} = 0,$$

where τ is the scaled time, ξ the radial coordinate in a reference frame moving with the one dimensional linear long wave speed [Eq. (C.3)], and the other variables have been defined in Appendix C. In the moving reference frame, this equation is identical to the BDO except for the boxed term proportional to $1/\tau$. This radial distortion term can be viewed as a damping applied to the BDO equation, for it causes the wave amplitude to decay as the initial wave energy excites progressively more fluid.

The time evolution of the BDO versus the CBDO is illustrated in Fig. B-4, where the results of numerically integrating the equations from an initial square wave of elevation forward in time (e.g., Vliegthart 1971; Melville 1983) are shown. Waves that move neither to the right nor to the left are moving at the one dimensional linear long wave speed; deviations from this speed are due to nonlinear, dispersive, and radial distortion effects. The essential difference is that in the cylindrical case, the process of wave amplification is rapidly thwarted by the radial damping, leaving nonlinear waves moving at nearly the speed of linear ones.

To examine the difference between the BDO and the CBDO equations in more detail, each equation was initialized with the exact steady solution to the BDO equation for a single solitary wave [Eq. (B.6)]. The early time evolution is shown in Fig. B-5. As expected, the wave remains unchanged in the BDO system, while its amplitude decreases with time in the CBDO system. The wave also becomes asymmetric in the CBDO system, with the slope becoming progressively sharper on the trailing edge, as the wave moves radially outward.

The asymmetry that develops in the cylindrical case is quite interesting. It is accompanied by the development of a "shelf" or wave of depression when the initial plane wave is moving radially outward. (The "shelf" becomes a wave of elevation when the wave is moving inward.) This is shown clearly in Fig. B-6, where an initial solitary wave of amplitude 10 is integrated forward in

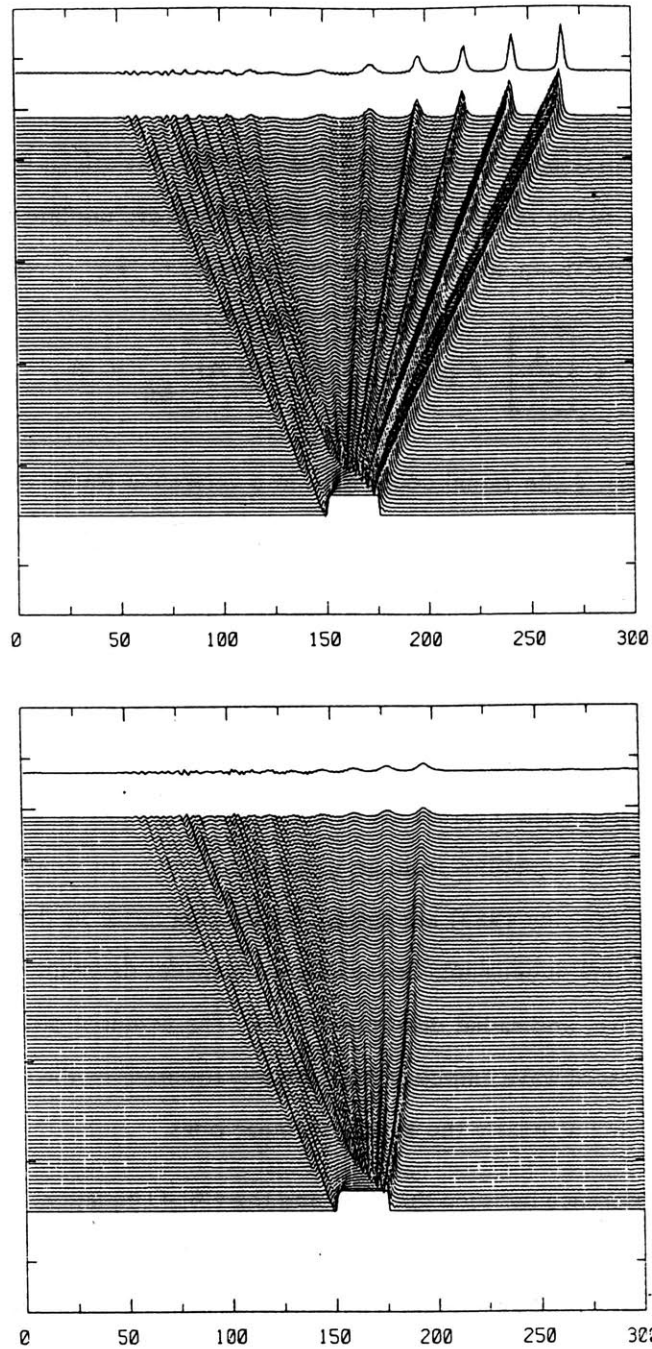


Fig. B-4. Numerical integration for 100 nondimensional time units (one trace for each) of (Top) BDO equation and (Bottom) CBDO equation, for an initial finite wave of elevation (amplitude of 1). The horizontal axis is the nondimensional space coordinate moving at the linear long wave speed. In the cylindrical problem, the initial time τ_0 was 5. The values of α and δ used for both equations were 1.5 and 0.48, respectively.

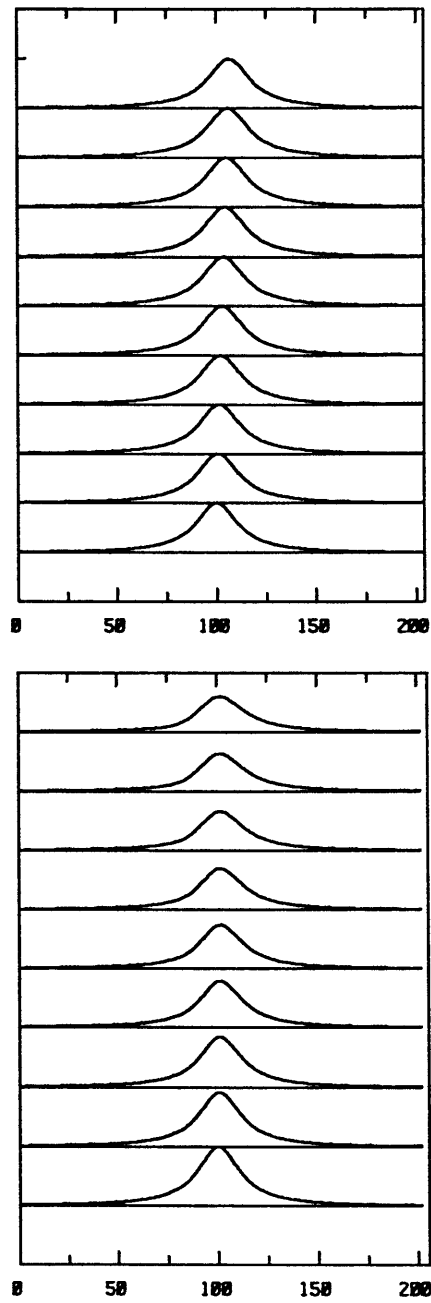


Fig. B-5. Early time evolution of solitary wave. (Top) Wave remains unchanged in BDO system since it is exact solution to steady equation. (Bottom) Amplitude is reduced and wave becomes asymmetric in CBDO system. Initial wave amplitude was 1, τ_0 was 1, and times are shown at intervals of 0.2.

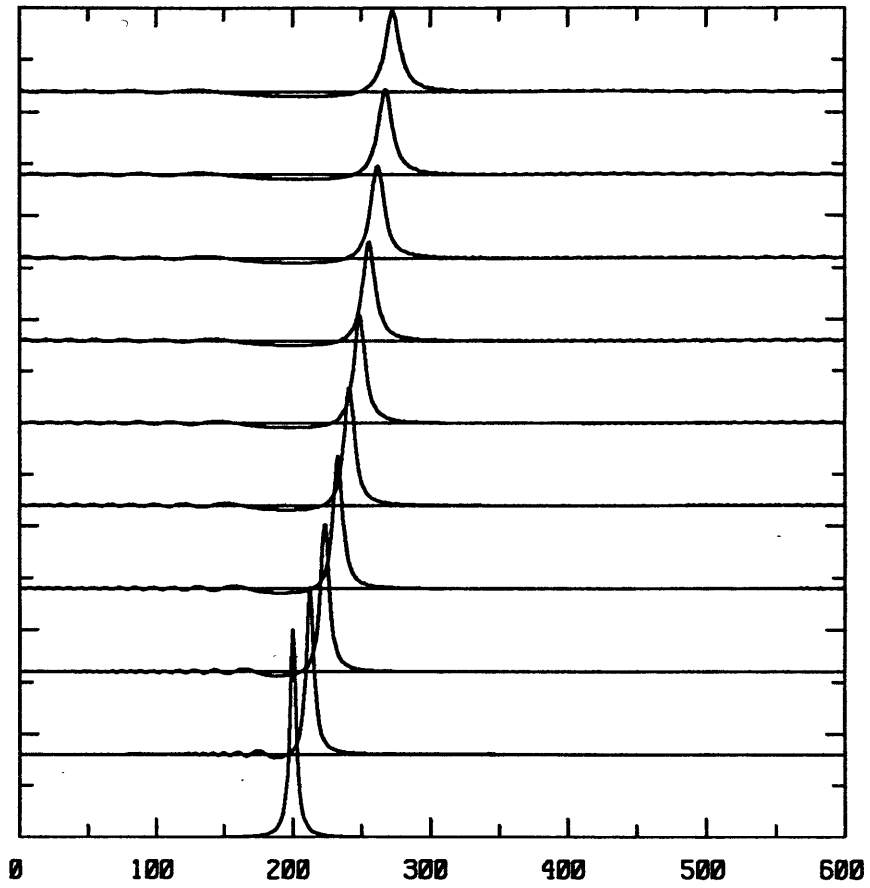


Fig. B-6. Plane BDO solitary wave evolution in the CBDO system. The initial wave amplitude was 10. Time steps shown are 0.2 apart. The wave of depression following the solitary wave is a linear feature.

the CBDO system for 1.8τ units. The shelf wave is a linear feature. An analogous feature develops in the solution to the cylindrical KdV (CKdV) equation (Weidman and Zakhem 1988). This feature is not a numerical artifact; the measured wave amplitude profiles in a diverging channel made by Chang et al. (1979; Fig. B-7) prove that it is found in laboratory experiments as well. The effects of cylindrical geometry may account for the depressed outflow layer behind, and the unexplained asymmetry and amplitude decay with time, of the Oklahoma solitary wave studied by Doviak (Fig. V-6, middle and bottom).

The plane KdV wave in the CKdV system also exhibits amplitude decay as expected, but the rate of amplitude decay is not the same as in the CBDO system. In the top panel of Fig. B-8, the nondimensional amplitude versus range dependence is shown for the axisymmetric linear, CKdV, and CBDO systems. Notice the amplitude decays most rapidly in the CBDO system. In the linear system the dependence is $a \sim r^{-1/2}$, in the CKdV it is $a \sim r^{-2/3}$, and in the CBDO it is $a \sim r^{-0.775}$. Because of this sharper amplitude decay, and the nonlinear dependence of wave speed on amplitude, the trajectory of a CBDO wave will be closer to that of a linear wave than a CKdV wave would be. In the bottom panel of Fig. B-8, the range versus time dependence is shown for the

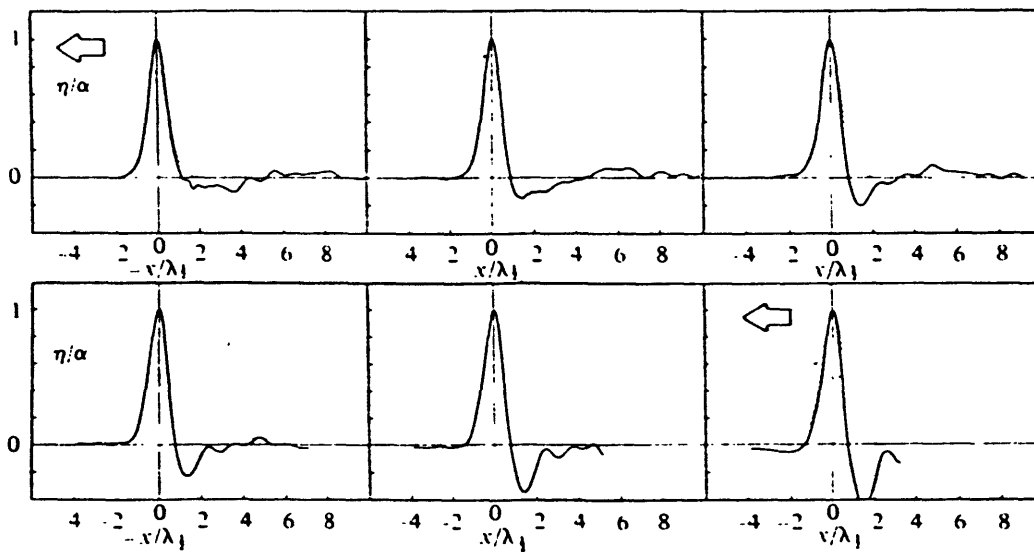


Fig. B-7. Measured temporal profiles (solid line) for initial wave amplitude of 0.4 in a diverging channel of 30 cm depth (KdV system). The profiles were measured at $x = 4.2, 17.6, 30.9, 37.6, 50.9, \text{ and } 64.3$. Taken from Chang et al. (1979).

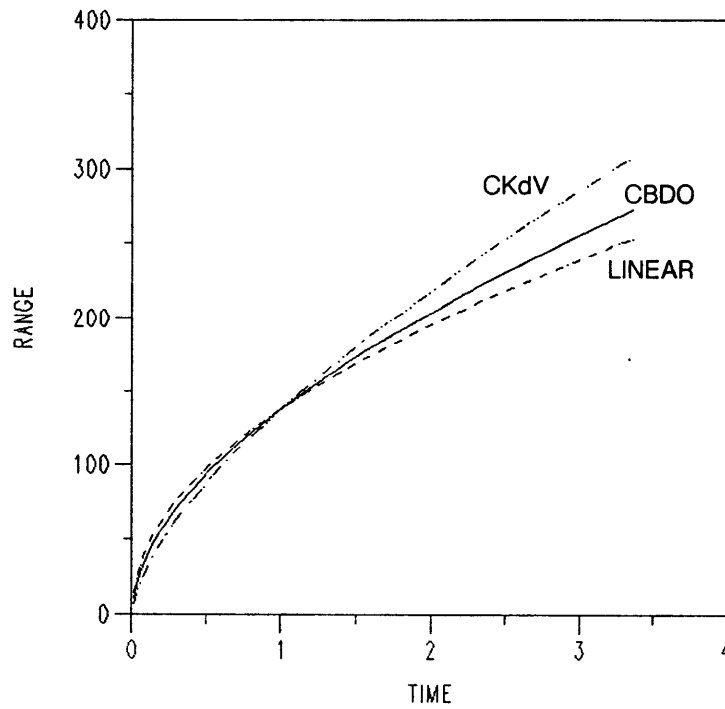
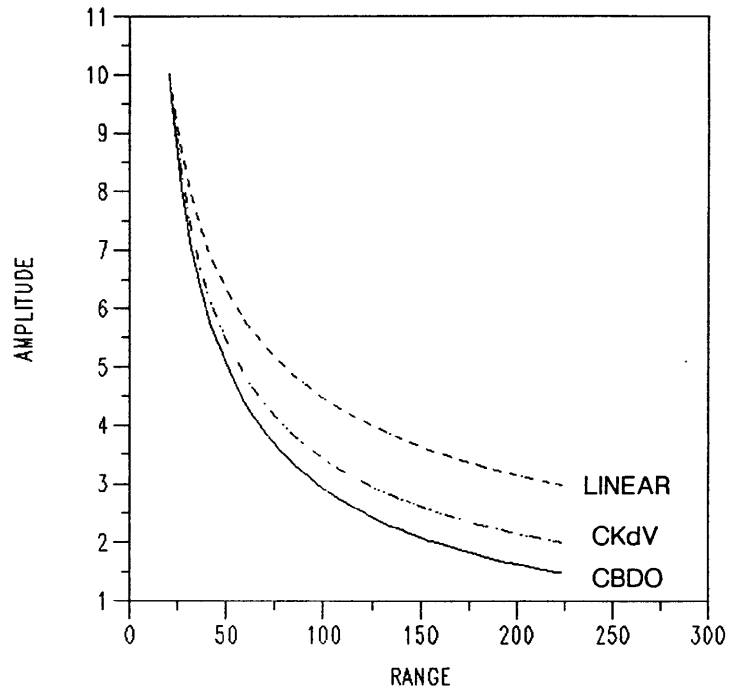


Fig. B-8. (Top) Amplitude versus range dependence of linear, KdV, and BDO waves in an axisymmetric geometry. (Bottom) Wave peak position as a function of time for the same three wave systems.

three systems. In the linear system the dependence is $r \sim t^{1/2}$ in the CKdV it is $r \sim t^{2/3}$, [although this was derived by Maxworthy (1980) using $a \sim r^{-1/2}$ appropriate for linear waves; the correct dependence may be $r \sim t^{0.6}$], and in the CBDO it is $r \sim t^{-0.57}$.

One feature noted by Weidman and Zakhem (1988) was that disturbances generated by a piston displacement in a laboratory tank passed through a distinct linear regime before undergoing a rather abrupt transition to the nonlinear regime, in terms of the observed amplitude dependence on radial distance. They note that all of their numerical experiments started with the exact KdV plane wave solution exhibited only the expected nonlinear dependence. To examine the time dependence of wave amplitude in the CBDO system for more realistic initial conditions, a numerical integration was started with a rounded square pulse with an amplitude of 2 (Fig. B-9, top). As in the BDO system, the amplitude begins to increase with time, but the radial distortion soon takes over and the expected decay begins. The dash-dot curve in Fig. B-9 shows the amplitude dependence that would be observed had the initial disturbance been an exact BDO plane wave in the CBDO system. No increase in amplitude is seen as with the arbitrary initial disturbance, and the initial decay is more steep, but in either case a linear regime is not observed. At later times, the amplitude decay for the BDO plane wave and the square wave initial condition matches. It would be very interesting to perform a series of laboratory experiments for which the CBDO equation is a good model, and initiate disturbances with dense fluid intrusions; perhaps a linear regime would be identified initially for those waves as well.

To summarize, the behavior of the CBDO equation suggests that amplitude increases away from the wave source will not occur for waves generated by axisymmetric thunderstorms, because the geometric damping exceeds any tendency for the solitary wave amplitudes to increase as in the one dimensional BDO system. In terms of their trajectories, CBDO waves may be indistinguishable from linear ones. However, if the solitary wave disturbance has or develops a planar geometry, it may well propagate undiminished for long distances away from the source, and may actually amplify with time.

3) Solitary Waves Versus Undular Bores

Christie (1989) was the first to examine the evolution of an internal deep fluid bore, governed by the BDO equation. He modelled both an infinitely long bore and a bore of finite length, arguing that the latter providing a more realistic model for the morning glory disturbances observed in northern Australia (Smith 1988). The finite bore certainly provides a better model than

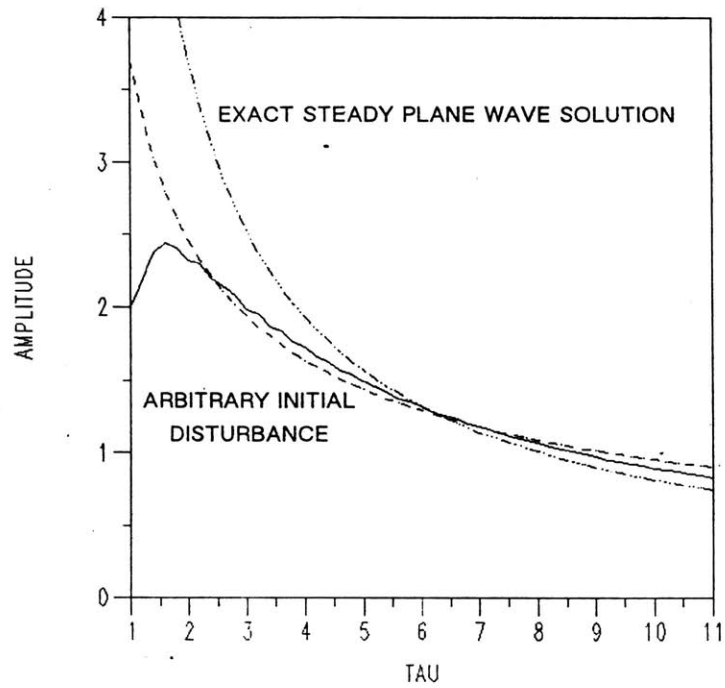
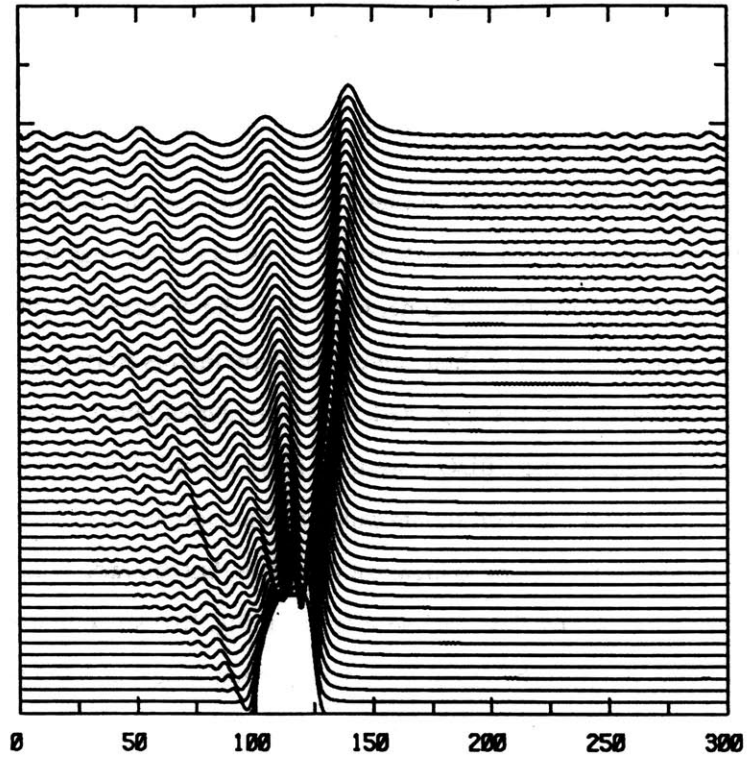


Fig. B-9. (Top) CBDO waves evolving from an initial rounded square wave with amplitude of 2. (Bottom) Amplitude vs. τ dependence of leading wave shown above.

the infinite bore for the pool of cold air flowing out beneath a convective storm system (although taking account of the geometry is crucial). Figure B-10 shows Christie's numerical integration results; a steady state is not approached in either the finite length or infinite bore simulations because no dissipation is included. In this sense it may be misleading to call these bores; they are actually evolving solitary wave trains.

Christie (1989) also examined bore solutions to the BDO-Burgers equation, the BDO equation with a term included to represent the effects of turbulent diffusion, and found that the solution rapidly evolved to a stable time-independent state. The solution remained smooth when strong dissipation was included, and became undular when weak dissipation was included. This is very similar to the solution of the KdV-Burgers equation, which has been used to model the morning glory phenomenon by Egger (1983; 1984). The individual waves of undular bore-like features in the atmosphere have been referred to as solitary waves by e.g., Christie et al. (1979). This is probably correct if a relative steady state has not been reached. A nearly energy-conserving solution that permits the leading undulations to separate from the bore as one or more solitary waves may well be appropriate for many atmospheric cases.

The infinite bore model may realistically describe the atmospheric situation of a synoptic scale cold air mass and its cold front. The "rope cloud", a very thin line of shallow clouds along the leading edge of some cold fronts could well be a nonlinear phenomenon related to the undular bore (Simpson 1987), perhaps as it evolves into one or more solitary waves. That solitary wave theory could possibly explain certain very narrow, large amplitude pressure waves was suggested long ago by Abdullah (1956), and researchers have recently found that it may well explain certain longer wavelength "singular" large amplitude pressure waves (Bosart and Sanders 1986). Tepper (1950) suggested that a pre-frontal pressure jump, supposedly generated when a piston-like impetus from the cold front occurred, could be the cause of some pre-frontal squall lines. Several researchers found that an inversion or duct invariably existed prior to the advent of these narrow squall lines.

The structure of these sharp fronts has been compared recently to that of gravity current fronts (e.g., Shapiro, 1984; Seitter and Muench 1985; Shapiro et al. 1985) but, just as in most gravity current studies, account of the stratification of the air ahead of the current was not taken. Shapiro et al. (1985) note that "the leading edge of the density current and its hydraulic head propagated at a greater horizontal velocity than the normal wind component beneath the head,

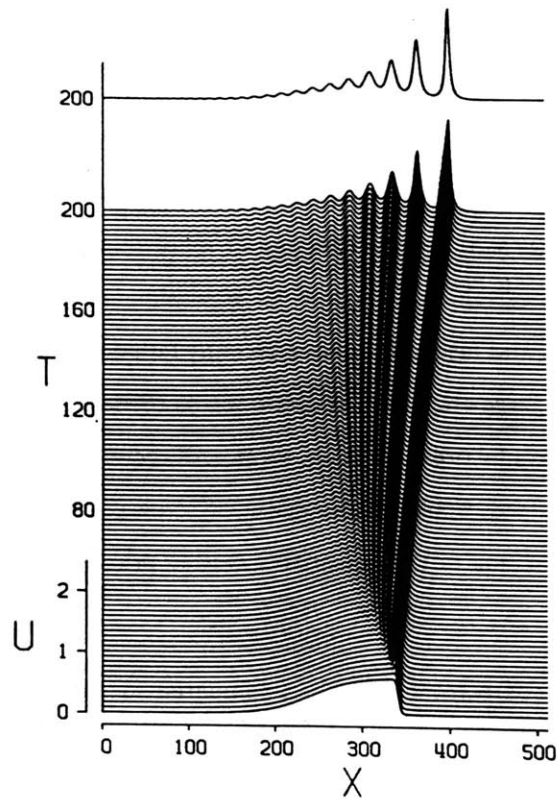
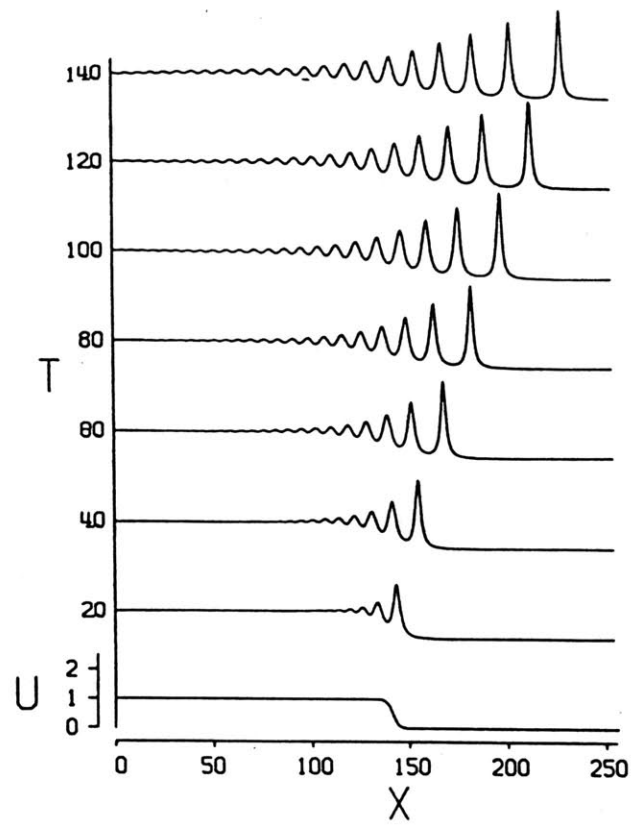


Fig. B-10. Numerical integration of the BDO equation for (Top) an initially smooth deep-fluid bore wave, and (Bottom) a long, but finite-length, wave of elevation. Taken from Christie (1989).

i.e., 15 m/s compared with 9 m/s”, but Smith and Reeder (1988) note that “this is *not* a characteristic of a gravity current”. Any effort at analysis of these mesoscale fronts has largely focussed on determining frontogenetical forcing, etc. Perhaps application of the BDO(-Burgers) equation, extended to include the Coriolis force if necessary, to the rope cloud cases presented in those papers might help in heuristically explaining the observed structures [even though solitary wave theory appeared not to be the likely explanation for the narrow line convection analyzed by Koch (1984)].

APPENDIX C. Derivation of the Cylindrical BDO Equation

In this appendix, the details of the derivation of the cylindrical Benjamin–Davis–Ono (CBDO) equation are given. The derivation is based on the work of Ablowitz and Segur (1980), who derived an equation governing the evolution in two spatial dimensions of long internal waves in deep fluids. Their derivation was, in turn, based on the nonlinear perturbation method first used by Ono (1975) to derive the time dependent equation governing one dimensional internal waves in stratified fluids of great depth. This equation has come to be known as the BDO equation [Eq. (B.1)], although the earlier work of Benjamin (1967) and Davis and Acrivos (1967) was concerned only with the *steady* propagation of a *single* algebraic solitary wave. The CBDO equation has not previously been derived in the literature. The cylindrical Korteweg–deVries (CKdV) equation has been discussed previously; it was first derived by Maxon and Viccelli (1974) for ion acoustic waves and first discussed in the context of surface gravity waves by Miles (1978). Weidman and Zakhem (1988) recently summarized the past work on the CKdV and compared its theoretical and numerical solutions with their own laboratory experimental data on surface waves and with experimental data on internal waves obtained by Maxworthy (1980).

The natural cylindrical geometry of thunderstorm outflows suggests that radial and vertical motions in an incompressible, inviscid, stably stratified fluid be considered. The unperturbed base state of the fluid is motionless, with pressure and density varying in height only, and in hydrostatic balance. It is useful to think of a continuous background density (ρ) distribution such as

$$\rho_0(z) = \rho_\infty \left\{ 1 + \delta e^{-\frac{z}{h}} \right\} \quad z > 0 ,$$

where z is the vertical coordinate, and ρ_∞ is the constant value of the density approached as $z \rightarrow \infty$. In the atmosphere, h is a measure of the surface inversion thickness, and δ a small number, typically ~ 0.01 . An equivalent intrinsic length scale for other perhaps more realistic density profiles, typifying the “depth” of the waveguide, is

$$h = \left[\frac{\rho(z) - \rho_\infty}{-\frac{d\rho_0}{dz}} \right]_{\min} .$$

Although the derivation will be phrased in terms of the density distribution, it is much more common to think of atmospheric stability in terms of the potential temperature structure. For a

moist atmosphere with the same Brunt–Vaisala frequency as an incompressible stratified fluid, the virtual potential temperature (θ_{v0}) can be related to the density as follows (assuming the Coriolis force can be neglected)

$$\rho_0(z) = \frac{\rho_0(0) \theta_{v0}(0)}{\theta_{v0}(z)}.$$

An example of the virtual potential temperature structure in a typical atmospheric inversion is presented in Fig. C-1.

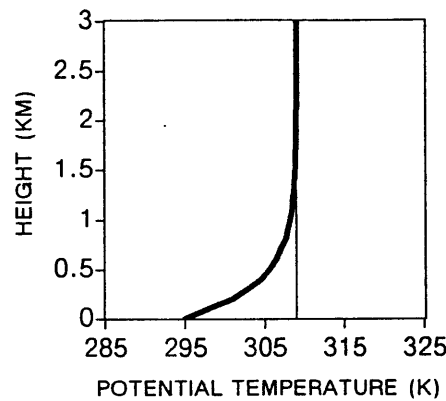


Fig. C-1. Example of environmental virtual potential temperature profile that could support surface gravity waves in the atmosphere. Adapted from Doviak and Chen (1988).

The goal in this derivation will be to isolate long waves, in which nonlinearity balances dispersion. Defining ϵ to be a measure of dispersion

$$\epsilon = h / \lambda,$$

the waves to be described are long in the sense that ϵ is small, i.e. $\epsilon \ll 1$. Nonlinearity can be measured as the ratio of wave amplitude a to h ; Koop and Butler (1981) emphasized that in deep fluids

$$a / h = O(\epsilon).$$

[This is fundamentally different from the scaling described by KdV theory, where $a/h = O(\epsilon^2)$.]

The approach used in isolating the governing equation will be to expand the dependent variables in

the nonlinear system of equations in terms of the small parameter ϵ , and to solve the equations through the lowest two orders.

The appropriate equations of motion for this axisymmetric system are

$$\begin{aligned}
 \rho \left[u_t + u u_r + w u_z \right] &= -p_r , \\
 \rho \left[w_t + u w_r + w w_z \right] &= -p_z - \rho g , \\
 u_r + \boxed{\frac{u}{r}} + w_z &= 0 , \\
 \rho_t + u \rho_r + w \rho_z &= 0 ,
 \end{aligned} \tag{C.1}$$

where u is the radial velocity, w the vertical velocity, p the pressure, g the gravitational acceleration, r the radial coordinate, and t is time. The subscripts indicate partial differentiation with respect to the given variable. The only difference between this system of equations and those for a planar geometry is the boxed term, inversely proportional to the radial coordinate, in the continuity equation. The required boundary conditions are

$$\begin{aligned}
 w &= 0 \quad \text{at} \quad z = 0 , \\
 |u, w| &\rightarrow 0 \quad \text{as} \quad z \rightarrow \infty ,
 \end{aligned}$$

and the initial conditions are

$$\begin{aligned}
 u, w &= 0 , \\
 \rho &= \rho_0(z) , \\
 \frac{d\rho_0}{dz} &= -\rho_0 g .
 \end{aligned} \tag{C.2}$$

The fluid can be divided up into two regions: an “inner” region at the surface in which the density variations are important, and in which h is a natural length scale for the vertical coordinate, and an “outer” region above in which density variations are negligible. The scaling for the vertical coordinate will be different in the two regions, and the solution to the problem will be found by requiring that the two representations of the vertical velocity match in the region of

overlap. The deep fluid, long wave limit of the linear dispersion relation [i.e., $\omega = k c_0 (1 - \beta|k|)$; Benjamin 1967], was used to determine the relative space and time scaling so that the slow time evolution at second order would balance with nonlinearity (e.g., Dodd et al. 1982).

Small amplitude, long waves travelling in the radial direction can be obtained by using the following scaling in the lower layer

$$\begin{aligned}
 \zeta &= \frac{z}{h}, \\
 \xi &= \frac{\epsilon (r - c_0 t)}{h}, \\
 \tau &= \frac{\epsilon^2 c_0 t}{h}, \\
 \frac{1}{r} &= \frac{\epsilon^2}{h} \left(\frac{1}{\tau + \epsilon \xi} \right) \sim \frac{\epsilon^2}{h \tau}.
 \end{aligned}
 \tag{C.3}$$

By transforming to a reference frame moving with the linear, nondispersive, one dimensional wave velocity c_0 , the interactions between dispersion and nonlinearity can be investigated clearly in a system where they are the same order of magnitude. The dependent variables are expanded in powers of ϵ with the expansion variables now being functions of the scaled independent variables

$$\begin{aligned}
 u &\sim \epsilon c_0 (u_1 + \epsilon u_2), \\
 w &\sim \epsilon^2 c_0 (w_1 + \epsilon w_2), \\
 p &\sim p_0(\zeta) + \epsilon \rho_\infty c_0^2 (p_1 + \epsilon p_2), \\
 \rho &\sim \rho_0(\zeta) + \epsilon \rho_\infty (\rho_1 + \epsilon \rho_2).
 \end{aligned}$$

After applying these scalings, inserting these expansions, and using Eq. (C.2), the equations of motion (C.1) become, in order

$$\begin{aligned}
(\rho_0 + \epsilon \rho_\infty \rho_1) \left\{ \frac{\epsilon^3 c_0^2}{h} (u_1)_\tau - \frac{\epsilon^2 c_0^2}{h} (u_1)_\xi - \frac{\epsilon^3 c_0^2}{h} (u_2)_\xi \right. \\
\left. + \frac{\epsilon^3 c_0^2}{h} u_1 (u_1)_\xi + \frac{\epsilon^3 c_0^2}{h} w_1 (u_1)_\zeta \right\} = \\
- \frac{\epsilon^2 c_0^2}{h} \rho_\infty (p_1)_\xi - \frac{\epsilon^3 c_0^2}{h} \rho_\infty (p_2)_\xi,
\end{aligned}$$

$$\begin{aligned}
(\rho_0 + \epsilon \rho_\infty \rho_1) [O(\epsilon^3)] &= - \frac{1}{h} \frac{d\rho_0}{d\zeta} - \rho_0 g \\
&- \frac{\epsilon c_0^2}{h} \rho_\infty (p_1)_\zeta - \epsilon \rho_\infty \rho_1 g \\
&- \frac{\epsilon^2 c_0^2}{h} \rho_\infty (p_2)_\zeta - \epsilon^2 \rho_\infty \rho_2 g,
\end{aligned}$$

$$\frac{\epsilon^2 c_0}{h} (u_1)_\xi - \frac{\epsilon^3 c_0}{h} (u_2)_\xi + \boxed{\frac{\epsilon^3 c_0}{h} \frac{u_1}{\tau}} + \frac{\epsilon^2 c_0}{h} (w_1)_\zeta + \frac{\epsilon^3 c_0}{h} (w_2)_\zeta = 0,$$

$$\begin{aligned}
\frac{\epsilon^3 c_0^2}{h} \rho_\infty (\rho_1)_\tau - \frac{\epsilon^2 c_0^2}{h} \rho_\infty (\rho_1)_\xi - \frac{\epsilon^3 c_0^2}{h} \rho_\infty (\rho_2)_\xi \\
+ \frac{\epsilon^3 c_0^2}{h} \rho_\infty u_1 (\rho_1)_\xi + \frac{\epsilon^3 c_0^2}{h} \rho_\infty w_1 (\rho_1)_\zeta \\
+ \frac{\epsilon^2 c_0^2}{h} w_1 \frac{d\rho_0}{d\zeta} + \frac{\epsilon^3 c_0^2}{h} w_2 \frac{d\rho_0}{d\zeta} = 0.
\end{aligned}$$

The non-numeric subscripts here and in all equations that follow indicate partial differentiation with respect to that variable. After collecting terms in like powers of ϵ , the leading order equations for the lower layer are obtained

$$\begin{aligned}
(u_1)_\xi - \frac{\rho_\infty}{\rho_0} (p_1)_\xi &= 0, \\
(p_1)_\zeta + \frac{g h}{c_0^2} \rho_1 &= 0, \\
(u_1)_\xi + (w_1)_\zeta &= 0, \\
-\rho_\infty (p_1)_\xi + w_1 \frac{d\rho_0}{d\zeta} &= 0.
\end{aligned} \tag{C.4}$$

These are the same equations that result at lowest order in Ono's (1975) derivation of the one dimensional governing equation. If u_1 , p_1 , and ρ_1 are eliminated in favor of w_1 , these four equations reduce to

$$\left[\rho_0 (w_1)_\zeta \right]_\xi - \frac{g h}{c_0^2} \frac{d\rho_0}{d\zeta} w_1 = 0. \tag{C.5}$$

The radial and temporal variation of the vertical velocity can be separated from its vertical dependence by defining two new functions A and ϕ as follows

$$w_1 = - (A(\xi, \tau))_\xi \phi(\zeta). \tag{C.6}$$

Substituting this into Eq. (C.5) provides the vertical structure equation for the waves

$$\frac{d}{d\zeta} \left(\rho_0 \frac{d\phi}{d\zeta} \right) - \frac{g h}{c_0^2} \frac{d\rho_0}{d\zeta} \phi = 0. \tag{C.7}$$

In the limit as $\zeta \rightarrow \infty$, ρ_0 approaches a constant value and thus $d\rho_0/d\zeta \rightarrow 0$. In this limit, Eq. (C.7) determines that $d^2\phi/d\zeta^2 \rightarrow 0$, or equivalently that $d\phi/d\zeta \rightarrow \text{constant}$. However, the solution will not remain bounded unless this constant is equal to zero. The value of ϕ itself in this limit can be chosen arbitrarily. Equation (C.7), together with the boundary conditions summarized below, constitute an eigenvalue problem for $1/c_0^2$. Although there are infinitely many solutions to this problem, the gravest mode is usually the solution of physical interest. The value of ϕ in the limit as

$\zeta \rightarrow \infty$ has been chosen as 1 to provide a normalization condition for the eigenfunction. The boundary conditions for Eq. (C.7) are

$$\begin{aligned}\phi(0) &= 0, \\ \phi(\infty) &= 1, \\ \frac{d\phi}{d\zeta} &\rightarrow 0 \quad \text{as } \zeta \rightarrow \infty.\end{aligned}\tag{C.8}$$

Equation (C.6), together with Eqs. (C.4), defines all the lowest order unknowns in terms of A and ϕ [letting $' = d(\)/d\zeta$]

$$\begin{aligned}w_1 &= -A \xi \phi, \\ u_1 &= A \phi', \\ \rho_1 &= -A \phi \frac{\rho'_0}{\rho_\infty}, \\ p_1 &= A \phi' \frac{\rho_0}{\rho_\infty}.\end{aligned}\tag{C.9}$$

The equations of motion at the next order in ϵ become

$$\rho_0 \left((u_1)_\tau - (u_2)_\xi + u_1 (u_1)_\xi + w_1 (u_1)_\zeta \right) - \rho_\infty \rho_1 (u_1)_\xi + \rho_\infty (p_2)_\xi = 0,$$

$$(p_2)_\zeta + \frac{g}{c_0^2} \frac{h}{2} \rho_2 = 0,$$

$$(u_2)_\xi + \boxed{\frac{u_1}{\tau}} + (w_2)_\zeta = 0,$$

$$\rho_\infty (\rho_1)_\tau - \rho_\infty (\rho_2)_\xi + \rho_\infty u_1 (\rho_1)_\xi + \rho_\infty w_1 (\rho_1)_\zeta + w_2 \rho'_0 = 0.$$

The first order variables can be written in terms of A and ϕ according to Eqs. (C.9), and again all of the second order dependent variables can be eliminated in favor of the vertical velocity

$$\begin{aligned}
(\rho_0 (w_2)_\zeta)_\zeta - \frac{g h}{c_0^2} \frac{d \rho_0}{d \zeta} w_2 = & \\
& \frac{g h}{c_0^2} \left(-A_\tau \phi \rho_0' + A A_\xi (\phi \phi' \rho_0' + \phi^2 \rho_0'') - A A_\xi (\phi \phi' \rho_0') \right) \\
& \boxed{-\frac{A}{\tau} (\rho_0 \phi'' + \rho_0' \phi')} \quad (C.10) \\
& -A_\tau (\rho_0 \phi'' + \rho_0' \phi') \\
& -A A_\xi (\rho_0' (\phi')^2 + 2 \rho_0 \phi' \phi'' - (\rho_0 \phi \phi'')' + (\rho_0' \phi \phi')').
\end{aligned}$$

All three of the gh/c_0^2 terms on the right hand side can be expressed in terms of ρ_0 , ϕ , and A alone by substituting from Eq. (C.7), the ζ derivative of Eq. (C.7) multiplied by ϕ , and Eq. (C.7) multiplied by ϕ' , respectively. After grouping the exact differentials (aided by adding and subtracting terms like $2\rho_0\phi'\phi''$) and collecting terms in like coefficients of A and its derivatives, Eq. (C.10) becomes

$$\begin{aligned}
(\rho_0 (w_2)_\zeta)_\zeta - \frac{g h}{c_0^2} \frac{d \rho_0}{d \zeta} w_2 = & -A_\tau (2 (\rho_0 \phi')') \\
& \boxed{-\frac{A}{\tau} (\rho_0 \phi')'} \quad (C.11) \\
& + A A_\xi (-3 (\rho_0 (\phi')^2)' + 2 \rho_0 \phi' \phi'' + 2 (\rho_0 \phi \phi'')').
\end{aligned}$$

The second order equations have been reduced to an inhomogeneous equation for w_2 , the homogeneous portion of which is the same as Eq. (C.5). This equation has w_2 as a nonresonant particular solution only if the nonhomogeneous terms satisfy an orthogonality condition with the solution to the homogeneous problem

$$\int_0^\infty (LHS) \phi d \zeta = \int_0^\infty (RHS) \phi d \zeta, \quad (C.12)$$

where LHS represents all of the terms on the left hand side of Eq. (C.11), and RHS those on the right. Applying the solvability condition (C.12), integrating by parts, and using the boundary conditions (C.8), yields

$$\begin{aligned}
\rho_0 \{ \phi (w_2)_\zeta - \phi' w_2 \} \Big|_{\zeta \rightarrow \infty} = & \\
\left(\boxed{-\frac{A}{\tau}} - 2 A_\tau \right) \left[\rho_0 \phi' \Big|_{\zeta \rightarrow \infty} - \int_0^\infty \rho_0 (\phi')^2 d\zeta \right] & \quad (C.13) \\
+ A A_\xi \left[-3 \rho_0 (\phi')^2 \phi \Big|_{\zeta \rightarrow \infty} + 2 \rho_0 \phi^2 \phi'' \Big|_{\zeta \rightarrow \infty} + 3 \int_0^\infty \rho_0 (\phi')^3 d\zeta \right] & .
\end{aligned}$$

The surface terms at $\zeta = 0$ all vanish because w (and thus w_2 and ϕ) vanishes there. We can already anticipate that the surface terms involving ϕ' and ϕ'' will vanish as $\zeta \rightarrow \infty$ because of the requirement that ϕ remain bounded in the lower layer. The unknown ζ derivative of w_2 will be found by matching to the solution in the upper layer.

The assumption is made that the only motion in the nearly constant density fluid of the upper layer is excited by waves in the lower layer. Thus the horizontal (radial) scaling in the two layers must be consistent and the vertical scaling need not be stretched relative to the horizontal in this "outer" layer. The radial and vertical velocities will be the same order in ϵ . The scaling for the upper layer and the ϵ expansions for the dependent variables are

$$\begin{aligned}
R &= \frac{\epsilon (r - c_0 t)}{h}, \\
Z &= \epsilon \frac{z}{h} = \epsilon \zeta, \\
\tau &= \frac{\epsilon^2 c_0 t}{h}, \\
u &\sim \epsilon^2 c_0 U_1, \\
w &\sim \epsilon^2 c_0 W_1, \\
p &= P_0 + \epsilon^2 \rho_\infty c_0^2 P_1, \\
\rho &= \rho_0 + \epsilon^2 \rho_\infty \rho_1, \\
\rho_0 &= \text{constant} (\equiv \rho_\infty).
\end{aligned}$$

Substituting these into the equations of motion (C.1), the leading order equations are identical to those found in the upper layer for the plane wave problem by Ono (1975)

$$\begin{aligned}(U_1)_R &= \frac{c_0}{\rho_0} (P_1)_R, \\(W_1)_R &= \frac{c_0}{\rho_0} \left((P_1)_Z - \rho_1 g \right), \\(U_1)_R + (W_1)_Z &= 0, \\(\rho_1)_R &= 0.\end{aligned}$$

These equations reduce to Laplace's equation for the vertical velocity ($Z > 0$)

$$W_1 \xi \xi + W_1 Z Z = O(\epsilon^2), \quad (\text{C.14})$$

subject to the following boundary conditions

$$\begin{aligned}W_1 &\rightarrow 0 \quad \text{as } Z \rightarrow \infty, \\W_1 &\rightarrow 0 \quad \text{as } |R, \xi| \rightarrow \infty.\end{aligned}$$

The boundary conditions at $Z=0$ are obtained by requiring the vertical velocity in the upper layer match that in the lower layer in the region of overlap between the two layers. This region is defined as

$$\frac{\epsilon^p z}{h} = O(1), \quad 0 < p < 1.$$

The matching could take place over a region or, in the case of a discontinuous profile of density or its vertical derivative, the matching would take place at a sharp interface defined by a constant density surface. Matching the vertical velocity at $Z=0$ ($\zeta \rightarrow \infty$) gives

$$\begin{aligned} \epsilon^2 c_0 (w_1 + \epsilon w_2) &= \epsilon^2 c_0 W_1 \\ O(\epsilon^2): \quad w_1 &= - (A)_{\xi} = W_1 \\ O(\epsilon^3): \quad w_2 &= 0 \end{aligned} \quad \text{at } \begin{array}{l} Z = 0 \\ \zeta \rightarrow \infty . \end{array} \quad (C.15)$$

The bottom boundary condition for Eq. (C.14) is now known; it describes the forcing that drives all of the motion in the infinite upper layer. Laplace's equation together with these boundary conditions define a classical Dirichlet problem, the general solution of which is known [e.g., Hildebrand 1976; p. 474, Eq. (230)]. For the boundary conditions here, the solution is

$$W_1 = \frac{1}{\pi} \int_{-\infty}^{\infty} - (A)_{\xi} \frac{Z \, d\tilde{\xi}}{(\xi - \tilde{\xi})^2 + Z^2} ,$$

assuming W_1 ($Z=0$) is bounded and piecewise continuous for all values of ξ .

The matching across the two layers is completed by requiring that the vertical derivatives of the respective vertical velocities as well as the velocities themselves are equal; this ensures the unique analytic continuation of W_1 as required. The vertical derivative of W_1 evaluated at the lower boundary ($Z=0$) is

$$(W_1)_Z \Big|_{Z=0} = -\frac{1}{\pi} \left[\int_{-\infty}^{\infty} - (A)_{\xi} \frac{d\tilde{\xi}}{(\xi - \tilde{\xi})} \right]_{\xi} ,$$

where the bar across the integral sign signifies the Cauchy principal value of the integral. (Notice that the partial derivative with respect to ξ of the integral is indicated.) Ono (1975) was able to identify this integral with the Hilbert transform

$$(W_1)_Z \Big|_{Z=0} = \mathfrak{H}(A)_{\xi\xi} ,$$

where

$$\mathfrak{H}(A) = \frac{1}{\pi} \int_{-\infty}^{\infty} \frac{A(\tilde{\xi})}{\xi - \tilde{\xi}} \, d\tilde{\xi} .$$

Matching the vertical derivatives of the vertical velocity in each layer, at $Z=0$ ($\zeta \rightarrow \infty$) gives

$$\epsilon^2 (w_1)_\zeta + \epsilon^3 (w_2)_\zeta = \epsilon^3 (W_1)_z$$

$$O(\epsilon^2): \quad (w_1)_\zeta = \phi' = 0 \quad \text{at } Z = 0 \quad (\text{C.16})$$

$$O(\epsilon^3): \quad (w_2)_\zeta = (W_1)_z = [\mathfrak{H}(A)]_{\xi\xi} \quad \text{at } \zeta \rightarrow \infty .$$

These matching conditions provide all the information necessary to evaluate the surface terms in Eq. (C.13), the second order perturbation solution in the lower layer. The information yielded from the matching conditions in Eqs. (C.15) and (C.16) can be summarized as

$$\begin{aligned} \phi &= 1 \\ \phi' &\rightarrow 0 \\ \phi'' &\rightarrow 0 \\ w_2 &= 0 \quad \text{at } \zeta \rightarrow \infty . \quad (\text{C.17}) \\ (w_2)_\zeta &= [\mathfrak{H}(A)]_{\xi\xi} \\ \rho_0 &\equiv \rho_\infty \end{aligned}$$

The desired cylindrical BDO equation is obtained by using these conditions to evaluate the surface terms in Eq. (C.13). This yields, after dividing through to clear the coefficient of the first term,

$$A_\tau + \boxed{\frac{A}{2\tau}} + \alpha A A_\xi - \delta [\mathfrak{H}(A)]_{\xi\xi} = 0, \quad (\text{C.18})$$

where

$$\alpha = \frac{3 \int_0^\infty \rho_0 (\phi')^3 d\zeta}{2 \int_0^\infty \rho_0 (\phi')^2 d\zeta}, \quad (\text{C.19})$$

$$\delta = \frac{\rho_\infty}{2 \int_0^\infty \rho_0 (\phi')^2 d\zeta}, \quad (\text{C.20})$$

and $c_0 = 1$ because of the scaling used. The only difference between the CBDO and the BDO equations is the boxed term in Eq. (C.18). Its form is exactly analogous to the modified KdV

equation that results from cylindrical geometry. It is applicable in regions where the effects of radial distortion are weak, away from the origin.

When the inner and outer solutions are matched across a sharp interface, the correct matching conditions are that the pressure at the interface and the velocity normal to the interface be equal. Ablowitz and Segur (1980) have shown that the resulting evolution equation is, however, unchanged. In the idealized case of a two layer fluid, each with a constant density, $\alpha = 3/2$ and $\delta = \rho_{\infty}/2\rho_0$, where ρ_{∞} and ρ_0 are the densities of the upper and lower fluid, respectively. Aspects of the behavior of the CBDO equation are discussed in Appendix B.

LIST OF FIGURES

- Fig. I-1. The path of Eastern Flight 66 on 24 June 1975 in the vertical plane including the glide slope of runway 22-L at JFK Airport. The downburst (later defined as microburst) speed was estimated to be 6.7 m/s (22 fps) at 60 m (200 ft) agl. Taken from Fujita (1976). 10
- Fig. I-2. Frequencies of downdraft speeds measured by the Thunderstorm Project, 1946 and 1947 (Byers and Braham, 1949; Table 10). The observed downburst (microburst) data point from the Eastern Flight 66 crash at JFK airport in 1975 is also plotted. Taken from Fujita and Byers (1977). 11
- Fig. I-3. Hypothetical wind trace of a gust front and a microburst by Fujita (1980a). This type of wind trace was recorded several times during the NIMROD Project (Fujita 1979; Wakimoto 1981). As indicated, time increases from right to left. 11
- Fig. I-4. (Top) Schematic views of wet and dry microbursts. Wet microbursts are expected to occur in the wet regions of the world, while dry microbursts are commonly seen in the dry regions with high bases of convective clouds. (Bottom) Outflow microbursts are the most commonly observed type of microburst. Some rotor microbursts develop inside macrobursts behind their gust fronts. Caption and figures taken from Fujita (1985). 14
- Fig. I-5. Schematic drawing of an aircraft encounter with a microburst. Notice that the increased headwind lifts the plane above its intended glideslope while the increased tailwind causes the plane to fall below its intended glideslope. 16
- Fig. I-6. Definition of F-factor wind shear hazard index. Typical threshold values (F_0) for jet transport range from 0.10 - 0.15. Notice that all of the aircraft accidents have taken place in the quadrant associated with divergent horizontal winds and downward vertical velocities along the flight path. Adapted from Targ and Bowles (1988). 16
- Fig. I-7. Daily count of NIMROD microbursts as determined by computer analysis of surface weather station data. The number of wet (> .25 in. rain) and dry microbursts is shown on the figure. Taken from Fujita and Wakimoto (1983a). 18
- Fig. II-1. (Top) Cumulus stage of a thunderhead is characterized by updrafts throughout the cloud cell. (Middle) Mature stage of thunderhead brings rain and/or hail, lightning, thunder, and downdrafts. (Bottom) dissipating stage of the thunderhead is reached as downdrafts occur throughout the cell. Brisk upper winds may shift the cloud top, producing the familiar anvilhead. Drawn by Viemeister (1961) after Byers and Braham (1949). 24
- Fig. II-2. Radial-vertical cross sections from baseline axisymmetric simulation for stream function at 1 min intervals starting with 4 min and ending with 15 min. Thick solid line represents 10 dBZ radar reflectivity contour and the thick dashed line encloses area outside of precipitation shaft with temperature deviations from ambient of less than -1 K. The contour interval for stream function is 8×10^5 Kg/s, with intermediate contours dashed. Taken from Proctor (1988b). 25
- Fig. II-3. Schematic of updraft, downdraft and entrainment (inflow) flows within a typical Cb, based on a composite of observational studies and numerical model studies. All flows are storm relative; E denotes entrainment. Other symbols are defined in the accompanying table. Taken from Knupp (1987). 26

- Fig. II-4. (Top) Horizontal radar sections through a multicell thunderstorm for four altitudes, at six times during the evolution of constituent cells. Reflectivity contours are at 10-dBZ intervals. Arrows depict the direction of cell motion and a geographical reference line for vertical cross sections appears at the bottom of the figure. Cell 3 is shaded to show the life history of an individual cell. (Bottom) Vertical radar sections of cell 3. From Chisolm and Renick (1972). 27
- Fig. II-5. Examples of "large clouds, sometimes having the appearance of altocumulus castellanus, which produce rain or snow that may or may not reach the surface. Based on the observational evidence obtained in JAWS". Adapted from Fujita (1985). 27
- Fig. II-6. (Top) RHI cross section of a virga shaft. (Bottom) Contours of reflectivity and Doppler velocity for the same virga shaft shown in top panel, except 2:15 min earlier. Taken from Fujita and Wakimoto (1983b). 29
- Fig. II-7. Axisymmetric model simulated radar reflectivity and superimposed vector field for a snow driven microburst at a) 22 min and b) 23 min after initiation. The contour values are 1, 10, 20, 25, 30, and 35 dBZ. Taken from Proctor (1989). 29
- Fig. II-8. In both panels, the temperature is plotted on the right and the dew point temperature is plotted on the left. (Top) Environmental sounding from Florida on a day when thunderstorms with strong downdrafts formed. The heavy dashed line at right represents a hypothetical downdraft that produces a maximum wind speed of 22 m/s; at left represents a downdraft colder by 1°C that produces a maximum wind gust of 31 m/s. From Caracena and Maier (1987). (Bottom) A composite of five afternoon soundings by Brown et al. (1982) for convective events that produced damaging surface winds associated with high-based cumulonimbi in the Front Range area of Colorado. Taken from Caracena et al. (1989). 31
- Fig. II-9. Outflow pattern of the surface wind under a line of radar echoes. Taken from U.S. Weather Bureau (1948). 32
- Fig. II-10. Schematic description of impinging and radial wall jets. D is the orifice diameter, u is the local mean velocity in the radial (r) direction, and U_m is the maximum radial velocity. Taken from Poreh et al. (1967). 33
- Fig. II-11. Radial velocity along azimuth of V_{max} vs radius from downdraft center. (a) Velocity vs radius for six times for an outflow observed on 14 July 1982 by the CP-3 radar. (b) Normalized velocity vs scaled radius for several cases from the Denver area at the time of maximum observed outflow differential velocity. Velocity is normalized to the maximum for each outflow and radius is scaled to the radius of the maximum velocity. Heavy dark line is mean profile; very heavy dark line is profile predicted from laboratory wall jet studies. Taken from Hjelmfelt (1988). 35
- Fig. II-12. Time series of radial wind speed at 20 m agl and at the four indicated ranges from the center of the axisymmetric numerically simulated storm shown in Fig. V-14 (neutral boundary layer). 36
- Fig. II-13. Nondimensional vertical profiles of thunderstorm outflow. The solid curve represents the profile from Proctor's (1988b) simulated DFW case; the long-dashed line represents profiles measured in laboratory wall jets by Bakke (1957); and the short-dashed line represents a profile measured with Doppler radar by Fujita (1981; his Fig. 30), after the translation speed of the storm is subtracted out. Taken from Proctor (1988b). 37
- Fig. II-14. Streamwise vorticity generation in the three-dimensional wall jet. (a) Developing flow region; (b) developed flow region. Adapted from Launder and Rodi (1983). 37

- Fig. II-15. Surface analysis of a thunderstorm complex that occurred on 9 July 1946 near Orlando. Data presented are identified in the lower left corner of each panel. Notice the strong divergence coincident with the surface rainfall maximum. Taken from Byers and Braham (1949). 39
- Fig. II-16. The unusual conditions which led to the Kano accident in 1956. The height indications are those of the accident investigation committee. Taken from Stewart (1958). 41
- Fig. II-17. Downdrafts from a thunderstorm can be hazardous to an airplane during a takeoff. Drawn by Viemeister (1961) to illustrate in general the meteorological conditions encountered by the plane that crashed taking off at Kano in 1956. 41
- Fig. II-18. Plot of F_x , a measure of the rate of change of the longitudinal (along-flight) component of winds normalized by the acceleration of gravity, vs $\Delta V/\Delta R$, the Doppler differential velocity divided by the distance over which it occurs, detected by radar at the surface in 39 microbursts in the Denver area. F_x more precisely measures the performance loss of an aircraft in a wind shear encounter. The horizontal line at $F_x = 0.13$ indicates the approximate value at which jet transport performance becomes marginal. Taken from Elmore and Sand (1989). Note that no account has been taken of the vertical velocity in this measure of F-factor (Fig. I-6). 43
- Fig. II-19. Distribution of the number of radar echoes from summer rainshowers according to the diameter of the 10 dBZ contour. The data were collected near Wallops Island, VA during the 4 months from May through August, 1973. The radar was operated in a fixed raster scan mode, once each 30 min, from 3:00 - 11:30 pm EST every day. Taken from Konrad (1978). 44
- Fig. II-20. Doppler-observed maximum low-altitude velocity differentials (ΔV_r) associated with microbursts, versus the radar reflectivity at a height of 500 m. Observations from the JAWS project near Denver. Taken from Wilson et al. (1984). 46
- Fig. II-21. Vertical velocity on the central axis in the lowest 2 km of the axisymmetric numerical simulation shown in Fig. V-14 (neutral boundary layer). Six different times are shown around the time of maximum vertical velocity ($t = 4$ min). 49
- Fig. II-22. (Top) (a) Profile of relative humidity (S) used in the calculations presented in (b). Resultant mixing ratios of graupel and rain (r_g and r_r) are shown. (b) Profiles of cooling rates from sublimation of graupel (GSUB), evaporation of rain (RVAP), melting of graupel (MELT) and the sum of all three (TOTAL). These quantities were obtained by simulating the release of graupel from above the melting level [labelled OC in (a)], and then computing subsequent melting, sublimation, and evaporation as the precipitation descended into a motionless environment (i.e., $w=0$). Assumed precipitation size distributions are given by Eqs. (8) and (9) in Knupp (1988). (Bottom) Total precipitation-induced diabatic cooling rates (sum of raindrop evaporation, graupel sublimation, and graupel melting) as a function of precipitation size. Curve 2 is the same as the curve labelled TOTAL in the Top panel. Both figures were taken from Knupp (1988). 51
- Fig. II-23. Each point represents a microburst identified during the JAWS project by radar observations. The ordinate is the reflectivity factor for the microburst at a height of about 500 m agl. The lapse rate of temperature in the environment was obtained from special radiosonde observations. Taken from Srivastava (1985). 55
- Fig. III-1. A model of a typical wet microburst environment characterized by a very dry midtropospheric layer overlaying a deep, wet, lower troposphere. Taken from Caracena (1988). 67

Fig. III-2.	Conceptual model of environmental extreme associated with wet microbursts. The wet extreme is characterized by a dry source layer that ejects pockets of dry air into underlying rain-filled and saturated air, producing the evaporation that can result in a microburst. The cloud tops are not drawn to scale; they can extend as high as 15 km agl in wet microburst storms. Taken from Caracena et al. (1989).	67
Fig. III-3.	Vertical profile of equivalent potential temperature from the Tuttle sounding of 0205 GMT, 14 April 1981. Taken from DiStefano (1983).	68
Fig. III-4.	Vertical velocity versus depth of penetrative thermals for various distributions of cloud liquid water content (g/Kg). The pseudo-adiabatic value of cloud water content was 10.8 g/Kg. The initial equivalent potential temperature of the penetrative thermal was 315 K. Taken from DiStefano (1983).	68
Fig. III-5.	Map of the FLOWS 1985 mesonet and radar configuration near Memphis, TN. Mesonet station numbers indicate the station location, letters like "CF" and "E" indicate the FAA LLWAS stations (center field, east, etc.), and the black spots indicate the radar locations. The three lines near the LLWAS stations schematically depict the runways at the Memphis International Airport.	70
Fig. III-6.	Profile of equivalent potential temperature plotted versus pressure (log scale) for 25 June 1985 in the Memphis area. Sounding is composite of soundings from Little Rock and Centreville. Dashed lines indicate the minimum value of equivalent potential temperature recorded at the surface, and its possible source altitude.	72
Fig. III-7.	RHI cross sections at 299° from FL-2 radar through the multicell complex at two times 18 min apart. (Top) 1807:26 UTC, (Bottom) 1825:24 UTC. Reflectivity is contoured in 10 dBZ increments from 20 to 50 dBZ. The dashed line in each cross section shows approximate height of the freezing level.	73
Fig. III-8.	Dual Doppler surface winds on 25 June 1985 at 1823 UTC. Maximum wind vector, equal to one grid space, is 18 m/s. Solid contours are surface reflectivity in 10 dBZ increments from 20 to 50 dBZ. Dashed contours are downward vertical velocity at 1.5 km agl in 5 m/s increments. Small shaded circle near (-17.0, 6.3) is mesonet station No. 23.	74
Fig. III-9.	FL-2 4.0° elevation angle PPI display of multicell storm near Memphis, TN on 25 June 1985. Notice the hook area of reflectivity next to a spiral weak echo region (notch) near the southern edge of the storm. The height of this area, at this range, is about 1.3 km agl. There are a number of these edge reflectivity spirals around the multicell complex. Small shaded circle near (-17.0, 6.3) shows position of mesonet station No. 23 at the surface.	76
Fig. III-10.	RHI cross sections at 291° from FL-2 radar through the multicell complex at 1824:53 UTC. The arrow below the RHI shows the location of FLOWS mesonet station No. 23.	77
Fig. III-11.	Data from FLOWS mesonet station No. 23 on 25 June 1985. Minute "8" on the horizontal axes corresponds to 1808 UTC, minute "38" to 1838 UTC. No rainfall was recorded. Average wind speed is the average over 1 min of 5 s samples; peak wind speed is the largest 5 s sample within the minute. Negative wind directions are from the northwest, positive - northeast.	78
Fig. III-12.	FLOWS 1985 mesonet and LLWAS winds (one full barb = 5 m/s) and contours of equivalent potential temperature in 5 K increments. Minutes 1819, 1820 and 1821.	80
Fig. III-12 (cont.)	Minutes 1822, 1823, and 1824 UTC.	81
Fig. III-12 (cont.)	Minutes 1825, 1826, and 1827 UTC.	82

Fig. III-12 (cont.) Minutes 1828, 1829, and 1830 UTC.	83
Fig. IV-1. Vertical cross section and horizontal plan view of the microburst at Dallas/Ft. Worth International Airport in which Delta Flight 191 crashed on 2 August 1985, as reconstructed by Fujita (1986).	88
Fig. IV-2. A conceptual model of the vertical airflow structure in the DFW microburst, based on analysis of flight recorder data by Bach and Wingrove (1985). Labelled contours are potential temperature (K); lines with arrows are streamlines. Arrows along dashed line (flight track) are vector winds encountered by the aircraft. Taken from Caracena et al. (1986).	88
Fig. IV-3. The concept of a series of horizontal vortices being caused by several microbursts embedded within one another appears in two places in the Southwest Airlines Operations Manual, Pilot Windshear Guide, revised 27 November 1987. Text from the manual was retyped.	89
Fig. IV-4. Vertical cross section of the evolution of the microburst wind field based on a summary of data collected in the JAWS project. T is the time of initial divergence at the surface. The shading denotes the vector wind speeds. The outer dashed boundary represents wind speeds less than 5 m/s. Taken from Wilson et al. (1984).	91
Fig. IV-5. (Top) Pressure, temperature, horizontal wind speed, and vertical wind speed measured at the Boulder Atmospheric Observatory tower (described by Kaimal and Gaynor 1983). (Bottom) Vector field associated with the outflow vortex passing through the tower. The values shown are 1 s averages of 10 Hz samples. Taken from Bedard and Caplan (1987).	93
Fig. IV-6. A sequence of telephoto pictures showing the curling features of the dust cloud behind the leading edge of the outflow from a "virga microburst". The pictures were taken by Brian Waranauskas looking south from the CP-3 site on 15 July 1982 during the JAWS project. Taken from Fujita (1985).	94
Fig. IV-7. Three particle plots showing interface instabilities at different density ratios. Top series: 1.1 : 1 density ratio at times 0, 0.089, 0.179, 0.269, 0.358, 0.425. Middle series: 2 : 1 density ratio at times 0, 0.045, 0.089, 0.179, 0.224. Bottom series: 10 : 1 density ratio at times 0, 0.025, 0.049, 0.073, 0.097, 0.121. Taken from Daly (1967).	96
Fig. IV-8. Schematic diagram of modulated air jet exiting nozzle and striking plate. Taken from Didden and Ho (1985).	97
Fig. IV-9. Schematic representation of an atmospheric density current. Taken from Goff (1976).	99
Fig. IV-10. Illustration of the positive circulation acceleration at a numerically modelled gust front. η is the unit normal vector out of the plane. The potential temperature, θ , is contoured in 1 K intervals from 306 to 319 K. C is the circulation, t is time, T is temperature, and p is pressure. Taken from Mitchell and Hovermale (1977).	100
Fig. IV-11. (Top) Unidirectional model simulation. Outflow depth as a function of horizontal distance at the 300th and 400th time steps is shown. Initial column height 2000 m. (Bottom) Comparable axisymmetric simulation. Initial column height 2500 m. The accompanying table gives the definitions of model terms shown in the figures. Taken from Addis (1984).	102
Fig. IV-12. Instantaneous release of dense gas into calm air seen from above in the Thorney Island experiments. Taken from Johnson (1985).	103

- Fig. IV-13. Plan view of a dense cloud, similar to that shown in Fig. IV-12, at various times after release in calm conditions. Taken from Picknett (1981). 103
- Fig. IV-14. Schematic representation of the average conditions at the time of maximum outflow measured for 13 Memphis cases of collapsing thunderstorms. The strongest winds were measured in the lowest radar beam (essentially "at surface"). The average maximum outflow wind speed differential was 20.3 m/s over a distance of 4.9 km. In the upper part of the figure, reflectivity is contoured, and labelled in dBZ. Below 1 km, the Doppler velocity is schematically contoured to show typical isodop pattern at time of maximum outflow speeds. 104
- Fig. IV-15. The four stages of a thunderstorm gust front. The advancing precipitation roll at low levels is detected by the radar. The "precipitation roll" is a horizontal roll formed by airflow that is deflected upwards by the ground. Taken from Wakimoto (1982). 105
- Fig. IV-16. RHI cross-section taken with the CP-2 Doppler radar on July 20, 1986 during the COHMEX project in Huntsville, AL. Contours of reflectivity are stippled, as is the entire region greater than 50 dBZ. Doppler velocities are contoured in solid (positive, away from radar) and dashed (negative, toward radar) lines. Taken from Wakimoto and Bringi (1988). 106
- Fig. IV-17. Depiction of the four stages on the Andrews Air Force Base microburst. They are: 1st stage (descending stage): midair microburst descends, 2nd stage (contact stage): microburst hits the ground, 3rd stage (mature stage): stretching of the ring vortex intensifies storm, 4th stage (breakup stage) runaway vortex rolls induce burst swaths. Taken from Fujita (1984). 107
- Fig. IV-18. (Top) A simple idealized picture of the descent of cold air from a thunderstorm. The hazard to aircraft is thought to be due to the variations of horizontal wind. The width of the descending air is <4 km, and the depth of the outflow along the ground is a few hundred meters. (Bottom) The early stages in the development of a microburst. Most of the spreading mass of cold air is concentrated into an intense leading-edge vortex. This is sometimes followed by a second vortex. The horizontal scale is similar to that in the top picture. Taken from Linden and Simpson (1985). 108
- Fig. IV-19. Isometric projection of scaled interface depth (D) as a function of scaled range (R) and time (T). Taken from Garvine (1984). 111
- Fig. IV-20. The characteristic (R,T) plane for the sample calculation showing the leading front, trailing front, and representatives of both families of characteristics for $0 < T < 3$. The solid dot indicates where fitting of the trailing front began. Taken from Garvine (1984). 111
- Fig. IV-21. Tank to test the effect of widening on the form of the head of a gravity current, originally in a channel with parallel sides. Taken from Simpson (1987). 113
- Fig. IV-22. The effect of widening the channel of the form of a gravity current head. The width increases from 10 cm to 20 cm between the two white lines which are 30 cm apart. The time interval is 5.7 s, and g' , the reduced gravity, is 14 cm/s². Taken from Simpson (1987). 113
- Fig. IV-23. Radial-vertical cross-sections of temperature deviation from ambient and superimposed wind vectors from Proctor's axisymmetric DFW simulation (neutral boundary layer). The fields are at (a) 11 min, (b) 12 min, (c) 13 min, (d) 13.5 min, (e) 14 min. The contour interval for temperature deviation from ambient is 1 K. The vertical coordinate is magnified relative to the horizontal. Contours with negative values are indicated by dashed lines. Taken from Proctor (1988b). 115

- Fig. IV-24. Line sketch for a series of radial ring discontinuities in a horizontal spreading cooling tower plume from John E. Amos Power Plant, drawn by Chen (1980) from a photograph by Kramer and Seymour (1976). 117
- Fig. IV-25. Line sketch for a series of radial ring discontinuities in horizontally spreading cooling water discharge plume from Sheboygan Power Station, drawn by Chen (1980) from airborne thermal imagery by Scarpace and Green (1973). 117
- Fig. IV-26. Tank in the form of a sector for the release of a fixed volume of dense fluid to form an axisymmetrical gravity current. Taken from Simpson (1987). 119
- Fig. IV-27. Shadowgraphs of a volume of salt water collapsing into fresh, in the sector shaped tank shown in Fig. IV-26. Total depth is 40 cm, and reduced gravity, g' , is 47 cm/s^2 . (i) $h_0/H = 0.25$; (ii) $h_0/H = 1$. In both experiments, r_0 was 60 cm; this distance is indicated in the figures by the first double vertical lines (from the right). The thin vertical lines are spaced 10 cm apart. H , h_0 and r_0 are identified in Fig. IV-26. Taken from Simpson (1987). 119
- Fig. IV-28. Isotachs of $(u-c)$ in m/s (left) and isentropes in K (right) for different mean inflow speeds, and thus different inflow Froude numbers. In each case the depth and temperature of the inflow air were held constant. (a) $Fi = 0.28$, (b) $Fi = 0.56$, (c) $Fi = 1.13$. Taken from Haase and Smith (1989a). 122
- Fig. IV-29. The nominal dependence of the cooling functions on time for constant cooling rate experiments. The base cooling rate in each was $-0.075 \text{ }^\circ\text{C/s}$. The function shown has 4 min of constant cooling, from minute 1 to 5. This interval of constant cooling was lengthened to 10 min, 16 min, and 36 min in the other three experiments. The experiments each continued for at least 14 min after the cooling was turned off. 123
- Fig. IV-30. Constant cooling experiment. The flow is shown every minute from 7 min to 16 min into the simulations. The cooling in the simulation at left ended at 6 min; at right, cooling ended at 12 min. Potential temperature is contoured every 2°C ; uppermost continuous contour shown is -2°C . Domain shown is 12 km wide and 3 km high. 124
- Fig. IV-31. Constant cooling experiment. The flow is shown every minute from 14 min to 23 min into the simulations. The cooling in the simulation at left ended at 18 min; at right, cooling remained constant during depicted times. Potential temperature is contoured every 2°C ; uppermost continuous contour shown is -2°C . Domain shown is 12 km wide and 3 km high. 125
- Fig. IV-32. Illustration of the stages in the development of an individual Kelvin-Helmholtz billow, a wave pattern sometimes leading to cloud formation at the wave crests. Thick lines correspond to the detectable clear air radar echo, which starts as a single layer (upper half of figure) and finishes as a double layer (lower half of figure). Schematic vertical profiles of temperature and wind speed are indicated before and after occurrence of Kelvin-Helmholtz instability. Taken from Hardy (1972). 127
- Fig. IV-33. Contour plots of perturbation potential temperature from the control simulation (top) and two variable mixing simulations (bottom two panels) at 20 min into each simulation. The vertical depth of the domain is 10 km, the width, 30 km. The contoured values range from -6 to 0 K in each plot, but the contour interval in the top plot is 0.7 K , middle 1.0 K , and bottom 0.6 K . The numerical damping coefficients specified in the horizontal (K_y) and vertical (K_z) are labelled in each plot. Adapted from Droegemeier and Wilhelmson (1987). 130

- Fig. IV-34. Vertical sections at 2234, 2239, and 2241 through the KHI billow b. The cross sections show storm relative wind vectors and vertical velocity in 3 m/s intervals. The thick solid line indicates the top of the scan volume. The sections are aligned relative to the leading edge of the outflow. Taken from Mueller and Carbone (1987). 132
- Fig. IV-35. Experimental generation of an internal bore by an advancing gravity current. Taken from Simpson (1987). 132
- Fig. IV-36. Vertical cross section of vector winds through a gust front on 5 August 1982 near Denver, Colorado. The vertical resolution is 0.3 km, and vertical velocities are contoured each 3 m/s. "X1" marks the center of rotation and "D" is the center of surface divergence under the downdraft portion of the circulation. Taken from Mahoney (1988). 134
- Fig. IV-37. Dots are observations of velocity components (a) perpendicular, and (b) parallel to the solitary wave front, as observed at 5 tower levels. Refer to Doviak and Chen (1988) for explanation of the various curves. The large "hump" in the perpendicular flow is the solitary wave, and it is hypothesized that the smaller sinusoidal variations are manifestations of KHI. Taken from Doviak and Chen (1988). 136
- Fig. IV-38. Schematic representation of storm kinematic structure. Taken from Carbone (1982). 137
- Fig. IV-39. (Top) The 0.4 and 1.2 km agl storm relative flow (plan view) in the region of the northern most closed vortex is shown at 2241. The shaded areas indicate updrafts > 3 m/s with darker areas indicating cores > 6 m/s. The downdraft, > 3 m/s, is hatched. Contours of vertical vorticity at intervals of 10.0 m/s per km are shown in black. At 0.4 km a subjective gust front line is indicated. The location of the vertical cross section shown below is indicated with the letters G,H at 1.2 km. (Bottom) Cross section through the vortex, indicated above by G,H. Contours of vertical velocity with intervals of 3 m/s are shown. The axis of maximum vertical vorticity is marked with a black solid line. Labelled ticks on the horizontal axis are 1 km apart. Taken from Mueller and Carbone (1987). 138
- Fig. IV-40. Proposed circulation inducing a microburst at the leading edge of a squall line outflow, adapted from Klemp and Rotunno (1983). Dashed contours indicate downdrafts, solid contours indicate updrafts. The stippled area represents reflectivity greater than 30 dBZ. The small scale downdraft in the "spearhead" shaped reflectivity region is the microburst. Streamlines indicate storm relative flow. In this scenario, it is the mesoscale circulation which distorts the radar echo and induces the microburst, not vice versa. Taken from Wolfson (1983). 139
- Fig. V-1. Calculated shape of waves of finite amplitude for three thicknesses of lower layer. Vertical scale is ratio of displacement to corresponding "small-amplitude" displacement. Taken from Gossard and Richter (1970). 144
- Fig. V-2. Russell's (1845) observation of the evolution of a solitary wave in a wave tank, reproduced from the original drawing by Miles (1980). 144
- Fig. V-3. Schematic illustration of the undershoot behavior of an aircraft during a hypothetical head-on encounter with a solitary wave on final approach to the runway. Taken from Christie and Muirhead (1983b). 146
- Fig. V-4. Numerical integration for 100 nondimensional time units (one trace for each) of (Top) BDO equation and (Bottom) CBDO equation, for an initial finite wave of elevation (amplitude of 1). The horizontal axis is the nondimensional space coordinate moving at the linear long wave speed. In the cylindrical problem, the initial time t_0 was 5. The values of a and d used for both equations were 1.5 and 0.48, respectively. 148

- Fig. V-5. Time series of temperature (T), pressure (P), wind direction (WD) and wind speed (WS) for the passage of a pressure jump line (PJ2) at the Regional Air Monitoring System station No. 122. Adapted from Shreffler and Binkowski (1981). 149
- Fig. V-6. (Top) Samples of winds (lightly traced arrows) measured at NSSL tower in central Oklahoma at four levels in the NW-SE cross section of the gust for the time period 2300-2320 CST on 11 May 1980. The velocity scale is listed in the upper left corner and applies to both the horizontal and vertical speeds. Bold arrows are Doppler radar estimates of wind at 2245 projected onto this cross section. The dashed streamlines are subjectively estimated in the data void region between 500 and 1000 m. Taken from Doviak and Ge (1984). (Middle) Equivalent potential temperature in K (tp is the time of the peak in the cross-wave wind component. (Bottom) Scenario for the evolution of the thunderstorm generated solitary wave. Taken from Doviak and Christie (1989). 151
- Fig. V-7. Observations of low-level internal gravity waves. Adapted from Crook (1988). . 152
- Fig. V-8. (Top) Schematic diagram of the 9 May 1981 cold outflow based on tower and Doppler radar observations. The tower sampled roughly the lower half on the gravity current and the radar provided information on the flow fields higher up. The three wave-like disturbances identified as A, B, and C are still located entirely behind the gravity current front. The streamlines are in a frame of reference translating with the windshift line. (Bottom) Illustration of the passage of significant events at five mesonet (SAM) stations oriented in a line normal to the front. The pressure jump (PRJ) occurs first at all stations followed immediately by the windshift (WNDSHT), the rise in the dry-bulb temperature (T RISE), the first speed peak (SP1) and pressure peak (PP1), and then the second speed peak (SP2) and pressure peak (PP2). The leading edge of the gravity current is delineated by the time when the virtual potential temperature begins to fall ($\theta_v B$). TB defines the time that the dry-bulb temperature falls below the pre-frontal value. Note how all of the events are moving at a nearly constant speed, while the $\theta_v B$ curve lags by an ever-increasing amount of time. The shaded region highlights the increasing time between the bore front and the gravity current front. Taken from Fulton (1987). 154
- Fig. V-9. Observations of gust front speed versus surface pressure rise. The best-fit line representing the value of F (shown here as k), excluding the numerical data of Mitchell and Hovermale (1977), was found to be 0.79 with a correlation coefficient of 0.84. Taken from Seitter (1986). 155
- Fig. V-10. Apparatus to study the collapse of a mixed region in an axisymmetric geometry. Showing method of mixed fluid containment, trapping of gravity current within a cylindrical solitary wave and formation of streaky structure as waves leave the mixed region behind. Taken from Maxworthy (1980). 157
- Fig. V-11. Summary of leading edge contours for scale model microbursts of various initial volumes at the time of deepest penetration or largest lateral extent. The larger volumes (indicated in units of ml) produced greater downward momentum; and thus penetrated farther into the stable layer. The downdraft salinity was 5%, and the surface layer was 10% in each case. Taken from Young et al. (1989). 157
- Fig. V-12. Idealized virtual potential temperature profile based on DFW crash observations (Doviak, personal communication), used as potential temperature profile in axisymmetric simulations. Profiles of temperature are identical except 300 m deep stable layer was added at the surface for one experiment. 160

- Fig. V-13. The shape of the cooling function for the neutral and stable boundary layer simulations (also doubles as a DFW storm simulation). Base cooling rate was -0.075 °C/s. 160
- Fig. V-14. Potential temperature perturbation is contoured every 2_C, and wind vectors are drawn to indicated scale every 200 m (10 grid points). Domain shown is 10 km wide and 3 km high. At each minute, the top panel shows the neutral boundary layer run, the bottom, the stable boundary layer. Minutes 4 and 5 of the simulation are shown. 161
- Fig. V-14. (Continued) At each minute, the top panel shows the neutral boundary layer run, the bottom, the stable boundary layer. Minutes 6 and 7 of the simulation are shown. 162
- Fig. V-14. (Continued) At each minute, the top panel shows the neutral boundary layer run, the bottom, the stable boundary layer. Minutes 8 and 9 of the simulation are shown. 163
- Fig. V-14. (Continued) At each minute, the top panel shows the neutral boundary layer run, the bottom, the stable boundary layer. Minutes 10 and 11 of the simulation are shown. 164
- Fig. V-14. (Continued) At each minute, the top panel shows the neutral boundary layer run, the bottom, the stable boundary layer. Minutes 12 and 13 of the simulation are shown. 165
- Fig. V-14. (Continued) At each minute, the top panel shows the neutral boundary layer run, the bottom, the stable boundary layer. Minutes 14 and 15 of the simulation are shown. 166
- Fig. V-14. (Continued) At each minute, the top panel shows the neutral boundary layer run, the bottom, the stable boundary layer. Minutes 16 and 17 of the simulation are shown. 167
- Fig. V-14. (Continued) At each minute, the top panel shows the neutral boundary layer run, the bottom, the stable boundary layer. Minutes 18 and 19 of the simulation are shown. 168
- Fig. V-15. Vertical velocity is contoured in 2 m/s increments. Dashed contours indicate negative values. At each minute, the top panel shows the neutral boundary layer run, the bottom, the stable boundary layer. Minutes 9 and 15 of the simulation are shown. 169
- Fig. V-16 F factor calculated for a 3° landing glideslope. Values are contoured in increments of 0.1. Solid contours indicate positive (performance decreasing) values of F; dashed contours indicate negative values. Domain shown is 10 km wide and 3 km high. At each minute, the top panel shows the neutral boundary layer run, the bottom, the stable boundary layer. Minutes 6 and 7 of the simulation are shown. 171
- Fig. V-16 (Continued) F factor calculated for a 3° landing glideslope. Values are contoured in increments of 0.1. At each minute, the top panel shows the neutral boundary layer run, the bottom, the stable boundary layer. Minutes 8 and 9 of the simulation are shown. 172
- Fig. V-16. (Continued) F factor calculated for a 3° landing glideslope. Values are contoured in increments of 0.1. At each minute, the top panel shows the neutral boundary layer run, the bottom, the stable boundary layer. Minutes 10 and 11 of the simulation are shown. 173

- Fig. V-17. Comparison of the hazardous area below 500 m agl in the numerical simulation shown in Fig. V-14. The total cross-sectional area normalized by 400 m² (the area of one model grid point) as a function of model simulation time for positive (performance decreasing) values of F is shown in the top two panels, and for negative (performance increasing) values of F is shown in the lower two panels. The two curves shown in each panel are for the neutral boundary layer and stable boundary layer experiments, as indicated. 174
- Fig. V-18. Time cross section of meteorological parameters observed at Andrews AFB located just to the south of the rainfall center line. Note that the area of the microburst (black circle) is significantly smaller than the overall area of the mesoscale outflow which affected the air force base. Taken from Fujita (1984). 177
- Fig. V-19. Distribution of rainfall and wind damage in and around Andrews AFB caused by the microburst storm on August 1, 1983. Damaging winds are shown by black circles with arrows attached. Rainfalls are in 0.01 inch units. Taken from Fujita (1984). 177
- Fig. V-20. A schematic view of the ring vortex which encircles the downflow of a microburst. It is expected that the ring vortex expands rapidly after the touchdown. The boat was hit by south-southwesterly winds as the vortex roll passed by. Taken from Fujita (1985). 178
- Fig. V-21. A series of density (kg/m³) sections across the front on September 22, 1984, by the yo-yo method at (a) 10:05 hrs, (b) 10:24 hrs, (c) 10:44 hrs, (d) 11:02 hrs, (e) 11:28 hrs. The maximum data spacing in the horizontal is about 12 m with an average of 6 m, whilst that in the vertical is 0.02 m. Each section took approximately 5 min to collect. Taken from Luketina and Imberger (1987). 179
- Fig. V-22. (Top) The evolution of the main cell, shown at (a) 1730, (b) 1805, (c) 1815, (d) 1830. Reflectivity at 500 m agl is contoured at 10, 30, 45, and 55 dBZ. Storm features are labelled. Surface mesonet winds are plotted (full barb = 5 m/s). Locations of gust front boundaries A and B are shown. Doppler analysis domains are indicated by boxes labelled with the analysis times. The large box in (d) labelled 1832 is the area covered by the bottom figure. (Bottom) Composite illustration of storm features at 1832. Labelled features are discussed by Kessinger et al. (1988). Of primary interest are the horizontal rotors R1, R2, R3, and R4. The shaded area represents divergence > 5 m/s per km. The location of the PAM station affected by R3 and R4 is shown. Taken from Kessinger et al. (1988). 181
- Fig. V-23. Vertical velocity measured by the NSSL 400 m tall tower in Oklahoma on 13 April 1981. The data is contoured in units which, when multiplied by 0.023, equal the vertical wind speed in m/s. The leading edge of the gust front passed the tower at approximately 0328 GMT. Taken from DiStefano (1983). 182
- Fig. V-24. The shape of the cooling functions for variable flow rate experiments are shown. (Top) Pulsating cooling function. Base cooling rate was -0.05 °C/s. (Bottom) Step cooling function. Base cooling rate was -0.04 °C/s. The experiments continued for 30 simulated minutes. 184
- Fig. V-25. Pulsating cooling experiment. The flow is shown every min from 20 min to 27 min into the simulation. Potential temperature perturbation is contoured every 1°C; coldest contour shown is -7°C at minutes 23 and 24. Domain shown is 12 km wide and 3 km high. 185
- Fig. V-26. Single step cooling experiment. The flow is shown every minute from 15 min to 26 min into the simulation. Potential temperature perturbation is contoured every 2°C; coldest contour shown is -15°C at minutes 15 and 16. Domain shown is 12 km wide and 3 km high. 186

Fig. V-26. Single step cooling experiment (continued). Minutes 21-26 are shown. Potential temperature perturbation is contoured every 2°C. Domain shown is 12 km wide and 3 km high.	187
Fig. V-27. Peak wind speed (top curve) and rain rate during three rain and wind events recorded on June 6, 1985 at three different stations in the FLOWS mesonet. These curves illustrate a natural fluctuation within these events of 3-6 min. ...	189
Fig. V-28. Raingage trace from the National Weather Service DFW airport office at the Delta hangar. Taken from Fujita (1986).	190
Fig. V-29. Horizontal wind change vs. surface temperature decrease for neutral and stable cases studied by Goff (1975) as determined by Greene et al. (1977).	191
Fig. VI-1. Flight path wind estimates (last 60 s). (a) Horizontal components; (b) vertical component. Taken from Bach and Wingrove (1986).	193
Fig. VI-2. Flight path wind vectors (last 44 s). (a) Seen from above; (b) seen from west. Taken from Bach and Wingrove (1986).	193
Fig. VI-3. A conceptual model of the horizontal airflow structure in the DFW microburst, based on the analysis of flight recorder data by Bach and Wingrove (1986). Dashed line represents aircraft track. Taken from Caracena et al. (1986).	194
Fig. VI-4. Relative location of the Delta 191 flight path to the runway end and microburst center. TASS is the numerical model data. Adapted from Proctor (1988b).	194
Fig. VI-5. Comparison of the model simulated profiles and the actual profiles derived from the Delta 191 flight recorder data. The plots are (a) vertical velocity, (b) southern wind component, and (c) potential temperature deviation from 700 mb ambient potential temperature. Taken from Proctor (1988b).	196
Fig. VI-6. (Top) Vertical velocity (W) and (Bottom) North-south wind component (V) from axisymmetric numerical model-data compared with Delta 191 data supplied by Wingrove. The top panel shows the data encountered from the closer, younger thunderstorm outflow, and the bottom panel shows those encountered from the more distant, older outflow.	197
Fig. VI-6. (continued) (Top) East-west wind component (U), and (Bottom) Temperature perturbation (mean of 34.9 C has been removed) from axisymmetric numerical model data compared with Delta 191 data supplied by Wingrove. The top panel shows the data encountered from the closer, younger thunderstorm outflow, and the bottom panel shows those encountered from the more distant, older outflow.	198
Fig. VI-7. Proposed meteorological scenario during DFW crash. The spots indicate thunderstorm downdraft centers. The thick black line is the Delta 191 flight path during the last 90 s of flight. Runway is located at (0,0).	200
Fig. VI-8. F-factor calculations for the last 90 s of the Delta 191 flight that crashed at DFW. In each panel the solid curve shows the actual F-factor from the flight data, and the dotted curve shows F calculated from the numerical simulation. The top panel shows the model data from the close storm, and the bottom panel, data from the distant, older storm.	202
Fig. VI-9. Seven gust fronts on July 9, 1982 determined as based on the radar film from the National Weather Service Office, Slidell, LA. Location and movement were obtained by time -motion analyzer at the University of Chicago. Taken from Fujita (1983).	203

- Fig. VI-10. Enlarged traces of pressure, wind, and rainfall rate at Moisant Airport (New Orleans International) between 2040 and 2215 GMT on July 9, 1982. The airport was under the influence of ENE to NE winds during the pre-gust frontal dome period. After the passage of gust front Nos. 5 and 7, up to 30 kt gusts from the southerly direction dominated the airport area. Republic 632 was saved by the gust front while Texas International 794 reported no wind shear PAA 759 released brakes at 2107:56 and made the first contact with trees at 2109:00. Taken from Fujita (1983). 203
- Fig. VI-11. Schematic view of the JFK thunderstorm drawn on the basis of the geostationary satellite data. The circle identified as JFK is the location of the airport. An arc cloud is seen just to the south of the thunderstorm activity. Its southward advancement is prevented by the sea breeze. The arrowhead vectors denote the cloud motion in knots. Taken from Fujita (1976). 205
- Fig. VI-12. Three downburst cells (DBC) depicted on time-space coordinates. DBC 1 was on the runway threshold and DBC 2 affected seriously the approach effort of aircraft "H" and "I". DBC 3 blew aircraft "L" down to the ground, 2000 ft short of runway 22-L. Most of the airport was under the influence of sea breeze. The outflow from the downburst cells was distorted by the sea breeze front, resulting in the strong outflow winds to the north of the front. Taken from Fujita (1976). 205
- Fig. VI-13. Proposed scenario for JFK crash. The "microburst" was a thunderstorm downdraft coincident with the downdraft behind the leading circulation of an unquar gravity current. Both features contributed to the accident. The depicted arc cloud was visible on satellite imagery. Adapted from drawing by Fujita (1976). 206
- Fig. A-1. Plot of the square of the vertical velocity (w) vs the radius of the downdraft core (R), from the model results of P89 and KW (dashed curve). The predicted dependence, shown as the solid curve, was found to be $w^2 = 167 / (0.5 + 0.07 R^2)$. 213
- Fig. A-2. Plot of "FUNCTION" = $w^2/2 + 0.07 w^2 R^2$, for the data shown in fig. A-1. The function should equal 167 for a perfect fit to the predicted dependence based on Bernoulli's equation. 213
- Fig. A-3. Plot of the ratio of the maximum outflow speed to the maximum downdraft speed (U/W) vs radius of the precipitation core, from the numerical simulations by P89 and KW (dashed lines). The solid line, $U/W = -0.39 R - 0.65$, is the best approximation to both datasets. 216
- Fig. A-4. Plot of the square of the vertical velocity (w) vs liquid water content (L), from the numerical simulations by KW and DB (dashed lines). The solid lines represent the least squares linear fit to each dataset: $w^2 = 42.1 L + 183$ (KW) and $w^2 = 22.8 L + 171$ (DB). 216
- Fig. A-5. Plot of the ratio of the maximum outflow speed to the maximum downdraft speed (U/W) vs liquid water content, from the numerical simulations by KW and DB. 217
- Fig. A-6. Plot of a one-dimensional air parcel's temperature deviation (ΔT) from the environment vs the environmental lapse rate (Γ), for an initial rainwater mixing ratio of ~ 7 g/Kg (dashed line). The data were taken from Srivastava (1985), Fig 5.b, rightmost column. The solid line is the least squares nonlinear fit to the data: $\Delta T = -0.145 \Gamma^2 + 9.23$ 218
- Fig. A-7. Plot of the vertical velocity (w) vs the environmental lapse rate (Γ) from the numerical simulations by KW, for liquid water mixing ratios (L) of 2, 4, and 8 g/Kg (dashed lines). The solid lines represent the best fit for each mixing ratio using the mean of the slopes derived from the least squares linear fit for each mixing ratio curve individually: $w_2 = -4.175 \Gamma + 24.19$; $w_4 = -4.175 \Gamma + 20.99$; $w_8 = -4.175 \Gamma + 17.14$. 220

Fig. A-8.	Plot of the ratio of the maximum outflow speed to the maximum downdraft speed (U/W) vs environmental lapse rate, for liquid water mixing ratios (L) of 2, 4, and 8 g/Kg.	220
Fig. A-9.	Plot of analyzed maximum downdraft as a function of height of the transition level (TR , defined as the level at which the lapse rate changes from roughly dry adiabatic or conditionally unstable to approximately moist adiabatic or absolutely stable). Error bars indicate the uncertainty in vertical motion estimates. The bars labeled R and H are data taken from Rodi et al. (1983) and Hjelmfelt (1984), respectively. The solid triangles represent the transition levels, and the simulated downdraft speeds for the cases presented by Proctor (1989). The base figure, without the triangles, was taken from Knupp (1987).	221
Fig. A-10.	Plot of analyzed maximum downdraft as a function of height of the transition level from fig. A-9 (triangles), with least squares nonlinear fit superimposed (solid line). The equation for this curve is $W = 7.41 \sqrt{TR}$ where W is the maximum downdraft speed and TR is the transition level.	221
Fig. A-11.	Plots of numerical model output (dashed; from KW) and predicted values (solid) of maximum outflow velocity (U) and maximum downdraft velocity (W) vs environmental temperature lapse rate, for liquid water mixing ratios of 2 g/Kg (a), 4 g/Kg (b), and 8 g/Kg (c).	224
Fig. A-12.	Plots of numerical model output (dashed; from indicated model) and predicted values (solid) of maximum outflow velocity (U) and maximum downdraft velocity (W) vs liquid water mixing ratio. The aspect ratio used in the prediction is 1.0 in (a), 0.5 in (b) and 0.6 in (c).	225
Fig. A-13.	Plot of numerical model output (dashed; from indicated model) and predicted values (solid) of the ratio of maximum outflow velocity to maximum downdraft velocity (U/W) vs the radius of the precipitation core. The aspect ratio was ~ 1.0 in both models (but see Table A-1).	227
Fig. A-14.	Profiles of mean and median core reflectivity for all cells observed during Wallops Island summer data collection (see caption for Fig. II-19). The height of the peak in mean core reflectivity may indicate the average height of the melting level. Taken from Konrad (1978).	229
Fig. B-1.	Illustration of an arbitrary initial disturbance evolving into BDO solitary waves.	236
Fig. B-2.	Inversion height is initially increased locally to a height two times the inversion depth ("1"), three times the inversion depth ("2"), and 4 times the inversion depth ("3") as illustrated in the uppermost figure. The flow is allowed to evolve for 4.8 T (nondimensional time) units. The larger the initial condition, the more solitons evolve, and the larger they can become.	239
Fig. B-3.	Model calculation of the relative streamline pattern for a well-resolved amplitude ordered solitary wave family propagating in an inversion waveguide of effective depth of 400 m. Taken from Christie and Muirhead (1983b).	240
Fig. B-4.	Numerical integration for 100 nondimensional time units (one trace for each) of (Top) BDO equation and (Bottom) CBDO equation, for an initial finite wave of elevation (amplitude of 1). The horizontal axis is the nondimensional space coordinate moving at the linear long wave speed. In the cylindrical problem, the initial time t_0 was 5. The values of a and d used for both equations were 1.5 and 0.48, respectively.	242

- Fig. B-5. Early time evolution of solitary wave. (Top) Wave remains unchanged in BDO system since it is exact solution to steady equation. (Bottom) Amplitude is reduced and wave becomes asymmetric in CBDO system. Initial wave amplitude was 1, t_0 was 1, and times are shown at intervals of 0.2. 243
- Fig. B-6. Plane BDO solitary wave evolution in the CBDO system. The initial wave amplitude was 10. Time steps shown are 0.2 apart. The wave of depression following the solitary wave is a linear feature. 244
- Fig. B-7. Measured temporal profiles (solid line) for initial wave amplitude of 0.4 in a diverging channel of 30 cm depth (KdV system). The profiles were measured at $x = 4.2, 17.6, 30.9, 37.6, 50.9,$ and 64.3 . Taken from Chang et al. (1979). 245
- Fig. B-8. (Top) Amplitude versus range dependence of linear, KdV, and BDO waves in an axisymmetric geometry. (Bottom) Wave peak position as a function of time for the same three wave systems. 246
- Fig. B-9. (Top) CBDO waves evolving from an initial rounded square wave with amplitude of 2. (Bottom) Amplitude vs. t dependence of leading wave shown above. 248
- Fig. B-10. Numerical integration of the BDO equation for (Top) an initially smooth deep-fluid bore wave, and (Bottom) a long, but finite-length, wave of elevation. Taken from Christie (1989). 250
- Fig. C-1. Example of environmental virtual potential temperature profile that could support surface gravity waves in the atmosphere. Adapted from Doviak and Chen (1988). 253

LIST OF TABLES

- Table I-1. Aircraft accidents in the United States attributable to microbursts or low altitude wind shear associated with thunderstorms. Wind speed is given in meters per second, and cell diameters are given in kilometers. F/I/U indicates number of fatalities, injured, and uninjured. Information adapted from Viemeister (1961), Fujita (1985), Rudich (1986), and Laynor (1986). 15
- Table II-1. Maximum downdraft speed (m/s) versus maximum precipitation rate at cloud base (mm/hr) for precipitation made up of rain only, snow, and graupel. Taken from Krueger et al. (1986). 52
- Table II-2. Application of predictive model to 4 storm cases. The variables given are identified in Eqs. (II.4) and (II.5). The asterisks indicate outflow values estimated from single Doppler radar data; the vertical velocities for those cases were not estimated. The other data were derived from multiple Doppler analyses. 61
- Table A-1. Comparison of numerical model characteristics from P89 (Proctor 1989), KW (Krueger and Wakimoto 1985), and DB (Droegemeier and Babcock 1989). 212

REFERENCES

- Abdullah, A.J., 1956: A note on the atmospheric solitary wave. *J. Meteor.*, **13**, 381-387.
- Ablowitz, M.J., and H. Segur, 1980: Long internal waves in fluids of great depth. *Stud. Appl. Math.*, **62**, 249-262.
- Addis, R.P., 1984: A numerical model of surface outflows from convective storms. *Boundary-Layer Meteor.*, **28**, 121-160.
- Anderson, J.R., 1990: Numerical simulation of thunderstorm microburst outflows. Submitted to *Mon. Wea. Rev.*
- Anderson, J.R., K.K. Droegemeier, and R.B. Wilhelmson, 1985: Simulation of the thunderstorm subcloud environment. Preprints, *14th Conference on Severe Local Storms*, Indianapolis, Amer. Meteor. Soc., 147-150.
- Bach, R.E., and R.C. Wingrove, 1986: The analysis of airline flight records for winds and performance with application to the Delta 191 accident. *AIAA Atmospheric Flight Mechanics Conference*, AIAA-86-2227-CP, Williamsburg, 361-373.
- Bakke, P., 1957: An experimental investigation of a wall jet. *J. Fluid Mech.*, **2**, 467-472.
- Batchelor, G.K., 1956: On steady laminar flow with closed streamlines at large Reynolds number. *J. Fluid Mech.*, **1**, 177.
- Bedard, A.J., Jr., and T.J. LeFebvre, 1986: Surface measurements of gust fronts and microbursts during the JAWS project: Statistical results and implications for wind shear detection, prediction, and modeling. *NOAA Tech. Memo. ERL-WPL-135*. Wave Propagation Laboratory, Boulder, 112 pp.
- Bedard, A.J., and S.J. Caplan, 1987: Microburst vorticity. *AIAA 25th Aerospace Sciences Meeting*, AIAA-87-0440, Reno, 8 pp.
- Benjamin, T.B., 1967: Internal waves of permanent form in fluids of great depth. *J. Fluid Mech.*, **29**, 559-592.
- Benjamin, T.B., 1968: Gravity currents and related phenomena. *J. Fluid Mech.*, **31**, 209-248.
- Betts, A.K., and M.F. Silva Dias, 1979: Unsaturated downdraft thermodynamics in cumulonimbus. *J. Atmos. Sci.*, **36**, 1061-1071.
- Biron, P.J., and M.A. Isaminger, 1989: An analysis of microburst characteristics related to automatic detection from Huntsville, AL and Denver, CO. Preprints, *24th Conference on Radar Meteorology*, Tallahassee, Amer. Meteor. Soc., 269-273.
- Bluestein, H.B., and M.H. Jain, 1985: Formation of mesoscale lines of precipitation: Severe squall lines in Oklahoma during the spring. *J. Atmos. Sci.*, **42**, 1711-1732
- Blumen, W., 1984: An observational study of instability and turbulence in nighttime drainage winds. *Boundary-Layer Meteor.*, **28**, 245-269.

- Bohne, A.R., 1981: Radar detection of turbulence in thunderstorms. *Report No. AFGL-TR-81-0102*. Air Force Geophysics Laboratory, 62 pp.
- Bosart, L.F., and F. Sanders, 1986: Mesoscale structure in the megalopolitan snowstorm of 11-12 February, 1983. Part III. A large-amplitude gravity wave. *J. Atmos. Sci.*, **43**, 924-939.
- Boussinesq, M.J., 1892: Theorie des ondes et des remous qui se propagent le long d'un canal rectangulaire horizontal, en communiquant au liquide contenu dans ce canal des vitesses sensiblement pareilles de la surface au fond. *J. Math. Pures Appl.*, **17**, 55-108.
- Bracewell, R.N., 1986: *The Fourier Transform and Its Applications*. McGraw-Hill, New York, 474 pp.
- Braham, R.R., Jr., 1952: The water and energy budgets of the thunderstorm and their relation to thunderstorm development. *J. Meteor.*, **9**, 236.
- Brancato, G.N., 1942: *The meteorological behavior and characteristics of thunderstorms*. United States Dept. of Commerce Weather Bureau, 22 pp.
- Bray, R.S., 1986: Aircraft performance and control in downburst windshear. *Wind Shear - SAE SP-681*, No. 861698, 13-38.
- Bretherton, C.S., 1987: A theory for nonprecipitating convection between two parallel plates. Part I: Thermodynamics and "linear" solutions. *J. Atmos. Sci.*, **44**, 1809-1827.
- Britter, R.E., 1979, The spread of a negatively buoyant plume in a calm environment. *Atmos. Environ.*, **13**, 1241-1247.
- Britter, R.E., and P.F. Linden, 1980: The motion of the front of a gravity current travelling down an incline. *J. Fluid Mech.*, **99**, 531-543.
- Brown, J.M., K.R. Knupp, and F. Caracena, 1982: Destructive winds from shallow, high-based cumulonimbi. Preprints, *12th Conference on Severe Local Storms*, San Antonio, Amer. Meteor. Soc., 272-275.
- Browning, K.A., 1971: Structure of the atmosphere in the vicinity of large-amplitude Kelvin-Helmholtz billows. *Quart. J. Roy. Meteor. Soc.*, **97**, 283-299.
- Burrows, D.A., and L.F. Osborne, 1986: Precipitation loading in wet microbursts. Preprints, *23rd Conference on Radar Meteorology*, Snowmass, Amer. Meteor. Soc., J97-J100.
- Byers, H.R., and R.R. Braham, Jr., 1949: *The Thunderstorm*. U.S. Department of Commerce, Washington, DC, 287 pp.
- Campbell, S.D., and M.A. Isaminger, 1989: Using features aloft to improve timeliness of TDWR hazard warnings. Preprints, *3rd International Conference on the Aviation Weather System*, Anaheim, Amer. Meteor. Soc., 184-189.
- Caracena, F., 1978: A comparison of two downbursts of different meso scales. Preprints, *Conference on Weather Forecasting and Analysis and Aviation Meteorology*, Silver Springs, Amer. Meteor. Soc., 293-300.
- Caracena, F., 1982: Is the microburst a large vortex ring imbedded in a thunderstorm downdraft? Abstract, *EOS-Trans. Amer. Geophys. Union*, **63**, p.89.

- Caracena, F., 1987: The microburst as an aircraft hazard and forecast problem. *Bull. World Meteor. Org.*, **36**, 278–284.
- Caracena, F., 1988: The microburst: A challenge to aviation safety in the 1980s. *Air Line Pilot*, May, 18–23.
- Caracena, F., J. McCarthy, and J.A. Flueck, 1983: Forecasting the likelihood of microbursts along the front range of Colorado. Preprints, *13th Conference on Severe Local Storms*, Tulsa, Amer. Meteor. Soc., 261–264.
- Caracena, F., R. Ortiz, J. Augustine, 1986: The crash of Delta Flight 191 at Dallas–Fort Worth International Airport on 2 August 1985: Multiscale analysis of weather conditions. *NOAA Tech. Rep. ERL 430-ESG 2*, 33pp.
- Caracena, F., and M.W. Maier, 1987: Analysis of a microburst in the FACE meteorological mesonet network in southern Florida. *Mon. Wea. Rev.*, **115**, 969–985.
- Caracena, F., and J.A. Flueck, 1988: Forecasting and classifying dry microburst activity in the Denver area subjectively and objectively. *J. Aircraft*, **25**, 525–530.
- Caracena, F., R.L. Holle, and C.A. Doswell III, 1989: *Microbursts: A handbook for visual identification*. U.S. Dept. of Commerce, NOAA/ERL/NSSL, 35 pp.
- Carbone, R.E., 1982: A severe frontal rainband. Part I: Stormwide hydrodynamic structure. *J. Atmos. Sci.*, **39**, 258–279.
- Carbone, R.E., 1983: A severe frontal rainband. Part II: Tornado parent vortex circulation. *J. Atmos. Sci.*, **40**, 2639–2654.
- Carbone, R.E., J.W. Conway, N.A. Crook, and M.W. Moncrieff, 1990: The generation and propagation of a nocturnal squall line. Part I: Observations and implications for mesoscale predictability. Submitted to *Mon. Wea. Rev.*
- Chadwick, R.B., and E.E. Gossard, 1983: Radar remote sensing of the clear atmosphere—Review and applications. *Proc. IEEE*, **71**, 738–753.
- Chandrasekhar, S., 1961: *Hydrodynamic and hydromagnetic stability*. Oxford:Clarendon Press, 652 pp.
- Chang, P., W.K. Melville, and J.W. Miles, 1979: On the evolution of a solitary wave in a gradually varying channel. *J. Fluid Mech.*, **95**, 401–414.
- Charba, J., 1974: Application of gravity current model to analysis of squall–line gust front. *Mon. Wea. Rev.*, **102**, 140–156.
- Chen, C.J., and L.M. Chang, 1972: Flow patterns of a circular vortex ring with density difference under gravity. *J. Appl. Mech.*, **39**, 869–872.
- Chen, J.-C., 1980: Studies on gravitational spreading currents. Ph.D. thesis, California Institute of Technology, Report No. KH-R-40, 436 pp.
- Chen, J.-P., 1986: A numerical simulation of microbursts. M.S. Thesis, South Dakota School of Mines and Technology, 118 pp.

- Chereskin, T.K., and E. Mollo-Christensen, 1985: Modulational development of nonlinear gravity-wave groups. *J. Fluid Mech.*, **151**, 337–365.
- Cheung, T.K., and C.G. Little, 1990: Meteorological tower, microbarograph array, and sodar observations of solitary waves in the nocturnal boundary layer. UÇAR fellows at Naval Environmental Prediction Research Facility, submitted to ?.
- Chisolm, A.J., and J.H. Renick, 1972: The kinematics of multicell and supercell Alberta hailstorms. Alberta Hail Studies 1972, Research Council of Alberta Hail Studies, *Report No. 72-2*, 53 pp..
- Christie, D.R., 1989: Long nonlinear waves in the lower atmosphere. *J. Atmos. Sci.*, **46**, 1462–1491.
- Christie, D.R., and K.J. Muirhead, 1983a: Solitary waves: A hazard to aircraft operating at low altitudes, *Aust. Meteor. Mag.*, **31**, 97–109
- Christie, D.R., and K.J. Muirhead, 1983b: Solitary waves, A low-level wind shear hazard to aviation. *Int. J. Aviat. Safety*, **1**, 169–190.
- Christie, D.R., and K.J. Muirhead, 1985: Solitary waves and low-altitude wind shear in Australia. *Aviat. Safety Dig.*, **123**, 3–9.
- Christie, D.R., K.J. Muirhead, and A.L. Hales, 1978: On solitary waves in the atmosphere. *J. Atmos. Sci.*, **35**, 805–825.
- Christie, D.R., K.J. Muirhead, and A.L. Hales, 1979: Intrusive density flows in the lower troposphere: A source of atmospheric solitons. *J. Geophys. Res.*, **84**, 4959–4970.
- Chuang, S., F.H. Proctor, Z.W. Zack, and M.L. Kaplan, 1984: A numerical weather prediction system designed to simulate atmospheric downburst phenomena. *AIAA 22nd Aerospace Sciences Meeting*, AIAA-84-0352, Reno, 15 pp.
- Clarke, R.H., 1972: The morning glory: An atmospheric hydraulic jump. *J. Appl. Meteor.*, **11**, 304–311.
- Courtier, P., and O. Talagrand, 1987: Variational assimilation of meteorological observations with the adjoint vorticity equation. II. Numerical results. *Quart. J. Roy. Meteor. Soc.*, **113**, 1329–1347.
- Crook, N.A., 1986: The effect of ambient stratification and moisture on the motion of atmospheric undular bores. *J. Atmos. Sci.*, **43**, 171–181.
- Crook, N.A., 1988: Trapping of low-level internal gravity waves. *J. Atmos. Sci.*, **45**, 1533–1541.
- Crook, N.A., and M.J. Miller, 1985: A numerical and analytical study of atmospheric undular bores. *Quart. J. Roy. Meteor. Soc.*, **111**, 225–242.
- Cullen, J.A., and M.M. Wolfson, 1990: Predicting microburst hazard from thunderstorm day statistics: Methodology and preliminary results. *Project Report*, MIT Lincoln Laboratory, 66 pp. (in preparation).
- Daly, B.J., 1967: Numerical study of two fluid Rayleigh–Taylor instability. *Phys. Fluids*, **10**, 297–307.

- Daly, B.J., and W.E. Pracht, 1968: Numerical study of density–current surges. *Phys. Fluids*, **11**, 15–30.
- Das, P., 1979: A non–Archimedean approach to the equations of convection dynamics. *J. Atmos. Sci.*, **36**, 2183–2190.
- Davis, P.A., and W.R. Peltier, 1976: Resonant parallel shear instability in the stably stratified planetary boundary layer. *J. Atmos. Sci.*, **33**, 1287–1300.
- Davis, R.E., and A. Acrivos, 1967: Solitary internal waves in deep water. *J. Fluid Mech.*, **29**, 593–607.
- Didden, N., and C.–M. Ho, 1985: Unsteady separation in a boundary layer produced by an impinging jet. *J. Fluid Mech.*, **160**, 235–256.
- Didden, N., and T. Maxworthy, 1982: The viscous spreading of plane and axisymmetric gravity currents. *J. Fluid Mech.*, **121**, 27–42.
- DiStefano, J.D., 1983: Analysis of a thunderstorm downburst. S.M. Thesis, Department of Meteorology and Physical Oceanography, Massachusetts Institute of Technology, 120 pp.
- Dodd, R.K., J.C. Eilbeck, J.D. Gibbon, H.C. Morris, 1982: *Solitons and Nonlinear Wave Equations*. Academic Press, 630 pp.
- Dodge, J., J. Arnold, G. Wilson, J. Evans, and T. Fujita, 1986: The cooperative Huntsville meteorological experiment (COHMEX). *Bull. Amer. Meteor. Soc.*, **67**, 417–419.
- Donaldson, R.J., 1965: Methods for identifying severe thunderstorms by radar: A guide and bibliography. *Bull. Amer. Meteor. Soc.*, **46**, 174–193.
- Doviak, R.J., P.S. Ray, R.G. Strauch, and L.J. Miller, 1976: Error estimation in wind fields derived from dual–Doppler radar measurements. *J. Appl. Meteor.*, **15**, 868–878.
- Doviak, R.J., and R.S. Ge, 1984: An atmospheric solitary gust observed with a Doppler radar, a tall tower and a surface network. *J. Atmos. Sci.*, **41**, 2559–2573.
- Doviak, R.J., and S. Chen, 1988: Observations of a thunderstorm generated gust compared with solitary wave theory. *FAA Report No. DOT/FAA/SA–88/1*, 135 pp.
- Doviak, R.J., and D.R. Christie, 1989: Thunderstorm–generated solitary waves: A wind shear hazard. *J. Aircraft*, **26**, 423–431.
- Doviak, R.J., K.W. Thomas, and D.R. Christie, 1989: The wavefront shape, position, and evolution of a great solitary wave of translation. *IEEE Trans. on Geoscience and Remote Sensing*, **27**, 658–665.
- Doviak, R.J., S. Chen, and D.R. Christie, 1990: A thunderstorm generated solitary wave observation compared with nonlinear wave theory for a compressible fluid. Submitted to *J. Atmos. Sci.*
- Drazin, P.G., 1958: The stability of a shear layer in an unbounded heterogeneous inviscid fluid. *J. Fluid Mech.*, **4**, 214–224.

- Drazin, P.G., and R.S. Johnson, 1989: *Solitons: an Introduction*. Cambridge University Press, 226 pp.
- Droegemeier, K.K., 1988: Simulation of microburst vorticity dynamics. Preprints, *15th Conference on Severe Local Storms*, Baltimore, Amer. Meteor. Soc., J107-J110.
- Droegemeier, K.K., and R.B. Wilhelmson, 1986: Kelvin-Helmholtz instability in a numerically simulated thunderstorm outflow. *Bull. Amer. Meteor. Soc.*, **67**, 416-417.
- Droegemeier, K.K., and R.P. Davies-Jones, 1987: Simulation of thunderstorm microbursts with a supercompressible numerical model. Proceedings, *5th International Conference on Numerical Methods in Laminar and Turbulent Flow*. Montreal, 1386-1397.
- Droegemeier, K.K., and R.B. Wilhelmson, 1987: Simulation of thunderstorm outflow dynamics, Part I: Outflow sensitivity experiments and turbulence dynamics. *J. Atmos. Sci.*, **44**, 1180-1210.
- Droegemeier, K.K. and M.R. Babcock, 1989: Numerical simulation of microburst downdrafts: Application to on-board and look-ahead sensor technology. *AIAA 27th Aerospace Sciences Meeting*, AIAA-89-0821, Reno, 12 pp.
- Egger, J., 1983: The morning glory: A nonlinear wave phenomenon. *Mesoscale Meteorology - Theories, Observations and Models*, ed. by D.K. Lilly and T. Gal-Chen, Reidel Publishing Co., 339-348.
- Egger, J., 1984: On the theory of the morning glory. *Beitr. Phys. Atmosph.*, **57**, 123-134.
- Eilts, M.D., and R.J. Doviak, 1987: Oklahoma downbursts and their asymmetry. *J. Climate Appl. Meteor.*, **26**, 69-78.
- Einaudi, F., and J.J. Finnigan, 1981: The interaction between an internal gravity wave and the planetary boundary layer. Part I: The linear analysis. *Quart. J. Roy. Meteor. Soc.*, **107**, 793-806.
- Elmore, K.L., 1986: Evolution of a microburst and bow-shaped echo during JAWS. Preprints, *23rd Conference on Radar Meteorology*, Snowmass, Amer. Meteor. Soc., J101-J104.
- Elmore, K.L., and W.R. Sand, 1989: A cursory study of F-factor applied to Doppler radar. Preprints, *3rd International Conference on the Aviation Weather System*, Anaheim, Amer. Meteor. Soc., 130-134.
- Emanuel, K.A., 1981: A similarity theory for unsaturated downdrafts within clouds. *J. Atmos. Sci.*, **38**, 1541-1557.
- Emmanuel, C.B., 1973: Richardson number profiles through shear instability wave regions observed in the lower planetary boundary layer. *Boundary-Layer Meteor.*, **5**, 19-27.
- Erickson, C.O., and L.F. Whitney, 1973: Gravity waves following severe thunderstorms. *Mon. Wea. Rev.*, **101**, 708-711.
- Evans, J.E., and D. Johnson, 1984: The FAA transportable Doppler weather radar. Preprints, *22nd Conference on Radar Meteorology*, Zurich, Amer. Meteor. Soc., 246-250.

- Evans, J.E., and D.H. Turnbull, 1985: The FAA-MIT Lincoln Laboratory Doppler weather radar program. Preprints, *2nd International Conference on the Aviation Weather System*, Montreal, Amer. Meteor. Soc., 76-79.
- Evans, J., and D. Turnbull, 1989: Development of an automated windshear detection system using Doppler weather radar. *Proc. IEEE*, 77, 1661-1673.
- Fawbush, E.J., and R. C. Miller, 1954: A basis for forecasting peak wind gusts in non-frontal thunderstorms. *Bull. Amer. Meteor. Soc.*, 35, 14-19.
- Flierl, G.R., 1987: Isolated eddy models in geophysics. *Ann. Rev. Fluid Mech.*, 19, 493-530.
- Forbes, G.S., and R.M. Wakimoto, 1983: A concentrated outbreak of tornadoes, downbursts and microbursts, and implications regarding vortex classification. *Mon. Wea. Rev.*, 111, 220-235.
- Frank, H.W., and W.R. Moninger, 1977: Observations of atmospheric density currents with severe wind shear. *10th Conference on Severe Local Storms*, Omaha, Amer. Meteor. Soc., 160-167.
- Fritsch, J.M., 1975: Cumulus dynamics: Local compensating subsidence and its implications for cumulus parameterization. *Pure Appl. Geophys.*, 113, 851-867.
- Frost, W., and R.L. Bowles, 1984: Wind shear terms in the equations of aircraft motion. *J. Aircraft*, 21, 866-872.
- Fujita, T.T., 1963: Analytical Mesometeorology: A Review in *Severe Local Storms*, Meteorol. Monogr. Vol. 5, No. 27, Amer. Meteorol. Soc., 77-125.
- Fujita, T.T., 1976: Spearhead echo and downburst near the approach end of a John F. Kennedy airport runway, New York City. *SMRP Res. Pap. 137*, University of Chicago, Ill., 51 pp.
- Fujita, T.T., 1978: Manual of downburst identification for project NIMROD. *SMRP Res. Pap. 156*, University of Chicago, Ill., 104 pp.
- Fujita, T.T., 1979: Objectives, operation, and results of Project NIMROD. Preprints, *11th Conference on Severe Local Storms*, Kansas City, Amer. Meteor. Soc., 259-266.
- Fujita, T.T., 1980a: Meso-scale structure of downbursts depicted by Doppler radar. *SMRP Res. Pap. 181*, University of Chicago, Ill., 19 pp.
- Fujita, T.T., 1980b: Downbursts and microbursts - an aviation hazard. Preprints, *19th Conference on Radar Meteorology*, Miami Beach, Amer. Meteor. Soc., 94-101.
- Fujita, T.T., 1981: Tornadoes and downbursts in the context of generalized planetary scales. *J. Atmos. Sci.*, 38, 1511-1534.
- Fujita, T.T., 1983: Microburst wind shear at New Orleans International Airport, Kenner, Louisiana on July 9, 1982. *SMRP Res. Pap. 199*, University of Chicago, Ill., 39 pp.
- Fujita, T.T., 1984: Andrews AFB microburst: Six minutes after the touchdown of Air Force One. *SMRP Res. Pap. 205*, University of Chicago, Ill., 38 pp.

- Fujita, T.T., 1985: *The Downburst – Microburst and Macrobust*. Satellite and Mesometeorology Project, Department of the Geophysical Sciences, The University of Chicago, Ill., 122 pp.
- Fujita, T.T., 1986: *DFW Microburst*. Satellite and Mesometeorology Project, Department of the Geophysical Sciences, The University of Chicago, Ill., 154 pp.
- Fujita, T.T., and H.A. Brown, 1958: A study of mesosystems and their radar echoes. *Bull. Amer. Meteor. Soc.*, **39**, 538–554.
- Fujita, T.T., and H. R. Byers, 1977: Spearhead echo and downburst in the crash of an airliner. *Mon. Wea. Rev.*, **105**, 129–146.
- Fujita, T.T., and F. Caracena, 1977: An analysis of three weather-related aircraft accidents. *Bull. Amer. Meteor. Soc.*, **58**, 1164–1181.
- Fujita, T.T., and R.M. Wakimoto, 1981: Five scales of airflow associated with a series of downbursts on 16 July 1980. *Mon. Wea. Rev.*, **109**, 1438–1456.
- Fujita, T.T., and R.M. Wakimoto, 1983a: Microbursts in JAWS depicted by Doppler radars, PAM, and aerial photographs. Preprints, *21st Conference on Radar Meteorology*, Edmonton, Amer. Meteor. Soc., 638–645.
- Fujita, T.T., and R.M. Wakimoto, 1983b: JAWS microbursts revealed by triple-Doppler radar, aircraft, and PAM data. Preprints, *13th Conference on Severe Local Storms*, Tulsa, Amer. Meteor. Soc., 97–100.
- Fujita, T.T., and P.G. Black, 1988: Monrovia microburst of 20 July 1986: A study of “SST”. Preprints, *15th Conference on Severe Local Storms*, Baltimore, Amer. Meteor. Soc., 380–383.
- Fulks, J.R., 1951: The instability line. *Compendium of Meteorology*, Amer. Meteor. Soc., 647–652.
- Fulton, R., 1987: Observations of the interactions of a nocturnal thunderstorm outflow with a stable environment. M.S. Thesis, University of Oklahoma, 147 pp.
- Fulton, R., D.S. Zrnic’, and R.J. Doviak, 1986: Doppler radar and in-situ measurements of a nocturnal thunderstorm gust front. Preprints, *23rd Conference on Radar Meteorology*, Snowmass, Amer. Meteor. Soc., J85–J88.
- Fulton, R., D.S. Zrnic’, and R.J. Doviak, 1990: Initiation of a solitary wave family in the demise of a nocturnal thunderstorm density current. *J. Atmos. Sci.*, **47**, ?.
- Gardner, C.S., J.M. Greene, M.D. Kruskal, and R.M. Miura, 1967: Method for solving the Korteweg-deVries equation. *Phys. Rev. Lett.*, **19**, 1095–1097.
- Garvine, R.W., 1977: Observations of the motion field of the Connecticut River plume. *J. Geophys. Res.*, **82**, 441–454.
- Garvine, R.W., 1984: Radial spreading of buoyant, surface plumes in coastal waters. *J. Geophys. Res.*, **89**, No. C2, 1989–1996.
- Glauert, M.B., 1956: The wall jet. *J. Fluid Mech.*, **1**, 625–643.

- Goff, R.C., 1975: Thunderstorm-outflow kinematics and dynamics. *NOAA Tech. Memo ERL NSSL-75*. 63 pp.
- Goff, R.C., 1976: Vertical structure of thunderstorm outflows. *Mon. Wea. Rev.*, **104**, 1429-1440.
- Goldman, J.L., and P.W. Sloss, 1969: Structure of the leading edge of thunderstorm cold-air outflow. *6th Conference on Severe Local Storms*, Chicago, Amer. Meteor. Soc., 75-79.
- Goodman, S.J., D.E. Buechler, and P.D. Wright, 1988: Lightning and precipitation history of a microburst-producing storm. *Geophys. Res. Lett.*, **15**, 1185-1188.
- Goodman, S.J., D.E. Buechler, P.D. Wright, W.D. Rust, and K.E. Nielsen, 1989: Polarization radar and electrical observations of microburst producing storms during COHMEX. Preprints, *24th Conference on Radar Meteorology*, Tallahassee, Amer. Meteor. Soc., 109-112.
- Gossard, E.E., 1983: Aircraft hazard assessment from a clear-air radar and meteorological study of gravity wave events. US Dept. of Commerce, NOAA/ERL, *Report No. PB83-257139*, 18 pp.
- Gossard, E.E., and W. Munk, 1954: On gravity waves in the atmosphere. *J. Meteor.*, **11**, 259-269.
- Gossard, E.E., and J.H. Richter, 1970: The shape of internal waves of finite amplitude from high-resolution radar sounding of the atmosphere. *J. Atmos. Sci.*, **27**, 971-973.
- Gossard, E.E., J.H. Richter, and D. Atlas, 1970: Internal waves in the atmosphere from high-resolution radar measurements. *J. Geophys. Res.*, **75**, 3523-3536.
- Greene, G.E., J.A. Korrell, and P.A. Mandics, 1977: An analysis of the gust front hazard. Preprints, *10th Conference on Severe Local Storms*, Omaha, Amer. Meteor. Soc., 151-153.
- Greene, R.A., 1978: Airborne detection of low-level wind shear. *J. Aircraft*, **16**, 823-827.
- Gross, M.G., 1972: *Oceanography: A View of the Earth*. Prentice-Hall, Englewood Cliffs, NJ.
- Grundy, R.E., and J.W. Rottman, 1986: Self-similar solutions of the shallow-water equations representing gravity currents with variable inflow. *J. Fluid Mech.*, **169**, 337-351.
- Haase, S.P., and R.K. Smith, 1984: Morning glory wave clouds in Oklahoma: A case study. *Mon. Wea. Rev.*, **112**, 2078-2089.
- Haase, S.P., and R.K. Smith, 1989a: The numerical simulation of atmospheric gravity currents. Part I: Neutrally-stable environments. *Geo. Astro. Fluid Dyn.*, **46**, 1-33.
- Haase, S.P., and R.K. Smith, 1989b: The numerical simulation of atmospheric gravity currents. Part I: Environments with stable layers. *Geo. Astro. Fluid Dyn.*, **46**, 35-51.
- Hall, F.F., W.D. Neff, and T.V. Frazier, 1976: Wind shear observations in thunderstorm density currents. *Nature*, **264**, 408-411.
- Hamilton, R.E., 1970: Use of detailed intensity radar data in mesoscale surface analysis of the July 4 1969 storm in Ohio. Preprints, *14th Conference on Radar Meteorology*, Tucson, Amer. Meteor. Soc., 339-342.

- Hardy, K.R., 1972: Studies of the clear atmosphere using high power radar. Chapter 14 of *Remote Sensing of the Troposphere*, ed. by V.E. Derr, NOAA - ERL, and U. of Colorado, 33 pp.
- Hardy, K.R., K.M. Glover, and H. Otterstein, 1969: Radar investigations of atmospheric structure and CAT in the 3 to 20 km region, in *Clear Air Turbulence and its Detection*, ed. by Y.H. Pao and A. Goldberg, Plenum Press, 402-416.
- Harvey, J.K., and F.J. Perry, 1971: Flowfield produced by trailing vortices in the vicinity of the ground. *AIAA Journal*, **9**, 1659-1660.
- Havens, J.A., and T.O. Spicer, 1984: Gravity spreading and air entrainment by heavy gases instantaneously released in a calm atmosphere. *Symposium on Atmospheric Dispersion of Heavy Gases and Small Particles*, Int. Union of Theor. and Appl. Mech. (IUTAM), Delft, The Netherlands, ed. by G. Ooms and H. Tennekes, Springer Verlag, 177-188.
- Hicks, J.J., 1969: Radar observations of a gravitational wave in clear air near the tropopause associated with CAT. *J. Appl. Meteor.*, **8**, 627-633.
- Hildebrand, F.B., 1976: *Advanced Calculus for Applications*. Second Edition. Prentice Hall, 733 pp.
- Hinrichs, G., 1888: Tornadoes and derechos. *Amer. Meteor. J.*, **5**, 306-317, 341-349.
- Hiser, H.W., H.V. Senn, and C.L. Courtright, 1970: Identification of damaging surface winds in tropical thunderstorms utilizing incoherent weather radar and meteorological observations. Final Report, University of Miami, Rosenstiel School of Marine and Atmospheric Science, Report No. AFCRL-70-0542, 34 pp.
- Hjelmfelt, M.R., 1984: Radar and surface data analysis of a microburst in JAWS. Preprints, 22nd Conference on Radar Meteorology, Zurich, Amer. Meteor. Soc., 64-69.
- Hjelmfelt, M.R., 1988: Structure and life cycle of microburst outflows observed in Colorado. *J. Appl. Meteor.*, **27**, 900-927.
- Hjelmfelt, M.R., and R.D. Roberts, 1985: Microburst lines. Preprints, 14th Conference on Severe Local Storms, Indianapolis, Amer. Meteor. Soc., 297-300.
- Hjelmfelt, M.R., R.D. Roberts, and H.D. Orville, 1986: Observational and numerical study of a microburst line-producing storm. Preprints, 23rd Conference on Radar Meteorology, Snowmass, Amer. Meteor. Soc., J77-J80.
- Hjelmfelt, M.R., H.D. Orville, R.D. Roberts, J.P. Chen, and F.J. Kopp, 1989: Observational and numerical study of a microburst line-producing storm. *J. Atmos. Sci.*, **46**, 2731-2743.
- Holton, J.R., 1973: A one-dimensional cumulus model including pressure perturbations. *Mon. Wea. Rev.*, **101**, 201-205.
- Howells, P.C., R. Rotunno, and R.K. Smith, 1988: A comparative study of atmospheric and laboratory-analogue numerical tornado-vortex models. *Quart. J. Roy. Meteor. Soc.*, **114**, 801-822.
- Huppert, H.E., 1982: The propagation of two-dimensional and axisymmetric viscous gravity currents over a rigid horizontal surface. *J. Fluid Mech.*, **121**, 43-58.

- Ivan, M., 1986: A ring-vortex downburst model for flight simulations. *J. Aircraft*, **23**, 232-236.
- Isaminger, M.A. (1988): A preliminary study of precursors to Huntsville microbursts. *Project Report ATC-153*, MIT/Lincoln Laboratory, FAA Report No. *DOT-FAA-PM-87/35*, 22 pp.
- Johns, R.H., and W.D. Hirt, 1983: The derecho...A severe weather producing convective system. Preprints, *13th Conference on Severe Local Storms*, Tulsa, Amer. Meteor. Soc., 178-181.
- Johnson, D.R., 1985: Thorney Island trials: Systems development and operational procedures. From *Heavy Gas Dispersion Trials at Thorney Island*, Chemical Engineering Monograph No. 22, Elsevier Science Publishers, Amsterdam, ed. by J. McQuaid, 35-64.
- Kaimal, J.C., and J. Gaynor, 1983: The Boulder Atmospheric Observatory. *J. Appl. Meteor.*, **22**, 863-880.
- Kamburova, P.L. and F.H. Ludlam, 1966: Rainfall evaporation in thunderstorm downdrafts. *Quart. J. Roy. Meteor. Soc.*, **92**, 510-518.
- Kessinger, C.J., R.D. Roberts, and K.L. Elmore, 1986: A summary of microburst characteristics from low-reflectivity storms. Preprints, *23rd Conference on Radar Meteorology*, Snowmass, Amer. Meteor. Soc., J105-J108.
- Kessinger, C.J., D.B. Parsons, and J.W. Wilson, 1988: Observations of a storm containing mesocyclones, downbursts, and horizontal vortex circulations. *Mon. Wea. Rev.*, **116**, 1959-1982.
- Kessler, E., 1982: Model relationships among storm cloudiness, precipitation, and airflow. *Thunderstorms: A social, scientific and technological documentary, Vol. 2: Thunderstorm morphology and dynamics*, ed. by E. Kessler, U.S. Dept. of Commerce, NOAA ERL, U.S. Govt. Printing Office 1982-578-870, 602 pp.
- Keulegan, G.H., 1958: Twelfth progress report on model laws for density currents: The motion of saline fronts in still water. NBS Report No. 5831, 29 pp.
- Kingsmill, D.E., R.M. Wakimoto, and W.C. Lee, 1989: Kinematic and dynamic analysis of microburst producing thunderstorm. Preprints, *24th Conference on Radar Meteorology*, Tallahassee, Amer. Meteor. Soc., 146-149.
- Klemp, J.B., and R.B. Wilhelmson, 1978: The simulation of three-dimensional convective storm dynamics. *J. Atmos. Sci.*, **35**, 1070-1096.
- Klemp, J.B., and R. Rotunno, 1983: A study of the tornadic region within a supercell thunderstorm. *J. Atmos. Sci.*, **40**, 359-377.
- Klingbeil, D.L., 1987: An investigation of the internal structure of the thunderstorm outflow with particular attention to multiple surges. Ph.D. Thesis, Purdue University, 235 pp.
- Klingbeil, D.L., D.R. Smith, and M.M. Wolfson, 1987: Gust front characteristics as detected by Doppler radar. *Mon. Wea. Rev.*, **115**, 905-918.
- Knupp, K.R., 1987: Downdrafts within High Plains cumulonimbi. Part I. General kinematic structure. *J. Atmos. Sci.*, **44**, 987-1008.

- Knupp, K.R., 1988: Downdrafts within High Plains cumulonimbi. Part II. Dynamics and thermodynamics. *J. Atmos. Sci.*, **45**, 3965-3982.
- Knupp, K.R., 1989: Numerical simulation of low-level downdraft initiation within precipitating cumulonimbi: Some preliminary results. *Mon. Wea. Rev.*, **117**, 1517-1529.
- Knupp, K.R., and W.R. Cotton, 1985: Convective cloud downdraft structure: An interpretive survey. *Rev. Geophys.*, **23**, 183-215.
- Knupp, K.R., and D.P. Jorgensen, 1985: Case study analysis of a large-scale and long-lived downburst producing storm. Preprints, *14th Conference on Severe Local Storms*, Indianapolis, Amer. Meteor. Soc., 301-304.
- Koch, S.E., 1984: The role of an apparent mesoscale frontogenetical circulation in squall line initiation. *Mon. Wea. Rev.*, **112**, 2090-2111.
- Konrad, T.G., 1978: Statistical models of summer rainshowers derived from fine-scale radar observations. *J. Appl. Meteor.*, **17**, 171-188.
- Koop, C.G., and G. Butler, 1981: An investigation of internal solitary waves in a two-fluid system. *J. Fluid Mech.*, **112**, 225-251.
- Korteweg, D.J., and G. deVries, 1895: On the change of form of long waves advancing in a rectangular canal and on a new type of long stationary waves. *Phil. Mag.*, **39**, 422-443.
- Kramer, M.L., and D.E. Seymour, 1976: John E. Amos cooling tower flight program data, December 1975-March 1976. American Electric Power Service Corporation, Smith-Singer Meteorologists, Inc., 89 pp.
- Krueger, S.K., 1988: The role of entrainment by falling raindrops in microbursts. Preprints, *15th Conference on Severe Local Storms*, Baltimore, Amer. Meteor. Soc., J103-J106.
- Krueger, S.K., and R.M. Wakimoto, 1985: Numerical simulation of dry microbursts. Preprints, *14th Conference on Severe Local Storms*, Indianapolis, Amer. Meteor. Soc., 163-166.
- Krueger, S.K., R.M. Wakimoto, and S.J. Lord, 1986: Role of ice-phase microphysics in dry microburst simulations. Preprints, *23rd Conference on Radar Meteorology*, Snowmass, Amer. Meteor. Soc., J73-J76.
- Krumm, W.R., 1954: On the cause of downdrafts from dry thunderstorms over the plateau area of the United States. *Bull. Amer. Meteor. Soc.*, **35**, 122-125.
- Labitt, M., 1981: Coordinated radar and aircraft observations of turbulence. *Project Report ATC-108*, MIT/Lincoln Laboratory, FAA Report No. *FAA-RD-81-44*, 40 pp.
- Lalas, D.P., F. Einaudi, and D. Fua, 1976: The destabilizing effect of the ground in Kelvin-Helmholtz waves in the atmosphere. *J. Atmos. Sci.*, **33**, 59-69.
- Launder, B.E., and W. Rodi, 1983: The turbulent wall jet - measurements and modeling. *Ann. Rev. Fluid Mech.*, **15**, 429-459.
- Laynor, W.G., 1986: Summary of windshear accidents and views about prevention. *Wind Shear - SAE SP-681*, No. 861697, 1-12.

- Lee, W.-C., 1989: The evolution and structure of the bow echo/microburst events. *NCAR Cooperative Thesis No. 117*, Univ. of California, LA, 261 pp.
- Lemon, L.R., and C.A. Doswell, 1979: Severe thunderstorm evolution and mesocyclone structure as related to tornadogenesis. *Mon. Wea. Rev.*, **107**, 1184-1197.
- Linden, P.F., and J.E. Simpson, 1985: Microbursts: a hazard for aircraft. *Nature*, **317**, 601-602.
- Linden, P.F., and J.E. Simpson, 1986: Gravity-driven flows in a turbulent fluid. *J. Fluid Mech.*, **172**, 481-497.
- Lindzen, R.S., and A.J. Rosenthal, 1976: On the instability of Helmholtz profiles in stably stratified fluids when a lower boundary is present. *J. Geophys. Res.*, **81**, 1561-1571.
- List, E.J., 1982: Turbulent jets and plumes. *Ann. Rev. Fluid Mech.*, **14**, 189-212.
- Luketina, D.A., and J. Imberger, 1987: Characteristics of a surface buoyant jet. *J. Geophys. Res.*, **92**, 5435-5447.
- Maddox, R.A., 1980: Mesoscale convective complexes. *Bull. Amer. Meteor. Soc.*, **61**, 1374-1387.
- Mahoney, W.P., 1983: The development of downdrafts from the evaporation of hydrometeors. *Report No. AS-144*, University of Wyoming, Laramie, 146 pp.
- Mahoney, W.P., 1988: Gust front characteristics and the kinematics associated with interacting thunderstorm outflows. *Mon. Wea. Rev.*, **116**, 1474-1491.
- Mahoney, W.P., and A.R. Rodi, 1987: Aircraft measurements on microburst development from hydrometeor evaporation. *J. Atmos. Sci.*, **44**, 3037-3051.
- Mahoney, W.P., and K.L. Elmore, 1989: The source region and evolution of a microburst downdraft. Preprints, *24th Conference on Radar Meteorology*, Tallahassee, Amer. Meteor. Soc., 154-157.
- Malanotte-Rizzoli, P., 1982: Planetary solitary waves in geophysical flows. *Adv. Geophys.*, **24**, 147-224.
- Marshall, J.S., and W. McK. Palmer, 1948: The distribution of raindrops with size. *J. Meteor.*, **5**, 165-166.
- Marwitz, J.D., 1972: The structure and motion of severe hailstorms. Part II: Multicell storms. *J. Appl. Meteor.*, **11**, 180-188.
- Matsuno, Y., 1984: *Bilinear Transformation Method*. Academic Press, 223 pp.
- Maxon, S., and J. Viacelli, 1974: Cylindrical solitons. *Phys. Fluids*, **17**, 1614-1616.
- Maxworthy, T., 1972: The structure and stability of vortex-rings. *J. Fluid Mech.*, **51**, 15-32.
- Maxworthy, T., 1974: Turbulent vortex rings. *J. Fluid Mech.*, **64**, 227-239.
- Maxworthy, T., 1980: On the formation of nonlinear internal waves from the gravitational collapse of mixed regions in two and three dimensions. *J. Fluid Mech.*, **96**, 47-64.

- Maxworthy, T., 1983: Gravity currents with variable inflow. *J. Fluid Mech.*, **128**, 247–257.
- McCarthy, J., J.W. Wilson, and T.T. Fujita, 1982: The Joint Airport Weather Studies Project. *Bull. Amer. Meteor. Soc.*, **63**, 15–22.
- McClimans, T.A., 1978: Fronts in fjords. *Geophys. Astrophys. Fluid Dynamics*, **11**, 23–34.
- Melville, W.K., 1983: Wave modulation and breakdown. *J. Fluid Mech.*, **128**, 489–506.
- Metcalf, J.I., 1975: Gravity waves in a low-level inversion. *J. Atmos. Sci.*, **32**, 351–361.
- Middleton, G.V., 1966: Experiments on density and turbidity currents. *Can. J. Earth Sci.*, **3**, 523–546.
- Miles, J.W., 1978: An axisymmetric Boussinesq wave. *J. Fluid Mech.*, **84**, 181–191.
- Miles, J.W., 1980: Solitary waves. *Ann. Rev. Fluid Mech.*, **12**, 11–43.
- Miles, J.W., and L.N. Howard, 1964: Note on a heterogeneous shear flow. *J. Fluid Mech.*, **20**, 331–336.
- Miller, M.J., and M.W. Moncrieff, 1983: The dynamics and simulation of organized deep convection. Article 6.f in *Mesoscale Meteorology – Theories, Observations and Models*. Edited by D.K. Lilly and T. Gal-Chen. NATO ASI Series C: Mathematical and Physical Sciences, **114**, 451–496.
- Mitchell, K.E., and J.B. Hovermale, 1977: A numerical investigation of the severe thunderstorm gust front. *Mon. Wea. Rev.*, **105**, 657–675.
- Moran, J.M., and M.D. Morgan, 1989: *Meteorology. The Atmosphere and the Science of Weather*. Second edition, Macmillan Publishing Co., New York, pp. 337–338.
- Mueller, C.K., and R.E. Carbone, 1987: Dynamics of a thunderstorm outflow. *J. Atmos. Sci.*, **44**, 1879–1898.
- Nolen, R.H., 1959: A radar pattern associated with tornadoes. *Bull. Amer. Meteor. Soc.*, **40**, 277–279.
- Noonan, J.A., and R.K. Smith, 1985: Linear and weakly nonlinear internal wave theories applied to “Morning Glory” waves. *Geophys. Astrophys. Fluid Dynamics*, **33**, 123–143.
- Ono, H., 1975: Algebraic solitary waves in stratified fluids. *J. Phys. Soc. Japan*, **39**, 1082–1091.
- Orville, H.D., R.D. Farley, and J.P. Chen, 1986: Some important cloud microphysical factors in the creation of microbursts. *23rd Conference on Radar Meteorology*, Snowmass, Amer. Meteor. Soc. (Paper J12.2 hand-out at conference, did not appear in preprint volume).
- Paluch, I.R., 1979: The entrainment mechanism in Colorado cumuli. *J. Atmos. Sci.*, **36**, 2462–2478.
- Parsons, D.B., and R.A. Kropfli, 1990: Dynamics and fine structure of a microburst observed with dual-Doppler radar. Submitted to *J. Atmos. Sci.* in July.

- Peterson, E.C., 1985: JAWS microbursts occurring from orographic vortex streets. Preprints, *14th Conference on Severe Local Storms*, Indianapolis, Amer. Meteor. Soc., 256-259.
- Picknett, R.G., 1981: Dispersion of dense gas puffs released in the atmosphere at ground level. *Atmos. Environ.*, **15**, 509-525.
- Poreh, M., Y.G. Tsuei, and J.E. Cermak, 1967: Investigation of a turbulent radial wall jet. *J. Appl. Mech., Trans. ASME, Ser. E*, **34**, 457-463.
- Proctor, F.H., 1985: Numerical simulation of precipitation induced downbursts. Preprints, *2nd International Conference on the Aviation Weather System*, Montreal, Amer. Meteor. Soc., 257-264.
- Proctor, F.H., 1988a: Numerical simulation of the 2 August 1985 DFW microburst with the three-dimensional terminal area simulation system. Preprints, *15th Conference on Severe Local Storms*, Baltimore, Amer. Meteor. Soc., J99-J102.
- Proctor, F.H., 1988b: Numerical simulations of an isolated microburst. Part I: Dynamics and Structure. *J. Atmos. Sci.*, **45**, 3137-3160.
- Proctor, F.H., 1989: Numerical simulations of an isolated microburst. Part II: Sensitivity experiments. *J. Atmos. Sci.*, **46**, 2143-2165.
- Przybylinski, R.W., and D.M. DeCaire, 1985: Radar signatures associated with the derecho, a type of mesoscale convective system. Preprints, *14th Conference on Severe Local Storms*, Indianapolis, Amer. Meteor. Soc., 228-231.
- Purdum, J.F.W., 1982: Subjective interpretation of geostationary satellite data for nowcasting. *Nowcasting*, ed. by K.A. Browning, Academic Press, 149-166.
- Roberts, L., and T. Wan, 1985: A simplified model of the turbulent microburst. *NASA Tech. Report JIAA-TR-59*, 20 pp.
- Roberts, R.D., and J.W. Wilson, 1986: Nowcasting microburst events using single Doppler radar data. Preprints, *23rd Conference on Radar Meteorology*, Snowmass, Amer. Meteor. Soc., R14-R17.
- Rodi, A.R., K.L. Elmore, and W.P. Mahoney, 1983: Aircraft and Doppler air motion comparisons in a JAWS microburst. Preprints, *21st Conference on Radar Meteorology*, Edmonton, Amer. Meteor. Soc., 624-629.
- Rottman, J.W., and J.E. Simpson, 1984: The initial development of gravity currents from fixed-volume releases of heavy fluids. *Symposium on Atmospheric Dispersion of Heavy Gases and Small Particles*, Int. Union of Theor. and Appl. Mech. (IUTAM), Delft, The Netherlands, ed. by G. Ooms and H. Tennekes, Springer Verlag, 347-359.
- Rottman, J.W., and J.E. Simpson, 1989: The formation of internal bores in the atmosphere: A laboratory model. *Quart. J. Roy. Meteor. Soc.*, **115**, 941-963.
- Rudich, R.D., 1986: Weather-involved U.S. air carrier accidents 1962-1984: A compendium and brief summary. *AIAA 24th Aerospace Sciences Meeting*, AIAA-86-0327, Reno, 7 pp.

- Russell, J.S., 1845: Report on waves. *Rep. 14th Meet. Brit. Assoc. Adv. Sci.*, York, 1844, London: John Murray, 311–390.
- Scarpace, F.L., and T. Green, 1973: Dynamic surface temperature structure of thermal plumes. *Water Resources Res.*, **9**, 138–153.
- Schlesinger, R.W., 1984: Mature thunderstorm cloud-top structure and dynamics. A three-dimensional numerical study. *J. Atmos. Sci.*, **41**, 1551–1570.
- Schultz, T.A., 1988: A multiple-vortex-ring model of the DFW microburst. *AIAA 26th Aerospace Sciences Meeting*, AIAA-88-0605, Reno, 8 pp.
- Scorer, R.S., 1985: A vivid mechanical picture of turbulence. Article in *Turbulence and Diffusion in Stable Environments*, edited by J.C.R. Hunt. Oxford:Clarendon Press, 97–110.
- Scott, A.C., F.Y.F. Chu, and D.W. McLaughlin, 1973: The soliton: A new concept in applied science. *Proc. IEEE*, **61**, 1443–1483.
- Seitter, K.L., 1986: A numerical study of atmospheric density current motion including the effects of condensation. *J. Atmos. Sci.*, **43**, 3068–3076.
- Seitter, K.L., and H.S. Muench, 1985: Observation of a cold front with rope cloud. *Mon. Wea. Rev.*, **113**, 840–848.
- Shapiro, A.M., and G.S. Benton, 1988: A similarity model of axisymmetric convection. Preprints, *15th Conference on Severe Local Storms*, Baltimore, Amer. Meteor. Soc., J87–J92.
- Shapiro, M.A., 1984: Meteorological tower measurements of a surface cold front. *Mon. Wea. Rev.*, **112**, 1634–1639.
- Shapiro, M.A., T. Hampel, D. Rotzoll, and F. Mosher, 1985: The frontal hydraulic head: a micro- α scale (~ 1 km) triggering mechanism for mesoconvective weather systems. *Mon. Wea. Rev.*, **113**, 1166–1183.
- Shreffler, J.H., and F.S. Binkowski, 1981: Observations of pressure jump lines in the midwest, 10–12 August 1976. *Mon. Wea. Rev.*, **109**, 1713–1725.
- Simpson, J.E., 1969: A comparison between laboratory and atmospheric density currents. *Quart. J. Roy. Meteor. Soc.*, **95**, 758–765.
- Simpson, J.E., 1972: Effects of the lower boundary on the head of a gravity current. *J. Fluid Mech.*, **53**, 759–768.
- Simpson, J.E., 1987: *Gravity Currents in the Environment and the Laboratory*. Ellis Horwood Ltd., 244 pp.
- Simpson, J.E., D.A. Mansfield, and J.R. Milford, 1977: Inland penetration of sea-breeze fronts. *Quart. J. Roy. Meteor. Soc.*, **103**, 47–76.
- Simpson, J.E., and R.E. Britter, 1979: The dynamics of the head of a gravity current advancing over a horizontal surface. *J. Fluid Mech.*, **94**, 477–495.

- Simpson, J.E., and R.E. Britter, 1980: A laboratory model of an atmospheric mesofront. *Quart. J. Roy. Meteor. Soc.*, **106**, 485–500.
- Sinclair, P.C., 1973: Severe storm velocity and temperature structure deduced from penetrating aircraft. Preprints, *8th Conference on Severe Local Storms*, Amer. Meteor. Soc., 25–31.
- Sinclair, P.C., J.F.W. Purdom, and R.E. Dattore, 1988: Thunderstorm outflow structure. Preprints, *15th Conference on Severe Local Storms*, Baltimore, Amer. Meteor. Soc., 233–239.
- Smith, M., 1986: Visual observations of Kansas downbursts and their relation to aviation weather. *Mon. Wea. Rev.*, **114**, 1612–1616.
- Smith, R.K., 1988: Travelling waves and bores in the lower atmosphere: The “Morning Glory” and related phenomena. *Earth–Sci. Rev.*, **25**, 267–290.
- Smith, R.K., and M.J. Reeder, 1988: On the movement and low-level structure of cold fronts. *Mon. Wea. Rev.*, **116**, 1927–1944.
- Smyth, W.D., and W.R. Peltier, 1989: The transition between Kelvin–Helmholtz and Holmboe instability: An investigation of the overreflection hypothesis. *J. Atmos. Sci.*, **46**, 3698–3720.
- Sohl, C.J., W.L. Read, M.L. Branick, J.C. Lowery, and C.P. Jansen, 1987: Observed microbursts in the NWS Southern Region during 1986: Four case studies. *NOAA Tech. Memo. NWS SR-121*, 45 pp.
- Squires, P., 1958: Penetrative downdraughts in cumuli. *Tellus*, **10**, 381–389.
- Srivastava, R.C., 1967: A study of the effect of precipitation on cumulus dynamics. *J. Atmos. Sci.*, **24**, 36–45.
- Srivastava, R.C., 1985: A simple model of evaporatively driven downdraft: Application to a microburst downdraft. *J. Atmos. Sci.*, **42**, 1004–1023.
- Srivastava, R.C., 1987: A model of intense downdrafts driven by the melting and evaporation of precipitation. *J. Atmos. Sci.*, **44**, 1752–1773.
- Stern, M.E., 1975: *Ocean Circulation Physics*, Academic, New York.
- Stewart, O., 1958: *Danger in the Air*, Philosophical Library, New York. 195 pp.
- Straka, J., 1989: Hail growth in a highly glaciated central high plains multi-cellular hailstorm. Ph.D. Thesis, University of Wisconsin–Madison, 413 pp.
- Talman, C.F., 1907: Notes from the Weather Bureau library – Thunderstorms and squalls. *Mon. Wea. Rev.*, **35**, 264.
- Targ, R., and R.L. Bowles, 1988: Windshear avoidance: Requirements and proposed system for airborne lidar detection. *Airborne and Spaceborne Lasers for Terrestrial Geophysical Sensing*, *SPIE Vol. 889*, 54–64.
- Talagrand, O. and P. Courtier, 1987: Variational assimilation of meteorological observations with the adjoint vorticity equation. I. Theory. *Quart. J. Roy. Meteor. Soc.*, **113**, 1311–1328.

- Telford, J.W., 1975: Turbulence, entrainment and mixing in cloud dynamics. *Pure Appl. Geophys.*, **113**, 1067–1084
- Tepper, M., 1950: A proposed mechanism of squall lines: The pressure jump line. *J. Meteor.*, **7**, 21–29.
- Teske, M.E., and W.S. Lewellen, 1977: Turbulent transport model of a thunderstorm gust front. Preprints, *10th Conference on Severe Local Storms*, Omaha, Amer. Meteor. Soc., 143–150.
- Thomas, N.H., and J.E. Simpson, 1985: Mixing of gravity currents in turbulent surroundings: Laboratory studies and modelling implications. In *Turbulence and Diffusion in Stable Environments*, ed. by J.C.R. Hunt, Clarendon Press, Oxford, 61–95.
- Thorpe, A.J., M.J. Miller, and M.W. Moncrieff, 1980: Dynamical models of two-dimensional downdraughts. *Quart. J. Roy. Meteor. Soc.*, **106**, 463–484.
- Thorpe, S.A., 1968: A method of producing shear in a stratified fluid. *J. Fluid Mech.*, **32**, 693–704.
- Tripoli, G.J., and W.R. Cotton, 1986: An intense, quasi-steady thunderstorm over mountainous terrain. Part IV. Three-dimensional numerical simulation. *J. Atmos. Sci.*, **43**, 894–912.
- Tung, K.K., T.F. Chan, and T. Kubota, 1982: Large amplitude internal waves of permanent form. *Stud. Appl. Math.*, **66**, 1–44.
- Turnbull, D., J. McCarthy, J. Evans, D. Zrnic', 1989: The FAA Terminal Doppler Weather Radar (TDWR) program. Preprints, *3rd International Conference on the Aviation Weather System*, Anaheim, 414–419.
- Turner, J.S., 1973: *Buoyancy Effects in Fluids*. Cambridge University Press, 368 pp.
- Tuttle, J.D., V.N. Bringi, H.D. Orville, and F.J. Kopp, 1989: Multiparameter radar study of a microburst: Comparison with model results. *J. Atmos. Sci.*, **46**, 601–620.
- U.S. Weather Bureau, 1948: A report on thunderstorm conditions affecting flight operations. *Technical Paper No. 7*, Washington DC, April, 32 pp.
- Viemeister, P.E., 1961: *The Lightning Book*. Original edition: Doubleday, Garden City, NY. Second edition: MIT Press, Cambridge MA, 1972, 316 pp.
- Vliegthart, A.C., 1971: On finite-difference methods for the Korteweg–deVries equation. *J. Engin. Math.*, **5**, 137–155.
- Wakimoto, R.M., 1981: Investigations of thunderstorm gust fronts from Project NIMROD data. Ph.D. Thesis, The University of Chicago, 129 pp.
- Wakimoto, R.M., 1982: The life cycle of a thunderstorm gust front as viewed with Doppler radar and rawinsonde data. *Mon. Wea. Rev.*, **110**, 1060–1082.
- Wakimoto, R.M., 1985: Forecasting dry microburst activity over the high plains. *Mon. Wea. Rev.*, **113**, 1131–1143.
- Wakimoto, R.M., 1988: Operational aspects of a microburst-producing storm during MIST. Preprints, *15th Conference on Severe Local Storms*, Baltimore, Amer. Meteor. Soc., 384–387.

- Wakimoto, R.M., and V.N. Bringi, 1988: Dual polarization observations of microbursts associated with intense convection: The 20 July storm during the MIST project. *Mon. Wea. Rev.*, **116**, 1521–1539.
- Wakimoto, R.M., and J.W. Wilson, 1989: Non-supercell tornadoes. *Mon. Wea. Rev.*, **117**, 1113–1140.
- Wakimoto, R.M., C.J. Kessinger, and D.E. Kingsmill, 1989: Visual and dual-Doppler analysis of low-reflectivity microbursts. Preprints, *24th Conference on Radar Meteorology*, Tallahassee, Amer. Meteor. Soc., 77–80.
- Waranauskas, B.R., 1985: The rotor microburst: A new explanation for burst swath damage. Preprints, *14th Conference on Severe Local Storms*, Indianapolis, Amer. Meteor. Soc., 260–263.
- Weidman, P.D., and R. Zakhem, 1988: Cylindrical solitary waves. *J. Fluid Mech.*, **191**, 557–573.
- Weisman, M.L., and J.B. Klemp, 1982: The dependence of numerically simulated convective storms on vertical wind shear and buoyancy. *Mon. Wea. Rev.*, **110**, 504–520.
- Weisman, M.L., J.B. Klemp, and J.W. Wilson, 1983: Dynamic interpretation of notches, WERs, and mesocyclones simulated in a numerical model. Preprints, *21st Conference on Radar Meteorology*, Edmonton, Amer. Meteor. Soc., 39–43.
- Weisman, M.L., and J.B. Klemp, 1984: The structure and classification of numerically simulated convective storms in directionally varying wind shears. *Mon. Wea. Rev.*, **112**, 2479–2498.
- Wexler, R., 1955: An evaluation of the physical effects in the melting layer. Proceedings, *5th Conference on Weather Radar*, Ft. Monmouth, Amer. Meteor. Soc., 329–334.
- Whitham, G.B., 1974: *Linear and Nonlinear Waves*. Wiley & Sons, 636 pp.
- Wilson, J.W., R.D. Roberts, C. Kessinger, and J. McCarthy, 1984: Microburst wind structure and evaluation of Doppler radar for airport wind shear detection. *J. Climate Appl. Meteor.*, **23**, 898–915.
- Wilson, J.W., and W.E. Schreiber, 1986: Initiation of convective storms at radar-observed boundary-layer convergence lines. *Mon. Wea. Rev.*, **114**, 2516–2536.
- Wingrove, R.C., and R.E. Bach, 1987: Severe winds in the DFW microburst measured from two aircraft. *AIAA Guidance, Navigation, and Control Conference*, AIAA-87-2340, 477–482.
- Wolfson, M.M., 1983: Doppler radar observations of an Oklahoma downburst. Preprints, *21st Conference on Radar Meteorology*, Edmonton, Amer. Meteor. Soc., 590–595 and S.M. Thesis, Department of Meteorology and Oceanography, Massachusetts Institute of Technology, 99 pp.
- Wolfson, M.M., 1988a: Characteristics of microbursts observed in the continental U.S. Preprints, *15th Conference on Severe Local Storms*, Baltimore, Amer. Meteor. Soc., 372–379.
- Wolfson, M.M., 1988b: Characteristics of microbursts in the continental United States. *The Lincoln Laboratory Journal*, **1**, 49–74.

- Wolfson, M.M., 1989: The FLOWS automatic weather station network. *J. Atmos. Oceanic Technol.*, **6**, 307-326.
- Wolfson, M.M., J.T. DiStefano, and D.L. Klinge, 1984: An automatic weather station network for low-altitude wind shear investigations. *Project Report ATC-128*, MIT/Lincoln Laboratory, FAA Report No. *DOT-FAA-PM-84/13*, 58 pp.
- Wolfson, M.M., J.T. DiStefano, and B.E. Forman, 1986: The FLOWS automatic weather station network in operation. *Project Report ATC-134*, MIT/Lincoln Laboratory, FAA Report No. *DOT-FAA-PM-85/27*, 266 pp.
- Wood, I.R., 1966: Studies in unsteady self preserving turbulent flows. *Univ. of South Wales, Water Research Lab.*, Report No. 81.
- Yau, M.K., 1979: Perturbation pressure and cumulus convection. *J. Atmos. Sci.*, **36**, 690-694.
- Young, G.S., and R.H. Johnson, 1984: Meso- and microscale features of a Colorado cold front. *J. Climate Appl. Meteor.*, **23**, 1315-1325.
- Young, J.W., F.D. Lane, and A.J. Bedard, 1989: The effect of a ground-based inversion layer on an impacting microburst. *AIAA 27th Aerospace Sciences Meeting*, AIAA-89-0810, Reno, 7 pp.
- Zabusky, N.J., and M.D. Kruskal, 1965: Interaction of "solitons" in a collisionless plasma and the recurrence of initial states. *Phys. Rev. Lett.*, **15**, 240-243.
- Zeman, O., 1982: The dynamics and modeling of heavier-than-air, cold gas releases. *Atmos. Environ.*, **16**, 741-751.
- Zorpette, G., 1986: The menacing microburst. *IEEE Spectrum*, **23**, 50-56.

BIOGRAPHICAL NOTE

Marilyn Mitchell Wolfson

Professional Experience

- 1983 **Staff Member**
to MIT Lincoln Laboratory Air Traffic Surveillance Systems
present Meteorological studies related to aviation avoidance of hazardous weather
- 1982 **Research Assistant** (with Kerry Emanuel)
to MIT Department of Meteorology
1983 Case study using Doppler radar data of downburst thunderstorm (graduated with Master's degree February, 1983)
- 1980 **Research Assistant** (with Sushil Atreya)
University of Michigan Department of Atmospheric and Oceanic Sciences
Thermodynamic study of Jovian atmosphere
- 1979 **Summer Fellow** (with Wei-Chyung Wang and William Rossow)
NASA Goddard Institute for Space Studies - Columbia University
Climate sensitivity of radiative-convective climate model with cloud feedback

Education

- Ph.D.** 1990 Meteorology, Massachusetts Institute of Technology.
Thesis: Understanding and Predicting Microbursts
- S.M.** 1983 Meteorology, Massachusetts Institute of Technology.
Thesis: Doppler Radar Observations of an Oklahoma Downburst.
- B.S.** 1979 Atmospheric Science, University of Michigan College of Engineering, *Magna Cum Laude.*

Honors and Awards

- MIT Lincoln Laboratory Staff Associate Ph.D. Program, 1985-1990
- Sigma Xi, scientific honor society, Associate member, 1983; Full Member, 1988
- Ida M. Green Fellow, MIT, 1980-1981
- National Science Foundation Graduate Fellowship, Honorable mention, 1980
- NASA Goddard Institute for Space Studies Summer Fellowship
Planetary Atmospheres and Climate Program, 1979

Outstanding Achievement Award, Undergraduate in Atmospheric Science
University of Michigan, 1979

Tau Beta Pi, engineering honor society, Member, 1979

Dean's List, University of Michigan College of Engineering, 1977-1979

Professional Societies and Committees

American Meteorological Society, Member

American Meteorological Society Committee on Severe Local Storms
3 year term beginning January, 1988

PUBLICATIONS

Journal Articles

Wolfson, M.M., 1989: The FLOWS automatic weather station network. *J. Atmos. Ocean. Technol.*, **6**, 307-326.

Wolfson, M.M., and T.T. Fujita, 1989: Correcting wind speed measurements for site obstructions. *J. Atmos. Ocean. Technol.* **6**, 343-352.

Wolfson, M.M., 1988: Characteristics of microbursts in the continental United States. *The Lincoln Laboratory Journal*, **1**, 47-72.

Klinge, D.K., D.R. Smith, and M.M. **Wolfson**, 1987: Gust front characteristics as detected by Doppler radar. *Mon. Wea. Rev.*, **115**, 905-918.

Wang, W.C., W.B. Rossow, M.S. Yao, and M.M. **Wolfson**, 1981: Climate sensitivity of a one-dimensional radiative-convective model with cloud feedback. *J. Atmos. Sci.*, **38**, 1167-1178.

Conference Papers

Wolfson, M.M., 1988: Characteristics of microbursts observed in the continental U.S. *Preprints, 15th Conference on Severe Local Storms*, Baltimore, Amer. Meteor. Soc., 372-379.

Wolfson, M.M., 1987: The FLOWS automatic weather station network. *Preprints, 6th Symposium on Meteorological Observations and Instrumentation*, New Orleans, Amer. Meteor. Soc., 294-299.

Wolfson, M.M., and T.T. Fujita, 1987: Correcting wind speed measurements for site obstructions. *Preprints, 6th Symposium on Meteorological Observations and Instrumentation*, New Orleans, Amer. Meteor. Soc., 358-363.

Wolfson, M.M., J.T. DiStefano, and T.T. Fujita, 1985: Low-altitude wind shear characteristics in the Memphis, TN area based on mesonet and LLWAS data. *Preprints, 14th Conference on Severe Local Storms*, Indianapolis, Amer. Meteor. Soc., 322-327.

Wolfson, M.M., 1983: Doppler radar observations of an Oklahoma downburst. *Preprints, 21st Conference on Radar Meteorology*, Edmonton, Amer. Meteor. Soc., 590-595.

Lincoln Laboratory Project Reports

Donovan, M.F., and **M.M. Wolfson**, 1988: Selected Dual Doppler wind shear events during the 1987 Operational Test and Evaluation of the Enhanced LLWAS system at Stapleton International Airport. *Project Report ATC-158*, MIT/Lincoln Laboratory, FAA Report No. *DOT/FAA/PS-88-9*, 146 pp.

Wolfson, M.M. and M.J. Iacono, 1987: A comparison of PAM-II and FLOWS mesonet data during COHMEX. *Project Report ATC-154*, MIT/Lincoln Laboratory, FAA Report No. *DOT/FAA/PM-87-36*, 47 pp.

Rinehart, R.E., J.T. DiStefano, and **M.M. Wolfson**, 1987: Preliminary Memphis FAA/Lincoln Laboratory Operational Weather Studies Results. *Project Report ATC-141*, MIT/Lincoln Laboratory, FAA Report No. *DOT/FAA/PM-86-40*, 198 pp.

Wolfson, M.M., J.T. DiStefano, and B.E. Forman, 1986: The FLOWS automatic weather station network in operation. *Project Report ATC-134*, MIT/Lincoln Laboratory, FAA Report No. *DOT/FAA/PM-85-27*, 266 pp.

Wolfson, M.M., J.T. DiStefano, and D.L. Klinge, 1984: An automatic weather station network for low-altitude wind shear investigations. *Project Report ATC-128*, MIT/Lincoln Laboratory, FAA Report No. *DOT/FAA/PM-84-13*, 58 pp.